JANUARY 1980

Low Enrichment Fuel Evaluation and Analysis Program

Summary Report for the Period
January, 1979 - December, 1979

WILLIAM KERR, Project Director

Department of Nuclear Engineering
and the
Michigan-Memorial Phoenix Project

January, 1980

LOW ENRICHMENT FUEL EVALUATION AND ANALYSIS PROGRAM

Summary Report for the Period
January, 1979 - December, 1979

William Kerr, Project Director
Department of Nuclear Engineering
and the
Michigan-Memorial Phoenix Project
The University of Michigan
Ann Arbor, Michigan

Project Participants

William Kerr

John S. King

John C. Lee

William R. Martin

Reed R. Burn

Forrest B. Brown

David C. Losey

David K. Wehe

Keith Flint

CONTENTS

FIGURES

TABLES

I. Introduction

The University of Michigan Department of Nuclear Engineering and the Michigan-Memorial Phoenix Project are engaged in a cooperative effort with Argonne National Laboratory to test and analyze low enrichment fuel in the Ford Nuclear Reactor. The effort is one element of the Reduced Enrichment Research and Test Reactor (RERTR) Program, which is itself one facet of the overall U.S. policy seeking to minimize the risk of nuclear weapons proliferation. The principal RERTR program objective is to improve the proliferation resistance of nuclear fuels used in research and test reactors by providing the technical means for reducing the uranium enrichment in these fuels to substantially less than the 90% to 93% enrichment currently used.

The key technical basis of the program is to reduce the uranium enrichment while increasing, at the same time, the uranium loading of each fuel element in order to compensate for the reactivity loss due to the larger ^{238}U content. The required uranium loading can be achieved by increasing the uranium density in the fuel meat and by increasing the fuel volume fraction while ensuring that fuel elements operate within their thermal-hydraulic limits.

A near-term objective of the program is to demonstrate and implement enrichment reductions from 93% to 20% or, where that is impractical, to 45% within the next two years, based on currently qualified fuel fabrication technology. A key ingredient of the effort to meet this objective is a whole-core demonstration with reduced enrichment fuel. This will allow detailed testing and evaluation of the low enrichment fuel and its impact on research and test reactor performance and utilization.

The Ford Nuclear Reactor (FNR) at the University of Michigan has been selected for the low-power whole-core demonstration. This demonstration project includes development of methods to analyze MTR-type fuel and core configurations, assisting in the design and analysis of the low enrichment fuel, preparation of fuel procurement specifications, preparing the requisite safety analysis report revision and license amendment application, procuring the operating license amendment, planning and conducting the experimental program, and analyzing the results of the experiments, including comparisons with analytical predictions. This effort has been divided into various phases. The initial phase includes the work necessary to design and specify the fuel, to obtain approval of the necessary license amendments, to define the experimental program, and to experimentally characterize the current FNR core

to provide a basis for comparison with the low enrichment core. Subsequent phases will include the actual whole-core testing of the low enrichment fuel along with the necessary measurements and analysis of the experimental results. In addition, this later work will include further verification and improvement of calculational methods beyond that completed in the initial phase. Thus at the conclusion of this program, the impact of the low enrichment fuel on the FNR performance and utilization will have been assessed experimentally and compared with analytical predictions using the methods developed in the course of this investigation. These methods should also be of general use for analysis of other research and test reactor configurations.

The current status of the program is reflected in this summary report and is summarized in Section VII. Because of delays in procuring the low enrichment fuel for the FNR, the work in the initial and subsequent phases has overlapped somewhat, and the distinction between the various phases is no longer clear. Overall, though, it would appear that the initial phase is basically complete, and effort is now being aimed at refining the experimental program and the analytical models, and comparing experimental results and analytical predictions of the current FNR core.

This report is organized into sections corresponding generally to the technical tasks outlined in the Statement of Work dated December 18, 1978. It should be noted that the draft revision to the Safety Analysis Report has been included as Appendix A to this report in order to minimize the amount of duplicate effort and results. Section VII of this report contains a summary and conclusions we have arrived at to date. Also, recommendations for further effort have been included.

II. Generic Neutronic Model Development and Verification

The FNR currently uses highly enriched uranium (HEU) MTR-type fuel. To provide the means for a valid prediction of the impact of low enriched uranium (LEU) fuel on FNR operation, safety, and research usage, a generic neutronics model has been developed. This model is based on standard, well-verified production codes which are routinely used in reactor analyses. These codes have been modified only when necessary to accommodate the special characteristics of small low-power research reactors with plate-type fuel. As such, the methods of analysis should be applicable to a large number of research reactors and accessible to many computing installations. Summaries of the calculational model are presented in References 1 and 2, and in Appendix A. The following sections provide a detailed description of the calculational model and its verification.

A. Computer Codes - Modifications and Verification

A brief description of the codes used is given in Table 1. The following subsections detail the modifications, verification, and special considerations for each code.

1. LEOPARD

a. Modifications to LEOPARD

The LEOPARD code is a spectrum analysis code orginally developed for application to commercial light water reactor lattices consisting of cylindrical fuel rods. The code performs a unit cell analysis on a "supercell" consisting of a lattice or periodic portion of the core and a nonlattice region. Our modifications, listed in Table 2, permit the analysis of MTR-type plate geometry and provide increased flexibility in code usage. Except for the slab geometry option, no changes were made in the basic calculational model used by the LEOPARD code.

b. Verification of the Modified LEOPARD Code

The LEOPARD code contains many engineering approximations to reduce computation time and utilizes an early industrial cross section data base. To assess its applicability to the analysis of HEU and LEU plate-type fuel, comparisons were made with critical experiments and more accurate calculations.

A comparison of measured and calculated parameters for two TRX rodded UO_2 critical lattices[14] shown in Table 3 illustrates the typical accuracy of the LEOPARD code for lattices of 1.3% enriched fuel rods.

Table 1. List of Neutronics Computer Codes

Code Name	Project Use	Comments	References
LEOPARD	- generate few-group constants - depletion	0-D unit cell 54 fast groups (MUFT) 172 thermal gps. (SOFOCATE) B-1 leakage correction	3,4
HAMMER	- generate few-group constants - verify LEOPARD - control rod calculations	1-D integral transport 54 fast groups 30 thermal groups THERMOS scheme B-1 leakage correction ENDF/B-IV library	5
2DB	- compute k_{eff}, flux + power + burnup distributions	2-D diffusion theory depletion capability	6
ANISN	- ex-core flux	1-D discrete ordinates transport theory	7
TWOTRAN	- control rod calculations	2-D discrete ordinates transport theory	8
VENTURE	- benchmark 3-D calculations - determine transverse buckling for 2DB	3-D diffusion theory	9
PDQ7	- benchmark 3-D calculations	3-D diffusion theory	10
1DX	- leakage flux calculations	1-D diffusion theory	11

Table 2. Modifications to the LEOPARD Code

Modification	Purpose	Method	Reference
Slab geometry option	analysis of plate-type fuel	•ABH method for thermal disadvantage factors for slabs •volume fractions, mean chord length, Dancoff factor redefined for slabs •minor input changes	12 13
lattice/non-lattice edits	allow separate few-group constants for lattice and inactive side plates	neutron conservation, with separate disadvantage factors for lattice region	
σ_a^{Xe} edited separately	allow for space-dependent xenon feedback in 2DB	remove Σ_a^{Xe} from few-group constants, pass σ_a^{Xe} to 2DB	
output few-group constant tablesets as functions of depletion	automate data transfer to 2DB allow interpolation in 2DB based on depletion	create output file compatible with modified 2DB	
restart capability	allow parametric calculations at any depletion step	save all parameters needed to re-initialize code	
added thermal expansion coefficient for Al.	allow thermal expansion of meat and clad	minor addition to input routine	
allow input multiplier for fission product buildup factor	burnup >> commercial reactor, correlation in code must be extended	minor input change	

Table 3. TRX Rodded UO_2 Critical Lattice Results

	W/F = 2.35			W/F = 4.02		
Parameter[a]	experiment[b]	LEOPARD	% Difference	experiment	LEOPARD	% difference
ρ^{28}	1.311	1.2763	-2.6%	.83	.7792	- 6.1%
δ^{25}	.0981	.0999	+1.8%	.0608	.0608	----
δ^{28}	.0914	.0893	-2.3%	.0667	.0596	-10.6%
CR*	.792	.7703	-2.7%	.644	.6218	- 3.4%
B^2	.0057	.00557	-2.3%	.005469	.00526	- 3.8%
k[c]	1.0	.9965	.35%	1.0	.9944	.56%

Notes: (a) $\rho^{28} = \frac{\text{U-238 epithermal capture}}{\text{U-238 thermal capture}}$

$\delta^{25} = \frac{\text{U-235 epithermal fission}}{\text{U-235 thermal fission}}$

$\delta^{28} = \frac{\text{U-238 fissions}}{\text{U-235 fissions}}$

$CR^* = \frac{\text{U-238 captures}}{\text{U-235 fissions}}$

B^2 = critical buckling

(b) WAPD-TM-931 (1970)

(c) Measured value assumed to be 1.0; calculated value is based on LEOPARD run with measured critical buckling input

A similar comparison is given in Table 4 for a very severe test - the TRX natural uranium slab criticals.[14] These experiments consisted of 11 one -inch thick natural uranium slabs driven to criticality by the leakage from a highly enriched driver lattice. As discussed in Reference 15, we believe calculated results compare reasonably well with the experiments, considering especially that the very large fuel plate thickness invalidates some assumptions of the LEOPARD code. Based on these comparisons, the LEOPARD code and its data base appear adequate for our analysis.

A more reasonable test of the modified LEOPARD code is given in Table A.4, where LEOPARD is compared with the more accurate HAMMER code for typical LEU and HEU MTR-type fuels. This comparison shows that results from the modified LEOPARD code are in good agreement with the more accurate and expensive integral transport calculations. For both the HEU and LEU plate-type fuel shown in Table A.4 and for numerous other cases we have examined, LEOPARD accurately predicts integral parameters (k_∞, ϕ_1/ϕ_2, material buckling, etc.) and shows reasonable agreement for few-group constants. We were unable to identify any significant errors in few-group constants and have concluded that differences illustrated by Table A.4 are principally due to the differences in the libraries utilized, i.e., the ENDF/B-IV data set used with the EPRI-HAMMER code vs. an early industrial data set used with the LEOPARD code.

Due to the short computing time and low cost of the LEOPARD code, coupled with its reasonable accuracy and depletion capability, we have used it for generating few-group constants for all routine core physics analysis.

c. Special Considerations in Applying LEOPARD to the FNR

(1) Particular care must be used in treating the non-lattice portion of a fuel assembly using the LEOPARD code. For both regular and special fuel assemblies for the FNR core, shown in Figures 1 and 2, the lattice region consists of the active portions of fuel plates and associated clad and moderator. The non-lattice region includes the inactive portions of fuel plates and associated water, the side plates, inter-assembly water gap, and (for special assemblies) the central waterhole and control rod guides. While LEOPARD will treat the fuel, clad, and moderator of the lattice explicitly, the non-lattice region must be homogenized by volume weighting.

Table 4. TRX Natural Uranium Slab Criticals

	W/F = .5			W/F = 1.09		
Parameter[a]	experiment[b]	LEOPARD	% difference	experiment	LEOPARD	% difference
ρ^{28}	2.63	2.591	-1.5%	1.21	1.106	- 8.6%
δ^{25}	.267	.326	-22%	.124	.147	+18.6%
δ^{28}	.264	.268	+1.5%	.190	.176	- 7.4%
CR*	2.056	1.910	-7.1%	1.387	1.283	- 7.5%
B^2	-.0037	-.0029	+22%	-.0013	-.00091	+30.0%
k[c]	1.0	1.028	+2.8%	1.0	1.011	+ 1.1%

Notes: (a) $\rho^{28} = \frac{\text{U-238 epithermal capture}}{\text{U-238 thermal capture}}$

$\delta^{25} = \frac{\text{U-235 epithermal fission}}{\text{U-235 thermal fission}}$

$\delta^{28} = \frac{\text{U-238 fissions}}{\text{U-235 fissions}}$

$CR^* = \frac{\text{U-238 captures}}{\text{U-235 fissions}}$

B^2 = critical buckling

(b) WAPD-TM-931 (1970)

(c) Measured value assumed to be 1.0; calculated value is based on LEOPARD run with measured critical buckling input

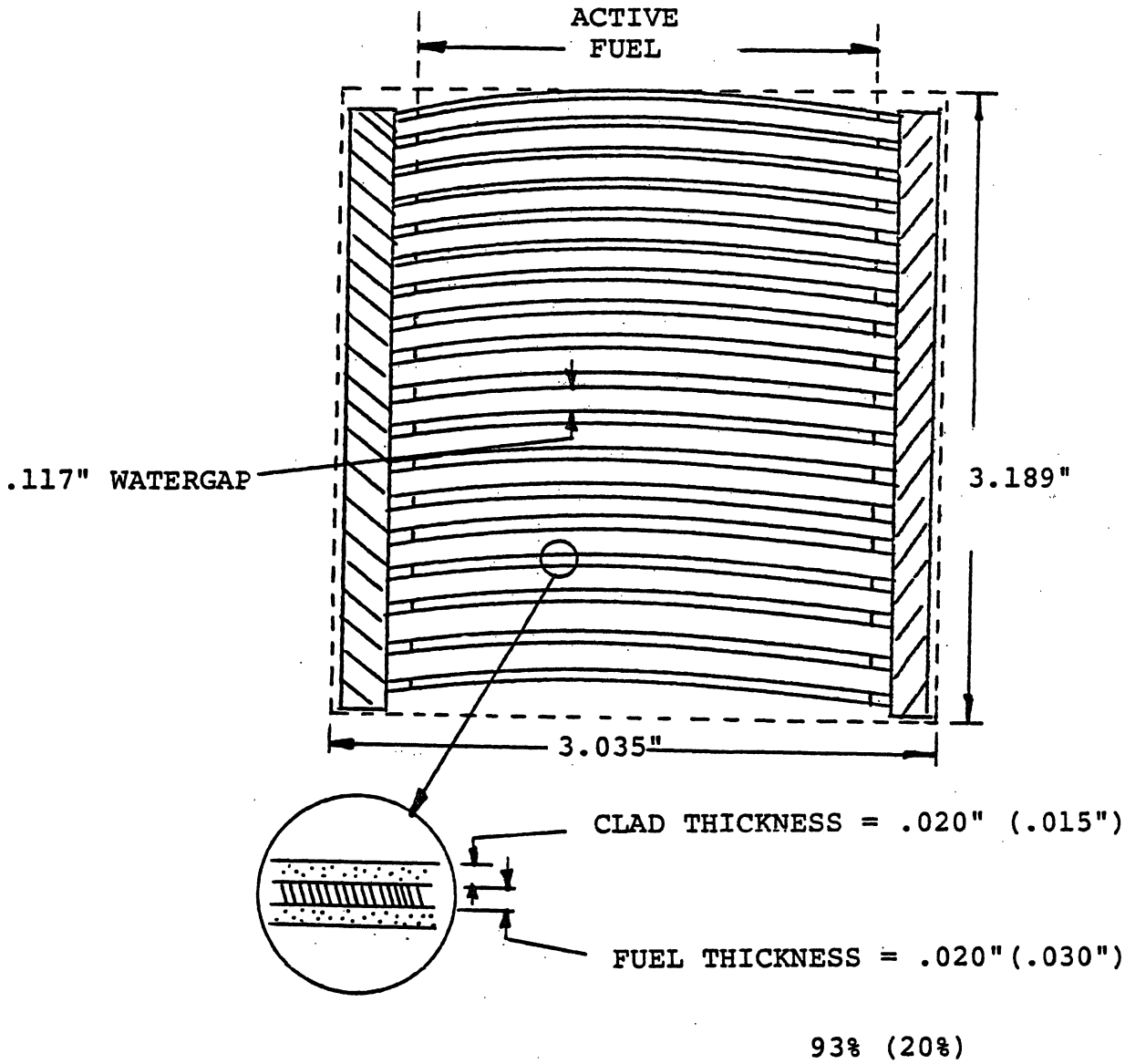

FIGURE 1. FNR REGULAR FUEL ELEMENT

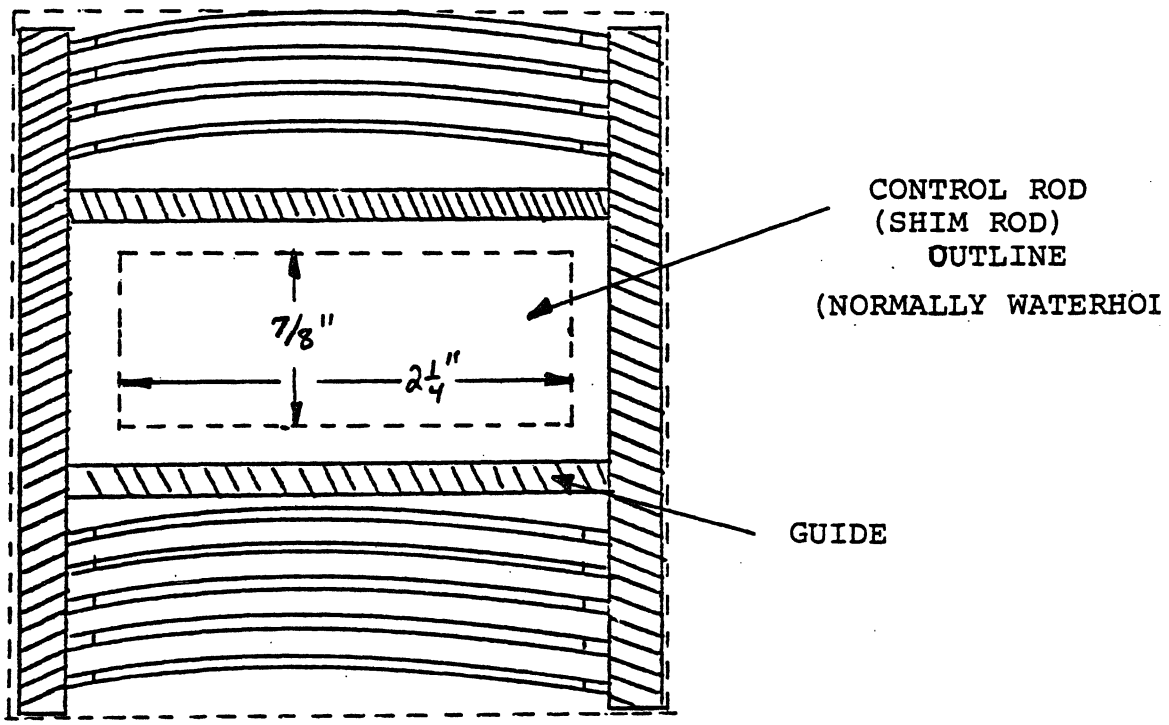

Figure 2. FNR Special Assembly

For the LEOPARD code to include the effects of the non-lattice region on the supercell spectrum, the user must input a non-lattice fraction (NLF) and a non-lattice peaking factor (NLPF). The NLF is computed readily as (non-lattice area)/(total assembly area). The NLPF is defined as a ratio of average thermal flux in the non-lattice to average moderator thermal flux in the lattice. Accurate NLPF's can only be obtained from more sophisticated calculations. Some results from these calculations are presented in Table 5. For regular assemblies, with small NLF, one-dimensional supercell calculations with the HAMMER code and two-dimensional fine-mesh 2DB calculations (with explicit representation of fuel plates and water channels) both yielded a NLPF of essentially 1.0. For special assemblies, the NLF=.588 and the geometry requires a two-dimensional approach. One-dimensional calculations for a half-assembly with the HAMMER and 2DB codes and with explicit representation of 4 or 5 fuel plates and the non-lattice region yielded a NLPF significantly greater than that predicted by a fine-mesh two-dimensional 2DB calculation for the equivalent configuration.

Our conclusion is that two-dimensional fine-mesh assembly-level calculations are necessary to determine the appropriate NLPF for input to LEOPARD. Further support for this conclusion is displayed in Figures 3, 4, and 5 where the thermal fluxes from fine-mesh 1/4-assembly calculations are shown. The NLPF is seen to be nearly unity for regular 18-plate assemblies, and is slightly less than unity for 10-plate Penn State fuel assemblies (which contain 172 grams ^{235}U each). The large NLPF and inherent two-dimensional nature of special assemblies can be seen in Figure 5.

(2) Uranium Isotope Concentrations

HEU fuel can contain measurable amounts of ^{234}U and ^{236}U due to both the enrichment process and the use of some reprocessed fuel. Table 6 shows uranium isotope concentrations for typical batches of FNR fuel. Although ^{234}U and ^{236}U yield more absorption than ^{238}U, none of these is a significant absorber in HEU fuel, as seen from Table 7. For generality, we have included all uranium isotopes in the LEOPARD input.

(3) D_2O and H_2O Reflector

In order to obtain few-group constants for D_2O and H_2O reflectors, microscopic cross-sections must be averaged over the core leakage spectrum, which is considerably softer than the in-core spectrum. This can be accomplished in an approximate manner using the LEOPARD code with the

Table 5. NLPF Calculations for HEU FNR Fuel

Geometry	Code	Mesh Points	NLPF
Regular Assembly:			
1-D unit cell	HAMMER	18	1.008
2-D 1/4 assembly	2DB	63x38	1.005
Special Assembly:			
1-D 4/9 assembly	HAMMER	20	1.30
1-D 1/2 assembly	2DB	63	1.292
2-D 1/4 assembly	2DB	63x38	1.154
Penn State Assembly:			
2-D 1/4 assembly	2DB	63x38	.993

$$\text{NLPF} = \frac{\overline{\phi}_{th}\ \text{nonlattice}}{\overline{\phi}_{th}\ \text{lattice moderator}}$$

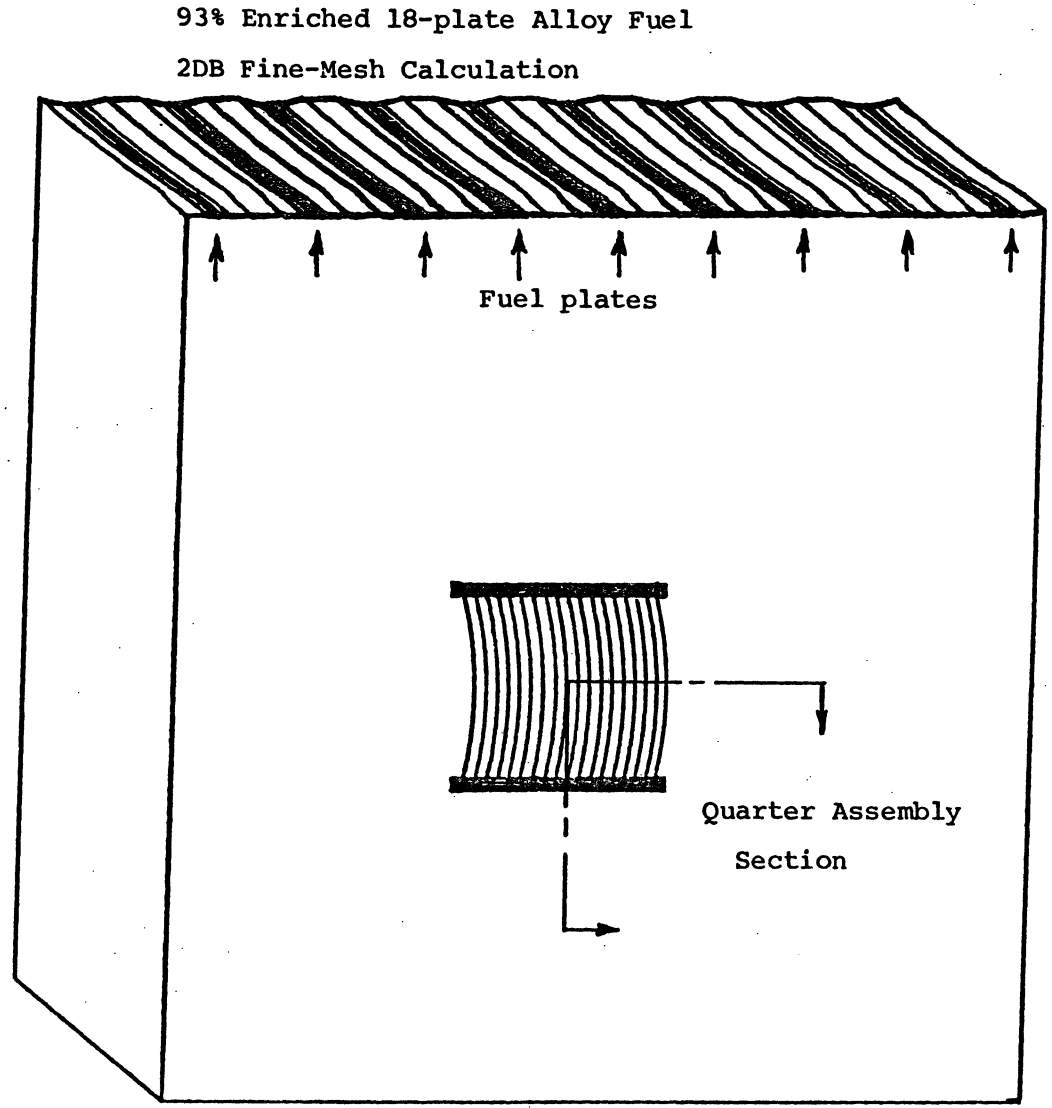

Figure 3. Regular Fuel Element Thermal Flux Distribution

93% Enriched 10-plate Alloy Fuel

2DB Fine-Mesh Calculation

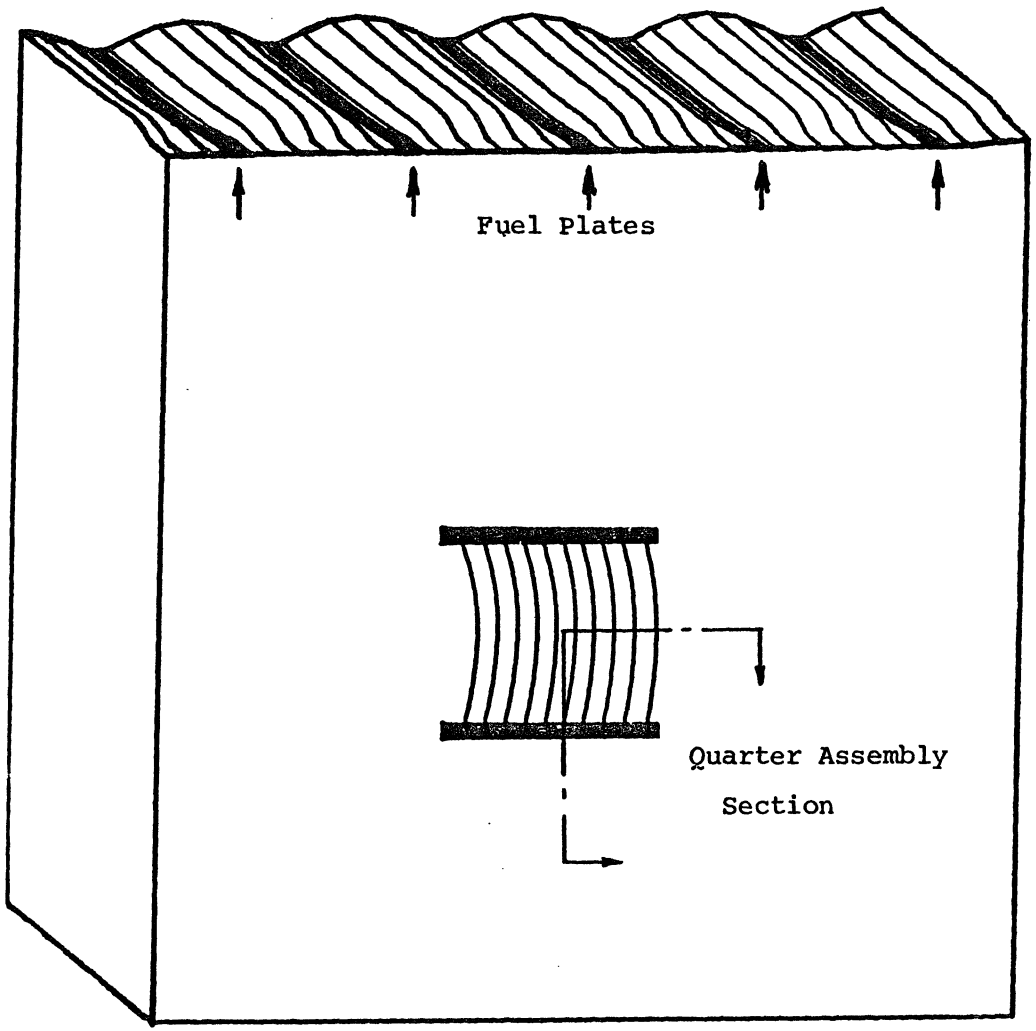

Figure 4. Penn State Fuel Element Thermal Flux Distribution

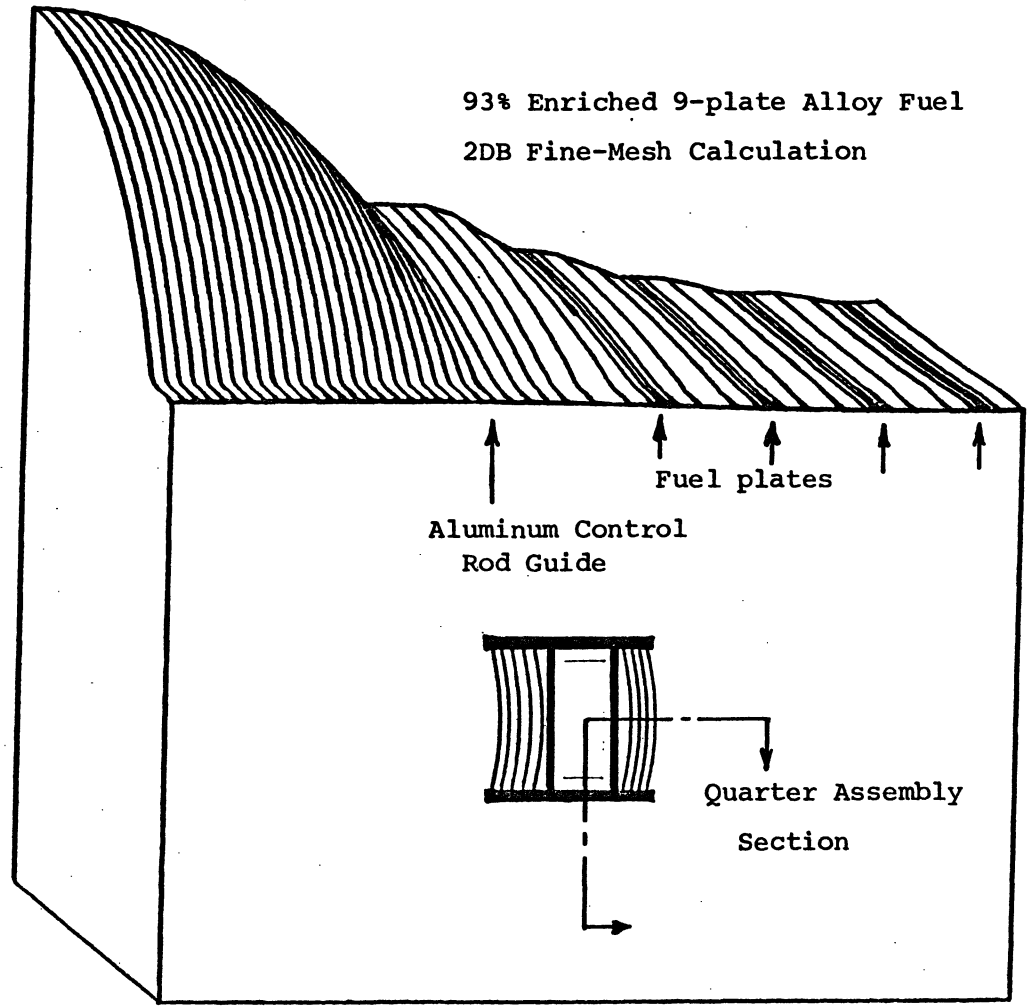

Figure 5. Special Fuel Element Thermal Flux Distribution

Table 6. Uranium Isotopic Concentrations for Recent FNR Fuel Elements

		FNR Fuels		
Isotope	Natural Uranium	93% Alloy	93% UAl_x	93% Penn State
U-234	.0055%	1.00 %	.61 %	1.00 %
U-235	.720%	93.17 %	93.19 %	93.26 %
U-236	---	.50 %	.42 %	.50 %
U-238	99.28%	5.33 %	5.78 %	5.24 %

Table 7. 93% FNR Alloy Fuel Neutron Loss Rates

	LEOPARD Unit Cell Calculation	
Absorption	Beginning of Life	End of Life
H	10.3	12.9
O	.55	.59
Al	5.1	6.3
U-234	.13	.15
U-235	48.6	48.5
U-236	.013	.10
U-238	.12	.14
X_e	-----	1.7
S_m	-----	.47
Pu-239	-----	.05
Fission Products	-----	2.2
Leakage	35.01	26.9
TOTAL	100.0	100.0

reflector represented as a large non-lattice region. We have arbitrarily chosen the NLF=.5 and the NLPF=1.0.

As discussed in Section II.C, D_2O cross sections are very sensitive to the amount of H_2O impurity present. We have used 1/4% H_2O impurity for all D_2O calculations, based on information from the FNR supplier.

2. The HAMMER Code

The HAMMER code is a one-dimensional integral transport spectrum code used for accurate calculations, benchmarking and verification of cross-section libraries[16,17], and difficult problems with strong spectral/spatial coupling. Our version of HAMMER is the recent EPRI version[5] which utilizes a data set based on the ENDF/B-IV cross section library.

a. Modifications to the HAMMER Code

Only minor modifications were needed to adapt the CDC version of the EPRI-HAMMER code to The University of Michigan computing system, which uses an Amdahl 470/V7 (similar to IBM 370).

An additional edit was added to print and save 2-group and 4-group cross-sections for separate material regions.

b. Verification of HAMMER

Three different methods were used to verify the HAMMER code: First, the code was compared against an older version of HAMMER[18] which utilized ENDF/B-II data for typical HEU and LEU fuel. No significant discrepancies were found. Second, several TRX criticals were analyzed and compared with measured values. Table 8 presents a comparison for one of the TRX slab criticals[14]. The agreement is good, considering the difficulty of the problem, and is much better than similar results from the LEOPARD code, which have been shown in Table 4. Third, HAMMER results for HEU, medium enrichment uranium (MEU), and LEU plate-type fuel were compared with results obtained from ANL[19] using the VIM[20] and EPRI-CELL[21] codes. Table 9 presents a representative comparison of the three codes. Based on these comparisons, we have concluded that the EPRI-HAMMER code is accurate and reliable.

c. Special Considerations in Applying HAMMER to the FNR

For application of one-dimensional codes to cross section generation for fuel assemblies, a common approach is the "supercell" concept: an assembly is represented by a unit cell consisting of four regions - fuel, clad, moderator, extra - with non-lattice materials homogenized in the extra region. For integral transport codes (HAMMER, THERMOS, EPRI-CELL thermal section, etc.) the supercell concept works well only if the extra

Table 8. HAMMER Results for TRX Slab Critical (W/F=1.09)

Parameter[a]	Experiment[b]	HAMMER	% Difference
ρ^{28}	1.21	1.191	-1.6%
δ^{25}	.124	.133	+7.5%
δ^{28}	.190	.186	-2.1%
CR*	1.387	1.342	-3.2%
B^2	-.0013	-.00136	4.6%
k[c]	1.0	.9982	- .18%

Notes: (a) $\rho^{28} = \frac{\text{U-238 epithermal capture}}{\text{U-238 thermal capture}}$

$\delta^{25} = \frac{\text{U-235 epithermal fission}}{\text{U-235 thermal fission}}$

$\delta^{28} = \frac{\text{U-238 fissions}}{\text{U-235 fissions}}$

$\text{CR*} = \frac{\text{U-238 captures}}{\text{U-235 fissions}}$

B^2 = critical buckling

(b) WAPD-TM-931 (1970)

(c) Measured value assumed to be 1.0; calculated value is based on HAMMER run with measured critical buckling input.

Table 9. Selected Results from Comparison of VIM, EPRI-CELL, EPRI-HAMMER

	VIM	ECELL	HAMMER
HEU			
k_∞	1.7652±.0035	1.7650(-.01)	1.76447(-.04)
σ^{25}_{f4}	355.14±.73	359.34(+1.2)	361.39(+1.7)
σ^{28}_{a3}	27.12±.078	27.683(+2.1)	25.951(-4.3)
MEU			
k_∞	1.7149±.0032	1.7208(+ .34)	1.7179(+.18)
σ^{25}_{f4}	347.19±.81	350.78(+1.0)	352.94(+1.7)
σ^{28}_{a3}	12.86±.29	12.01(-6.6)	12.387(-3.7)
LEU			
k_∞	1.6603±.0031	1.6656(+.32)	1.6598(-.03)
σ^{25}_{f4}	339.84±.88	342.82(+.9)	344.60(+1.4)
σ^{28}_{a3}	6.87±.12	6.51(-5.2)	6.808(-.90)

( ) = % difference from VIM

region comprises a small fraction of the total assembly. This is not true of FNR special assemblies, and an assembly-level representation is required instead of the simple supercell approach.

The reasoning behind this recommendation can be seen in Figure 6. A supercell representing a special assembly would result in a very "loose" lattice with little streaming between fuel plates. In the actual lattice, there is tight coupling between 4-5 plates and virtually no (thermal) streaming across the large water hole. To represent this in HAMMER, the clad, fuel, and moderator are represented explicitly for four unit cells next to 4/9 of the waterhole. This is essentially a "slice" through 4/9 of a special assembly, with a side plate region added in.

3. The 2DB Code

The 2DB code is a standard two-dimensional multigroup diffusion/depletion code. While it lacks some of the sophisticated options of PDQ7 and VENTURE, it is very inexpensive to run and can be modified easily.

a. Modifications to 2DB

Our modifications to the 2DB code, listed in Table 10, allow realistic simulation of major neutronics effects in the FNR. The principal modification is the capability for macroscopic depletion through interpolation in LEOPARD-generated cross-section tablesets. The original depletion calculation in the 2DB code is based on a microscopic depletion scheme with time-independent microscopic cross section. Figure 7, taken from LEOPARD output, shows that the spectrum-averaged microscopic fission cross section for ^{235}U in FNR fuel can vary by up to 1.5% over fuel life. Thus, it is important for criticality calculations to include depletion effects on microscopic cross-sections. By incorporating macroscopic depletion into the 2DB code, changes in both number density and microscopic cross sections are accounted for to a reasonable degree of accuracy. This is not strictly correct due to the dependence of isotopic production and loss rates on power level and temperature, but the assumption is made that the core will deplete at its average power level. The main exception is the xenon level. This has been accounted for by explicitly computing the xenon level as a function of local power and adding its contribution to the macroscopic absorption cross section as indicated in Table 10.

The modifications to the 2DB code affect only the initial setup and depletion steps; no changes were made to the inner or outer iteration schemes of the code.

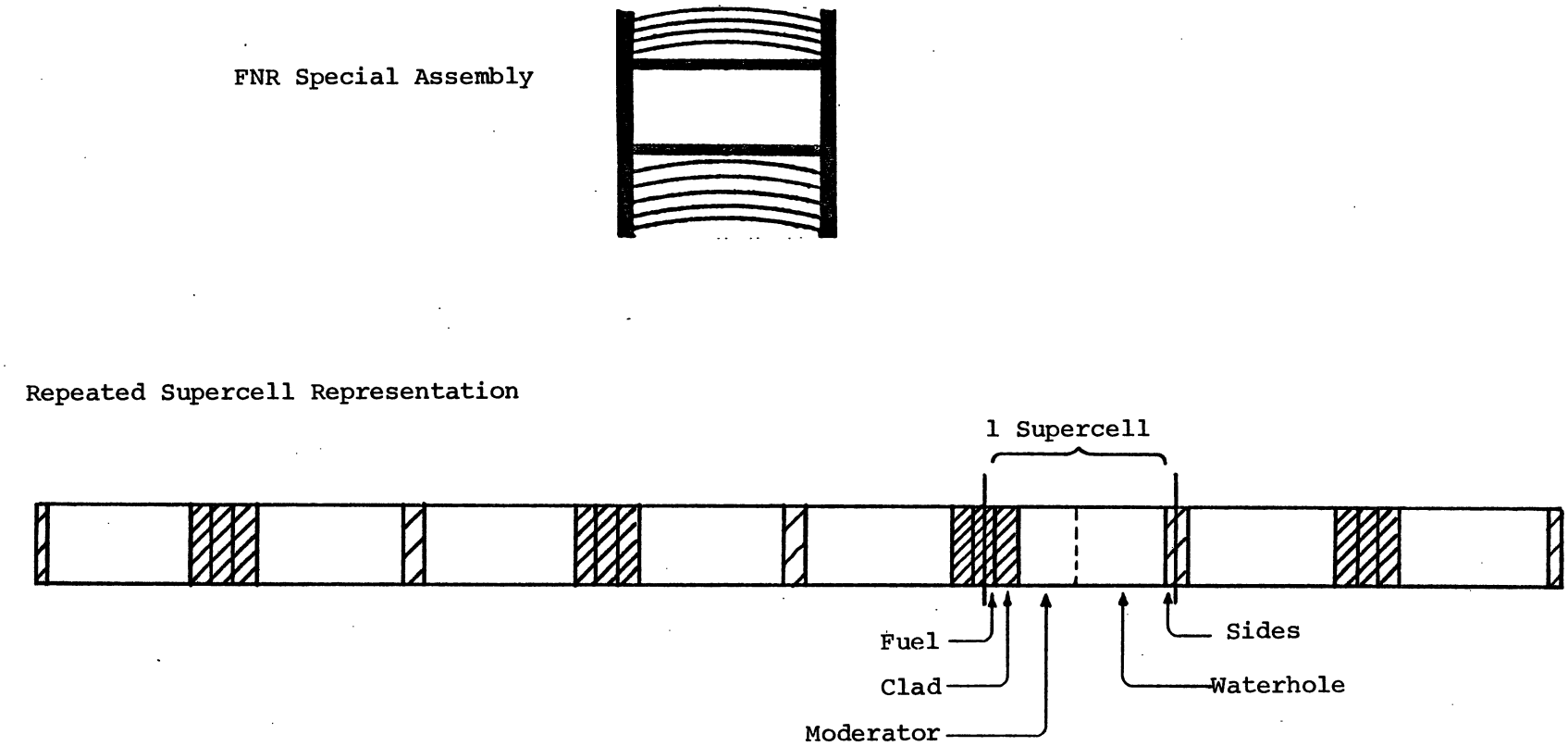

Figure 6. Supercell vs. Explicit Representation of FNR Special Assembly

Table 10. Modifications to 2DB

Modification	Purpose	Method
determine cross-sections by interpolation based on local fuel burnup	include spectrum effects due to local fuel depletion	quadratic Lagrangian interpolation in cross-section tableset from LEOPARD at each depletion step major input options added, extra scratch file and memory
space-dependent xenon	xenon feedback	N^{Xe} determined from local power and flux levels σ_{ag}^{Xe} interpolated as function of local fuel depletion from LEOPARD tableset Σ_{ag}^{Xe} added to Xe-free Σ_{ag}
option to interchange zone compositions	shuffling capability	minor input options added
dynamic memory allocation	reduced cost	A special setup routine (2START) determines memory space needed, acquires it, and links to 2DB.
interface with LEOPARD	reduced input setup	A special preprocessor (LINX) converts LEOPARD tablesets to the 2DB input format.
$\sigma_{s_{g\to g}}$, σ_{ag} relation	eliminate numerical inaccuracy when σ_{ag} is small	$\sigma_{s_{g\to g}}$ computed in 2DB from: $\sigma_{s_{g\to g}} = \sigma_{tg} - \sigma_{ag} - \Sigma_{g'} \sigma_{sg\to g'}$

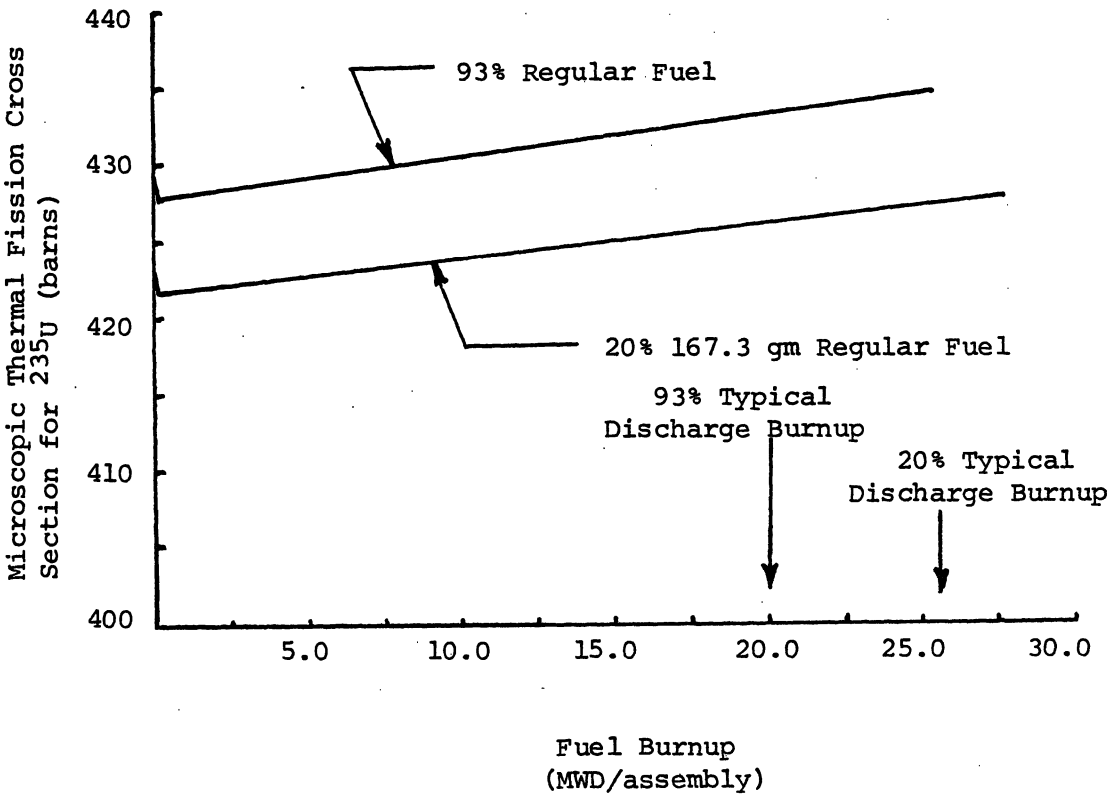

Figure 7. Cross Sections generated by the LEOPARD Code.

b. Verification of the 2DB Code

Using LEOPARD cross section sets in the modified 2DB code, several critical experiments were simulated and the results compared with measurements. A comparison of measured and calculated core eigenvalues and RMS deviation between measured and calculated flux or power distribution is given in Table A.5 for three representative cases: Case A is loading 33 of the Oak Ridge Bulk Shielding Reactor (BSR)[22], a clean core configuration. Cases B and C are typical FNR depleted cores. The fuel burnup distribution for Case B is shown in Figure A.3 and a comparison of measured and calculated assembly power is shown in Figure A.4.

c. Special Considerations in Applying 2DB to the FNR

(1) Number of Energy Groups

Nearly all analysis has been carried out with two neutron energy groups - 1 fast and 1 thermal, with a cutoff at .625 eV. Analysis of the BSR with four energy groups (3 fast, 1 thermal) yielded only marginal improvement in core eigenvalue and thermal flux distribution and was deemed to be not worth the added expense for routine calculations.

(2) Spatial Mesh

Three different spatial meshes, shown in Figure 8, have been used for FNR simulation: A 2x2 mesh per assembly, or homogeneous mesh, is used for inexpensive survey calculations. This mesh makes no distinction between active and non-active portions of an assembly, and thus cannot give detailed flux distributions. It has, however, proved to be reasonably accurate in computing core reactivity and assembly-averaged power distributions. Most of the detailed FNR analysis has utilized a 6x6 mesh per assembly. This discrete mesh structure allows explicit representation of active and non-active regions, as well as waterholes and control rods. To check the adequacy of the 6x6 mesh structure, several benchmark calculations were run using a 12x12 mesh per assembly. These 12x12 calculations are generally too expensive for routine use.

(3) Boundary Conditions

Zero-flux boundary conditions were used on all four boundaries for calculations without symmetry. To ensure that these boundary conditions would not affect the in-core flux, the core and heavy water tank were surrounded by 30-35 cm. of water. This water thickness was chosen to be large enough so that the arbitrary nature of the boundary was of no consequence.

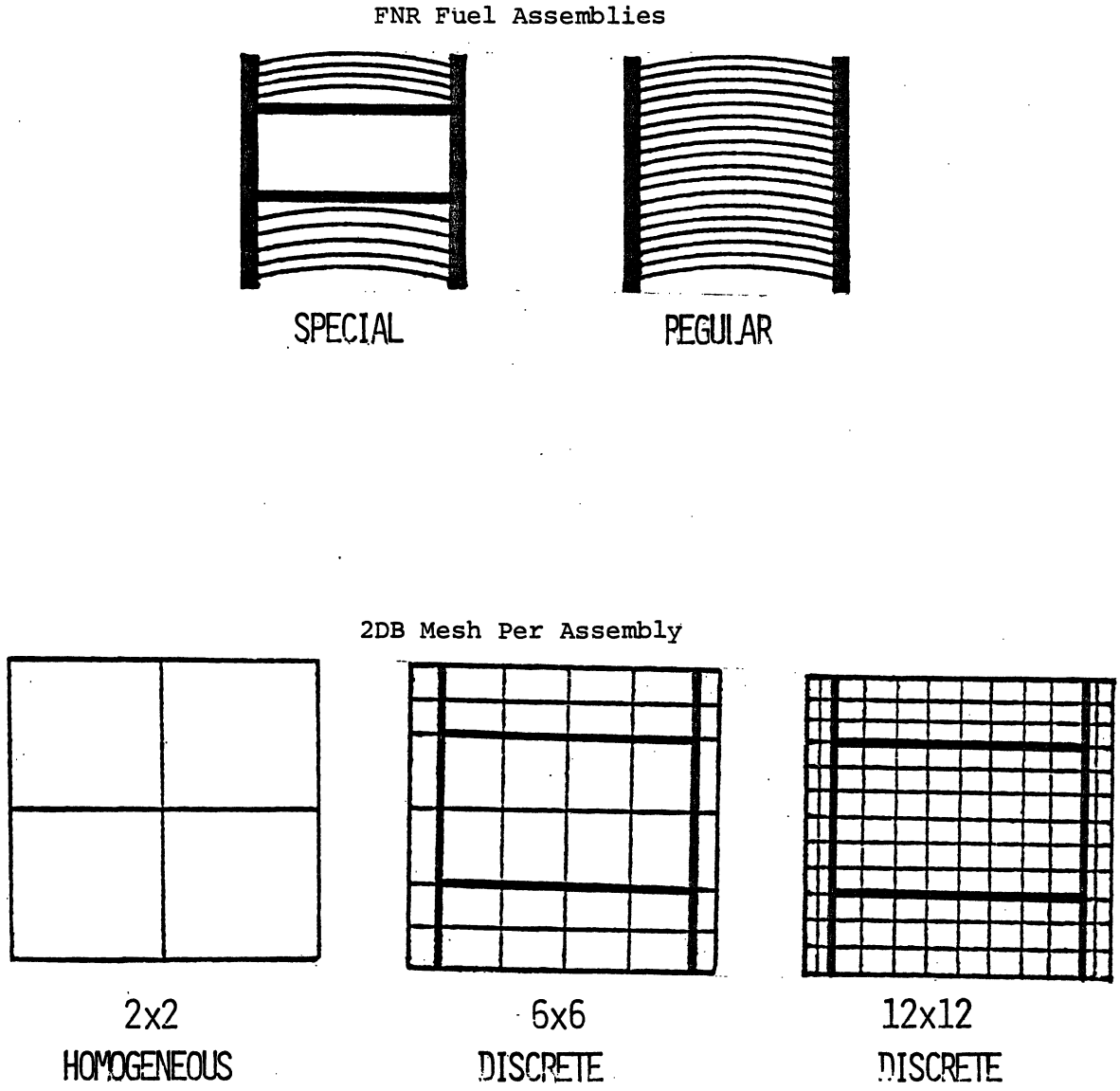

Figure 8. 2DB Mesh Description

(4) Transverse Buckling

For two-dimensional x-y calculations, the missing dimension is approximated through the use of a transverse buckling, B^2, which must be input to the 2DB code. Core eigenvalues are thus sensitive to the transverse buckling chosen. Our initial calculations used a value of $2 \times 10^{-3} cm^{-2}$, derived from an active core height of 23.75 inches with a reflector savings (based on thermal group cross sections) of 5 cm. Recently, three-dimensional calculations using the VENTURE code have indicated that a value of $1.76 \times 10^{-3} cm^{-2}$ should be used. (These calculations are described in Section II.D and are still being evaluated.)

Uncertainly in the transverse buckling could be a source of error in criticality calculations, since a 10% change in the transverse buckling yields about .8% $\Delta k/k$ change in the FNR core reactivity. Most calculations of interest, however, involve differences in reactivity, and we believe that errors due to transverse buckling are rather small for the purpose of comparing HEU vs. LEU fuel designs, if a consistent value is used for all calculations.

4. Other Standard Computer Codes

a. Three-Dimensional Diffusion Theory Codes

Both the VENTURE and PDQ7 codes have the capability for three-dimensional diffusion/depletion claculations. These codes were adapted to The University of Michigan computing system and checked out by comparison with sample problems and two-dimensional 2DB code calculations. Due to the high cost of three-dimensional calculations, these codes are not used for routine analyses. The VENTURE code is being used principally to determine the appropriate transverse buckling for two-dimensional 2DB calculations (see Section II.D). To date, the PDQ7 code has not been used to analyze the FNR.

b. Transport Theory Codes

The ANISN code and the TWOTRAN code perform transport theory calculations by the discrete ordinates method in one and two dimensions, respectively. Both of these codes have been used on The University of Michigan computing system for several years. They have been applied to the FNR without modification - the ANISN code for neutron leakage calculations (See Section II.C) and the TWOTRAN code for control rod calculations (see Section II.B).

5. Miscellaneous Computer Codes

Many short and specialized computer codes have been written to transfer data without error or to tabulate results for easier interpretation. Brief descriptions follow:

a. LINX

The LINX code automates the data link between the LEOPARD and 2DB codes. The output from one or more LEOPARD depletion calculations is combined into one depletion library for the 2DB code.

b. 2DBTOTT

This code will reformat cross-sections intended for the 2DB code to a format suitable for the TWOTRAN code.

c. 2DBED

This code is an extension of the edit sections in the 2DB code. Using standard data files created by the 2DB code, the 2DBED code can summarize and tabulate quantities of interest (zonal reaction rates, flux and power distributions, reactivity,etc.) from different calculations. This is useful for following the FNR core performance over many different cycles.

d. FNRFUEL

This code is currently used by the operating staff at the FNR primarily to document core and storage locations of fuel elements, and also to determine fuel element burnup and loading patterns. The code assumes a constant burnup rate of 1.23gm of ^{235}U/MWD, and uses cosine-shaped power distributions in the x- and y-directions, thus variations due to fuel burnup, thermal flux peaking in special elements, and empty locations are ignored.

To verify the accuracy of the FNRFUEL code in predicting fuel element burnup, results from the code were compared with 2DB burnup calculations. The comparison showed that in general the FNRFUEL code could predict the ^{235}U inventory of regular elements to within 1-2% error at any point in element life, although the relative error in fuel element burnup could be substantially larger. The fuel burnup calculation by the FNRFUEL code for special elements was not as accurate as for regular elements; typically the code underpredicts the ^{235}U inventory of special elements by up to 5% during fuel element life. It is important to note that the FNRFUEL code has been modified occasionally and that the above analysis is only valid for FNR cycles loaded after October 10, 1978.

e. SORT

The SORT code links the FNRFUEL data files to the 2DB code and thus provides an automated procedure for loading FNR data into the 2DB code. An FNR data file containing loading patterns and element burnups for any number of FNR cycles is accepted as input. Input data are available for all FNR cycles loaded since October 10, 1978. The input data are sorted by the code and the fractional fuel burnup data are then converted to fuel burnup data in units of MWD/MT. The code then creates a 2DB formatted input file, giving initial fuel element burnups and shuffling sequences for burnup calculations. Using the results of the 2DB burnup calculation the SORT code then has the capability to update the original FNRFUEL data files to reflect the more accurate prediction of fuel element burnup.

f. ZON

This routine writes the zone number arrays describing the FNR fuel assemblies for any mesh description in a form suitable for input to the 2DB code.

g. GES

This routine expands an input flux file generated for a coarse mesh 2DB setup into a form acceptable as an input flux guess for a subsequent 2DB calculation with a finer mesh description. For example, a flux file from a 6x6 mesh/assembly calculation may be expanded to serve as an initial guess in a 12x12 mesh/assembly calculation.

B. Control Rod Calculations

1. Description

The three shim-safety rods for the FNR are made of boron stainless steel containing 1.5 w/o natural boron. Their composition and dimensions are given in Table 11. These rods are essentially black to thermal neutrons and cause a drastic thermal flux depression when inserted. Since fine-mesh transport theory calculations for the whole core are prohibitively expensive, a method was developed to obtain effective few-group constants for control regions to be utilized in standard 2DB calculations. The methods developed have shown high accuracy in simulating measured rod worths for the FNR core.

2. HAMMER Analysis of Special Assembly with Control Rod

The generation of few-group constants to accurately represent a control rod is complicated by two problems: First, the methods and approximations in diffusion codes are often unreliable in regions of steep flux

Table 11. FNR Shim-Safety Control Rod Description

composition	boron stainless steel, 1.5 w/o natural boron
dimensions	2.1984 cm x 5.6683 cm x 61 cm
number densities*	($\times 10^{-24}$ atoms/cm^3)
^{10}B	.001108
^{11}B	.005184
Fe	.05644
Ni	.0113
Cr	.0164

*based on composition and density of boron stainless steel from Reference 23.

gradients. Second, the strong spectral/spatial coupling induced by a control rod necessitates careful selection of a spatial mesh. Both of these problems arise in analysis of the FNR rods.

a. Geometry

Since HAMMER is a one-dimensional code and since the FNR rods are many thermal mean free paths thick, a cylindrical geometry was chosen to generate cross-sections for the rod and adjacent water. (The neighboring lattice cross-sections are treated in Section II.B.3.) Since the rods are essentially black to thermal neutrons, it was deemed most important to preserve the rod surface area rather than volume. The geometry chosen is shown in Figure 9. For this calculation, the fuel, clad, and moderator were treated as a homogeneous mixture.

b. Selection of HAMMER Calculational Method

The thermal analysis section of the HAMMER code provides two options for the thermal integral transport calculation: The standard option, due to Honeck[24], is the basis of the THERMOS code.[25] Using this option, the region-to-region transport kernels are computed by a "ray-tracing" technique, and an approximation is applied to the Bickley-Naylor functions[26] involved. The second option, due to Carlvik[27], is the basis for the FLURIG[27] code. In this method, a transformation of variables results in a "slicing" technique which makes use of Gaussian quadrature. No function approximations are made.

Both methods were tried for a cylindricized control assembly and yielded different results. Varying the mesh spacing and examining intermediate results led us to the conclusion that the numerical scheme using Honeck's approach is not reliable for FNR control rods. The approximations used in computing the transport kernels between regions give inaccurate results for large, black absorbers. Additionally, using either a reflecting boundary or a "scattering ring" produced non-physical flux profiles near the outer boundary. Carlvik's scheme yielded reproducible results for several mesh spacings, and, with an analytic "white" boundary, showed no anomalies in the flux profile near the outer boundary.

c. Selection of Mesh and Material Regions

Due to the strong spectral/spatial coupling, it is not proper to represent the control rod by one set of few-group cross-sections. This is readily apparent in Figure 10 where the spectrum is shown as function of radial position. By trial and error, it was found that representing the rod by three distinct regions, with separate cross-sections for each, was

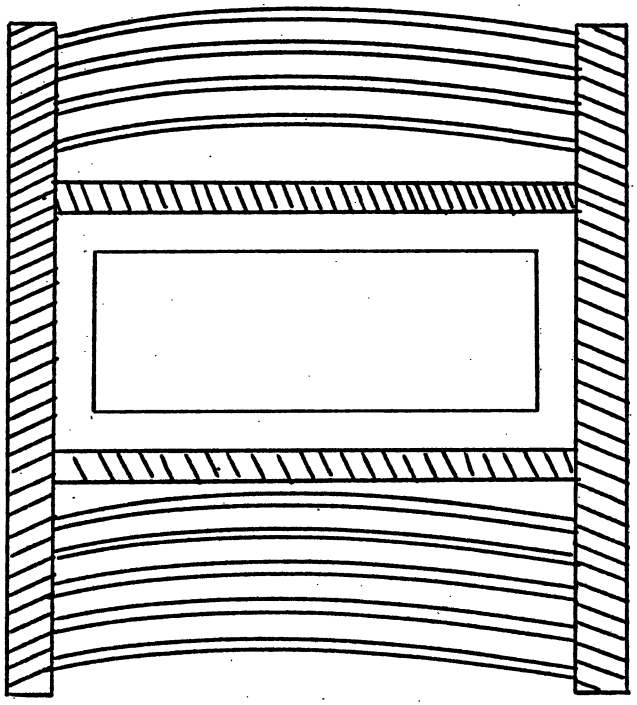

ACTUAL SPECIAL ELEMENT

(CONTROL ROD INSERTED)

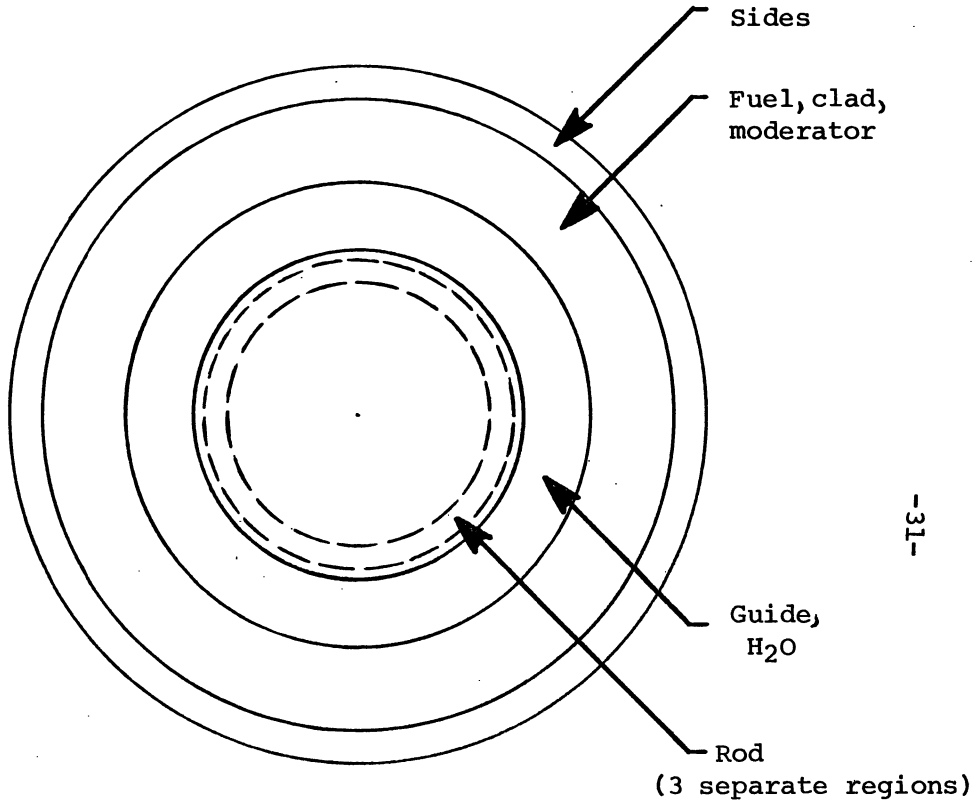

EQUIVALENT CYLINDRICAL GEOMETRY

Figure 9. HAMMER Geometry for Cylindricized FNR Special Assembly with Rod

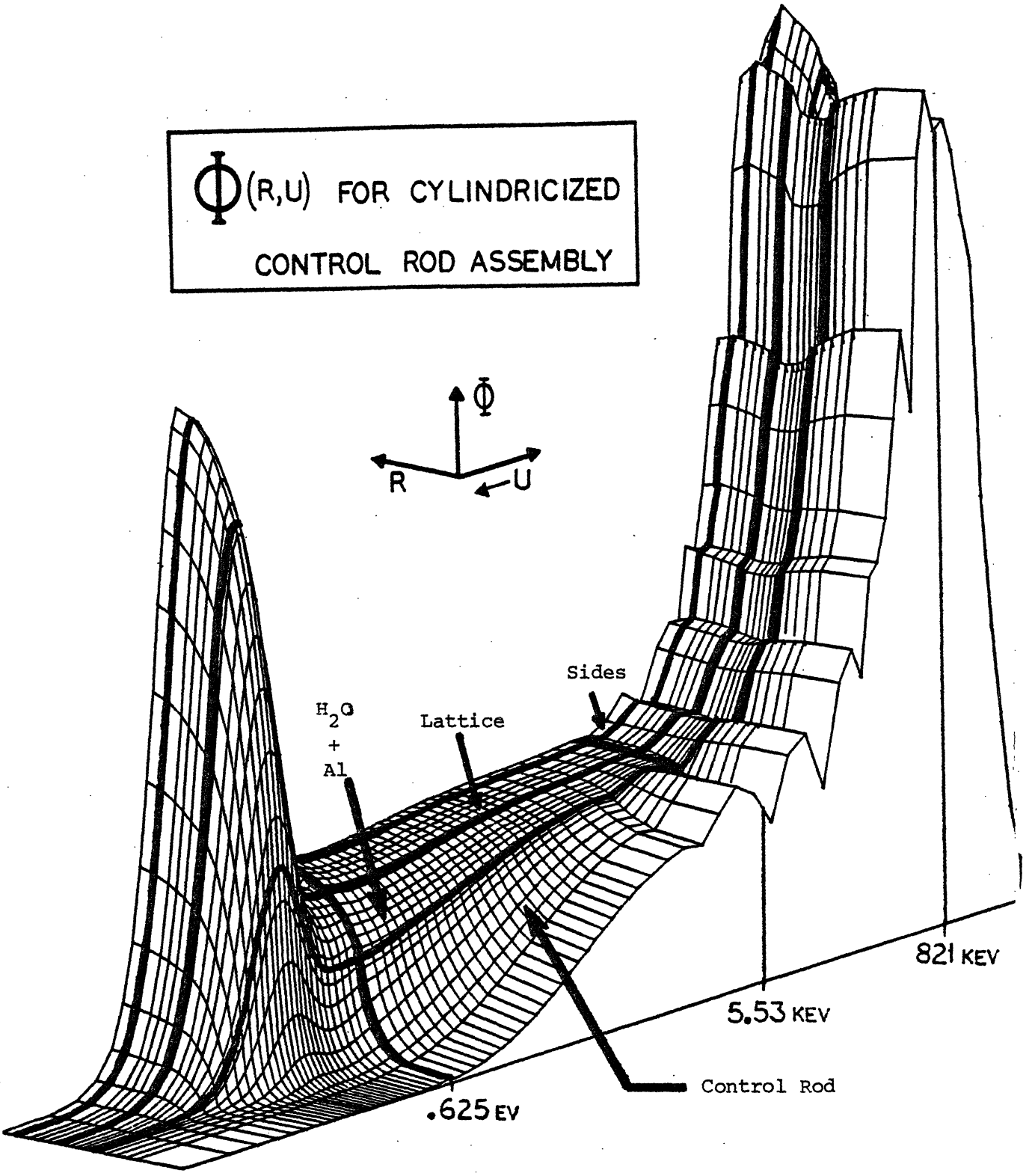

Figure 10. Flux Spectra as a Function of Position in the Cylindricized FNR Special Assembly with Rod

sufficient to allow a one-group TWOTRAN discrete ordinates calculation to closely match the 30-group HAMMER thermal flux profile. The TWOTRAN calculations were performed with cross sections obtained from the corresponding HAMMER calculation. A typical comparison is shown in Figure 11. The three regions of the control rod are: first, a surface layer .1 cm thick; second, another layer .3 cm thick; and third, the remaining central region of the rod. Most of the thermal absorption occurs in the two outer layers, with few thermal neutrons reaching the central region.

The selection of mesh spacing is very important for integral transport codes, which usually assume a flat flux in each mesh region. It is necessary to cluster the mesh points in areas of steep flux gradients, a task that must be done manually through trial and error.

3. Development of Effective Cross-Sections for Diffusion Theory Calculations

The control rod cross-sections obtained from HAMMER are not suitable for direct diffusion theory calculations. The strong absorption in the rod and the steep gradients at its boundaries grossly violate the underlying assumptions of diffusion theory. Direct use of the HAMMER-generated absorption cross sections results in an over-prediction of the neutron absorption rate in the control rod. To remedy this problem, HAMMER cross-sections for the rod, neighboring lattice, and surrounding fuel assemblies are used in a fine-mesh TWOTRAN calculation. Then, using the same mesh structure (6x6 per assembly) as for eventual whole core calculations, the problem is rerun with the 2DB code. Both fast and thermal absorption cross-sections for the rod are then adjusted until the diffusion theory fast and thermal absorption rates in each region match those of the benchmark TWOTRAN calculation. The resulting "effective control region" cross-sections are then used in global 2DB calculations with rod in and out to determine rod worth. This entire procedure is summarized pictorially in Figures 12 through 17:

a. Figure 12: Four HAMMER calculations are needed to develop few-group constants.

b. Figure 13: The HAMMER constants are used in a fine-mesh transport calculation of a special assembly (with rod) surrounded on each side by one half of a regular assembly, with reflecting boundaries.

The same problem is repeated using diffusion theory and the standard 6x6 mesh/assembly. (The rod and surrounding water must be homogenized.)

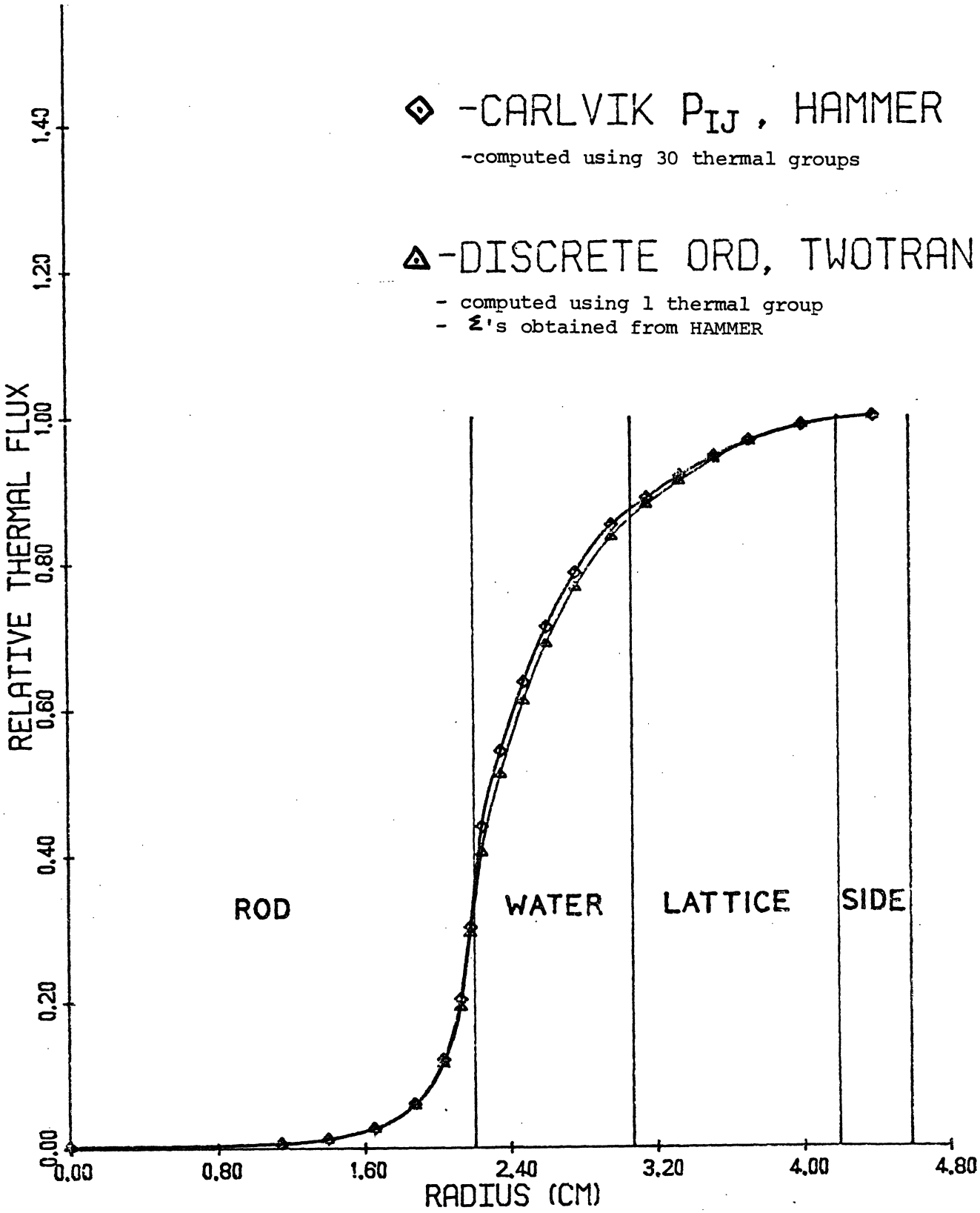

Figure 11. Comparison of Thermal Flux for Cylindricized FNR Assembly with Rod, HAMMER vs. TWOTRAN

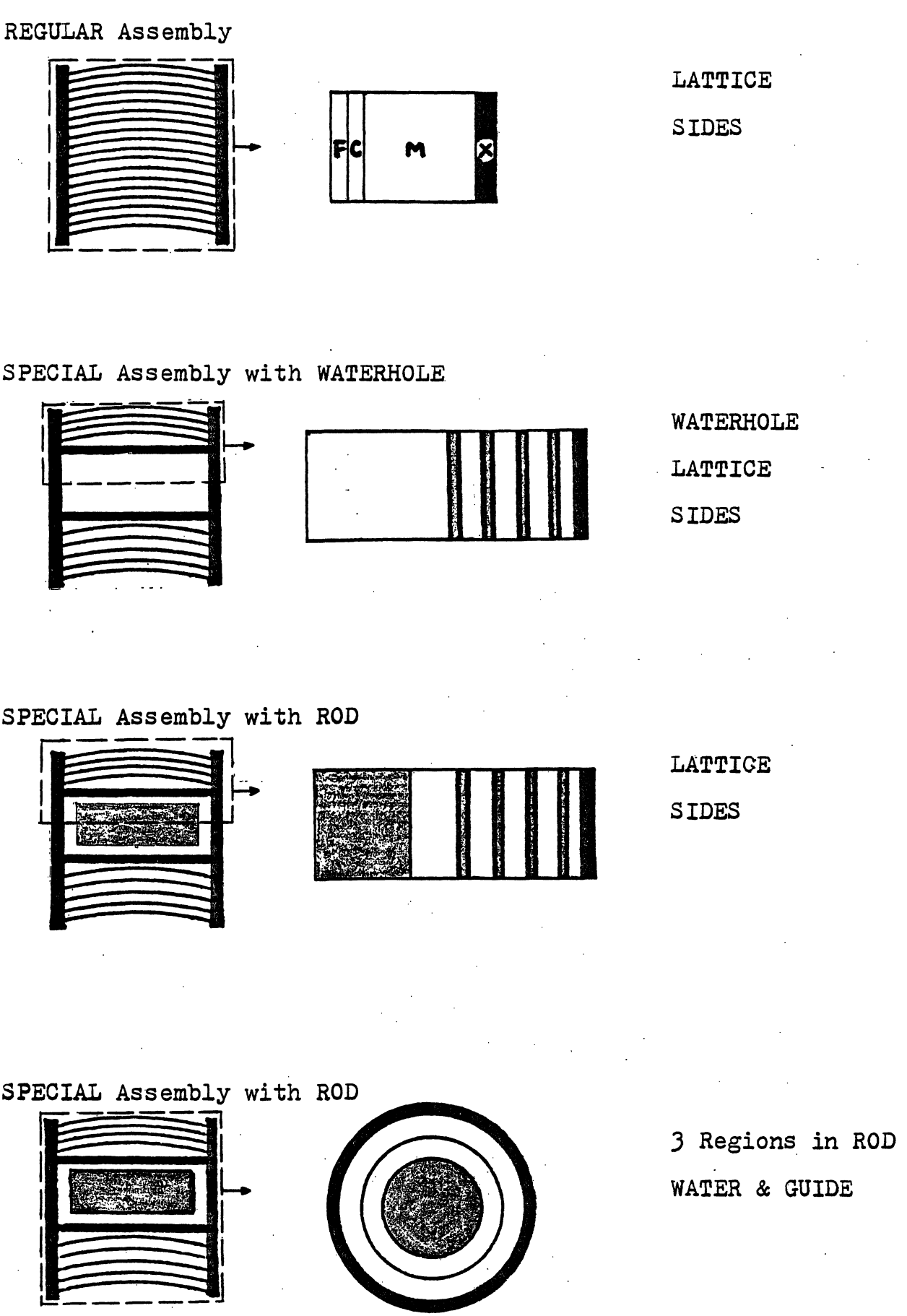

Figure 12. Geometry for HAMMER Calculations

c. Figure 14: The diffusion theory calculation is repeated, using different values for the thermal absorption cross-section of the control region (rod + surrounding water). From a plot of the ratio R_2 of thermal absorption in the control region to that in the lattice regions, an effective thermal absorption cross section for the control region is selected which yields R_2 equal to the value obtained from the TWOTRAN run.

d. Figure 15: A similar procedure is followed to determine an effective fast absorption cross-section of the control region.

e. Figure 16: The thermal flux distribution is shown for a whole-core 2DB calculation without control rod, used to obtain k_{eff} for the unrodded core.

f. Figure 17: The thermal flux distribution is shown for a whole-core 2DB calculation using the effective control region cross-sections to simulate an inserted control rod. From this run, k_{eff} is obtained for the rodded configuration.

g. By using k_{eff} for the rodded and unrodded cores, the reactivity worth of the control rod is determined. Step f. must be repeated for the other control rods.

The accuracy of this procedure is demonstrated in Table 12, where computed and measured rod worths are compared for FNR Cycle 67.

It should be noted that this procedure is moderately expensive - one calculation of control rod reactivity worth requires 4 HAMMER calculations, one fine-mesh TWOTRAN calculation (involving 4 assemblies), several small 2DB calculations (involving 4 assemblies), and two whole-core 6x6 mesh/assembly 2DB calculations.

Although the entire procedure could be repeated for different degrees of fuel depletion, it was found that, for the FNR, the effective cross-sections used for the rod were not sensitive to fuel burnup. Thus, to account for fuel depletion, only the first three HAMMER calculations in Figure 12 are needed; the effective control cross-sections need not be recomputed. The effective control cross-sections must, however, be recomputed for LEU fuel.

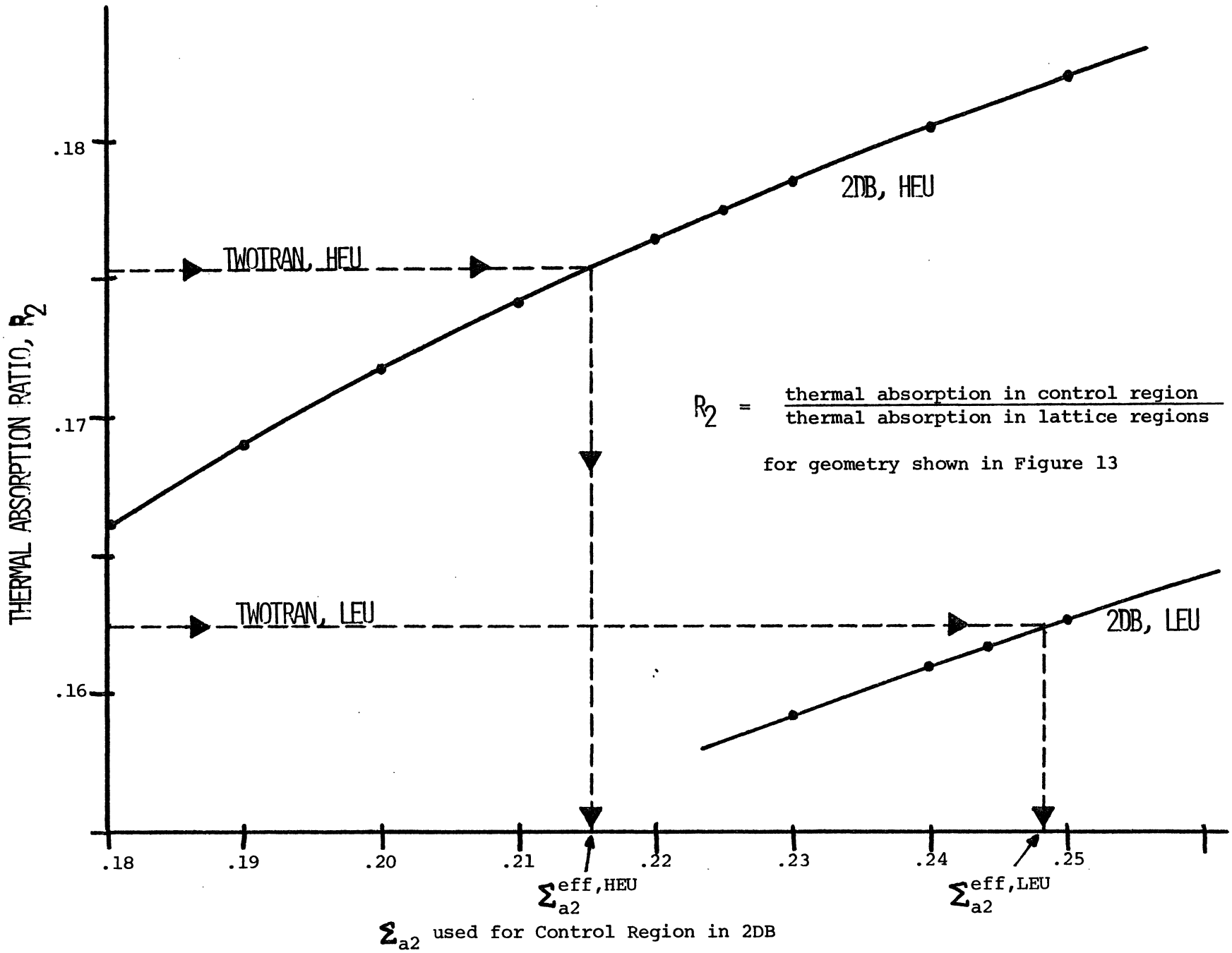

Figure 14. Determination of Effective Thermal Absorption Cross-Section of Control Region for use in 2DB

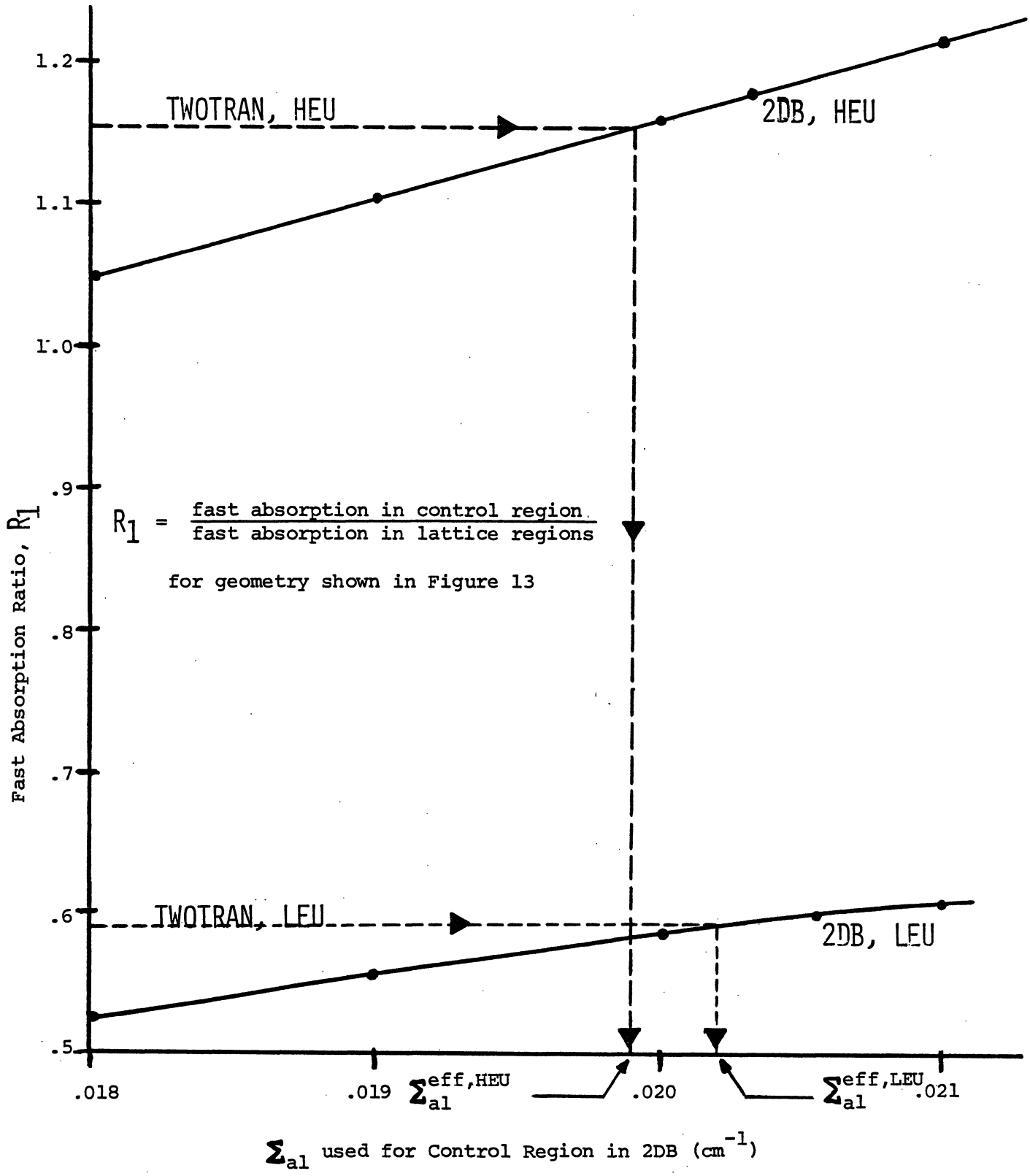

Figure 15. Determination of Effective Fast Absorption Cross-Section of Control Region for use in 2DB

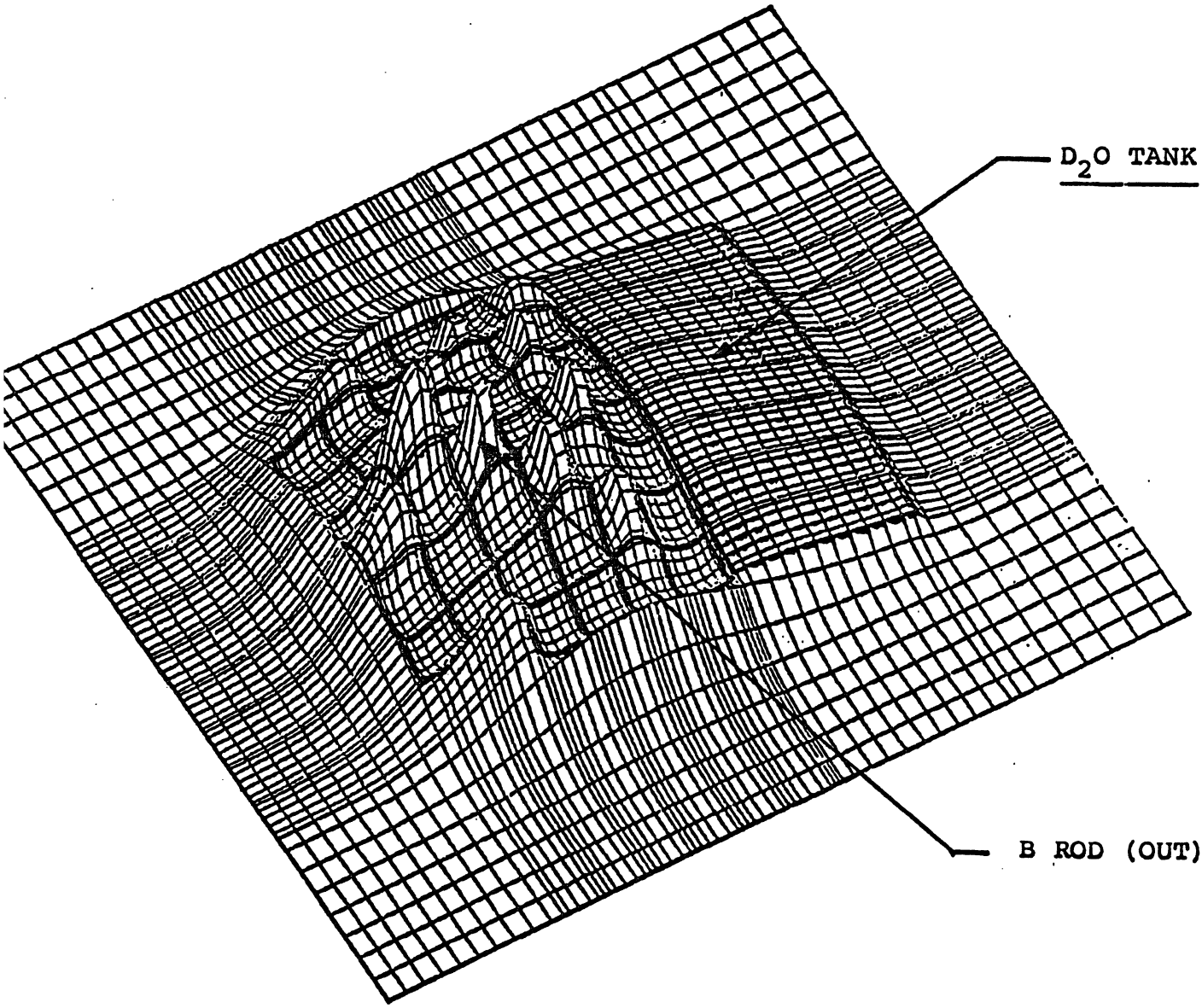

Figure 16. Thermal Flux Profile in the FNR with Rods Out
2DB Calculation for Cycle #67 (1971)

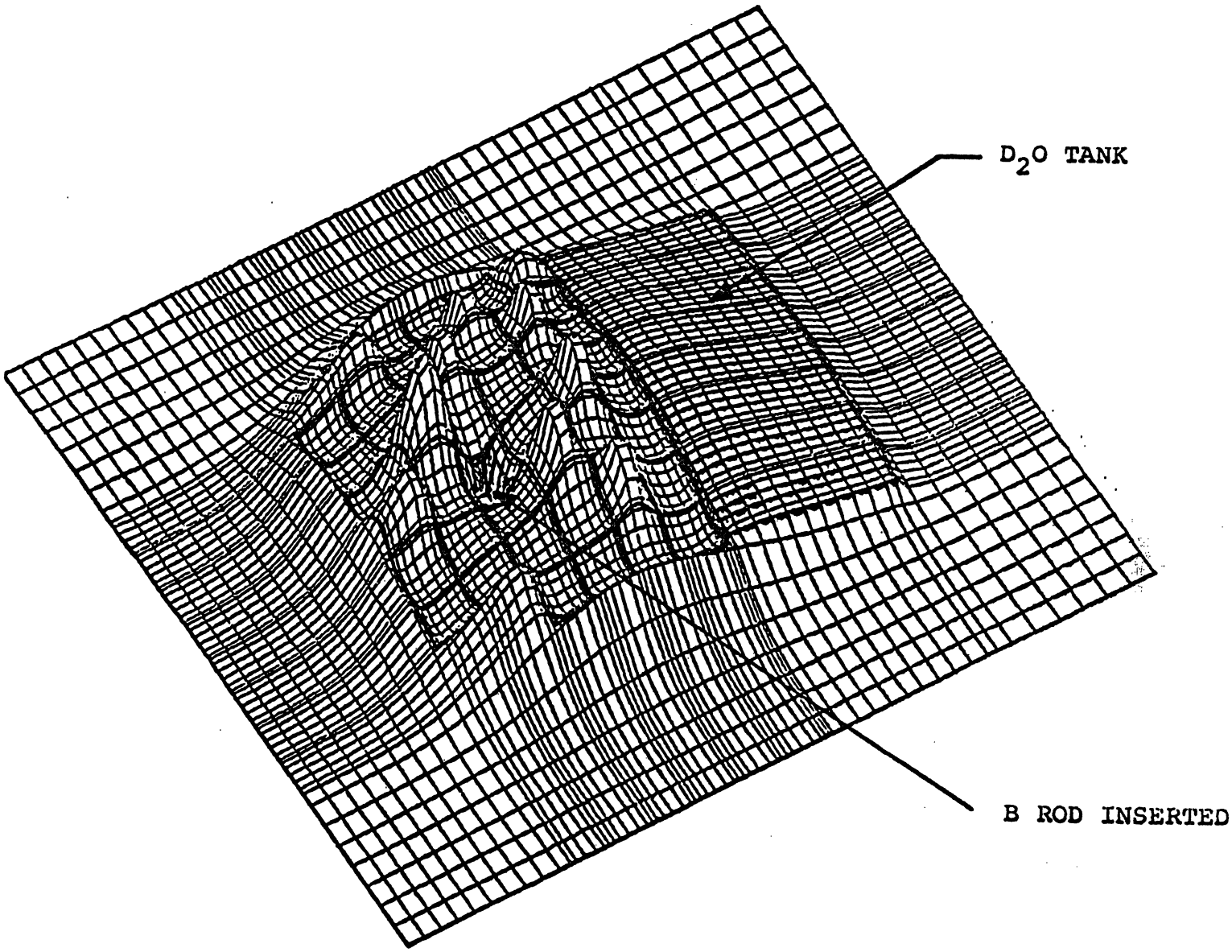

Figure 17. Thermal Flux Profile with B Rod Inserted
2DB Calculation for Cycle #67 (1971)

Table 12. Control Rod Reactivity Worth for FNR Cycle 67

Rod Location	Local Fuel Burnup	Rod worth ($\%\frac{\Delta k}{k}$)	
		measured	calculated
A	16%	2.22	2.20
B	24%	2.11	2.11
C	6%	1.72	1.73
Total		6.05	6.04

C. Ex-core Calculations

Preliminary work to predict the neutron leakage flux in the FNR heavy water tank has been directed at determining an acceptable calculational method for modeling the D_2O tank and at identifying critical parameters in the calculational method. The initial analysis of ex-core thermal fluxes in the D_2O tank has shown that some of the important considerations are the adequate modeling of the complex geometry, the generation of cross-sections for D_2O, and the correct modeling of transverse leakage.

1. Special Considerations for D_2O

D_2O must be treated carefully due to its extremely small absorption cross section, as indicated in Table 13, where typical diffusion lengths for D_2O and other materials are compared. This table indicates that H_2O contamination in D_2O has a substantial effect because the thermal absorption cross-section for H_2O is nearly 3 orders of magnitude larger than for D_2O. Heavy water supplies for the FNR typically contain about .25% H_2O.

Table 13 indicates that the thermal diffusion length is longer than the fast diffusion length for heavy water, whereas the opposite is true for light water. The significance of the large thermal diffusion length for D_2O is illustrated by the effect of a typical buckling correction which is included in two-dimensional core calculations. As shown in Table 13 the pseudo-absorption DB_z^2 term substantially decreases the effective distance thermal neutrons will diffuse through D_2O before being captured.

2. Transport and Diffusion Theory Comparison

Transport theory calculations are often necessary to predict the neutron flux at large distances into a reflector, due to the tendency of the angular flux to become forward peaked. Therefore, a series of ANISN calculations was made to assess the adequacy of diffusion theory in representing the D_2O reflector. The calculations were performed for 80 cm slabs of H_2O and D_2O with a plane source of fission neutrons. A 20-group structure was used, with epithermal cross-sections from the DLC-2 library and thermal cross-sections generated by the LEOPARD code. The scalar flux distribution was calculated using S_2 and S_{16} quadrature orders, the S_2 solution being essentially equivalent to a diffusion theory calculation. Figures 18 and 19 show comparisons of the ANISN solutions for 5 of the 20 energy groups. At large distances into the H_2O reflector the S_2 calculation underpredicts the scalar flux because the anisotropy is ignored. However,

Table 13. FNR Diffusion Length Comparisons

	Fast (cm)	Thermal (cm)
D_2O	--	170.0
D_2O+1/4% H_2O	17.7	130.0
H_2O	5.1	3.0
93% regular element	7.2	2.2
D_2O+0.25% H_2O+DB_z^2 (B_z^2= 1.14x10^{-3}cm^{-2})	15.2	28.9

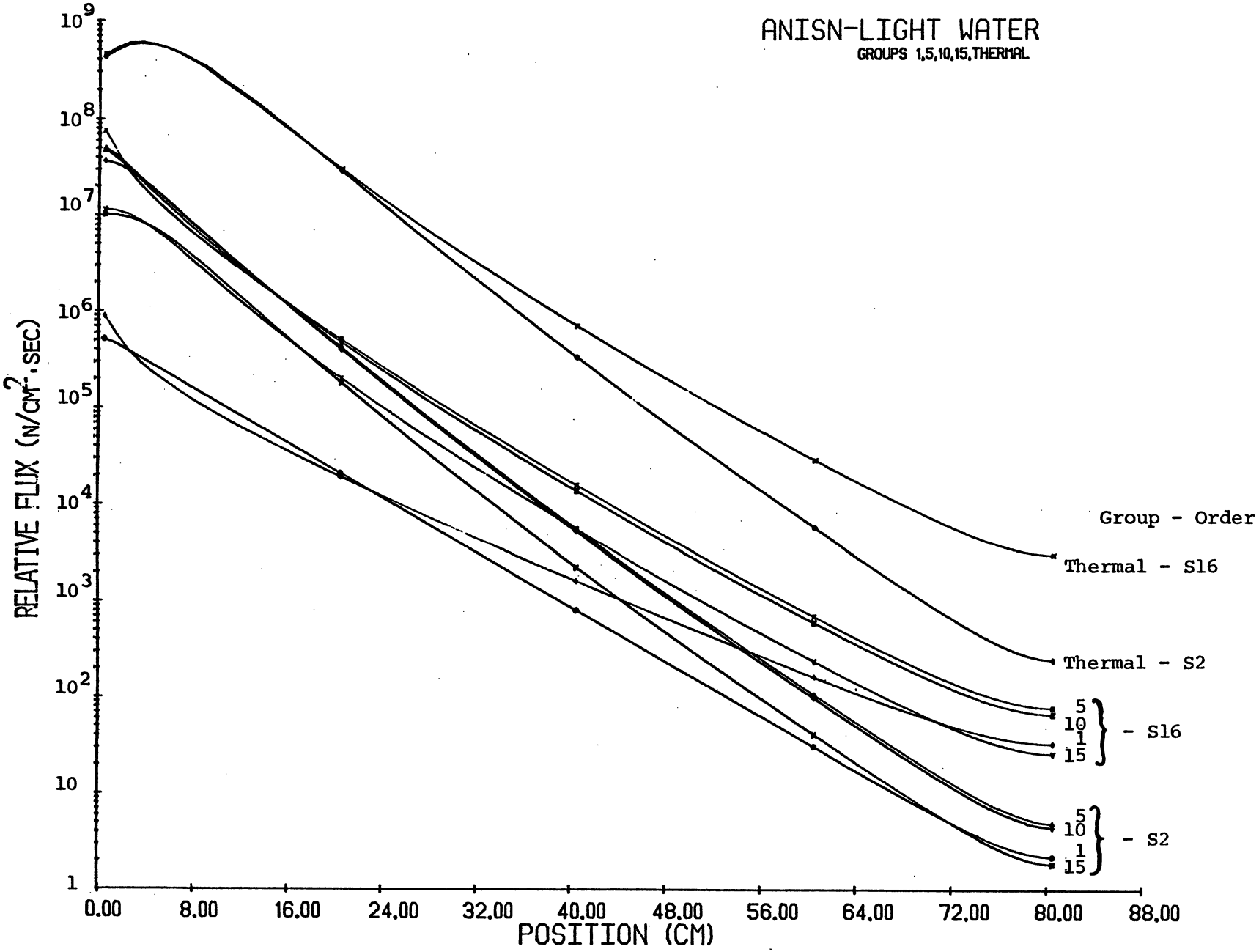

Figure 18. Neutron Flux Attenuation in Light Water

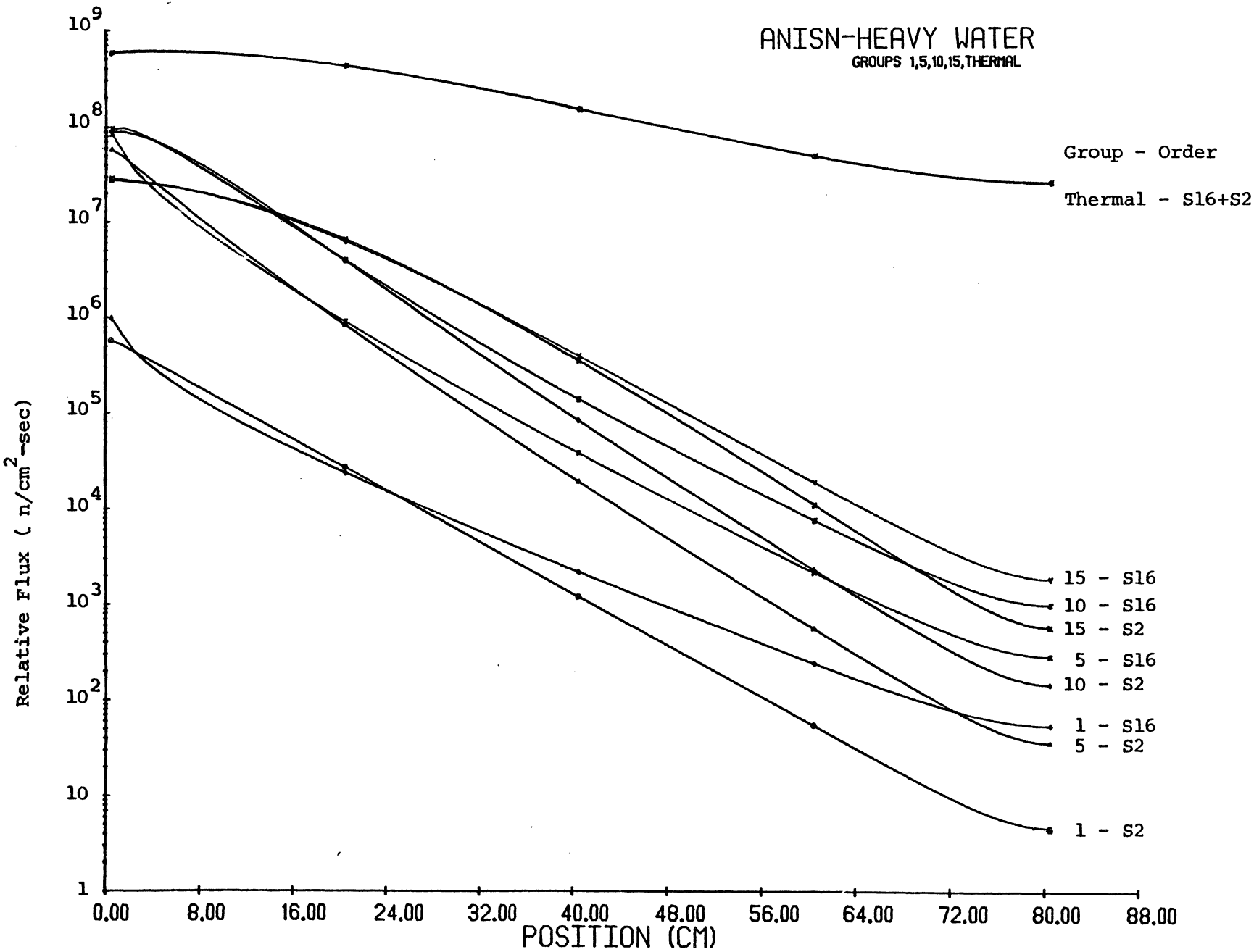

Figure 19. Neutron Flux Attenuation in Heavy Water

in heavy water the thermal flux is predicted accurately by the S_2 calculation at considerable distances into the slab. Therefore, diffusion theory should be adequate for the D_2O reflectors away from the core boundary, whereas calculations within the H_2O reflectors may necessitate a transport theory analysis.

3. Verification of the Calculational Methods

To further verify the accuracy of diffusion theory calculations in predicting the thermal flux distribution in a D_2O reflector, calculations were performed to simulate experimental data from the High Flux Beam Reactor (HFBR)[28]. The HFBR, shown in Figure 20, was chosen because the D_2O reflector is relatively free of components which require more detailed geometric modeling. The HFBR reactor core consists of 32 fuel elements which are similar to the FNR elements except the HFBR elements have a 240 gm/element loading compared to the 140 gm/element loading in the FNR. Another difference between the HFBR and the FNR is that D_2O serves as moderator, coolant, and reflector in the HFBR. The D_2O reflector is approximately 80 cm thick and spherically shaped, with penetrations for 15 beam tubes and irradiation thimbles.

Four group cross sections for the HFBR were generated with the LEOPARD code for D_2O, fresh fuel, and aluminum. The 1DX and 2DB codes were used to calculate thermal flux profiles in one and two dimensions, respectively. A number of geometries were tested to model the reactor shape. While the core shape is nearly cylindrical, the reactor vessel is spherical, so that both geometries were considered. Figure 21 shows that the geometry had only slight effect on the calculated flux distribution except for that caused by the change in core radius when the cylindrical core was modeled as a sphere. To model additional details in the D_2O reflector, such as the beam tubes, some calculations included extra regions of aluminum in the reflector. These more detailed calculations gave better agreement between calculated and experimental flux profiles.

Figure 21 shows the calculated and experimental flux profiles[28] for the HFBR, normalized to 1.0 at the flux peak. The results indicate that the thermal flux distribution in the HFBR can be predicted with reasonable accuracy using LEOPARD cross-sections and the 1DX or 2DB diffusion theory codes. Comparisons with and without additional reflector aluminum regions show that a large part of the discrepancy between experimental and calculated profiles may be caused by not modeling exactly the reactor geometry in the diffusion theory calculations.

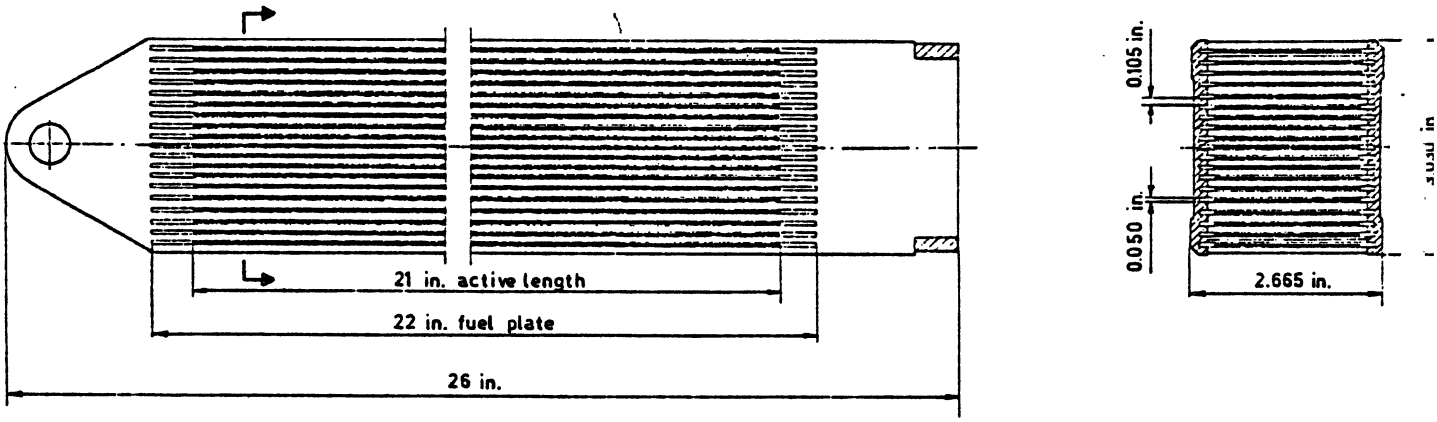

FUEL ELEMENT

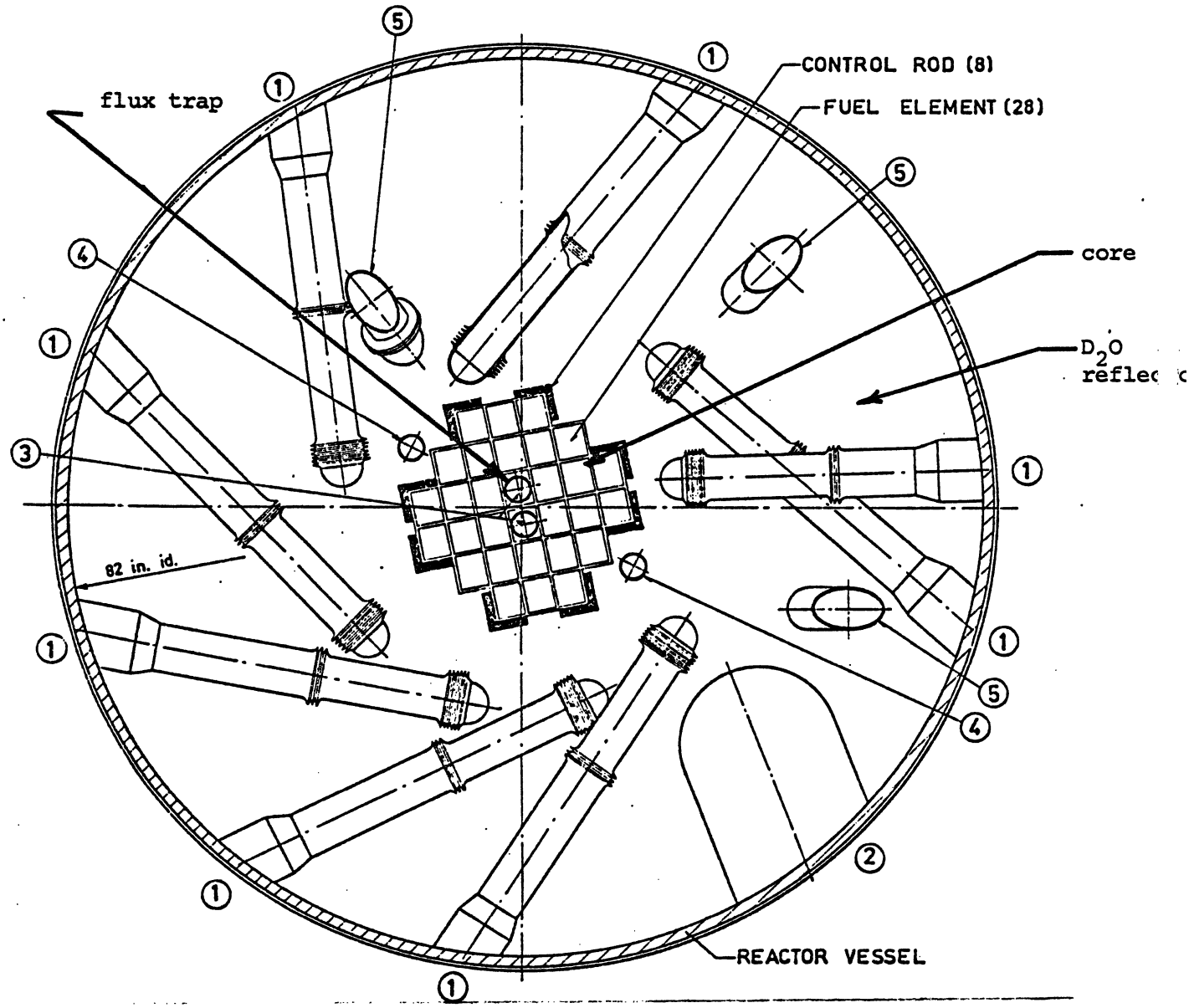

FIGURE 20. HFBR HORIZONTAL SECTION

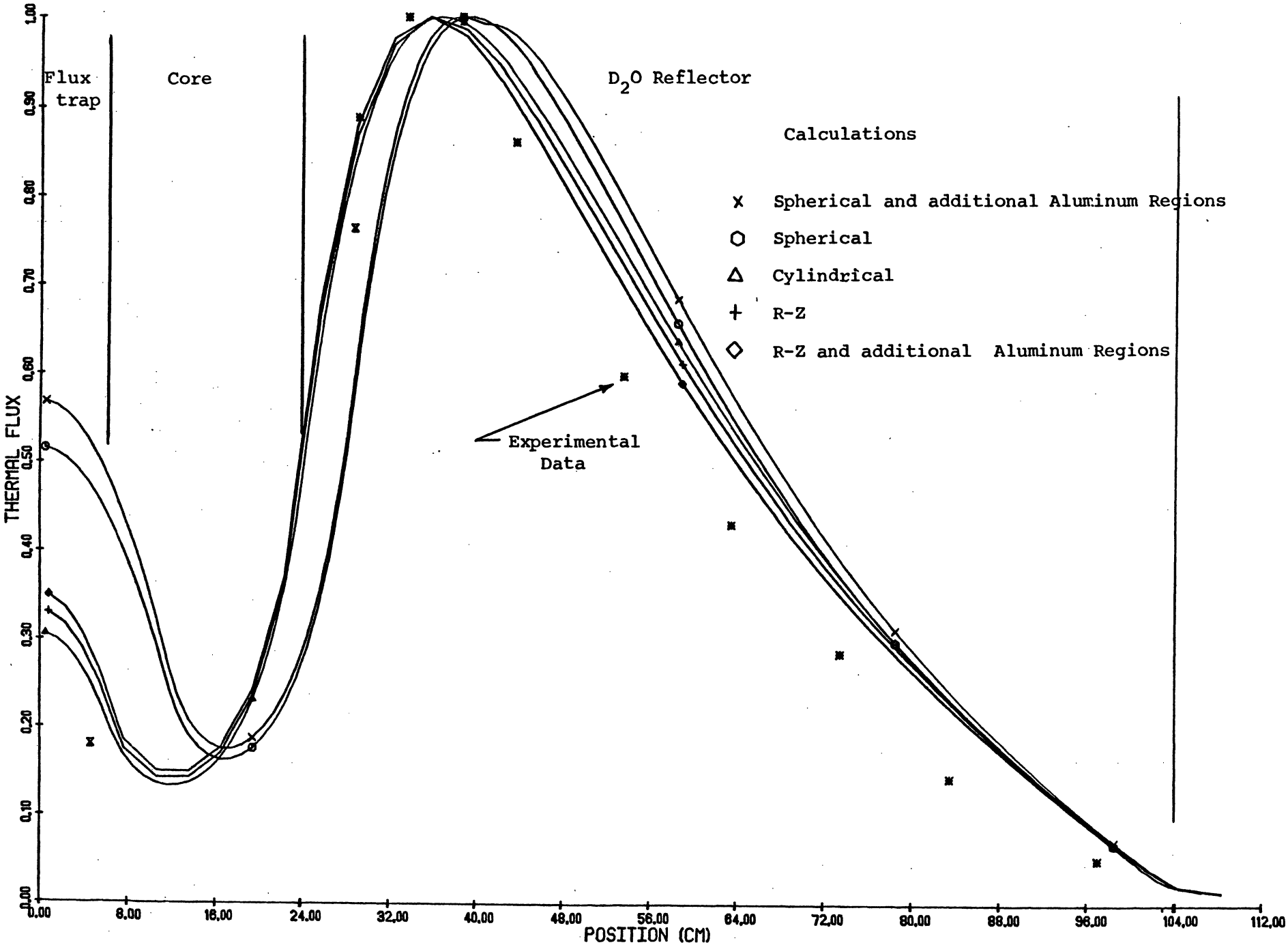

Figure 21. HFBR Thermal Flux

4. FNR Ex-core Calculations

Preliminary simulation of thermal flux profiles measured in the FNR D_2O tank during cycle 173A was performed to assess the accuracy of the calculational methods for the actual FNR configuration. The thermal flux was measured at three positions in the D_2O tank, as indicated in Figure 22 . Further details of the D_2O tank geometry are given in Appendix B.

Calculation of the leakage flux in the D_2O tank was performed using the 2DB code with a 2x2 mesh/assembly description, and transverse bucklings of $1.82 \times 10^{-3} cm^{-2}$ in the core and $1.14 \times 10^{-3} cm^{-2}$ in the D_2O reflector. For these calculations few details of the D_2O tank geometry were modeled. Only thimbles O, X, and P were included, while the other tank thimbles and the beam tubes were ignored. The thimbles are H_2O filled aluminum tubes extending into the D_2O tank and the effects of several different materials in the irradiation thimbles were considered.

Figure 23 compares the calculated and measured thermal flux profiles in the D_2O tank. When the thimbles are ignored and the D_2O tank is assumed to be filled with D_2O, a smooth flux profile is calculated, shown as the middle curve of Figure 23 . When the thimbles were modeled as entirely aluminum filled regions, the calculated flux, shown in the lower curve, was slightly depressed due to increased neutron absorption. The upper curve shows the calculated flux when the thimbles were modeled as entirely H_2O filled regions. At thimble X, the position closest to the core, the thermal flux was enhanced by increased fast neutron slowing down in H_2O. While at thimble O the thermal flux was depressed by increased thermal absorption in H_2O. The flux did not peak in thimble O because the fast neutron flux is significantly attenuated at that distance into the reflector, hence, the principal source of thermal neutrons is due to diffusion.

These calculations have indicated the importance of adequately modeling the D_2O tank geometry in ex-core calculations. Further simulation of the thermal flux profiles measured in the FNR will need to be performed to verify that the D_2O tank is properly modeled. Three-dimensional calculations will be necessary to include more details of the complex geometry.

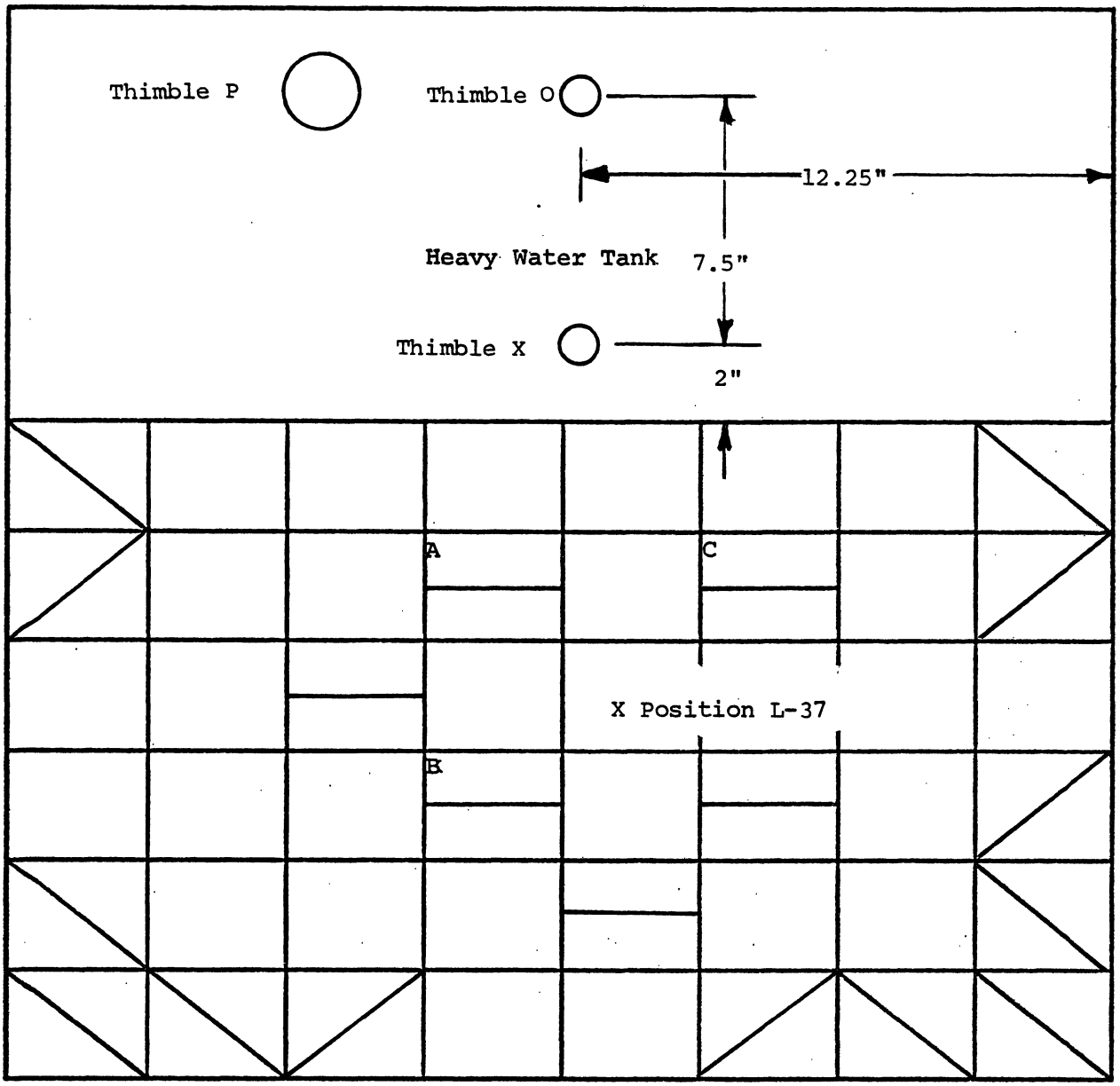

FNR Cycle 173A

Thermal Flux L-37: 1.21×10^{13} (n/cm^2-sec)

X: $.91 \times 10^{13}$ (n/cm^2-sec)

O: $.29 \times 10^{13}$ (n/cm^2-sec)

Figure 22. D_2O Tank Thermal Flux Measurements

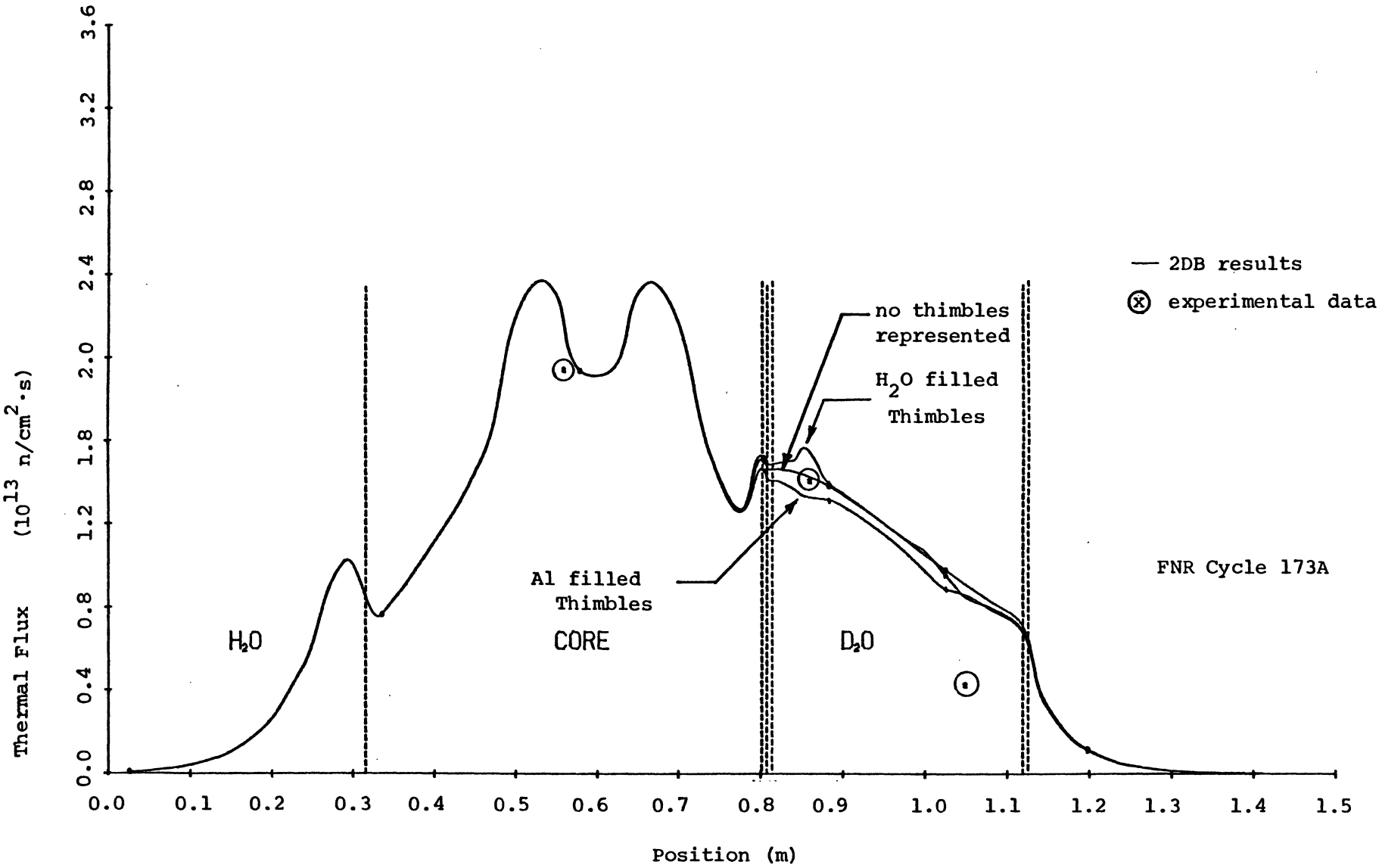

Figure 23. D_2O Tank Thermal Flux

D. Transverse Buckling Calculations

Two-dimensional diffusion theory calculations for a small reactor such as the FNR are sensitive to the input buckling used to model neutron leakage in the axial direction. The sensitivity of FNR calculations to buckling is a consequence of the importance of leakage which accounts for approximately one-third of the neutron losses.

A number of methods have been utilized to determine an appropriate buckling for the FNR. These methods are summarized in Table 14 and are described in the following paragraphs.

1. Buckling from Core Height and Reflector Savings

The core transverse buckling is calculated as:

$$B_z^2 = \left[\frac{\pi}{H + 2\delta}\right]^2$$

where the reflector savings is given by[29]:

$$\delta = \frac{D_{core} L_{Ref}}{D_{Ref}}$$

Since there is some question as to whether thermal or one-group cross-sections should be used in the above equation, both methods were used. The use of thermal group cross sections yielded a reflector savings of δ=5.2 cm and a core buckling of B_z^2=2.0x10^{-3}cm^{-2}. One group cross sections were then obtained from the core and reflector 2-group constants by appropriate flux weighting. Using these one-group constants yielded:

$$\delta = 9.41 \text{ cm} \quad \text{and} \quad B_z^2 = 1.6 \times 10^{-3}\text{cm}^{-2}.$$

2. Matching Experimental and Calculated Core Eigenvalue

For the June 1977 critical experiment, the value of B_z^2 obtained above with thermal group constants, B_z^2 = 2.0x10^{-3}cm^{-2}, yielded a critical core with an X-Y 2DB calculation. This may also be viewed as an alternative method of obtaining B_z^2.

3. Matching Experimental and Calculated Core Power Distribution

The FNR power distribution was measured for the cycle 67 core using thermocouples located at the inlet and outlet of each regular fuel assembly. For this measured power distribution, a buckling in the range 1.7-1.8x10^{-3}cm^{-2} yielded the minimum RMS deviation between the experimental and calculated assembly-averaged powers.

Table 14. Buckling Calculations

Method	Buckling ($x10^{-3}cm^{-2}$)	Comments
1. Reflector Savings and and Core Height	2.0 1.6	Thermal group constants only One-group constants.
2. Matching Eigenvalue Exp. vs. Calc.	2.0	June 1977 critical experiment
3. Matching Power Distribution Exp. vs. Calc.	1.8-1.7	FNR Cycle 67
4. Matching Eigenvalue R-Z vs. R	1.72 1.14	Core and H_2O reflector D_2O reflector
5. Matching thermal flux R-Z vs. R	1.82 1.14	Core and H_2O reflector D_2O reflector
6. 3-D Assembly Calculation	 1.721 1.720 1.76	Heterogeneous assembly: Non-lattice Lattice Homogeneous assembly
7. 3-D Full Core Calculation	1.76 1.65 1.66 1.10	Core Center H_2O reflector D_2O reflector Fast flux Thermal flux

4. Matching Eigenvalue in Finite Cylinder (R-Z) and Infinite Cylinder (R) Calculations

For a cylindrical reactor with azimuthal symmetry an effective three-dimensional problem can be solved with a simple two-dimensional R-Z calculation. Thus by comparing an R-Z calculation which is independent of axial buckling with a one-dimensional cylindrical calculation requiring axial buckling, an estimate of an appropriate buckling can be found.

In this method the axial buckling was calculated for the core region and the D_2O tank separately. To calculate the core buckling the FNR core was cylindricized assuming a uniform average core burnup and an H_2O reflector. The core eigenvalue from the R-Z calculation was matched in the one-dimensional radial calculation by adjusting the axial buckling.

Next, a radial D_2O reflector was simulated between the core and the H_2O reflector. The eigenvalue from the R-Z calculation was again matched in the one-dimensional radial calculation by using the original buckling for the core and H_2O reflector, while varying the buckling in only the D_2O reflector region.

5. Matching Thermal Flux Profile in R-Z and R Calculations

A method similar to that described in the preceding section was used here except that the thermal flux profile was matched only for a D_2O reflected core. Figure 24 presents a schematic of the two methods.

6. Three-dimensional Assembly Calculations

Several VENTURE assembly-level calculations were made using X-Y-Z geometry with reflective boundary conditions on all four sides of the assembly. These calculations were primarily to determine any variation in required axial buckling between homogeneous and heterogeneous descriptions.

7. Three-dimensional Core Calculations

Preliminary results from a full-core three-dimensional VENTURE calculation of axial bucklings at the core midplane are presented in Figure 25 . These results will be considered preliminary until verified by comparison with FNR experimental measurements, because the VENTURE calculation modeled the tank as being an entirely D_2O filled region. Actually, the geometry and material composition vary considerably in the D_2O tank and may have a significant effect on the calculated buckling.

The results of the buckling calculations shown in Table 14 indicate that an appropriate transverse buckling for the FNR core is most likely in the range of $1.7\text{-}1.8 \times 10^{-3} cm^{-2}$. The most accurate method for determining core transverse buckling is by full-core X-Y-Z VENTURE calculations. Other

R-Z Geometry

R Geometry

By Matching Eigenvalue

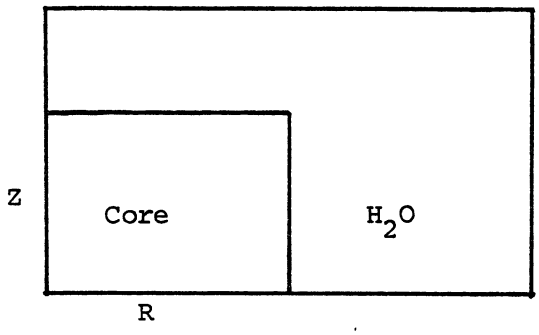

$k_R = k_{R-Z}$

$B^2 = 1.72 \times 10^{-3} cm^{-2}$

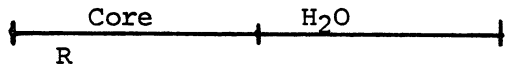

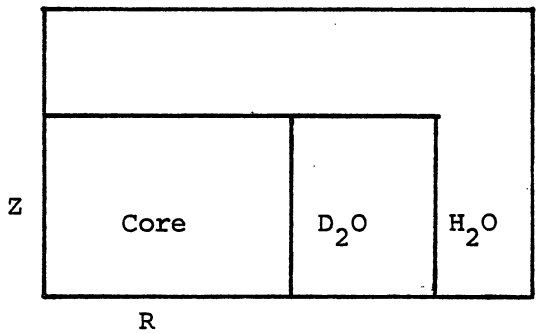

$k_R = k_{R-Z}$

$$B^2 = \begin{cases} 1.72 \times 10^{-3} cm^{-2}: & \text{core}+H_2O \\ 1.14 \times 10^{-3} cm^{-2}: & D_2O \end{cases}$$

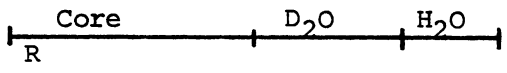

By Matching Thermal Flux Distribution

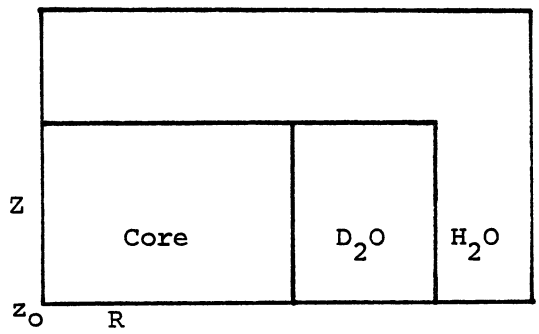

$\phi_T(R) \simeq \phi_T(R, Z_o)$

$$B^2 = \begin{cases} 1.82 \times 10^{-3} cm^{-2}: & \text{core}+H_2O \\ 1.14 \times 10^{-3} cm^{-2}: & D_2O \end{cases}$$

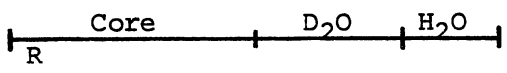

Figure 24. Axial Buckling Determination by Comparing R-Z vs. R Calculations

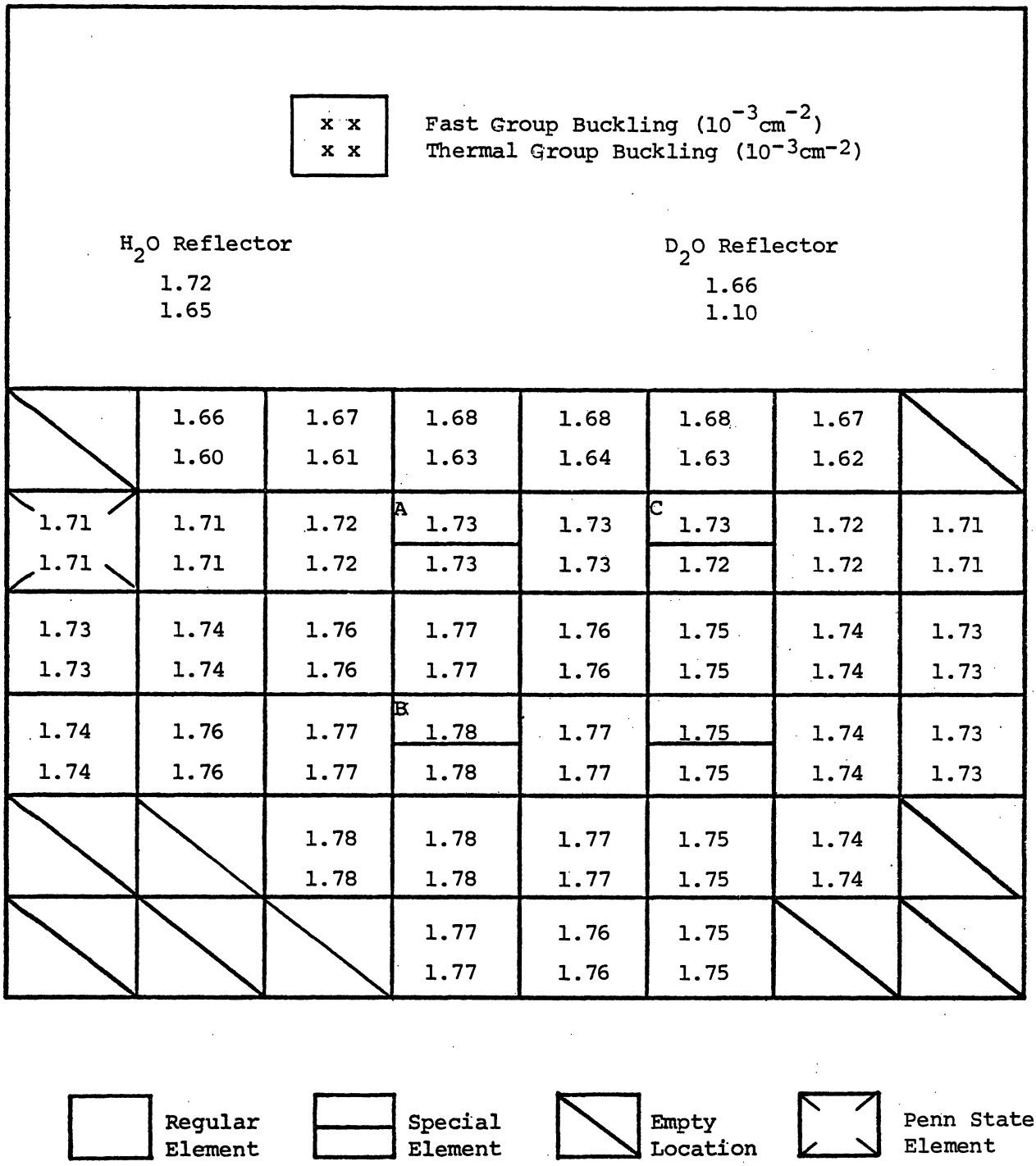

FNR Cycle 175D
VENTURE Calculation

Figure 25 . Axial Buckling at Core Midplane

methods such as R-Z comparisons yield reasonable results, but cannot predict the buckling on a zonal basis within the core.

Three-dimensional VENTURE calculations will be used to further refine the core buckling values. In particular, the effects of fuel element locaion and burnup could be analyzed. There remains considerable uncertainty in the appropriate buckling for the D_2O tank that may be resolved by more detailed three-dimensional calculations modeling thimbles and beam tubes in the D_2O tank.

III. Confirmation of Fuel Specifications

Using the calculational methods described in Section II, survey calculations were performed to analyze many possible LEU fuel designs for the FNR. Based upon these calculations and similar data developed at ANL,[30-33] we selected a particular LEU fuel design for detailed analysis. The proposed LEU fuel design and performance data on similar fuels are presented in Sections A.1 through A.8.

Our recommended LEU fuel for the FNR is 19.5% enriched with 167.3 grams of ^{235}U per 18-plate assembly. To accommodate the extra ^{238}U without changing fuel plate or assembly dimensions, the uranium loading in the fuel meat has been increased to 42 w/o and the fuel meat thickness has been increased to .030 inches (with a decrease in clad thickness to .015 inches).

Section A.9.3 presents a detailed core physics comparison of current FNR fuel and the proposed LEU fuel. For both batch fresh cores and an equilibrium core which models FNR operating experience, we have analyzed core power distributions, in-core and ex-core flux distributions, cycle length and operating characteristics, core excess reactivity and shutdown margins. Some of our principal conclusions derived from Section A.9.3 are:

A. For the FNR, operational restrictions and experimental requirements may preclude at present the use of significantly higher fuel loadings. Although higher loadings would give longer fuel life and thus improved economics, there would be a substantial decrease in shutdown margin (due to decreased rod worth) and also in thermal flux levels. While burnable poisons could mitigate the former, there is no remedy for the latter disadvantage.

B. The proposed LEU fuel containing 167.3 grams of ^{235}U per assembly represents a reasonable compromise, which would result in minimum perturbation in FNR operations and experimental usage, and minimum difficulty in obtaining license amendments.

C. A significant reduction in rod worths for the LEU fuel is noted in our calculations comparing batch HEU and LEU cores of the same size. A similar comparison for equilibrium core configurations studied so far indicates that the reduction in rod worths may be mitigated by increased core average fuel burnup in LEU cores. The results presented in Table A.9 showing the effect of different cycle lengths on the calculated rod worths for the three LEU

equilibrium core configurations are, however, preliminary, because the core size was not varied and hence the beginning-of-cycle reactivity was not matched between the cases.

IV. Safety Analysis Report

A draft version of the revised Safety Analysis Report has been forwarded to the Nuclear Regulatory Commission (NRC) for comment and has been included as Appendix A to this report. Following receipt and resolution of comments from the NRC, a final version will be submitted for approval. As noted in Appendix A, no reductions in FNR safety margins are expected from utilizing low enrichment fuel in the FNR core. However, there are a few outstanding items that require further examination:

1. The use of different fuel configurations, including oxide fuel
2. The accurate calculation of the power coefficient of reactivity.

Appendix A should be referenced for details concerning the above items and the specific analyses performed.

V. Thermal Hydraulics

Loss of coolant tests were carried out in 1952 at the Low Intensity Training Reactor (LITR).[34,35] In these tests, reactor coolant was suddenly drained from the reactor tank after the reactor had been operating for 138 hours at 1.25 megawatts. No emergency cooling was provided.

A peak temperature of 487 F (253 C) was measured at the midplane of a fuel plate in the center of the core approximately 135 minutes after the loss of coolant.

Based on these tests, ORNL concluded that the LITR would not be damaged by loss of coolant with no emergency core cooling after prolonged operation up to power levels of 3 megawatts. ORNL also concluded that heat losses by irradiation and convection were small in comparison to conductive losses into the 2000 pound aluminum grid plate and 3000 pound beryllium reflector that surrounded the core.

The LITR test results can not be applied directly to the Ford Nuclear Reactor (FNR). Although the fuel is nearly identical in shape and uranium content, the combined thermal mass of the FNR grid plate and heavy water reflector is 778 pounds. That smaller mass, which serves as the sink for heat conduction losses from the core makes direct use of the test results questionable. The following considerations are also relevant: The LITR was shutdown from 1.25 megawatts due to loss of moderator that occurred when the pool drained. Fission product heating following sustained operation at 1.25 megawatts was approximately 88 kilowatts. During a hypothetical FNR loss of coolant accident, caused by a six inch diameter beamport rupture, the core is calculated to remain covered by water for 690 seconds following shutdown. Fission product heating at time 690 seconds after shutdown is calculated to be approximately 44 kilowatts.

A single channel model of an FNR fuel element has been constructed. It consists of a single coolant flow channel with heated plates on either side. The heaters provide a square wave approximation to the fission product cosine distribution. The entire channel is surrounded by six inches of insulation.

Preliminary tests of the channel were conducted. Fission product heating in the hottest fuel plate in the core after loss of coolant has been calculated to be 160 watts. Since one side of each plate in the model is insulated, a plate power input of 80 watts simulates the hottest plate input in the single channel model; the total power in the two plates surrounding the channel is 160 watts. Experimental runs were made for total power inputs of 120, 160, 186 and 224 watts.

Figure 26 is a plot of the plate midplane temperature versus time for each of these power inputs.

Heat loss through the vermiculite insulation was estimated through Fourier's law of heat conduction, where the temperature gradient was obtained from the slope of the temperature profile at the fuel plate surface. Figure 27 is a plot of the insulation temperature profile at the midplane of the fuel plate model.

Application of Fourier's law and division by the peak to average axial power factor, 1.21, yields the following total power input - insulation loss combinations.

Total Power Input (watts)	Insulation Loss (watts)
120	27
160	30
186	41
224	50

These values depend upon the accuracy of the published value of vermiculite thermal conductivity, but they seem to indicate that approximately 20 percent of the input power is dissipated through the insulation.

As tests progressed, it seemed doubtful that natural convection up the channel would be adequate to account for all the heat dissipation other than conduction through the insulation. A small blocking device was placed at midplane in the channel. The 120 watt test was repeated. A plot of temperature versus time for the position eight inches from the top of the fuel channel is shown in Figure 28. The temperature profiles for unblocked and blocked flow are shown. The peak temperature for blocked flow is only about 50F greater then for unblocked flow. This seems to indicate that a large heat loss, possibly some form of radiation, has not been accounted for.

Continuing tests in the program will be devised to improve on the model. A new model will be constructed with two channels and three plates similar to Figure 29. One channel can be filled with insulation in order to repeat single channel tests. It was felt that more meaningful plate effects could be obtained by having a single central plate surrounded by two flow channels since, ultimately, plate temperatures are the desired parameters.

The improved model will have the capability of operating with blocked flow, controlled values of forced flow, and natural circulation. Heating plates will be placed above and below the channels in order to control radiative losses.

We will attempt to account for and quantify all heat transfer mechanisms and losses from the model.

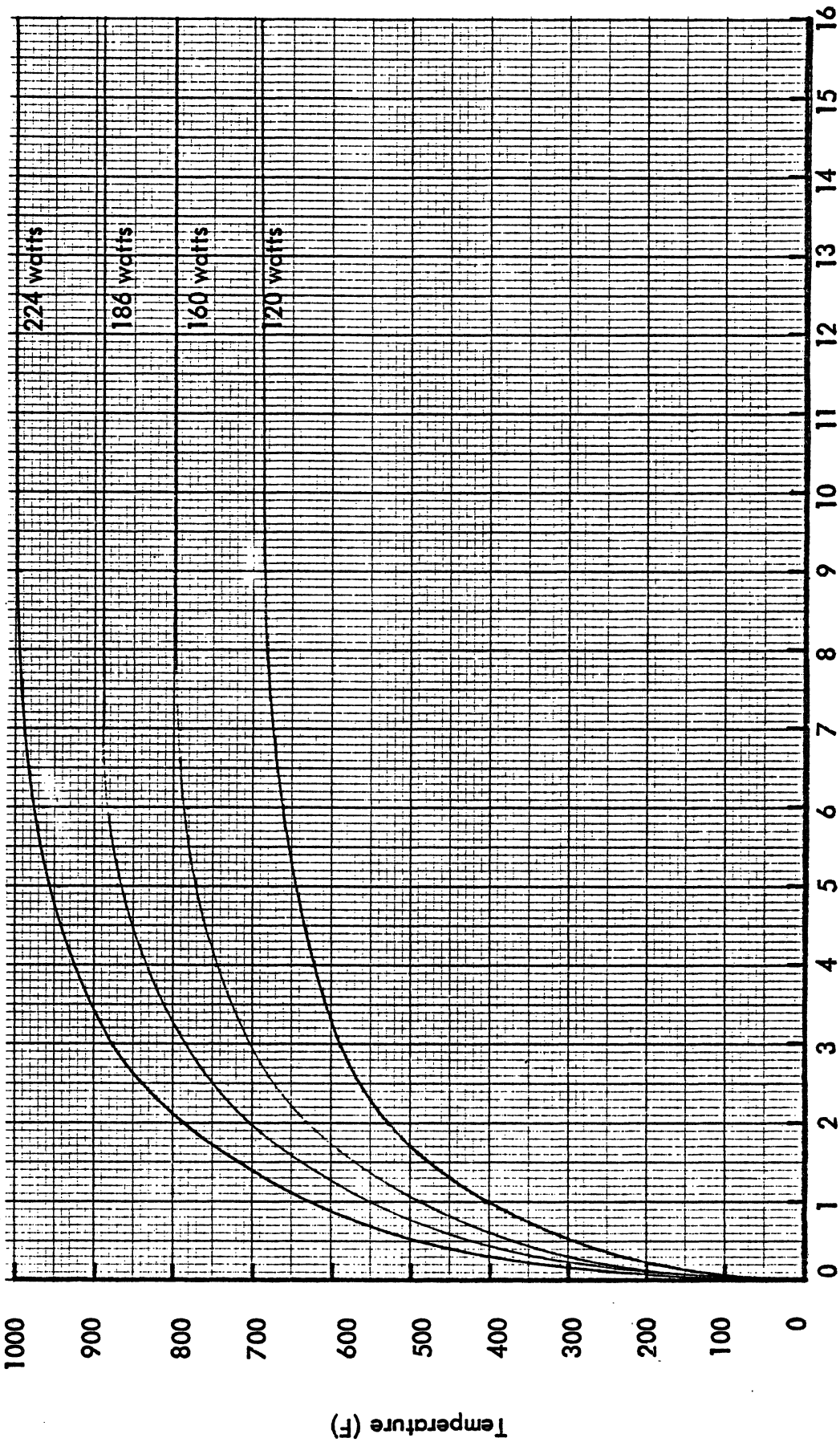

Figure 26. Fuel Plate Model Midplane Temperature Versus Time

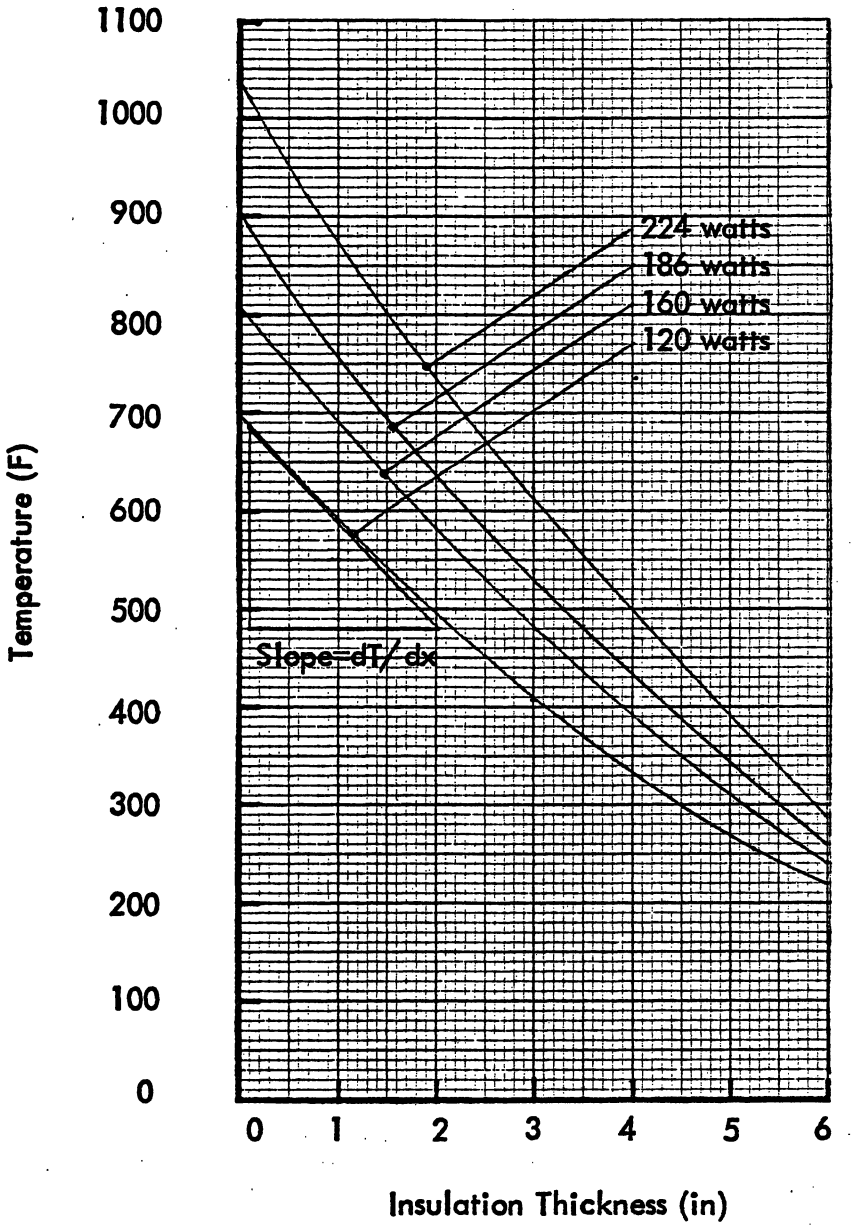

Figure 27. Fuel Plate Model Insulation Temperature at Midplane

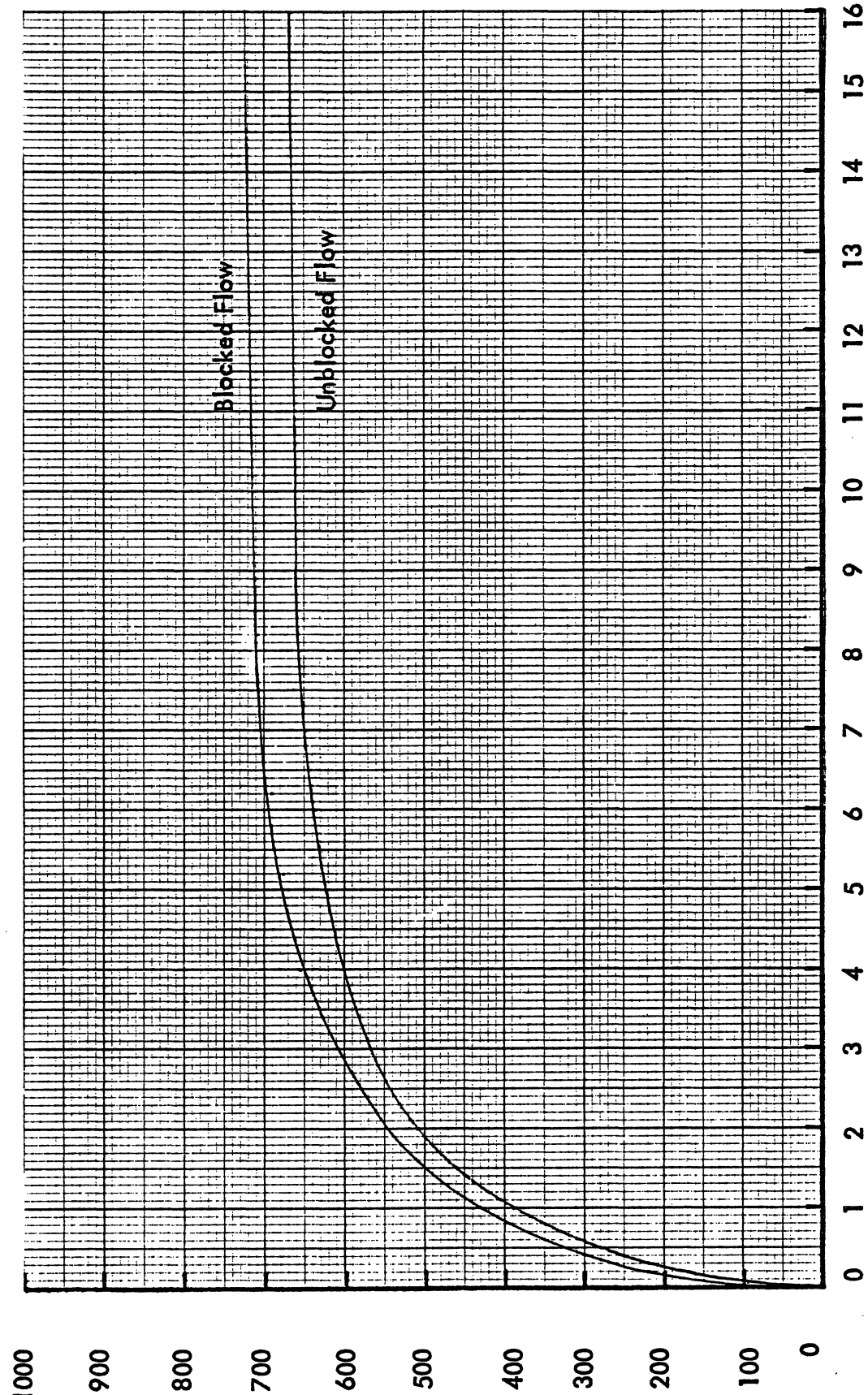

Figure 28. Fuel Plate Model Temperature Profiles at Eight Inches from Top for Unblocked and Blocked Flow

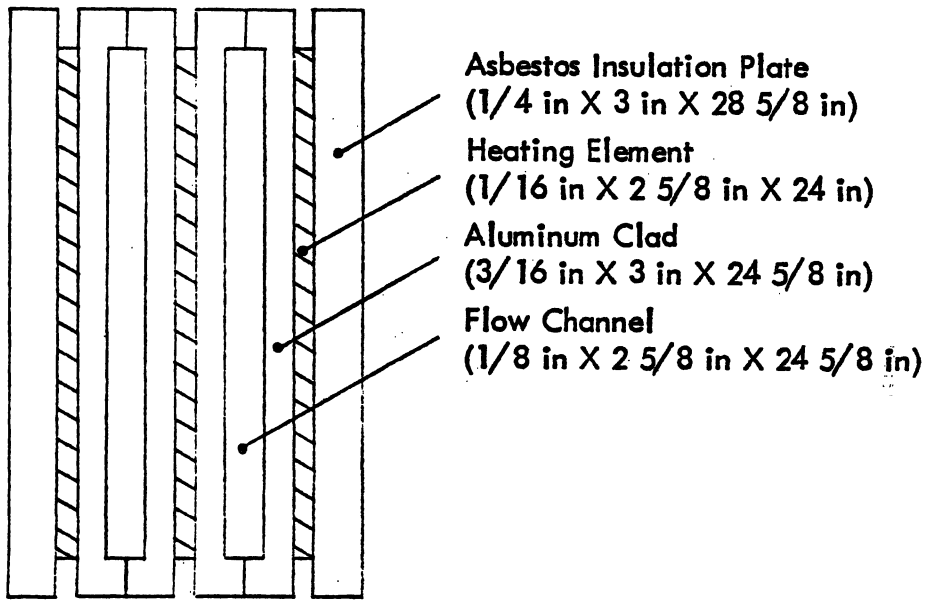

Figure 29. Fuel Plate Model Horizontal Section
Three Heaters - Two Channels

VI. Demonstration Experiment Program

A. Overview/Introduction

The demonstration experiments program has been developed to:

1) characterize the FNR in sufficient detail to discern and quantify neutronic differences between the high and low enriched cores.

2) provide the theoretical group with measurements to benchmark their calculations.

The experiments chosen to accomplish this task are:

1. Wire activation measurements to provide absolute flux normalization.

2. Rhodium detector flux maps to provide absolute thermal (in-core and ex-core) fluxes

3. Neutron diffraction measurements to determine the flux spectrum in the D_2O reflector

4. Control rod worth measurements and power defect measurements

5. Unfolding of foil activation measurements to determine the in-core flux spectrum.

The following sections of the report describe the principal results of the experiments performed so far. The report is written with the philosophy that the reader is familiar with these standard techniques. It should be emphasized that the experimental program has not been finished. Additional refinement and repetition of the experiments (particularly 1, 3, and 4 above) would be advantageous. Regarding the rhodium flux maps, testing and application of the rhodium detector transfer function analysis (described later) would make full-core rhodium flux maps a much quicker process. Lastly, the actual experimental work associated with the spectral unfolding still remains to be completed. Nevertheless, the results detailed in the report represent a major part of the experimental characterization of the high enriched FNR core.

B. Wire Activations for Absolute Flux Normalization

1. Purpose

The purpose of this phase of the experimental program was two-fold:

i) to provide measured values of the thermal flux in the core and D_2O tank for comparison with the results being generated by the 2DB code.

ii) to provide a means of absolute determination of the sensitivity of the rhodium detector (to be discussed in the next section).

2. Axial Flux Determination

a) Thermal flux determination

In order to obtain a measured value of the thermal flux, bare and cadmium covered iron wires were irradiated. The iron reaction:

$$Fe^{58}(n,\gamma)\,Fe^{59}$$

was used since the cross section varies as $1/v$ below 0.1 keV. The analysis follows that of Beckurts and Wirtz[36], where it is shown that

$$\Phi_{th} = \frac{R_b - F_{cD}\,R_{cD}}{N_o\,(\sigma_{2200}\cdot\sqrt{\pi}/2)}$$

where R_b/N_o = saturated activity of the bare wire per unit target nucleus

R_{cd}/N_o = saturated activity of the cadmium covered wire per unit target nucleus

$$F_{cD} = 1 + \frac{\left(\begin{array}{l}\text{activity produced by neutrons with energy between}\\ \text{the thermal cutoff } (E_{Tc}) \text{ and cadmium cutoff } (E_{cc})\end{array}\right)}{\left(\begin{array}{l}\text{activity produced by neutrons with energy greater}\\ \text{than the cadmium cutoff } (E_{cc})\end{array}\right)}$$

Φ_{th} = thermal flux = $\int_0^{E_{Tc}} \Phi(E)\,dE$

σ_{2200} = the 2200 m/sec cross section for the reaction.

The fact that the cross section varies as $1/v$ makes the evaluation of the thermal cutoff energy, the cadmium cutoff energy, and F_{cD} very straightforward, and yields

E_{Tc} = thermal cutoff energy = 0.089 eV

E_{cc} = cadmium cutoff energy = 0.55 eV

and $F_{cD} = 2.5$

It should be mentioned that for all activations performed, we have neglected corrections for self shielding, flux depression, and scattering in the foils, assuming they are small. Ge-Li detectors, calibrated with an NBS standard, were used in the counting.

The thermal flux determined by wire activations done axially along the core center is shown in Figure 30 . The data "points" are shown as bars since the 1" long wire segments actually integrate the flux over this distance. Note that the thermal flux reflector peaking is responsible for the increased values near the ends of the fuel plate. The fact that the flux peaks slightly below the core midplane is attributable to the location

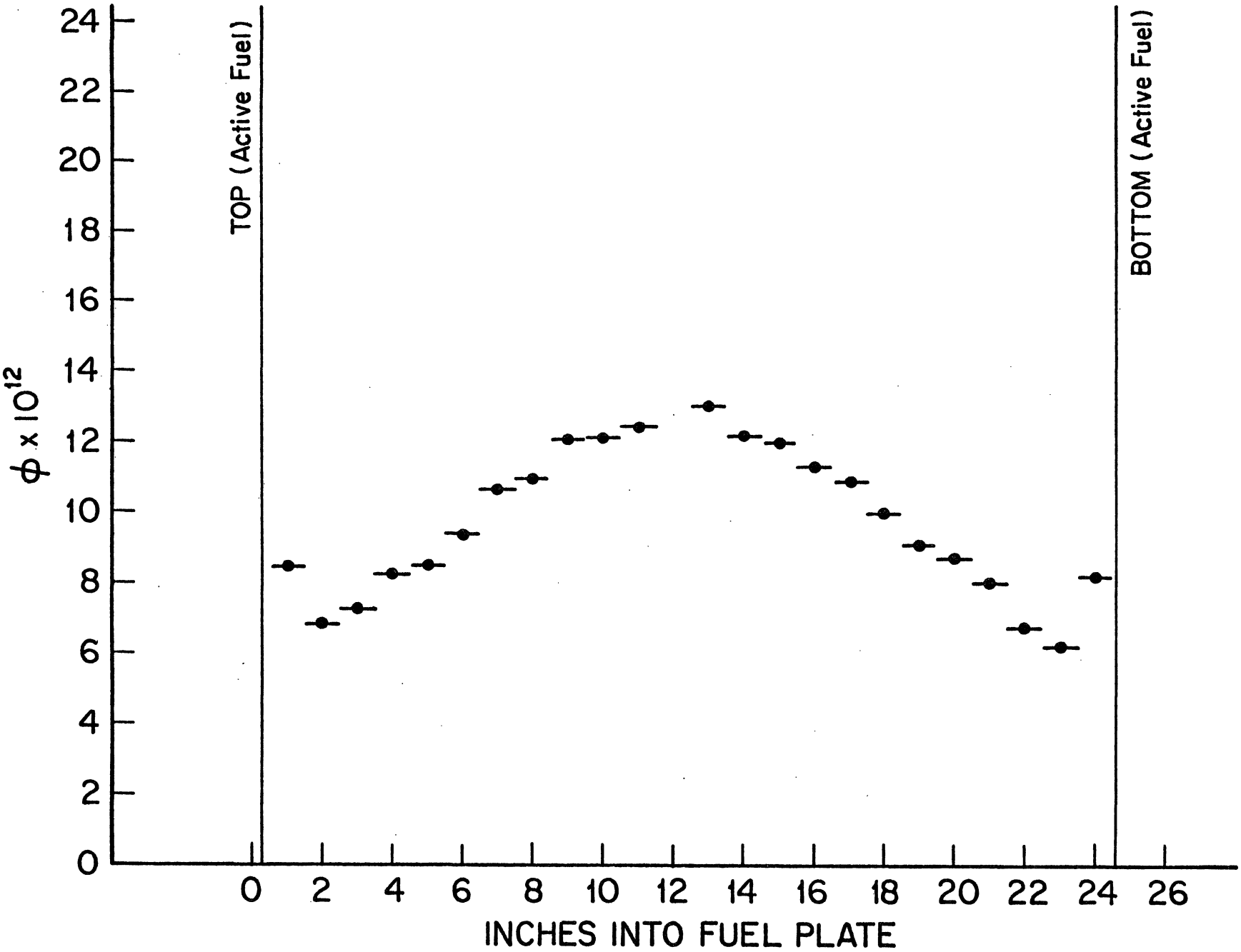

Figure 30. Wire Activation Results for ϕ_{th}
-Location L-37-

of the shim rod bank. The results have been compared to earlier measurements on the FNR, and were found to be in good agreement.

b) Intermediate "thermal" flux

The results generated by the computer codes, (such as LEOPARD and 2DB) will not agree with the results presented in Figure 30. The reason for this lies in their definition of the thermal flux. It is a common practice to define the thermal flux using the cadmium cutoff energy as the upper limit. For this reason, we define an "intermediate thermal flux", as:

$$\Phi_{IT} = \int_{E_{TC}}^{E_{CC}} \Phi(E)dE$$

In this energy region, the flux is assumed to behave as 1/E. Since the flux per unit lethargy is constant, it is not difficult to show:

$$\Phi_0 = \frac{R_{epi}}{N_0 I_{eff}}$$

where

Φ_0 = flux per unit lethargy

R_{epi}/N_0 = saturated activity produced by neutrons with energies greater than E_{cc} per unit target nucleus.

I_{eff} = effective resonance integral

Then the "intermediate thermal flux" may be evaluated as:

$$\Phi_{IT} = \Phi_0 \ln\left(\frac{E_{cc}}{E_{TC}}\right)$$

The activity from the cadmium covered iron wire $Fe^{58}(n,\gamma)Fe^{59}$ reaction can be used to determine Φ_0, and hence Φ_{IT} (or any integral flux in the 1/E range).

The correct flux to compare with the computer generated "thermal flux" is thus $\Phi_{th} + \Phi_{IT}$.

Figure 31 presents $\Phi_{th} + \Phi_{IT}$ for the axial center-of-core irradiations described above. The addition of Φ_{IT} adds as much as 10%, at the core center, to the value of Φ_{th}, and brings computer calculated fluxes closer to the measured fluxes. Also presented on Figure 31 are the results of an axial rhodium detector flux map made on the same fuel element. The rhodium points are based on the manufacturer's detector sensitivity and are uncorrected for epithermal neutrons. The large disagreements in the values of the flux are attributable to these epithermal neutron contributions to the rhodium detector signal, and are discussed in detail in section C. There the measured values of $\Phi_{th} + \Phi_{IT}$ will also be used to calculate the sensitivity of the rhodium

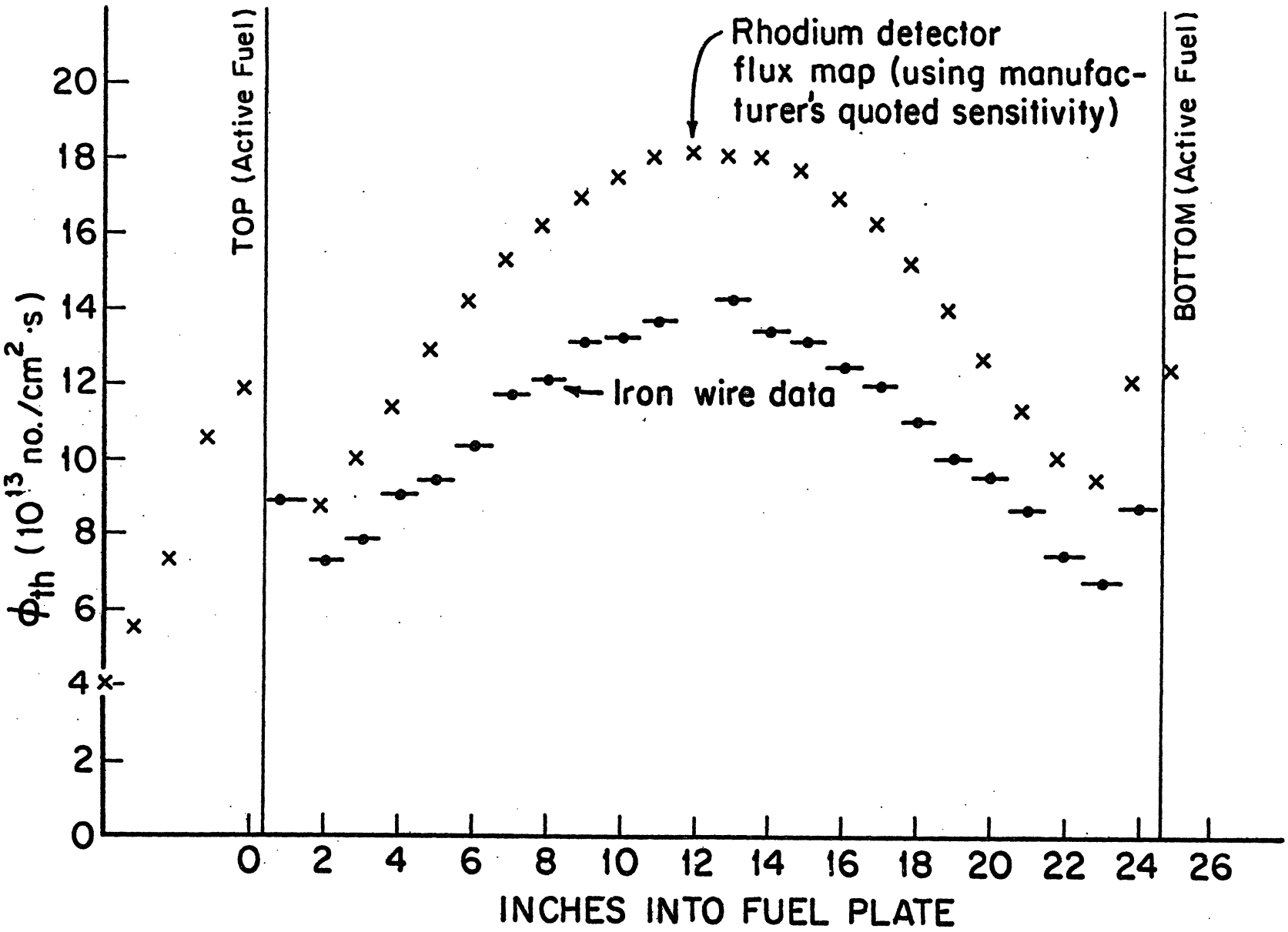

Figure 31. Wire Activation Results for $\phi_{th}+\phi_{IT}$

-Location L-37-

detector in the FNR.

c) Fast Flux

An additional benefit from activating iron is the threshold reaction:

$$Fe^{54}(n,p)\,Mn^{54}$$

which has a threshold at ~ 3.75 MeV. It is common to define an "effective threshold cross section", σ_{eff}, as

$$\sigma_{eff} \equiv \left[\frac{\int_{E_{th}^{eff}}^{\infty} \sigma(E)\phi(E)dE}{\int_{E_{th}^{eff}}^{\infty} \phi(E)dE}\right] \cdot \left[\frac{\int_{E_{th}}^{\infty} \sigma(E)\phi(E)dE}{\int_{E_{th}^{eff}}^{\infty} \sigma(E)\phi(E)dE}\right]$$

where

E_{th} = actual threshold energy

E_{th}^{eff} = a convenient value of energy

and

$\phi(E)$ is normally represented as the fission spectrum in the integrals.

In this case

$$\phi_f = \int_{E_{th}^{eff}}^{\infty} \phi(E)dE = \frac{R}{N\sigma_{eff}}$$

For the $Fe^{54}(n,p)Mn^{54}$ reaction, we chose $E_{th}^{eff} = 4$ MeV. The integrals were numerically performed using data from BNL-NCS-50446, the dosimetry file for cross sections. Then, defining a fast flux as:

$$\phi_F = \int_{4\,MeV}^{\infty} \phi(E)dE$$

one can obtain

$$\phi_F = \frac{R}{N\sigma_{eff}}$$

where $\frac{R}{N}$ = saturated Mn^{54} activity per unit Fe^{54} nucleus.

Thus, from the measurement of the Mn^{54} activity, one can obtain a measure of the fast flux, as defined above. Figure 32 shows the results of the measurement. Note that the flux scale is an order of magnitude smaller than for figures 30 and 31 , indicating the smaller size of this fast flux. The noticeable shift of the flux towards the bottom of the core has been discussed earlier.

Additional measurements of the fast flux using the threshold reaction:

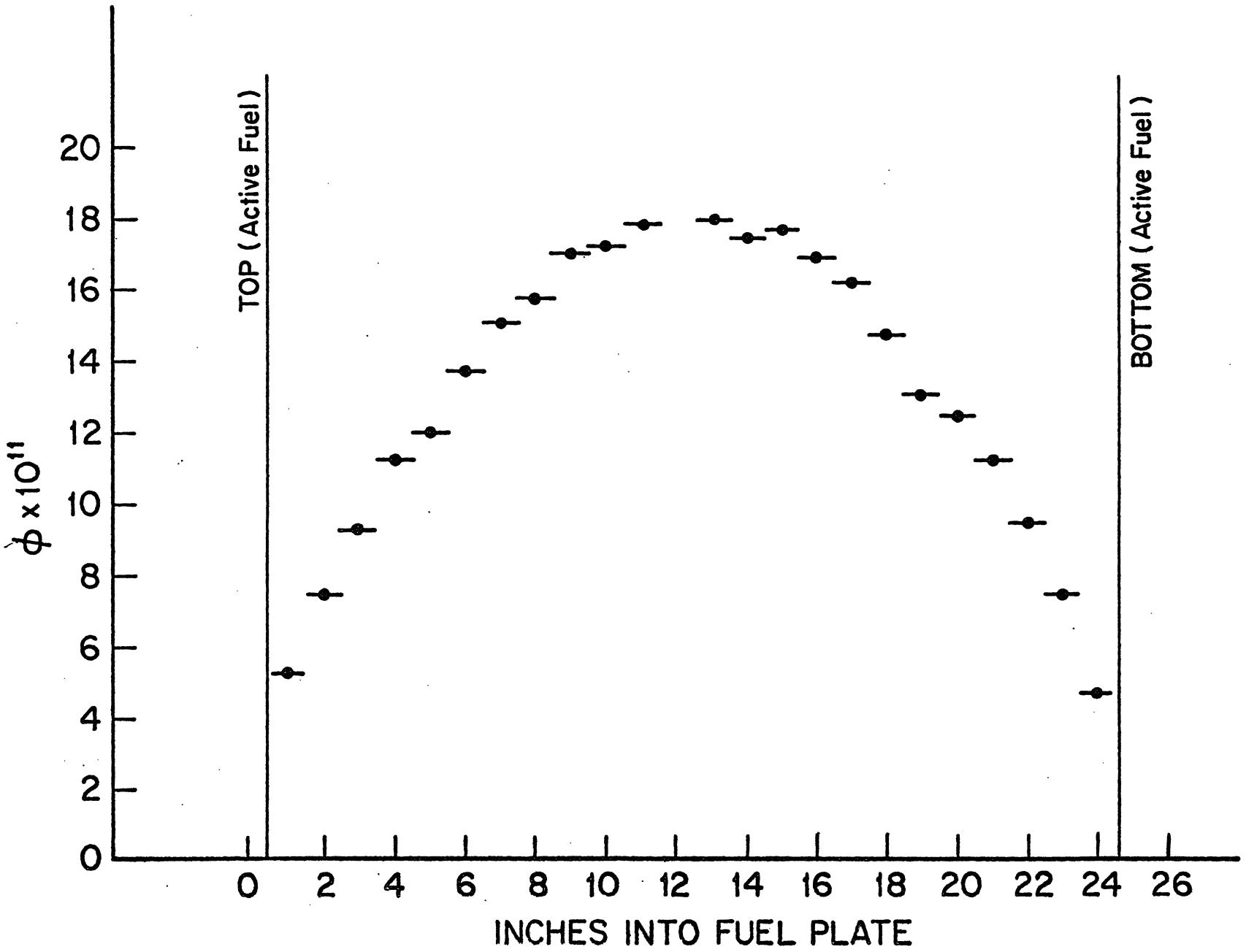

Figure 32. Wire Activation Results for ϕ_F
-Location L-37-

$Al^{27}(n,\alpha)\,Na^{24}$

with a threshold of ~8.15 MeV were made. The analysis was performed as outlined above, and yielded the energy integrated flux above 8 MeV. As might be expected, the results look like Figure 32 on a smaller scale.

d) Ratio of fast to thermal flux

Lastly, it is expected that the ratio of fast to thermal flux will change with the introduction of low-enriched fuel. One measure of this, (besides taking ratios of Figures 30, 31 , and 32) is the cadmium ratio. For the measurements described above, the iron cadmium ratio remained approximately constant in the core (except near the edges of the fuel) at about 9.7. The fact that the spectrum does not vary significantly throughout the normal fuel elements in the core greatly simplifies the measurements of the rhodium detector correction factors, as described in section C . But while Φ_{th}, Φ_{IT}, Φ_F, and the cadmium ratios calculated in this section can be used to quantitatively compare spectral shifts associated with switching to low enriched fuel, a complete set of foil activations coupled with an unfolding technique (described in section E) will be used for more detailed results.

3. Radial Flux Determination

One of the difficulties encountered in attempting to compute the flux in the D_2O reflector is the complex structure inside the tank. In order to provide benchmark values of the flux bare and cadmium covered iron wire irradiations were performed in the vertical penetrations of the D_2O tank.

Photographs of the D_2O tank are shown in Appendix B . The vertical penetrations into the D_2O tank are the 12 small, 1" inner diameter, pipes on the tank's top. These pipes extend down to within a few inches of the core midplane, and are filled with H_2O. Appendix B shows the spacing between penetrations, and the names associated with them, (e.g., D_2O tank position S). This nomenclature will be used throughout the rest of the report for specifying locations in the D_2O tank.

Bare and cadmium covered iron wires were irradiated in D_2O tank positions O and X. The results for the core center, and for D_2O tank positions O and X at an axial position 2" above the core midplane, are presented in Table 15. The thermal flux is seen to fall off much slower in the D_2O tank as compared to an H_2O reflector (see rhodium detector flux mapping data, section C). This is exactly what is expected. Further, the thermal flux quoted for D_2O tank

Table 15 . Comparison of Energy Integral Fluxes

	Core Center	D_2O Position X	D_2O Position O
Φ_{th}	1.21×10^{13}	$.913 \times 10^{13}$	$.287 \times 10^{13}$
Φ_{IT}	(0.117×10^{13})	$(.451 \times 10^{12})$	$(.169 \times 10^{11})$ ($\pm$13%)
Φ_F	0.172×10^{13}	0.139×10^{12}	negligible ($< 10^9$)
R_{CD}(Fe)	9.72	16.67	128

D_2O measurements made with water in tubes.

Double precision run causes negligible difference in above numbers

position X is in good agreement with previously measured values. The values of $\Phi_{th} + \Phi_{IT}$ are being used by the analytical group to fix the D_2O tank parameters for the computer calculations. The iron cadmium ratios are presented for future comparisons with low enriched fuel.

4. Conclusion

While the results presented in this section provide information on the fast and thermal fluxes for computer calculation comparisons and position dependent spectrum variations, they will also play an essential role in the calibration of the rhodium detector discussed in the next section.

C. Rhodium Detector Thermal Flux Mapping

1. Purpose and Introduction

The purpose of this phase of the experimental program was to measure the thermal flux* at many locations in the core and reflectors, in order to:

i) provide measured values to the analytic group performing the computer calculations. This ensures the codes are generating realistic results and provides additional confidence in their projections to low-enriched fuel.

ii) characterize the thermal flux profile associated with highly enriched fuel in order to quantitatively discern the changes associated with switching to low enriched fuel.

A rhodium self-powered neutron detector was chosen to accomplish the goals because:

i) its size, mobility, and sensitivity are such that it can measure the thermal flux at any axial point in almost any core lattice position,

ii) the time required to obtain a measured flux, once the sensitivity is known, is much less than for a wire activation, and

iii) the uncertainty in the measured value is comparable to that obtained from wire activations.

This section of the report briefly describes the physics associated with the rhodium self-powered neutron detector, the equipment used to perform the measurements, and the determination of the detector sensitivity. The results of axial and radial measurements are then presented, along with calculations of the estimated errors in the measurements. Finally, a technique being developed which may eliminate the most serious drawback in using the rhodium detector for full-core thermal flux maps is addressed.

---

*In contrast to Section VI.B, the "thermal flux" in this section is defined as: $\Phi_{th} = \int_0^{E_{cc}} \Phi(E)dE$ where the value of the upper integrand has been changed to the cadmium cut-off energy.

2. Theoretical Description of Rhodium Detectors

The operation of a rhodium self-powered neutron detector is based on the rhodium nuclear reaction:

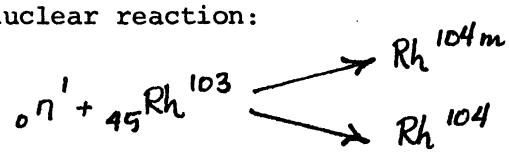

A typical self-powered detector is shown schematically below:

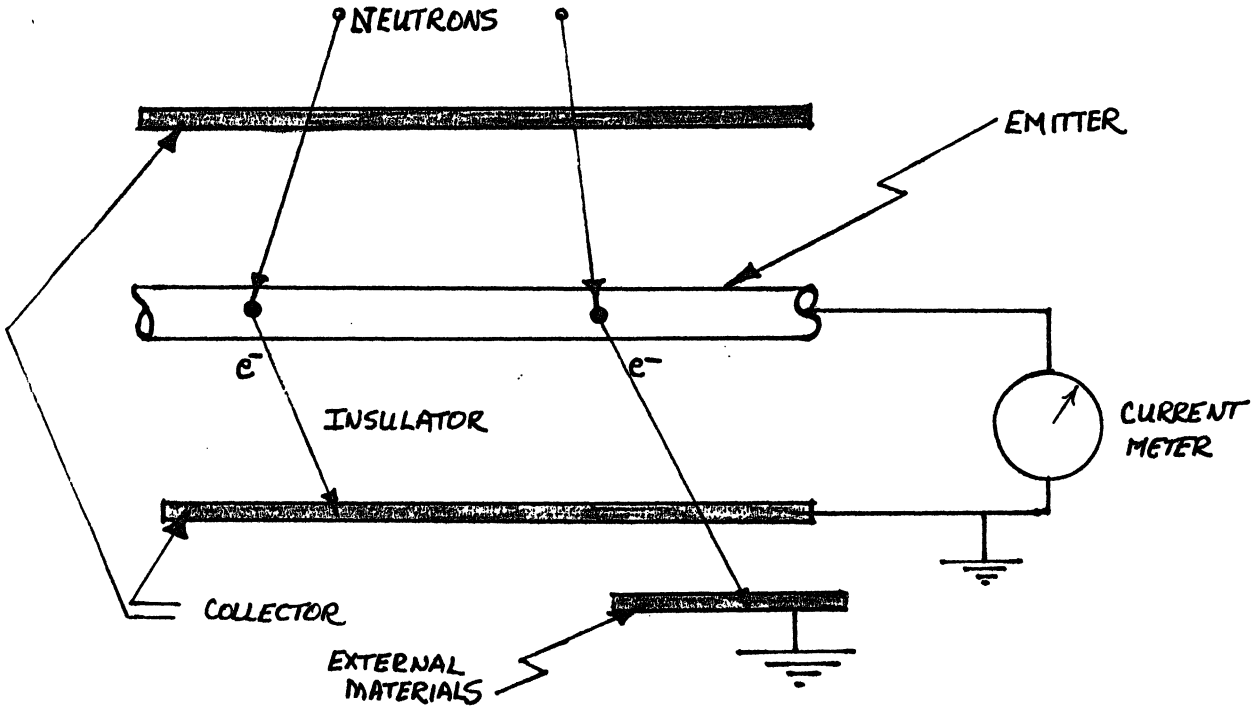

Neutrons which are captured in the rhodium emitter give rise to nucleii (Rh^{104}, Rh^{104m}) which decay by e^- emission. A simplified rhodium decay scheme is shown in Figure 33. Some of these electrons travel in such directions and have sufficient energy to escape the insulator, and are stopped in the collector. The charge thus produced on the rhodium emitter leads to a current which is measured by an external current meter, and is a direct indication of the neutron flux at the emitter.

A closer examination of the rhodium decay scheme (Figure 33) brings to light two important factors of the rhodium detector. First, the relatively high rhodium absorption cross section implies a relatively high neutron sensitivity. Indeed, rhodium has the highest sensitivity of any type of self-powered neutron detector. For the FNR, it is the only commercially available material which will yield large enough signals to give precision data. In Figure 34, the energy dependence of the rhodium absorption cross section

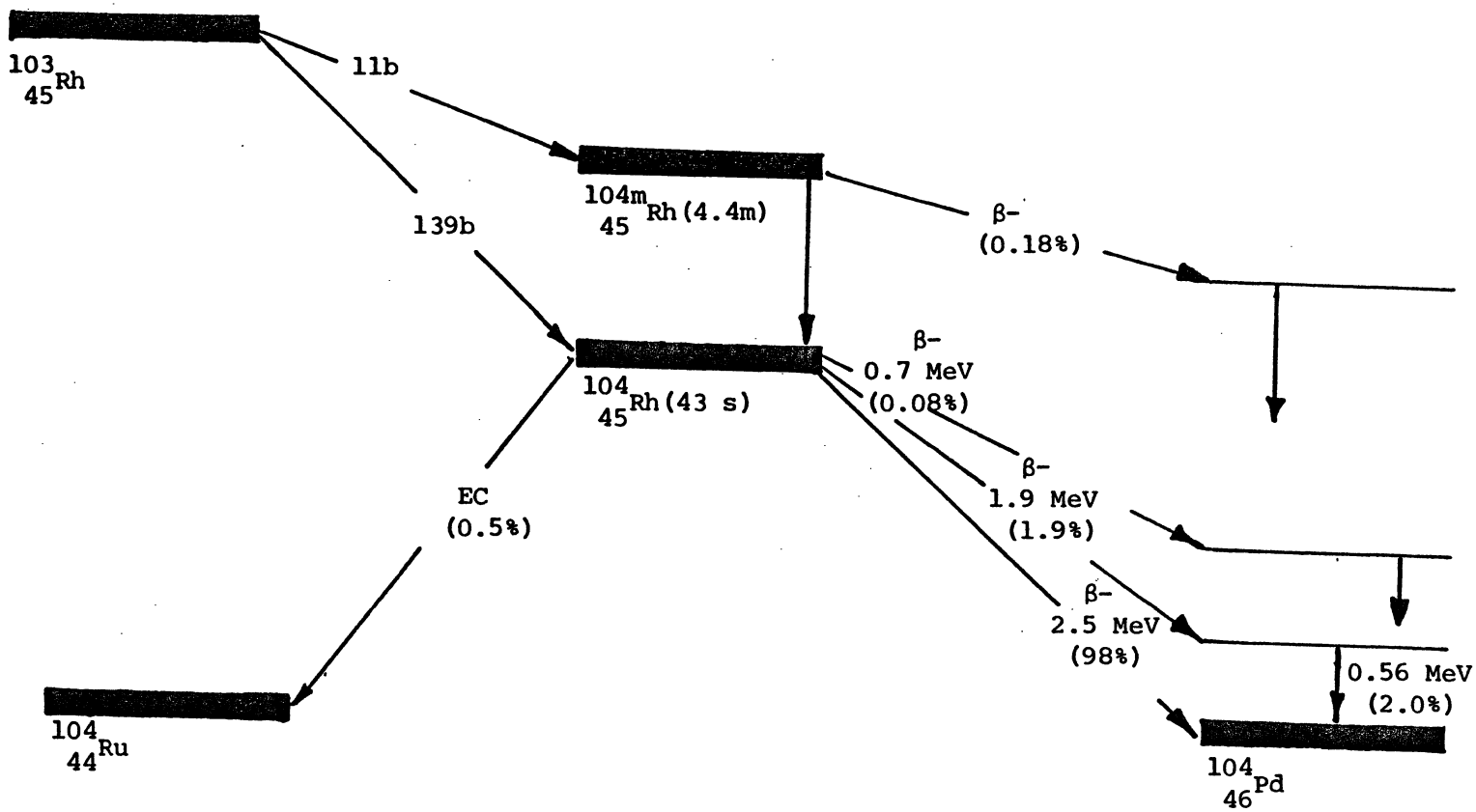

Figure 33. Rhodium Decay Scheme

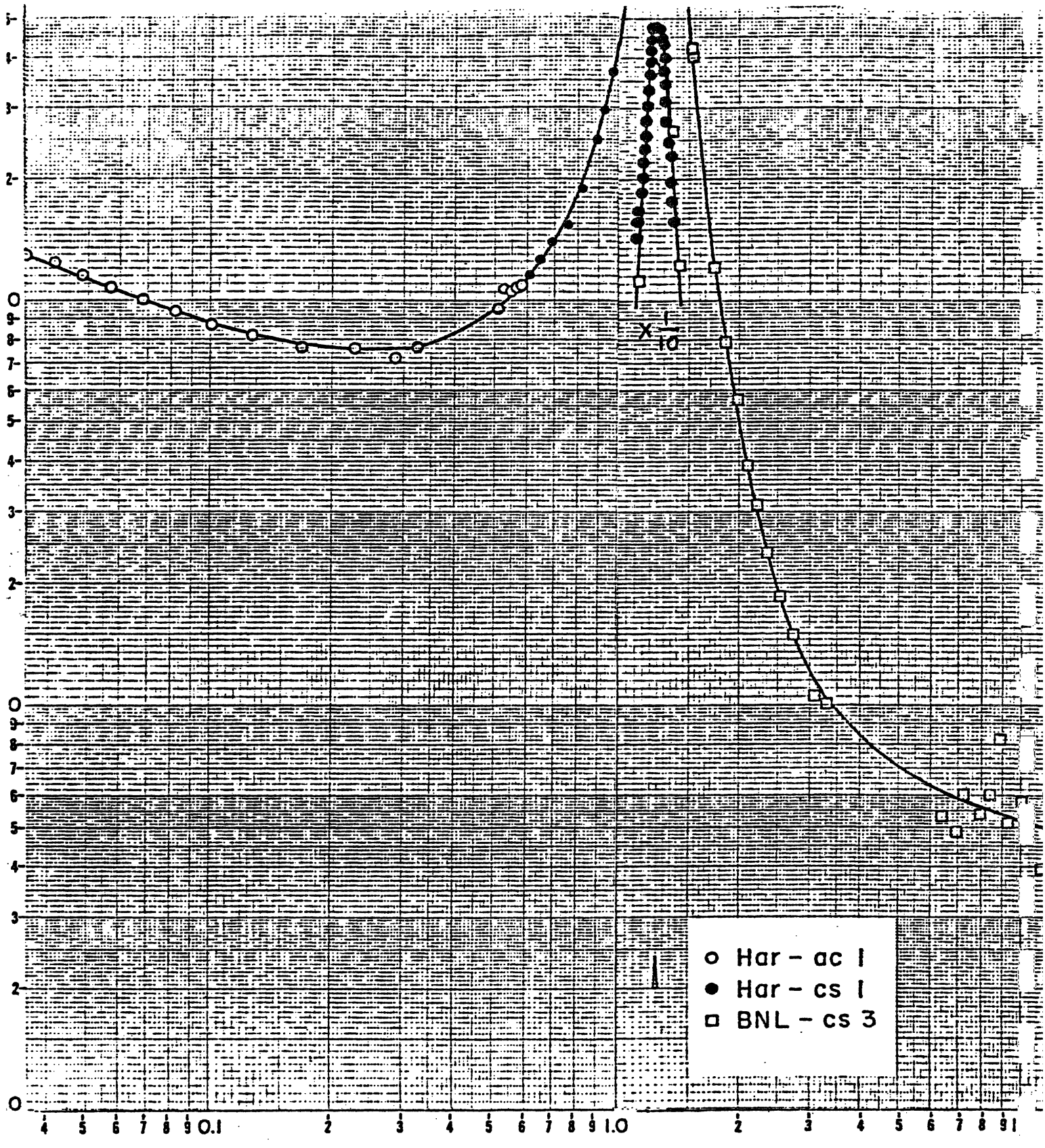

Figure 34. Rhodium Absorption Cross Section
(from BNL-325 - Second Edition)

is shown. The large resonance at 1.25 eV implies that the detector is also measuring neutrons in the epithermal range. Since the thermal flux is required, epithermal corrections need to be applied to the detector current, and are described later. Secondly, the presence of the metastable state of Rh-104, with its 4.4 minute half life, implies that the current may take several minutes to reach its equilibrium value after a change in flux. This can be seen more precisely by writing the appropriate rate equations and current equation for one energy group, and solving for the current. It can be shown that, following a step change in the flux at t=0, the time dependence of the current can be approximated by:

$$I(t) \approx I_o + \Delta I\left(1 - .085\, e^{-\lambda_m t} - .912\, e^{-\lambda_g t}\right) = I_o + (\Delta I)(f(t))$$

where I_o = initial equilibrium value of current for $t \leq 0$.

ΔI = change in the equilibrium value of the current as the result of the step change in flux

λ_g, λ_m = decay constants for the Rh^{104} ground and metastable states.

$f(t)$ = the time dependent function contained in parenthesis.

Using the above relationship yields:

t (min.)	$\frac{I(t)-I_o}{\Delta I}$ (%)
1	58%
2	81%
3	90%
5	95%
7	97%
9	98%
10	98%

In constructing this table, it is clear that the 4.4 minute half life of Rh^{104m} leads to the requirement of $\sim$10 minute wait times for $\sim$98% of the current change to occur. However, the quantity of interest is usually the error in the measured current, which is defined as:

$$\epsilon(t) = \left| 1 - \frac{I(t)}{I_f} \right|$$

where I_f is defined as the equilibrium value of the current after the flux change.

Using the above relations, algebra yields:

$$\epsilon(t) = (1-f(t))\left|1-\frac{I_o}{I_f}\right| = (1-f(t))\left|\frac{1}{1+\frac{f(t)}{\left(\frac{I(t)}{I_o}-1\right)}}\right|$$

The second expression is useful for on-line estimates of the detector current error as a function of time. Using the first relationship for a fixed value of the wait time, one can tabulate ϵ . For a wait time of 3 minutes, for example, we obtain

$\frac{I_o}{I_f}$	$\epsilon = \left\|1-\frac{I(t)}{I_f}\right\|$
.83	1.7%
1.2	2 %
.5	5 %
2	10 %
.1	9 %
10.	90 %

This shows that, for a given wait time, the detector should be moved into regions of increasing flux to minimize the error in the current. Or conversely, longer wait times are required for a given error in the current if the detector is moved in the direction of decreasing flux. Thus, while wait times on the <u>order</u> of several minutes are expected, the actual wait times required for a given error in the current cannot be predicted a priori*, but can be minimized through a judicial choice of detector measurement positions.

3. Equipment Description

In order to carry out this experimental program, several pieces of equipment were designed and fabricated. These are briefly discussed below.

The rhodium self-powered neutron detector (SPND) is shown in Figure 35. A bare lead, parallel to the emitter lead, is not shown on the figure, but was used to measure the current background. The detector was mounted on a paddle designed to minimize flux perturbations, and can be accurately positioned at any axial location in a regular or special fuel element.

Special adapters were built to allow the SPND assembly to be used in the vertical penetrations into the D_2O tank (discussed in Section B). These adapters sit on the vertical D_2O tank pipes, and provide a reference

*The easily derivable expression: $I_f = I_o + \frac{1}{f(t)}(I(t)-I_o)$ cannot be repeatedly used to shorten the wait time since I_o represents an equilibrium current prior to the step flux change. Techniques to eliminate the wait times are discussed later.

height and centering bar for the SPND assembly.

A special adapter was designed and built to measure the flux in the H_2O reflector south of the core. This adapter looks very similar to a regular fuel element, except that it has only four vertical channels for the detector. (See Figure 36). But unlike a regular fuel element which only has two channels which are accessible to our detector, all four channels can be used for measurements and were specifically located to bracket the anticipated narrow thermal flux peaking in the reflector. The adapter fits into an extension of the core grid plate, and rests snugly against a regular fuel element.

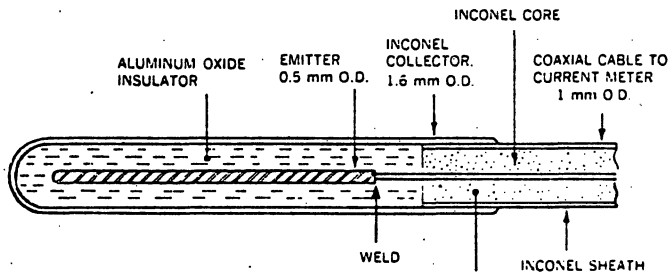

FIG. 35
SELF POWERED NEUTRON DETECTOR CONSTRUCTION

4. Determination of Detector Sensitivity

In order to transform the measurements of current into flux values, the sensitivity of the detector, S, must be known, i.e.

$$S = \frac{I}{\phi}$$

This parameter plays a crucial role in the data analysis, and its accurate determination is the subject of this section.

One technique to determine S is based on the theoretical calculations of Warren[37] . . The model he proposes includes the effects of 2200 m/sec neutron self-shielding in the emitter wire, the energy loss of the electrons in traversing the insulator and emitter, and correction for space-charge buildup on the insulator. A prescription is presented for determining the sensitivity of various types of detectors with different insulators and geometries. In general, the model is said to give reasonable agreement between measured and calculated sensitivities. When applied to our detector, Warren's model yields 2.97×10^{-21} amps/nϕ.

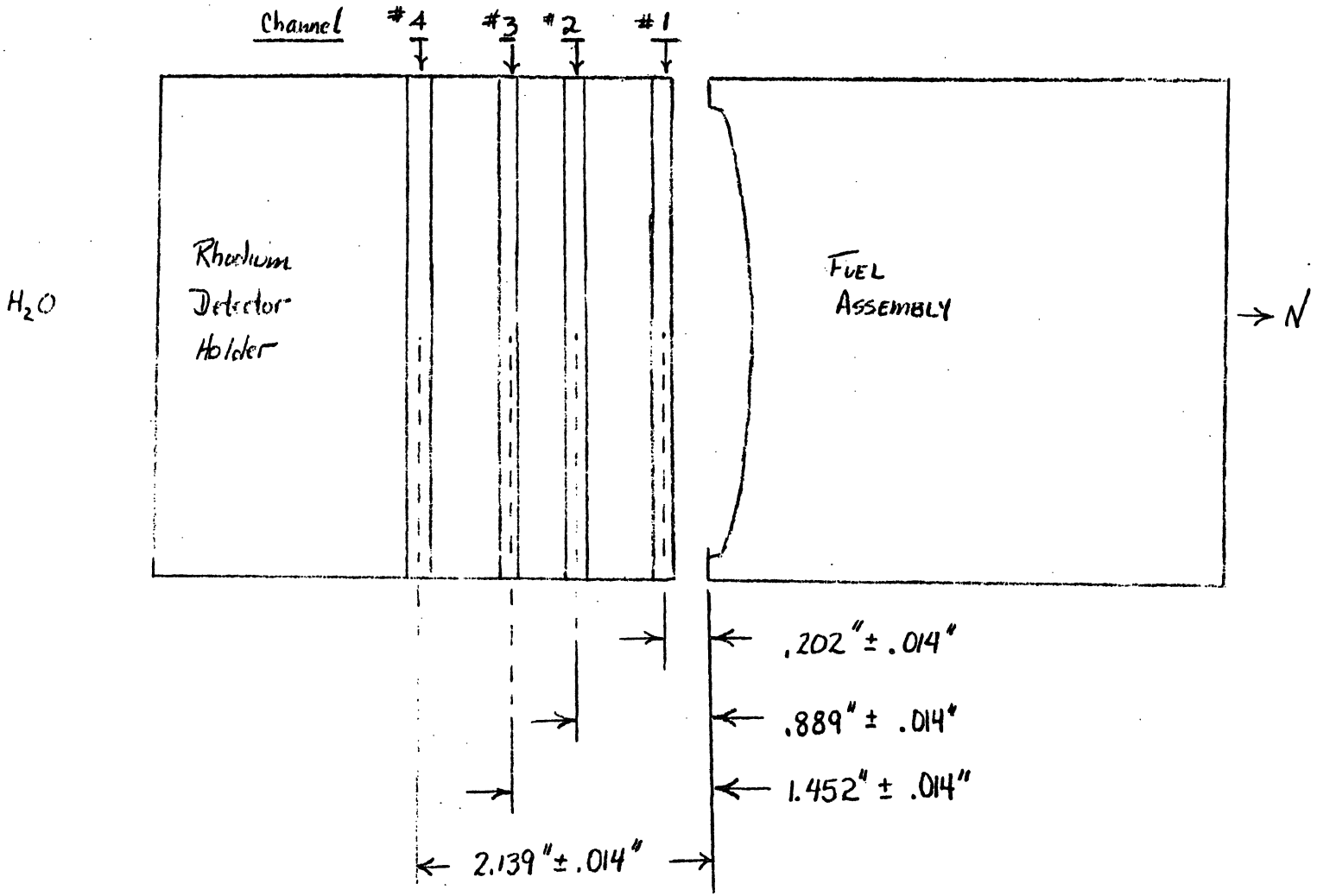

Figure 36. Radial Measurement Locations for Rhodium Detector Holder

The manufacturer's quoted sensitivity is 3×10^{-21} amps/n$\bar{v}$, close to the calculated value.

In a more recent work, Laaksonen [38] points out that "several simplifying assumptions were made in [Warren's] model which, in the case of a rhodium SPND in a relatively hard spectrum might be too rough. For example, it was assumed that the electron source in the emitter wire is spatially flat, and only 2200 m/sec neutrons were considered." Laaksonen shows that the sensitivity can be strongly spectral dependent, and hence brings into question the validity of the sensitivity which is calculated above. Furthermore, he notes that the manufacturer's quoted sensitivities are usually given as electric current per unit 2200 m/sec flux. For reactors with a spectrum different than that used in the calibration of the sensitivity, the manufacturer's value may not be appropriate. Finally, when the manufacturer's sensitivity was applied to the FNR rhodium detector data, the fluxes did not agree with the iron wire data presented earlier.

As a result of these uncertainties, a program to determine the absolute sensitivity of the rhodium detector used in the FNR spectrum was developed. Define:

$\underline{x}$ ≡ position vector

$f_{th}(\underline{x})$ ≡ fraction of detector current which is attributable to neutrons with energy below the cadmium cutoff energy, (E_{cc}).
≡ "epithermal correction factor"

$I_{th}(\underline{x})$ ≡ "thermal" detector current ≡ detector current which is attributable to neutrons with energy below E_{cc}.

$I_{tot}(\underline{x})$ ≡ total net detector current

$\Phi_{th}(\underline{x})$ ≡ thermal flux

Using these quantities, the sensitivity of the detector to thermal neutrons can be written as:

$$S_{th}(\underline{x}) = \frac{I_{TOT}(\underline{x})}{\Phi_{th}(\underline{x})} = \frac{I_{th}(\underline{x})}{f_{th}(\underline{x})\,\Phi_{th}(\underline{x})}$$

If the thermal current per unit thermal flux is assumed position independent*, and defined as S_I, then

*It has been shown that the thermal current per unit thermal flux is strongly dependent on the effective neutron temperature due to the non-1/v behavior of rhodium in the thermal energy region. Thus, the assumption is that the effective neutron temperature is position independent. The results obtained from spectral unfolding in the thermal region (described in Section D) will be used to check the validity of this approximation and make any needed corrections.

$$S_{th}(\underline{x}) = \frac{1}{f_{th}(\underline{x})} \cdot S_I$$

To determine S_I, where

$$S_I = \frac{I_{th}}{\Phi_{th}} = \frac{f_{th}(\underline{x})\, I_{tot}(\underline{x})}{\Phi_{th}(\underline{x})}$$

measured values of $\Phi_{th}(\underline{x})$, $I_{TOT}(\underline{x})$, and $f_{th}(\underline{x})$ are needed. The iron wire data of Section B is used to provide $\Phi_{th}(\underline{x})$*, the measurement of $f_{th}(\underline{x})$ is discussed below, and $I_{TOT}(\underline{x})$ comes from the rhodium detector. Using several axial positions at the core center, we find

$$S_I = 3.26 \times 10^{-21} \frac{\text{"thermal" amps}}{\text{thermal flux}},$$

which represents a 9% increase over the manufacturer's quoted sensitivity. The plots which follow use $S_I = 3\text{x}10^{-21} \frac{\text{thermal amps}}{\text{thermal flux}}$ since this improved value was not available at the time the plots were drawn. Hence, all plot values should be corrected to account for this 9% difference.

Thus, to determine the thermal sensitivity of the detector requires an evaluation of $f_{th}(\underline{x})$, the fraction of detector current attributable to thermal neutron absorption in the rhodium emitter. This quantity was measured at various positions, in and around the core, by activation of bare and cadmium covered rhodium wires. From the count rates of wires irradiated at position $\underline{x}$, one can determine $f_{th}(\underline{x})$ as:

$$f_{th}(\underline{x}) = 1 - \frac{A_{CD}(\underline{x},t)}{A_b(\underline{x},t)}$$

where $A_{CD}(\underline{x},t)$ = specific activity at time t of the cadmium covered rhodium wire irradiated at position $\underline{x}$

and $A_b(\underline{x},t)$ = specific activity at time t of the bare rhodium wire irradiated at position $\underline{x}$.

Because the rhodium wire activates so easily, has a short half-life, and long-lived impurities, the irradiations were performed at 100 kW to reduce their saturated activities.** Even so, the wires needed to be cut remotely (to 3/8") for unshielded counting and handling. The experimental group found that, with experience, the wires could be counted within ten minutes after the irradiation. A similar experimental technique has been used by Baldwin and Rogers [39] to study the

*It is implicitly assumed that the cadmium cutoff energy for iron is approximately equal to the cadmium cutoff energy for rhodium.

**Throughout this section, it is assumed that the spectrum does not change significantly as a function of FNR core loadings or power level. All measurements were made at or near 2 MW equilibrium xenon, however.

effect of varying boron concentrations on the rhodium detector response. While they choose to count the emitted electrons with proportional counters, the present experiments used GeLi detectors to count the .555 MeV gamma rays (See Figure 33). Dead time corrections proved to be significant, and were directly measured in a separate experiment. The results of an irradiation performed in the H_2O reflector are shown in Figure 37 . The remarkably straight line behavior of the data points is typical of the other irradiations.

The experimental results for $f_{th}(\underline{x})$ are presented in Table 16 . Radial locations are keyed to Figure 38 . As can be seen from the data for L-37 (center of core), L-40 (core edge), and L-67 (regular fuel element next to a special fuel element), the value of $f_{th}(\underline{x})$ in the core does not vary greatly (with the exception of special fuel elements). This is consistent with computer code predictions. For example, Figure 39 shows that the computer generated values of the ratio of epithermal (fast) to thermal flux remain approximately constant across (east-west) the core. As a result, a single value of $f_{th}(\underline{x}) \approx .8$ could have been applied to all <u>regular</u> fuel elements in the core without substantial error. Values for the epithermal correction factor are also presented for the H_2O reflector, special fuel element, and two D_2O tank locations. Values of $f_{th}(\underline{x})$ in locations which were not directly measured were interpolated from these measured results. For the H_2O reflector, the value of $f_{th}(\underline{x})$ measured in the second channel (outward from the core) is assumed applicable for all four channels. This is probably an acceptable approximation since the measured value of $f_{th}(x) = .93$ is already close to unity and should not vary by more than a few percent either way in the other channels.

Thus, with values of $f_{th}(\underline{x})$ defined for all points in the core, south H_2O reflector, and D_2O tank, the thermal sensitivity of the detector,

$$S_{th}(\underline{x}) = \frac{1}{f_{th}(\underline{x})} \cdot S_I$$

becomes a known function of position, and the thermal flux can be determined from rhodium detector net current readings as:

$$\Phi_{th}(\underline{x}) = \frac{I_{TOT}(\underline{x})}{S_{th}(\underline{x})}$$

The radial and axial measurements of $I_{TOT}(\underline{x})$ (and hence $\Phi_{th}(\underline{x})$), are discussed next.

---

*The epithermal correction factor is also assumed constant axially. This will be true except within a couple of inches at the ends of the fuel plates, as was shown by the iron wire cadmium ratio measurements (Section B).

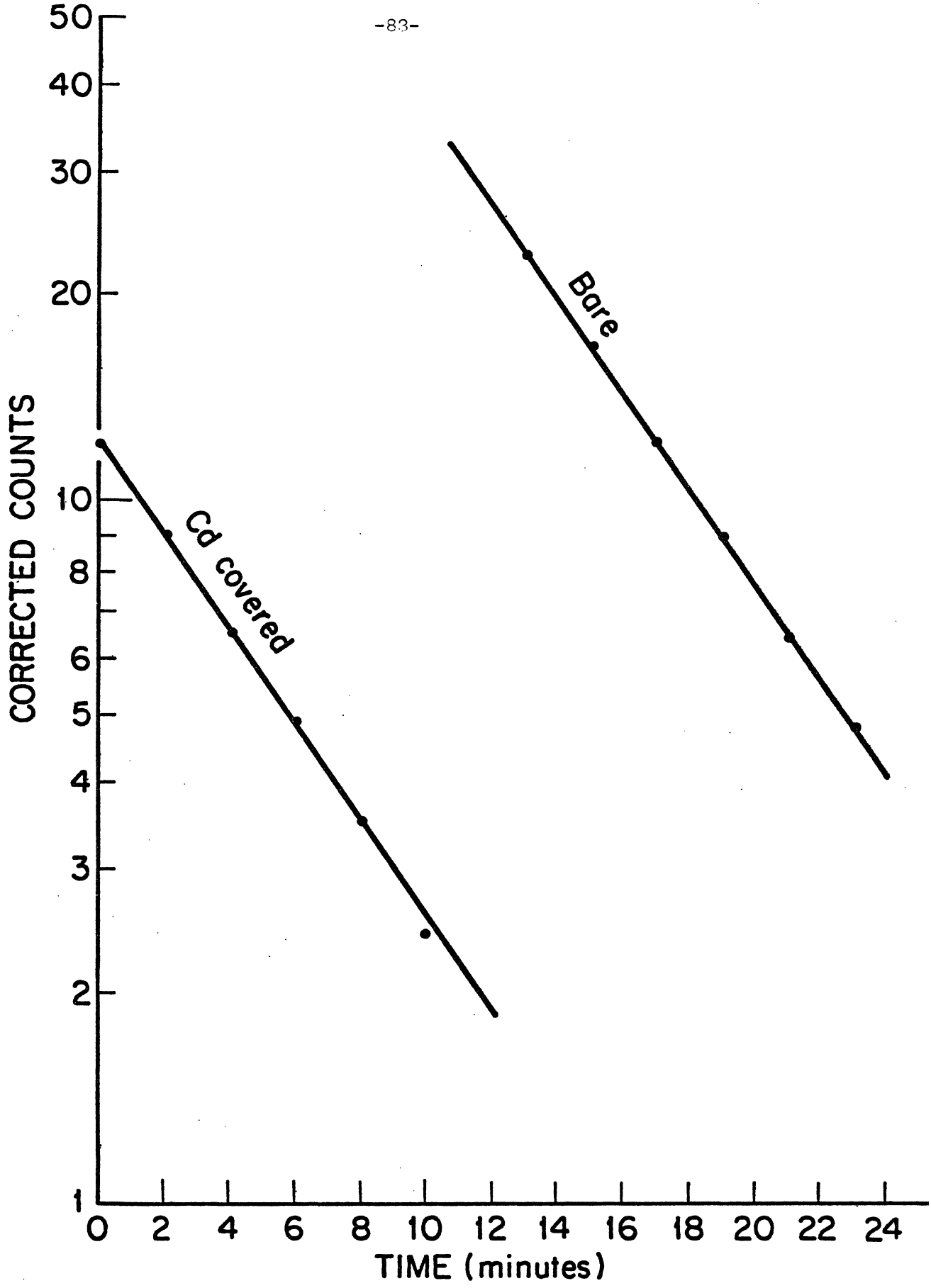

Figure 37. Typical Bare and Cadmium Covered Irradiation Decay Counting

Table 16. Epithermal Correction Factors

Lattice Location	Description	Correlation coefficients to straight line fits	$\frac{\text{Cadmium covered activity}}{\text{Bare activity}} = 1-f_{th}$
D-O	D_2O tank penetration O	.9999, .9999	.0282
L-67	Regular fuel element	.9999, .9999	.1677
L-37	Regular fuel element	.9999, 1.0000	.2093
L-40	Regular fuel element adjacent to H_2O reflector	.9997, 1.0000	.1703
L-40-A	Channel 2 in H_2O reflector element	.9994, .9998	.0726
D-X	D_2O tank penetration X	.9998, 1.0000	.1052
L-39	Special fuel element (measured in waterhole)	.9999, .9999	.0874

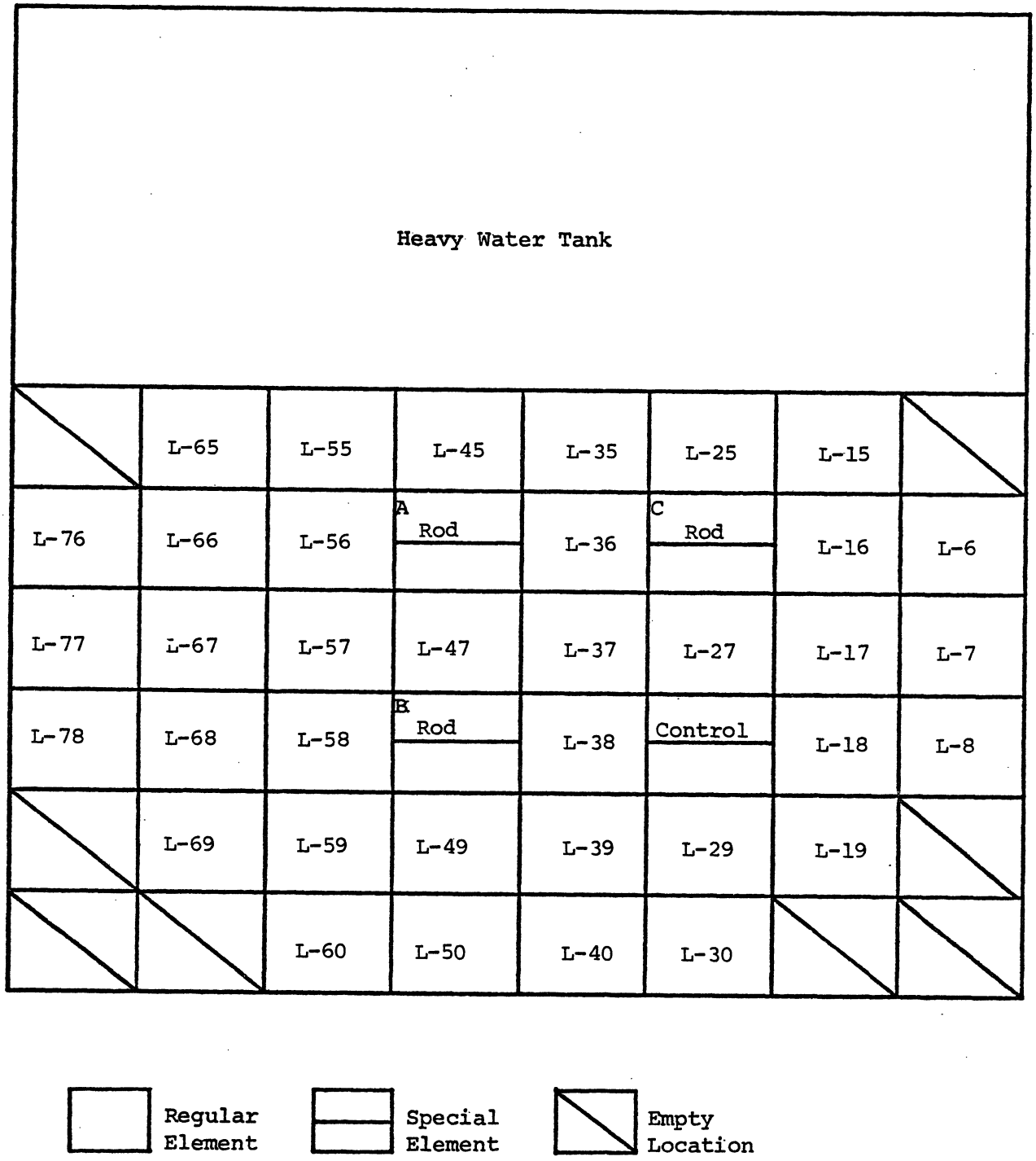

Figure 38. Key to Lattice Positions

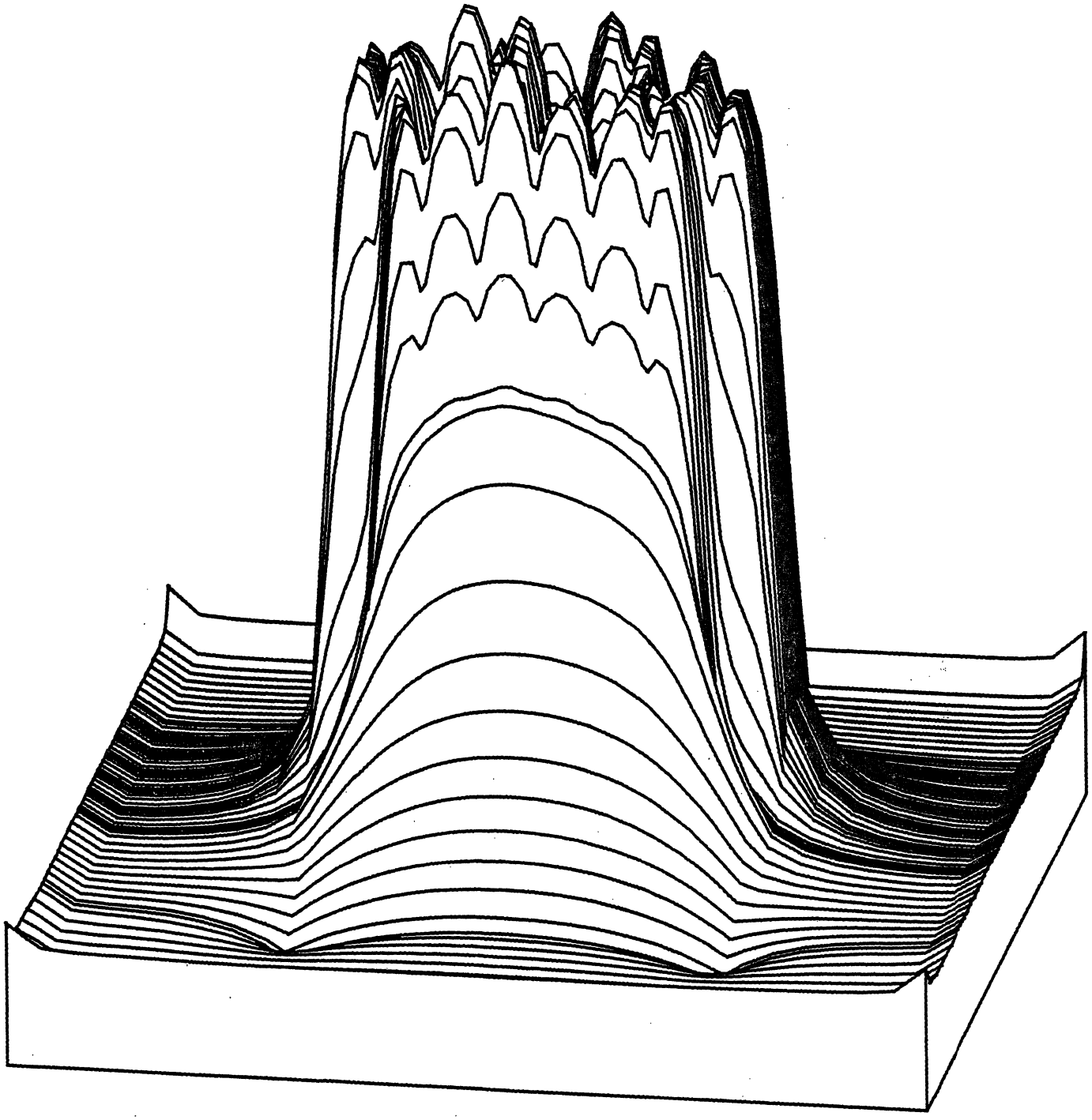

Figure 39. Ratio of Fast to Thermal Flux (2DB Calculation for May 22, 1979, FNR)

5. Rhodium Detector Flux Maps

a) Axial Profiles

Axial profiles have been measured in elements L-37, L-40, L-35, the H_2O reflector, and D_2O tank position S (See Appendix B). A typical axial rhodium detector flux map is shown in Figure 40 for L-37. The axial measurements have not yet been point-by-point corrected for variations in the epithermal contribution, which implies the thermal flux in the reflectors is too high by 10%. The values of Φ_{th} in the active fuel region are approximately 8% higher than predicted by the iron wire data. This is directly attributable to the choice of sensitivity, as discussed previously.

A comparison of axial profiles in L-35, L-37, L-40, and channel 2 in the H_2O reflector is shown in Figure 41 . The appropriate epithermal correction factor, $f_{th}(\underline{x})$, was applied to each element. By taking the ratios of measured points, it is seen that the axial profile remains constant for L-37 and L-40, but flattens close to the D_2O tank (L-35). Computer calculations also predict a constant axial profile throughout the core except near the D_2O tank. Channel #2 in the H_2O reflector shows a curvature comparable to that in L-35. These profiles provide valuable information on the axial buckling, as well as the axial correction factors needed later.

A D_2O tank axial profile for position S is shown in Figure 42 . Because the D_2O tank penetrations end above the core midplane an axial profile is required to provide a means of extrapolating the D_2O tank data to the midplane. The profile was assumed to be symmetric about the core midplane, and the axial peak value of the flux was conservatively extrapolated (probably subject to an error of less than 10%). Even so, the axial profile is more peaked than in element L-35. This is contrary to the computer predictions, possibly due to the difficulty in modelling the complex D_2O tank internal structure.

b) Radial Profiles

The rhodium detector was also used to provide radial flux profiles. Because of the long wait times associated with the use of the detector (discussed earlier), radial profiles were measured along only a few horizontal planes. In addition, reactor equipment (such as control rod drive motors, vertical beam tubes, etc.) blocked the access to 14 of the fuel elements and several of the D_2O tank penetrations. Measurements in the H_2O reflector were made with the adapter always positioned south of L-40, so that a complete north-south traverse of the core could be plotted. Channel locations in the H_2O reflector are specified in Figure 36 . Each of the two radial flux maps which were measured is discussed below.

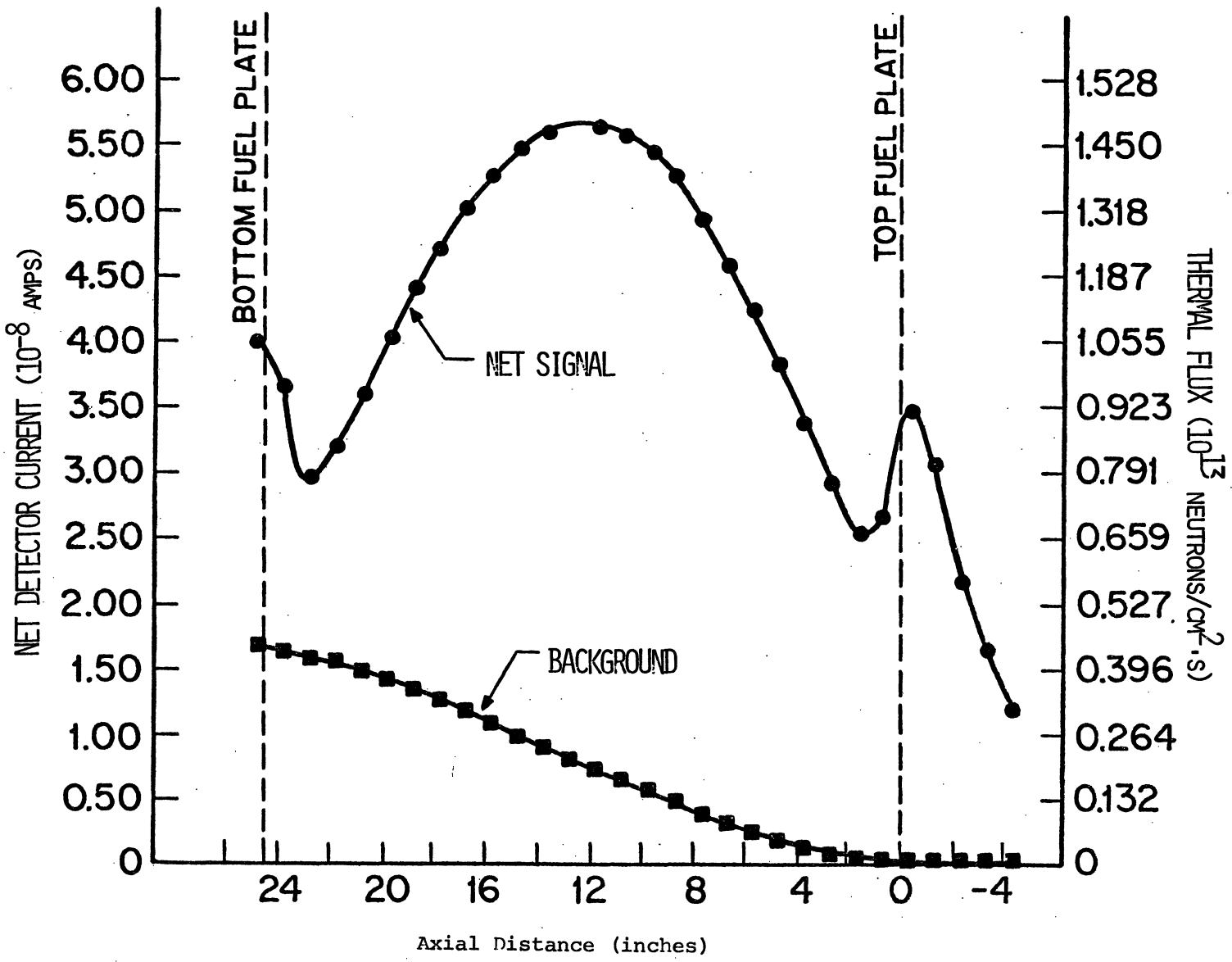

Figure 40. Axial Profile for Regular Fuel Element in Location L-37

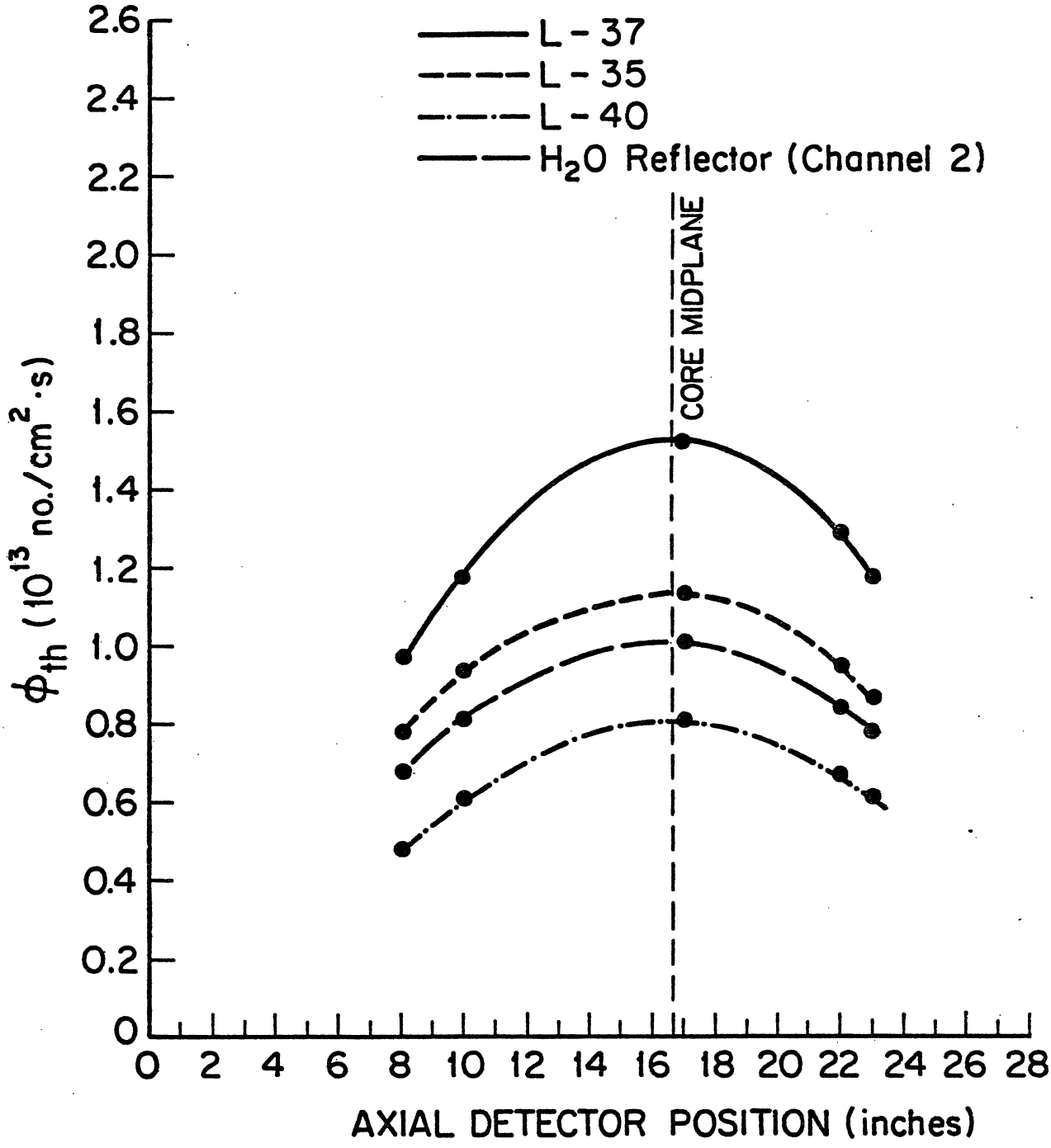

Figure 41. Axial profiles in H_2O, L-39, and L-40 Lattice Locations

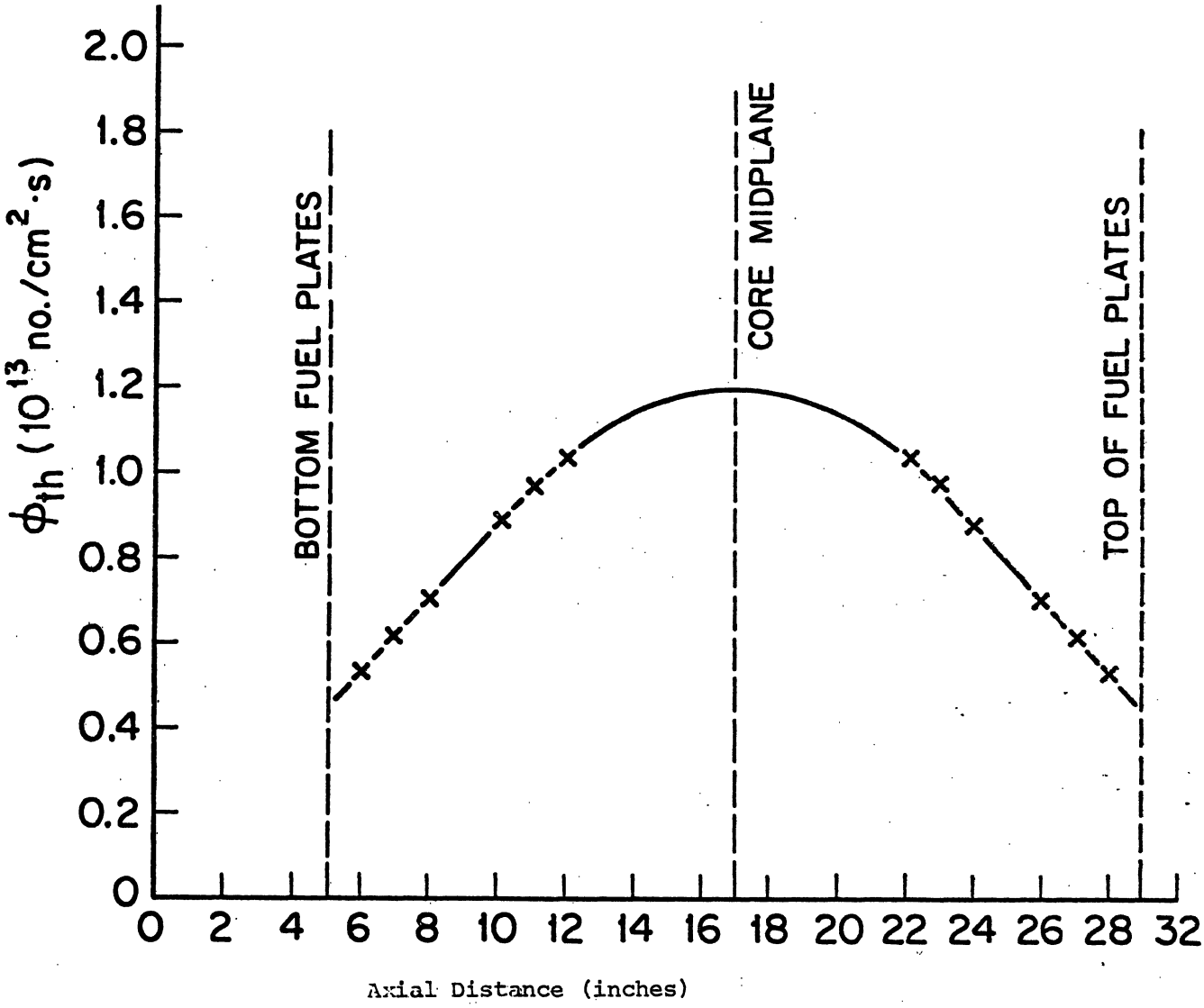

Figure 42. D_2O Axial Profile

The first radial flux map (denoted as map #1) measured the flux in all accessible fuel elements, the H_2O reflector, and two D_2O tank penetrations. The data was taken at three axial levels: 1/4 into the fuel, the core midplane, and 3/4 into the fuel element. Due to an error in the initial calibration of the detector assembly, all data were taken about one inch from the proper points. However, the axial profiles (described earlier) were used to adjust the data to correspond to the proper height. For the core midplane, the correction was negligibly small, due to the flatness of the flux there. Figure 43 shows a tabulation of the thermal flux values obtained. The fluxes are in units of 10^{13} n/cm^2-sec, and are presented as:

$$\frac{\text{thermal flux 1/4 into fuel}}{\text{thermal flux at midplane}}$$

$$\frac{\text{thermal flux 3/4 into fuel}}{\text{thermal flux at midplane}}$$

For the D_2O tank, no values are listed for points 3/4 into the fuel plate since the complex structure in the tank below the midplane makes extrapolations there highly questionable. North-south traverses through the core center (L-37) are plotted in Figure 44 for the three planes described above. The curves which are drawn between the data points are subject to interpretation, but are probably not far from the actual profile. Also shown on the plot is the core midplane data without the epithermal correction factor applied. Not only is the absolute value of the flux reduced by a sizeable amount, but the shape also changes due to the different values of $f_{th}(\underline{x})$.

For this map, core position L-39 contains a special fuel element*, which explains the large thermal peak measured in the waterhole. These measured values contain some additional uncertainty due to the inability to accurately position the detector radially. In the core, the 3/4-position fluxes remain higher than the 1/4-position fluxes. This is consistent with the iron wire data, and rhodium axial profiles discussed earlier. However, in the H_2O reflector, the opposite is true. This may be due to a large neutron absorber which was adjacent to the bottom of the H_2O adapter element. Regarding the points in the D_2O tank, it should be noted that neither position T nor position W is directly on a line containing the other elements for which the data is plotted. As is roughly shown in Figure 43 , W is quite close to the line, but T is about six inches west of the line. Hence the value for T is estimated (on the basis of the second radial map discussed later) to be about 9% low.

*The special fuel element, described in an earlier section, has several of the center fuel plates removed to allow room for shim or control rods. For this map, lattice positions L-39 and L-57 contain special fuel elements.

			T .753 .934	Heavy Water Tank		W 1.14 1.41	
	.622 .819 .620	.845 1.11 .836	.989 1.30 .984	.887 1.18 .938	.856 1.12 .872	.718 .918 .731	
			A	1.15 1.55 1.21	C		
.565 .706 .552	.824 1.06 .797	2.22 2.73 2.03	1.11 1.45 1.16	1.12 1.51 1.21	1.06 1.42 1.14	.892 1.20 .956	.732 .931 .746
			B	1.01 1.37 1.09	Control Rod		
		.703 .890 .697	.740 .957 .748	1.89 2.23 1.61	.777 1.02 .787	.670 .854 .679	
			.534 .651 .496	.536 .701 .570	.499 .637 .513		

H_2O reflector measurements (see below)

Regular Element

Special Element

Empty Location

Inaccessible due to control rod drive motors

.748	Channel 1
.918	
.692	
.749	Channel 2
.902	
.703	
.654	Channel 3
.807	
.617	
.576	Channel 4
.711	
.557	

Figure 43. Radial Flux Map #1 Tabulation of Fluxes

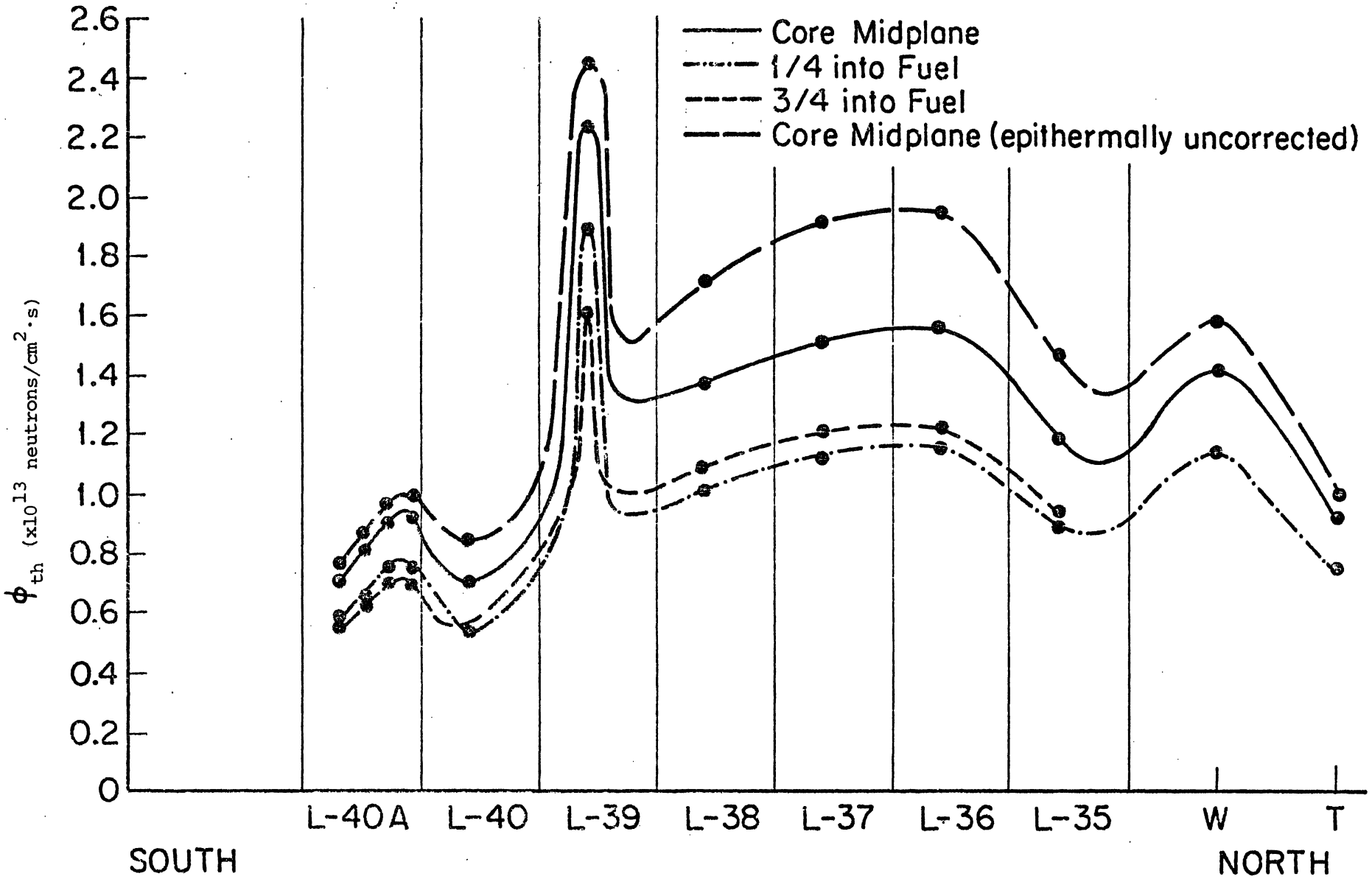

Figure 44. North-South Traverse Through L-37
Map #1

An east-west plot through the center-of-core element, L-37, is shown in Figure 45. A special element in L-57 is responsible for the large thermal flux peak there. In the regular fuel elements, the 3/4-position flux exceeds the 1/4-flux, with the difference decreasing away from the control rods. In the special element, the fact that the 1/4-position flux exceeds the 3/4-position flux is due to the inability to accurately position the detector radially in the waterhole. Any error in the 1/4-position will be accentuated when the detector is extended down to the 3/4-position. This explains the abnormally low value of the 3/4-position thermal flux which was measured.

An east-west plot of the thermal fluxes measured in fuel elements adjacent to the D_2O tank is shown in Figure 46 . The irregular shape of the plot around L-35 may be due to structure in the D_2O tank. Because of the gentle slope of the data, differences in the axial buckling between the two east-west plots is difficult to discern. Numerical evlauation of the axial bucklings has not yet been estimated from the data, but it would be interesting to compare these with the computer generated values.

The second radial flux map, denoted as map #2 and tabulated in Figure 47 , measured the flux in all accessible fuel elements, the H_2O reflector, and seven D_2O tank locations. The additional D_2O tank measurements (relative to the first map) were made possible by the removal of a vertical beam tube. The measurements were made at the core midplane, and at the 1/4- and 3/4-planes for a few selected elements along the north-south line through L-37. The D_2O tank measurements were made on the 1/4-plane, and extrapolated to the core midplane. For some of the regular fuel elements in the core, the detector would not fit in the channel normally used (just south of the fuel bail). Measurements were taken in a channel just north of the bail in these cases, and are designated by the suffix (N) on Figure 47 . The differences in the flux values between these two points is less than 2%, as shown by measurements taken on both sides of the bail in L-37. The core loading is slightly different than during the first map. A regular element replaced the special element that was in L-39, and the fuel element that was in L-50 was removed and not replaced. All other locations retained the same type of fuel element, although the individual fuel assemblies had been shuffled since the first map.

A north-south traverse through L-37 for the core midplane is shown in Figure 48 . The thermal flux is seen to behave much more smoothly without the special element in L-39. The D_2O tank data is much more complete in this plot, and shows a flux peak which is comparable to that at the center of core. Figure 49 compares the two north-south profiles from maps 1 and 2.

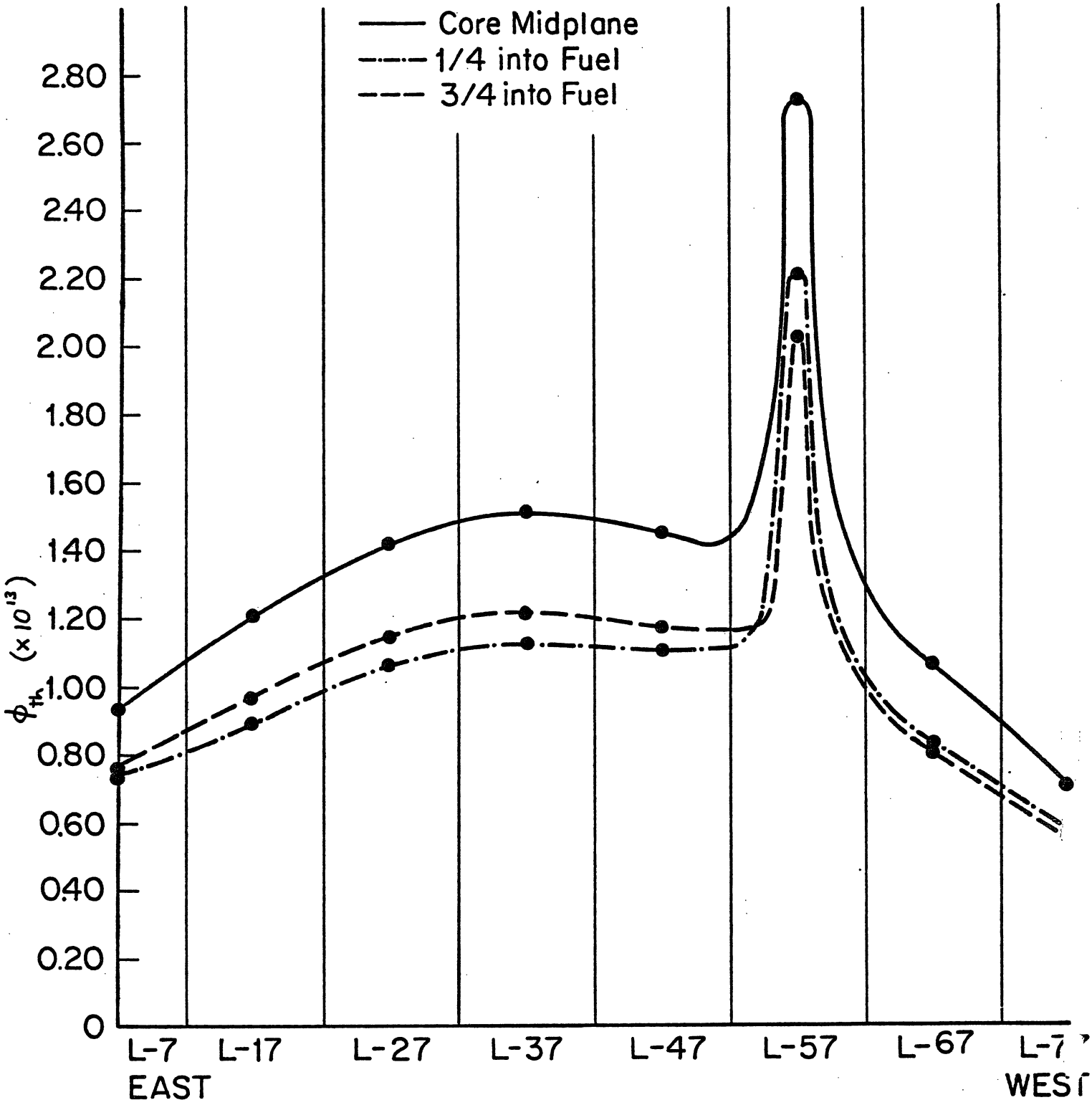

Figure 45. East-West Traverse Through L-37
Map #1

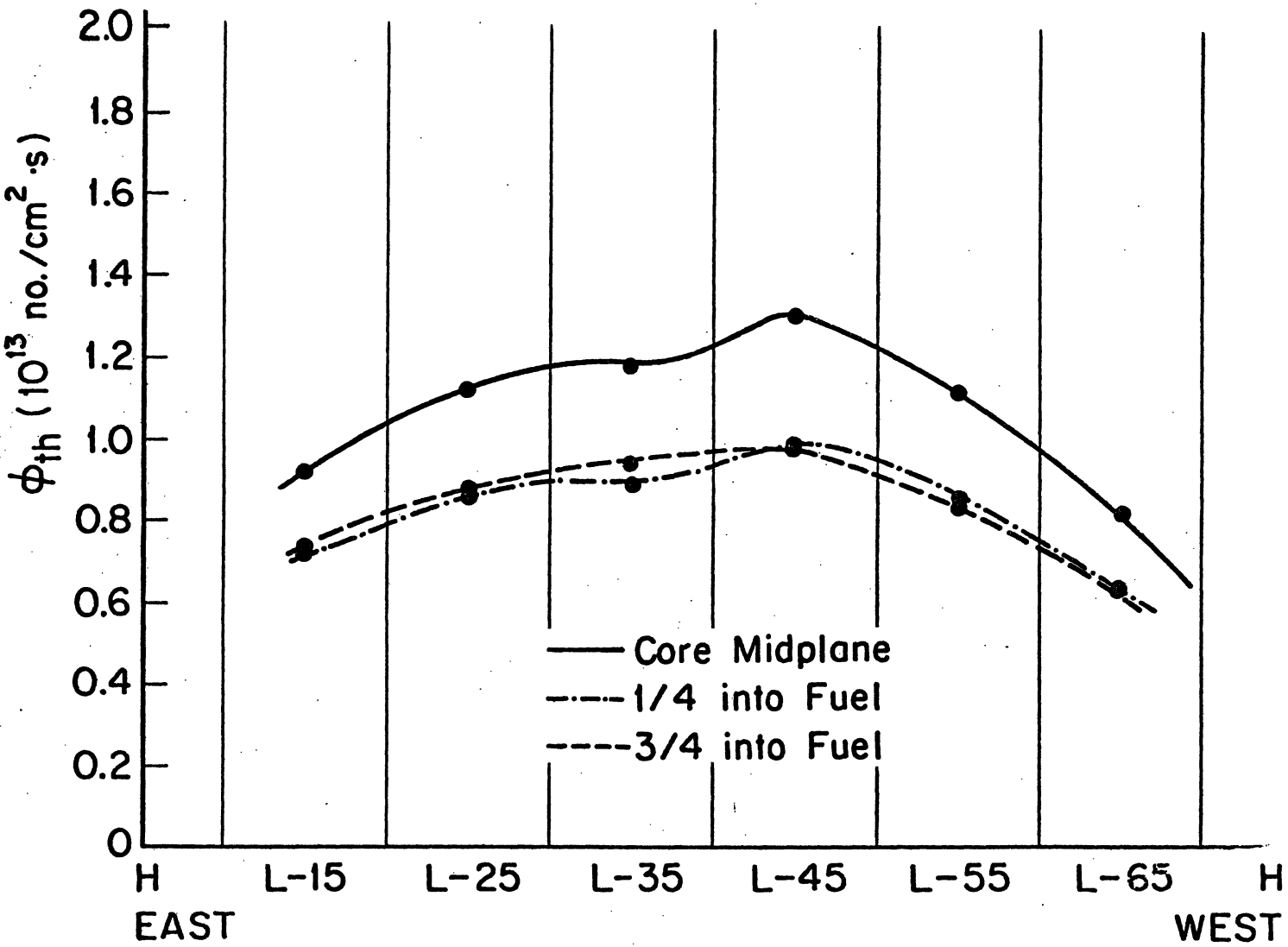

Figure 46. East-West Traverse Along Elements Adjacent to D_2O Tank Map #1

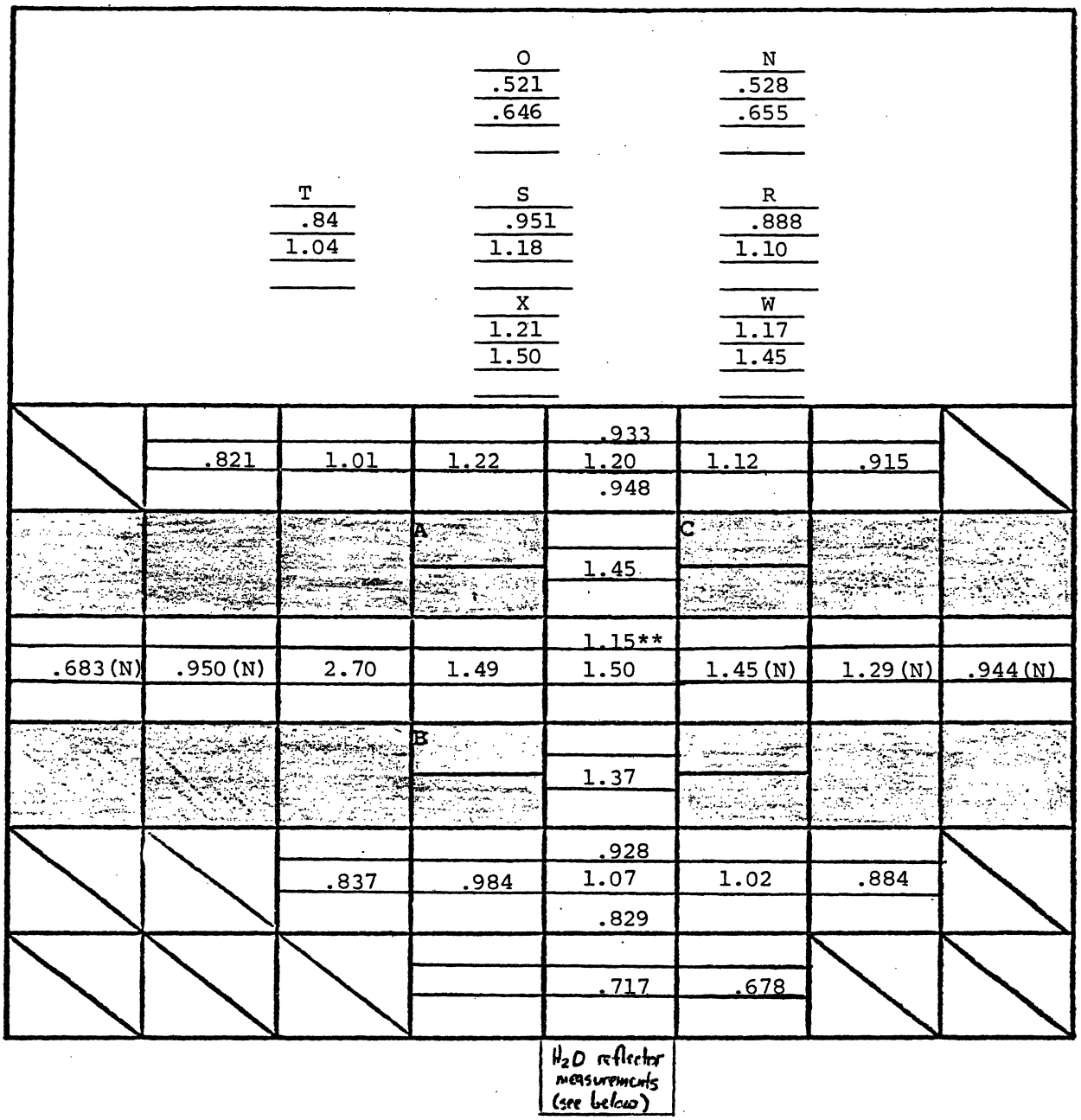

*All measurements made on south side of fuel element bail, except as denoted by (N).

**L-37 1.17(N) / 1.48(N) / 1.18(N)

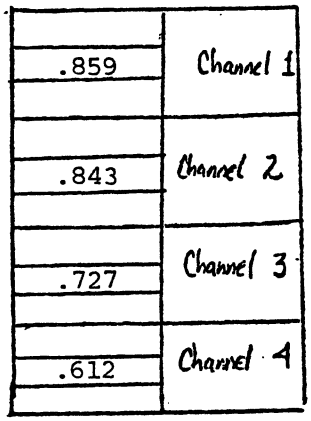

Figure 47. Radial Flux Map #2 Tabulation of Fluxes

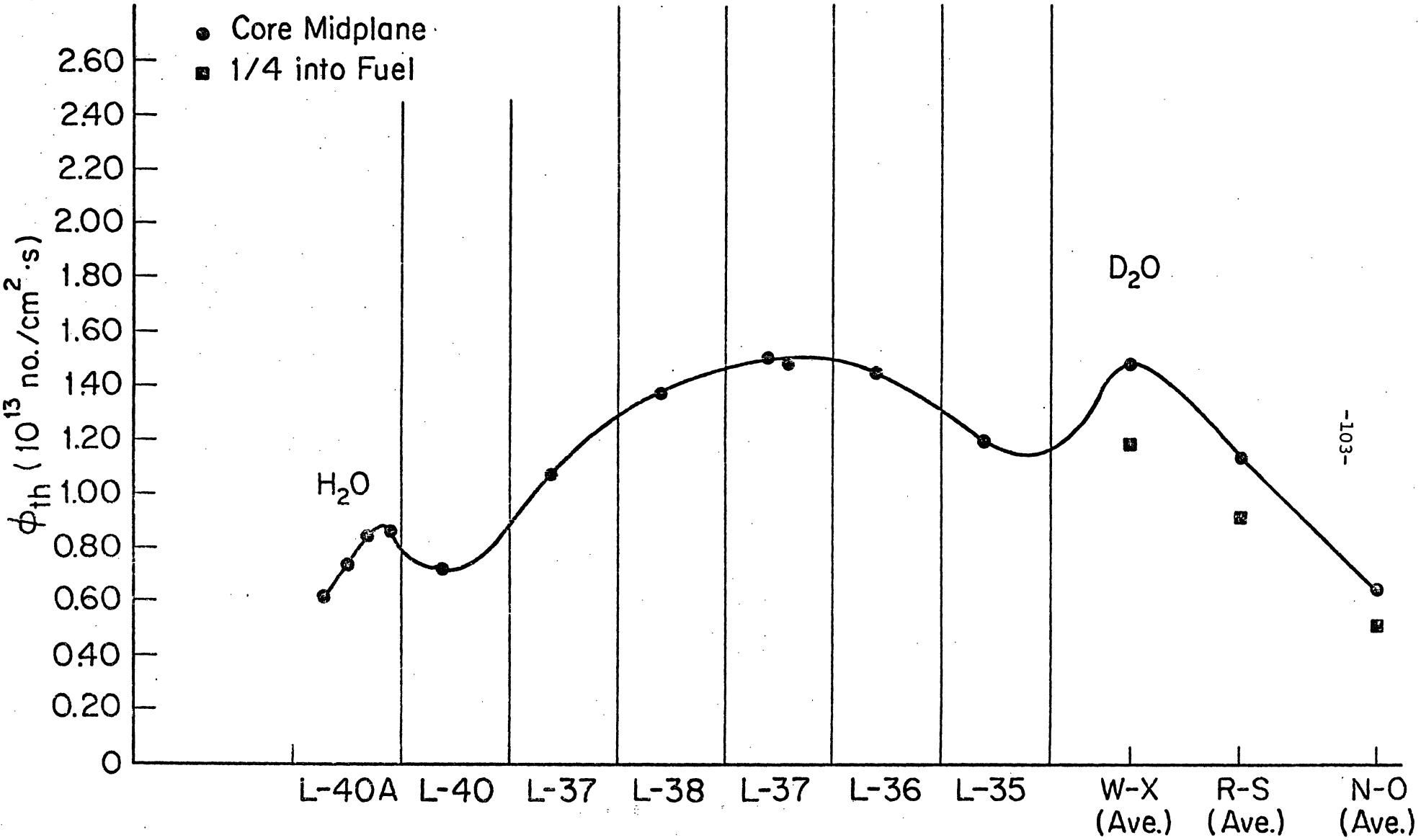

Figure 48. North-South Traverse Through L-37
Map #2

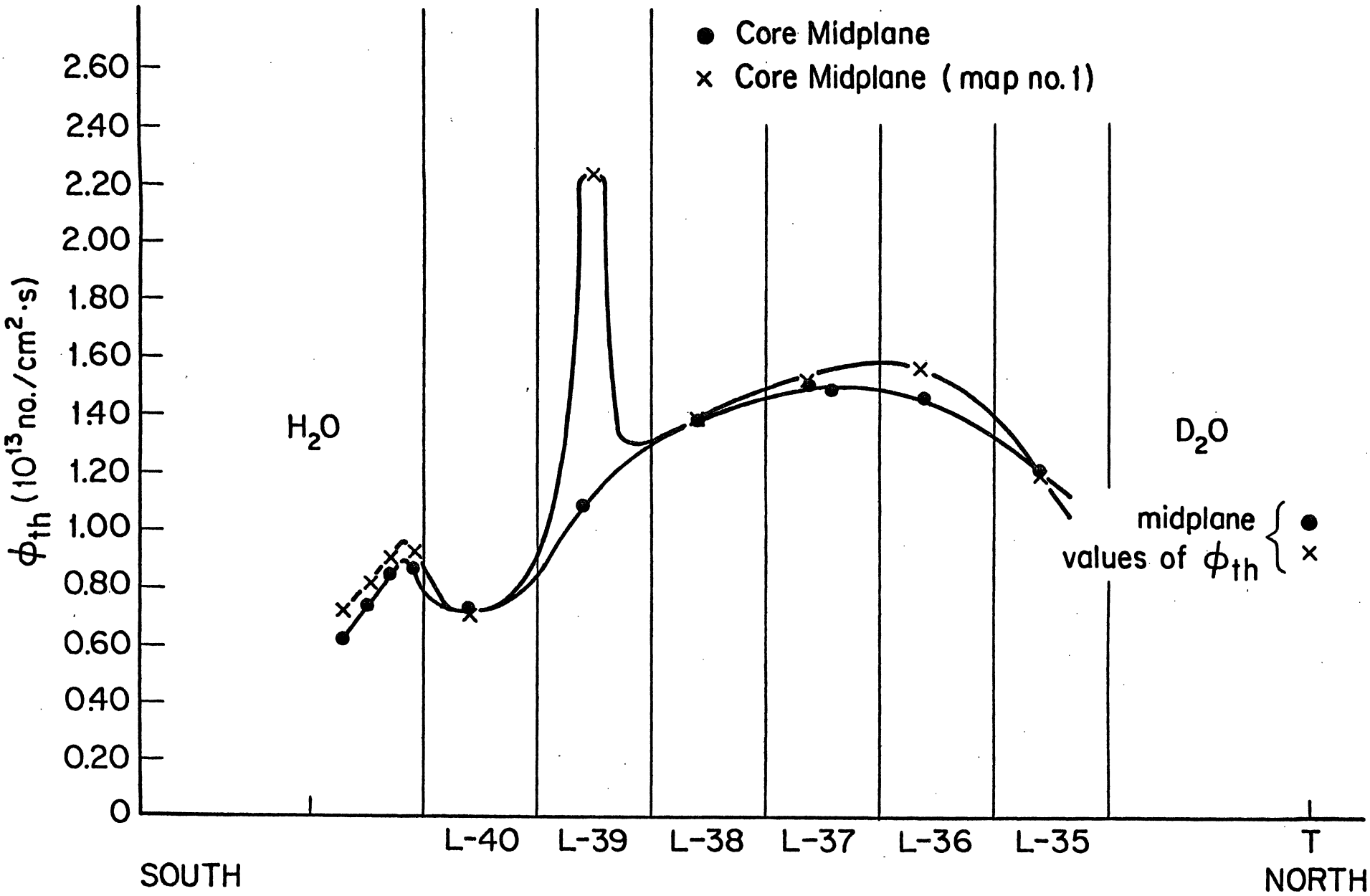

Figure 49. Comparison of North-South Traverses Through L-37
Maps #1 and #2

An east-west plot through the core center (L-37) is shown in Figure 50. For comparative purposes, core midplane data from map #1 is also shown. The remarkable agreement in the special fuel element (L-57) gives some confidence in our ability to determine the flux there. The fluxes across the core generally agree, with the maximum difference being 10% in L-67. Map #2 1/4-position and 3/4-position fluxes for L-37 differ by only about 3% and 2% respectively, from their values in map #1.

The east-west plot through the fuel elements adjacent to the D_2O is presented in Figure 51. The equivalent data from map #1 is presented for comparison. The irregular shape of the data around L-35 is not as apparent in map #2. This suggests that the special fuel element that was present in L-39 during map #1 may be responsible for the flux dip that was observed there, instead of structure in the D_2O tank.

The data which has been presented provides valuable information on the thermal flux in the FNR core. The data is currently being used to benchmark the computer codes used by the analytical group to predict thermal fluxes. In addition, the data also provides information on the effects of the special fuel elements on the thermal flux distribution in the core and D_2O tank. It further suggests that the current shuffling pattern of regular fuel elements does not significantly alter the thermal flux shape. Lastly, the data will be used to determine the changes which are attributable to the introduction of low enriched fuel to the FNR.

6. Estimate of Experimental Uncertainty in the Thermal Flux

In order to be able to meaningfully compare measured thermal fluxes under different fuel enrichments, an estimate of the uncertainty in the measured values is required. Since the errors associated with measurements in regular fuel elements, special fuel elements, D_2O tank, and H_2O reflector are different, each needs to be evaluated independently. In general, however, the thermal flux can be written as:

$$\phi_{th}(\underline{x}) = \left[\left(\frac{I_g(\underline{x}) - I_b(\underline{x})}{f_{th}(\underline{x})}\right) S_I\right] \cdot \chi \cdot \epsilon \cdot \xi$$

where

$I_g(\underline{x})$ = detector gross current signal

$I_b(\underline{x})$ = detector background current signal

$f_{th}(\underline{x})$ = epithermal correction factor

S_I = detector sensitivity

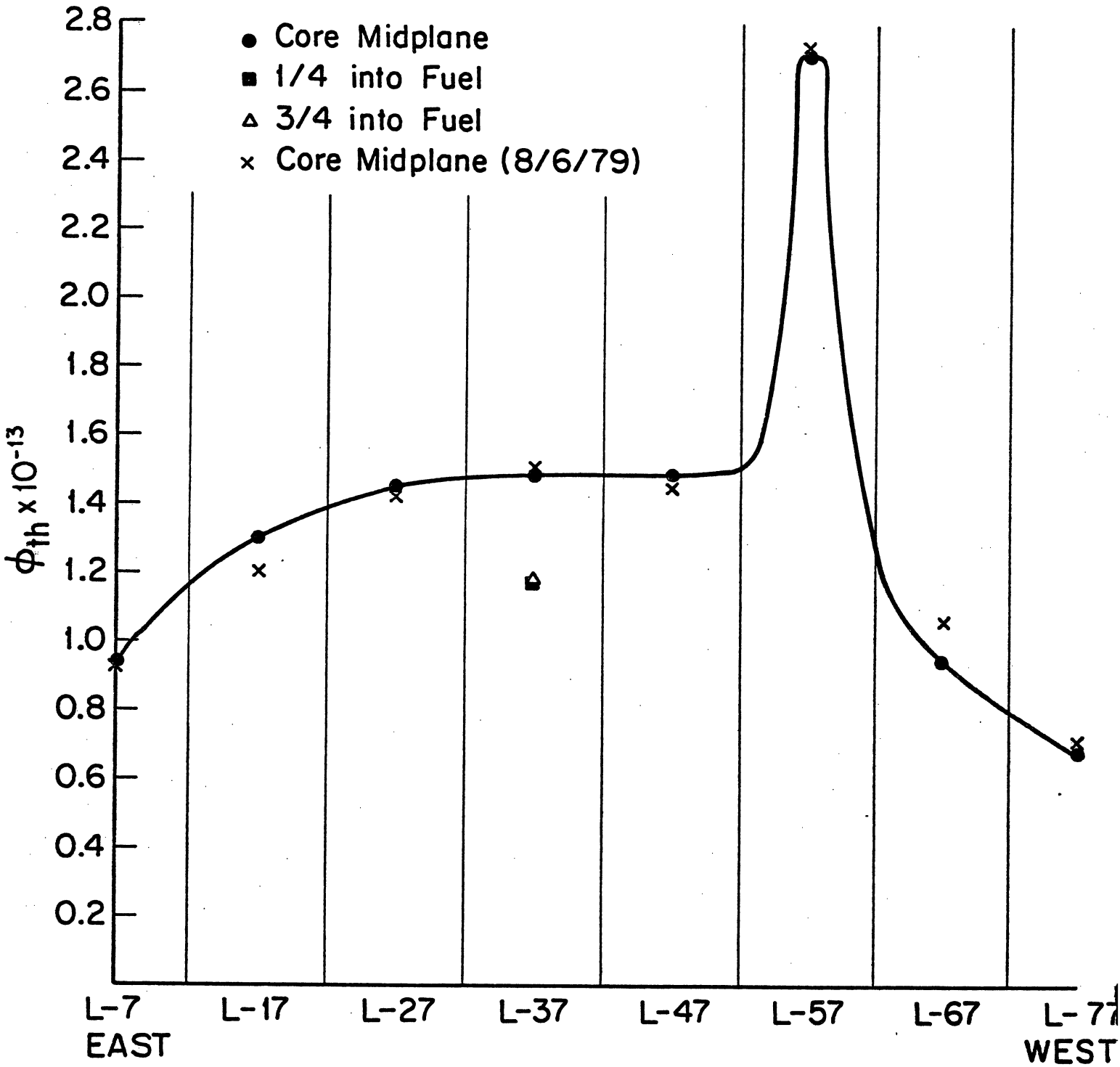

Figure 50. East-West Traverse Through L-37
Map #2

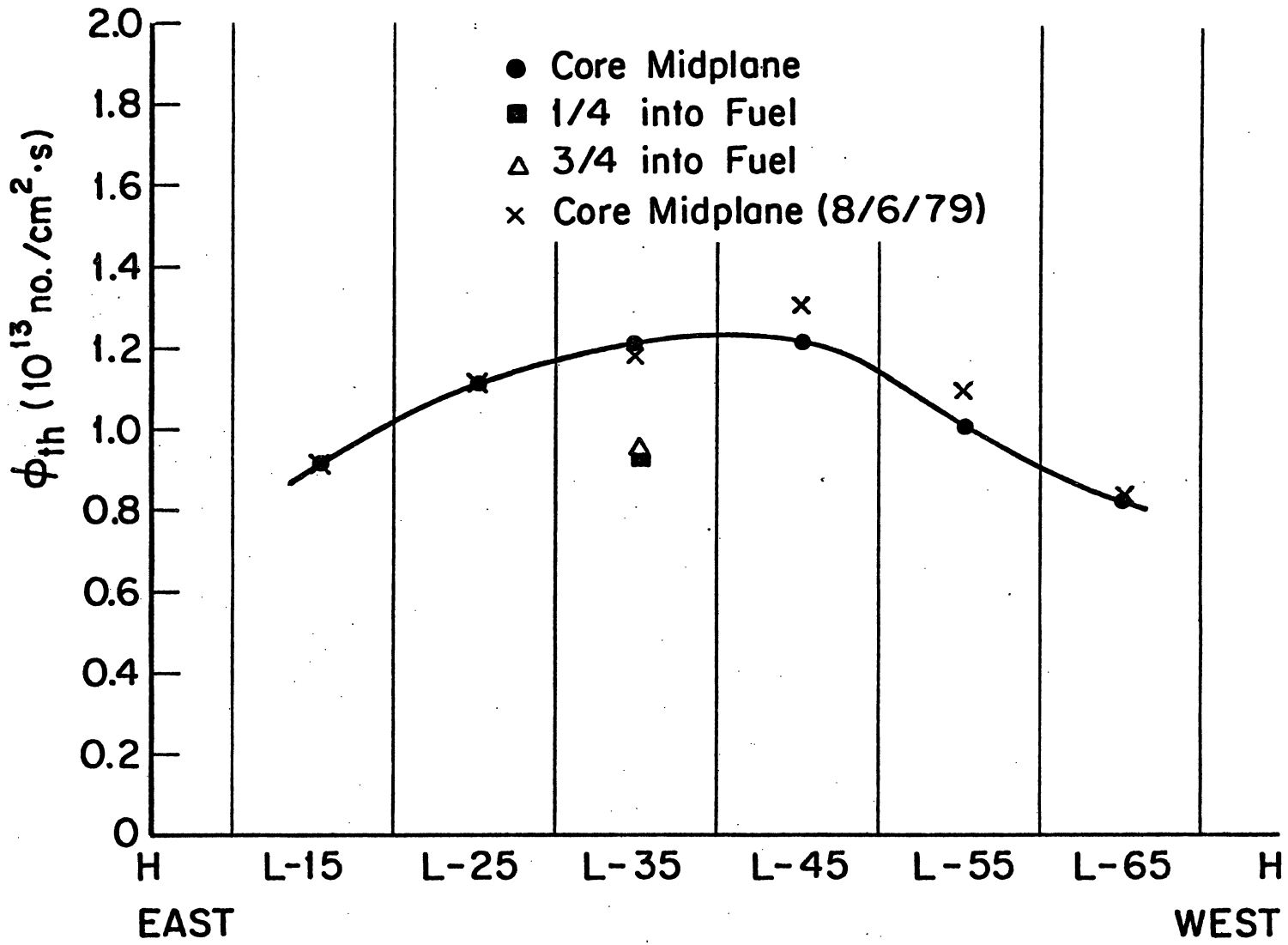

Figure 51. East-West Traverse Along Elements Adjacent to D_2O Tank
Map #2

and

χ = axial correction factor (applicable to D_2O tank midplane data, and 1/4-plane and 3/4-plane data on map #1)

ϵ = radial correction factor (applicable to measurements taken in the special fuel element waterhole)

ξ = correction factor for D_2O tank measurements which accounts for the H_2O in the heavy water tank vertical penetrations.

Then, the relative uncertainty in the flux can be written as:

$$\frac{\sigma_\phi}{\phi} \cong \left[\frac{\sigma_{I_g}^2 + \sigma_{I_b}^2}{(I_g(x) - I_b(x))^2} + \frac{\sigma_{S_I}^2}{S_I^2} + \frac{\sigma_\chi^2}{\chi^2} + \frac{\sigma_\epsilon^2}{\epsilon^2} + \frac{\sigma_\xi^2}{\xi^2} + \frac{\sigma_f^2}{f_{th}^2} \right]^{1/2}$$

Some of these quantities can be estimated for all measurement positions. Based upon the reproducibility of the current data, the relative uncertainty in the currents is less then 2%. The fact that the background lead is about one inch shorter than the rhodium emitter lead introduces a very small error (see Figure 35), and is not considered. The relative uncertainty in S_I is estimated to be less than 5%. This is not in disagreement with the values quoted by Joslin [40]. The relative uncertainty in the epithermal correction depends on the uncertainty in the measured values of f_{th}, and the interpolation scheme which is used to estimate f_{th} at other positions. The measured values are accurate to within a few percent, but by considering the range of values used in the interpolation for some elements, the relative uncertainty in $f_{th}(x)$ is probably about 4%.

For measurements in a regular fuel element or the H_2O reflector, a conservative estimate for the uncertainty in the thermal flux can thus be calculated from the relationship:

$$\frac{\sigma_\phi}{\phi} \cong \left[\frac{2\sigma_I^2}{I^2} + \frac{\sigma_{S_I}^2}{S_I^2} + \frac{\sigma_f^2}{f_{th}^2} \right]^{1/2}$$

as

$$\left(\frac{\sigma_\phi}{\phi}\right)_{reg,\, H_2O} \approx \underline{\underline{7\%}}$$

For a special fuel element, the inability to accurately determine the lateral position of the detector introduces an error which is largest near the

bottom of the core. Based upon the measurements, $\frac{\sigma_\varepsilon}{\varepsilon}$ is estimated at 10%, and yields

$$\left(\frac{\sigma_\phi}{\phi}\right)_{special} \approx 12\%$$

For the D_2O tank measurements, both α and ξ need to be evaluated. The magnitude of ξ is difficult to obtain, but the results of a computer run which included the effect of the H_2O (but not the aluminum pipe) suggest that $\sigma_\xi/\xi \lesssim 5\%$. The relative error associated with extrapolation of the data to the midplane can be estimated as $\sigma_\alpha/\alpha \approx 7\%$, so for the midplane,

$$\left(\frac{\sigma_\phi}{\phi}\right)_{D_2O} \approx 11\%$$

The above estimates of the uncertainty are rough, but provide a feeling for the relative accuracy of the quoted flux values. A reduction in the errors is possible by:

(1) performing additional iron wire activations to reduce the uncertainty in S_I,

(2) performing additional rhodium wire activations in unmeasured locations to reduce the uncertainty in the interpolations, and

(3) providing a channel in the special fuel element to fix the radial location of the detector.

7. Rhodium Detector Transfer Function Analysis

As described earlier, one of the major drawbacks associated with using a rhodium SPND is the several minute wait time required after a change in flux. This long wait time makes full-core flux maps impractical. Even the limited data presented in map #1 and map #2 involved substantial effort. An analytical technique which would eliminate the majority of the delay is being developed at the University of Michigan, and is briefly described in Reference 41. The analysis centers on developing the transfer function for the rhodium detector. If the transfer function is known, then the flux can be determined from the current without having to wait for the current to reach its equilibrium value. A full core flux map could be performed in a few hours, instead of a few days, should the technique yield accurate results. A detailed description of the technique, and an evaluation of its accuracy, will be presented in the project's final report.

D. Shim Rod Worth Measurement

In order to corroborate the theoretical calcuations of shim rod worths, a full length integral rod worth measurement was made using the asymptotic period method [42] . The results are shown in Figure 52 for the "C" rod and yielded an integral rod worth of 1.98 % Δk/k. Due to regulating limitations, this was the only shim rod which could be measured. The control rod is calibrated every cycle, and its integral worth was measured to be .322 % Δk/k.

E. Neutron Flux Spectra by Activation Analysis

1. Purpose

The purpose of this phase of the demonstration experiments is to define the in-core spectrum. The technique chosen is known as "Spectral Analysis by Neutron Detection" or "SAND" and involves the unfolding of the neutron spectrum from activation measurements of many foils.

2. Background

The concept of unfolding neutron spectra is based on the fact that at saturation, the activity can be assumed proportional to:

$$\int_0^\infty \sigma_i(E)\,\phi(E)\,dE$$

where $\sigma_i(E)$ is the cross section for the reaction being studied. If one assumes the cross sections are well known, then with many different activations, it may be possible to determine $\phi(E)$. This process of finding $\phi(E)$ given the saturated activities of several different foils represents the "unfolding".

The unfolding of neutron spectra has been a problem of serious interest for more than a decade, and yet the frequency of articles in the current literature underscores both the importance and the need for further refinements in the techniques. Oster [43] has catalogued the various generic approaches used in unfolding, and listed over 20 unfolding computer programs using these methods. Zipj [44] has compared three of the more standard computer codes, including CRYSTAL BALL and SAND-II. As such, we have chosen the SAND-II code [45] as our unfolding "workhorse". The code has been obtained from Oak Ridge, implemented on our computer system, and tested satisfactorily.

The SAND-II package obtained from Oak Ridge is actually a combination of four separate files. These include an elementary cross section processing code which operates on the supplied cross sections, a code which generates spectra for initial guesses or testing, and the actual unfolding code. It was found that the cross sections which are supplied are considerably out-of-date.

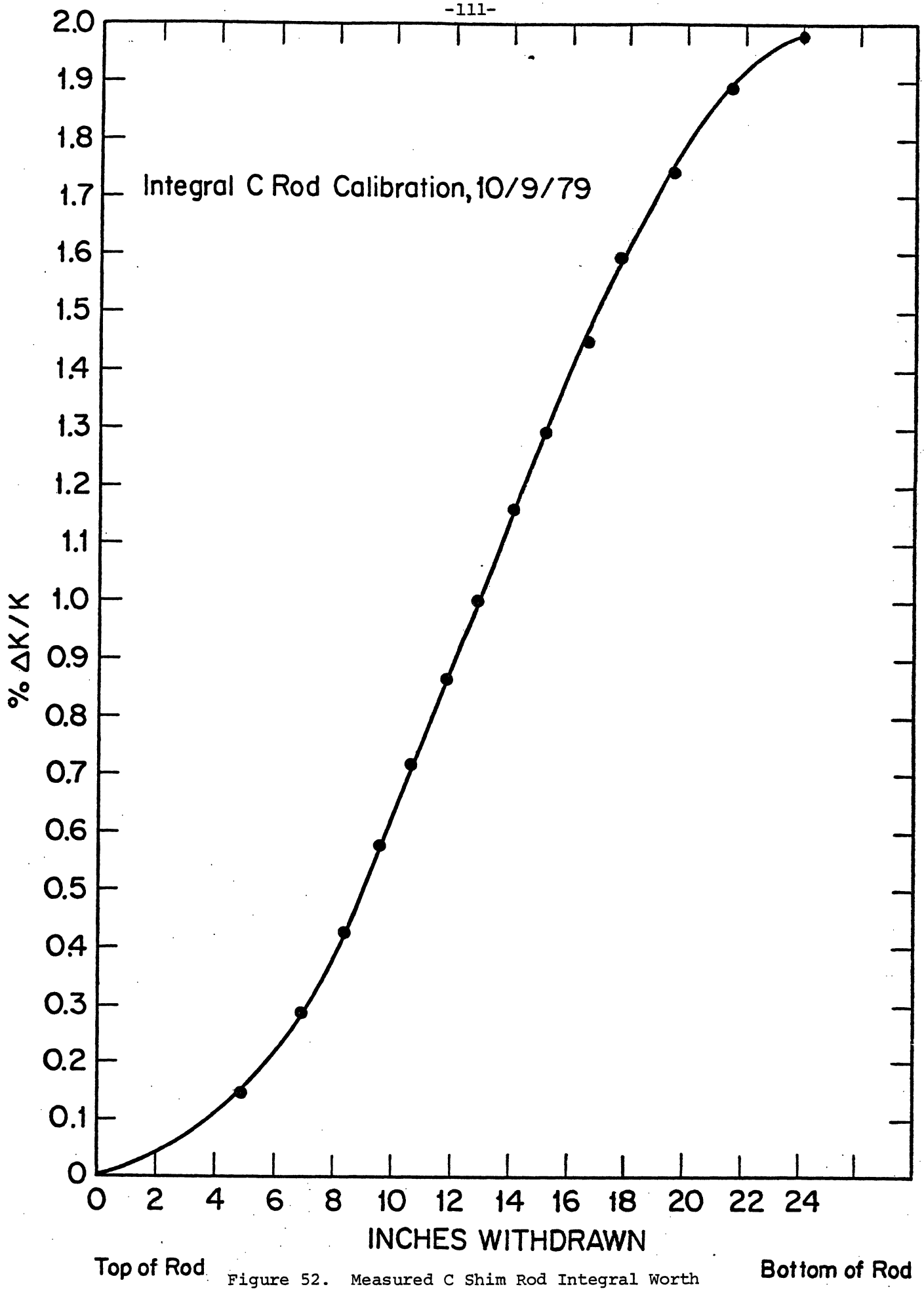

Figure 52. Measured C Shim Rod Integral Worth

ENDF-V cross sections, written in a SAND-II compatible format, are available from Brookhaven National Lab and have replaced the original cross sections in our package.

Since the introduction of the SAND-II codes in 1968, significant work has been performed to improve and refine the technique. For example, a smoothing feature has been added to reduce the amount of artificial structure present in the spectrum solution where severe cross section resonances are present. The iterative technique has also been significantly improved. As such, a state-of-the-art SAND-II type code package was obtained from Argonne National Lab. The SANDANL, RESATN, CSTAPE, and other associated codes incorporate the improvements mentioned above, with additional capabilities. For example, the RESATN code reads ENDF tapes and produces energy self-shielding factors to be used with the unfolding code. This correction is particularly important in strong resonance absorbers, such as gold, where errors as large as a factor of ten can be produced [46]. The SANDANL code includes a Monte-Carlo error analysis capability. The code will calculate the flux one standard deviation above and below the solution flux, as a result of a perturbation in the input spectrum and/or the cross sections.

Even with these refinements, the technique still has not reached its maturity. Recently, people [47] have begun questioning how to apply the new ENDF covariance data files to better quantify the uncertainty in the flux solution. In addition, since there are currently no known isotope reactions which provide the code with sensitivity in the region from about 10^{-3} to 1 MeV, additional work needs to be done in this area. Henry [48] has proposed a scheme to unfold over certain resonances, which may prove useful. Lastly, little effort has been made to accurately unfold the thermal flux. While Fulmer and Ruane [49] proposed an early least squares technique for the thermal flux, the unfolding codes have been principally applied in the high energy ranges where damage effects are more prevalent. It would be useful if the in-core neutron temperature could be determined by unfolding in the thermal region.

Thus, a significant part of this phase of the demonstration experiments has been the acquisition and implementation of the software, and an insight into the strengths and pitfalls of the neutron unfolding techniques. The other goal which was accomplished was the selection and acquisition of a first set of foils.

The selection of a set of foils plays a critical role in the accuracy of the unfolding process. Figure [53] shows the energy regions where 90% of the activity of 40 foil reactions is produced. For the unfolding process, one desires as many reactions as possible, as much energy coverage as possible, and as much

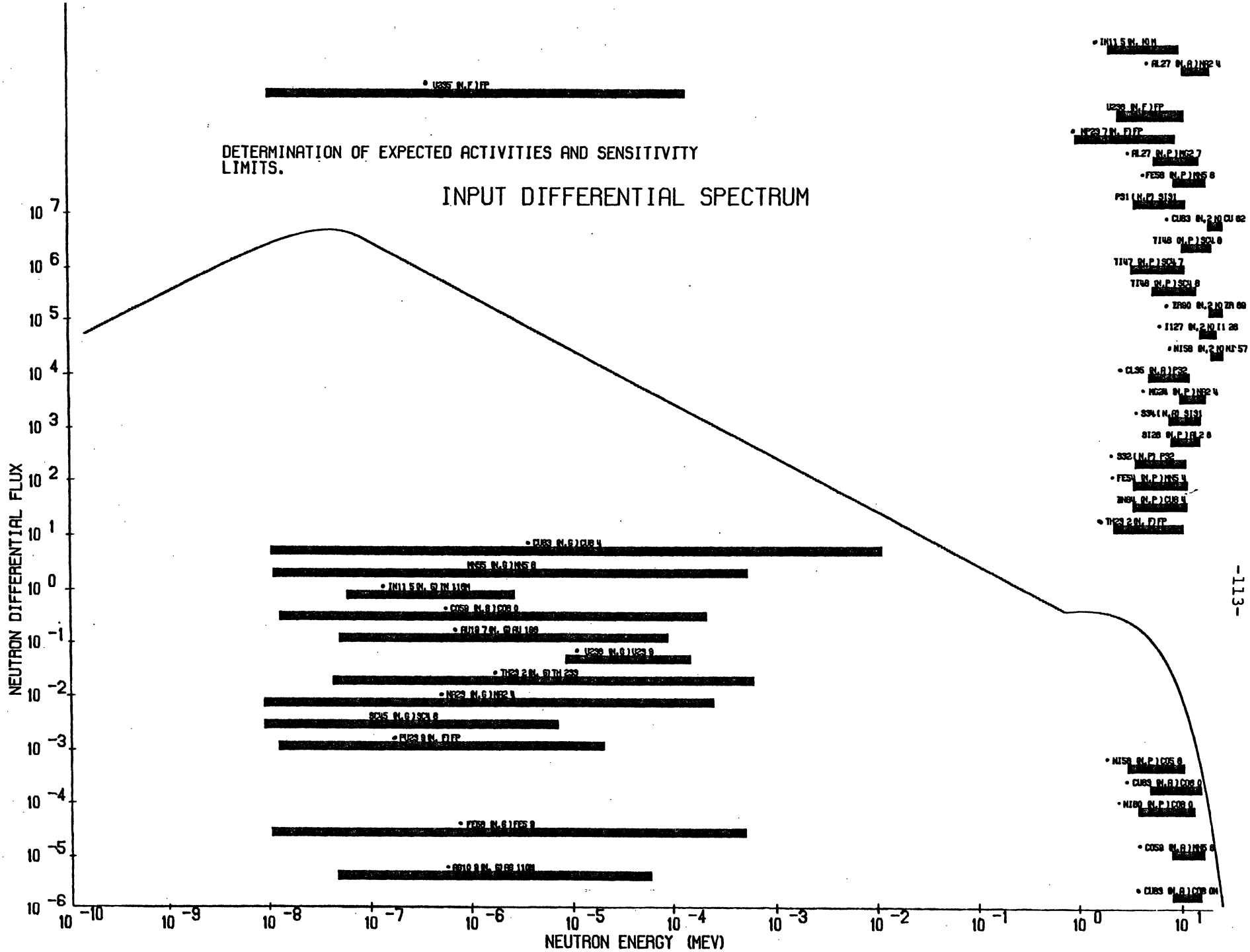

Figure 53. 90% Activity Regions for 40 Foil Reactions

overlap as possible. In addition, the irradiation-handling and counting processes impose additional constraints. For example, the foils cannot be packaged together, as is normally done, and still fit in the $\approx$ 1/8" slot between fuel plates. And uncertainties in the irradiation time make irradiations less than 10 minutes inadvisable. These and other considerations make the foils set selection procedure a difficult one.

To aid in the selection, the PRED code was written to predict the combinations of irradiation and wait times required to achieve the optimal count rate (including the energy dependence of the detector efficiency) on the fixed geometry, GeLi detector to be used. Varying foil thickness and diameters were considered, as well as the branching ratios for the various gammas to be counted, and isotopic abundances. The results yielded a set of six foil materials covering 17 reactions, and are summarized in Table 17.

The activation and counting of this set of foils still remains to be completed. With fissile and fissionable foils having recently arrived, these will be used in future irradiations to enhance the unfolding capability in the thermal region.

F. Measurement of the Thermal Neutron Spectrum at Beam Port Exits

The shape and temperature of the Maxwellian-like thermal neutron spectrum is an important characteristic of the reactor, both in core and at the beam port exits. To determine if significant changes will be introduced by the low enrichment design, the experimental program has included measurements of the beam port exit spectrum using a crystal diffractometer. The initial results obtained are described below. These measurements will be repeated to refine the technique, and this will be repeated before and after the new core is installed. An attempt to obtain in-core spectra will also be made in the near future, using a method of multiple foil activations.

1. Crystal Diffractometer Method

Data have been obtained on the FNR crystal diffractometer located at the exit of beam port I. Figure 54 is a drawing of the spectrometer and beam port geometry. The effective source plane is near the center of the D_2O reflector. Counting data is obtained using only the fission chamber monitor detector shown in Figure 54 . Counting rates are obtained as the monochromating crystal is rocked through Bragg angles about a given detector position $2\theta_o$, for a sequence of $2\theta_o$ positions. A silicon crystal, of narrow mosaic, is used in (111) transmission reflection, which has the advantages of no second order reflective contamination, "constant" crystal geometric profile, and

Table 17. Selected Trial Foils

Foil	Reactions	E Region	Irradiation Time	Foil #
A. Copper	$Cu^{63}(n,\gamma)Cu^{64}$	.0072eV → 7.6keV	1/2 hr	1
	$Cu^{63}(n,\alpha)Co^{60m}$	5.9 → 11 MeV	1/2 hr	1
	$Cu^{63}(n,2n)Cu^{62}$	11.9 → 16.3MeV	1/2 hr	1
	$Cu^{63}(n,\gamma)Cu^{64}$(Cd)	.5eV → 9.6keV	1 hr	2
B. Aluminum	$Al^{27}(n,p)Mn^{27}$(Cd)	3.4 → 9.2MeV	1/2 hr	3
	$Al^{27}(n,\alpha)Na^{24}$(Cd)	6.4 → 11.8MeV		3
C. Iron	$Fe^{58}(n,\gamma)Fe^{59}$	.0076eV → .36keV	45 minutes	4
	$Fe^{56}(n,p)Mn^{56}$	5.4 → 10.9MeV		4
	$Fe^{54}(n,p)Mn^{54}$	2.3 → 7.7MeV		4
	$Fe^{58}(n,\gamma)Fe^{59}$(Cd)	.525eV → 2.3keV		5
	$Fe^{59}(n,\alpha)Cr^{51}$	----		-
D. Titanium	$Ti^{46}(n,p)Sc^{46}$	3.4 → 9 MeV	1 hr	6
	$Ti^{47}(n,p)Sc^{47}$	2.1 → 6.9MeV		6
	$Ti^{48}(n,p)Sc^{48}$	6.6 → 12.7MeV		6
E. Zinc	$Zn^{64}(n,p)Cu^{64}$	2.3 → 7.7 MeV	1 hr	7
F. Indium	$In^{115}(n,n')In^{115m}$	1.2 → 5.8 MeV	1 hr	8
	$In^{115}(n,\gamma)In^{116m}$	.040eV → 1.8eV		8

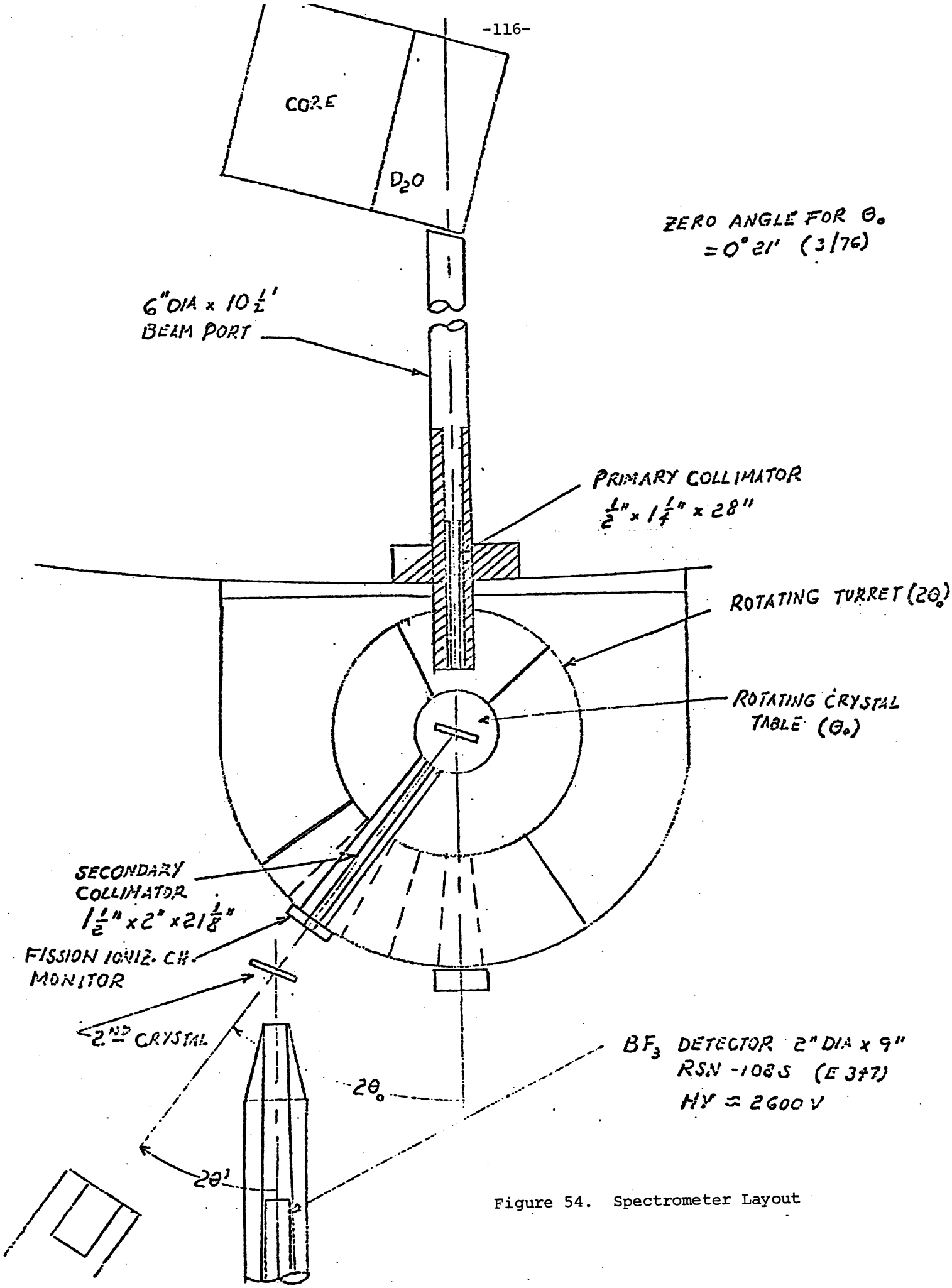

Figure 54. Spectrometer Layout

relatively reliable prediction of reflectivity versus θ_o . The count rate at each θ_o is, after background correction, given by

$$CR(\theta_o) = a \int_{-\infty}^{\infty} \epsilon(\theta)\, R(\theta-\theta_o)\, \phi(\theta)\, d\theta$$

where a is a constant geometry factor, $\epsilon(\theta)$ is the fission chamber efficiency versus θ (i.e., versus energy) and $R(\theta)$ is the crystal reflectivity. Because the latter term is sharply peaked in angle, the count rate is simply related to the flux by

$$CR(\theta) = a\, \epsilon(\theta_o)\, R(\theta_o)\, \phi(\theta_o)$$

The angular counting rate is converted to energy dependent flux $\phi(E)$ using the Bragg law. Figure 55 gives the results of points taken in two separate experiments.

The quality of the results obtained by the above simple relation depends on data reproducibility and on the accuracy of our knowledge of a, $\epsilon(\theta_o)$, and $R(\theta_o)$ as θ_o is varied. Attention to geometric detail should insure that a remains constant. Use of a highly transmitting fission chamber guarantees that $\epsilon(\theta_o)$ varies exactly as the U-235 fission cross section. $R(\theta_o)$, called the integrated reflectivity, must be calculated, and its variation with θ_o is of primary concern. We have followed the well known kinematic diffraction theory for mosaic crystals in obtaining $R(\theta_o)$[50,51,52]. This theory is known to give absolute values of low reliability but, for a given crystal, its prediction of the shape of $R(\theta_o)$ with θ_o should be accurate. $R(\theta_o)$ and its changes with θ_o depend on the mosaic width parameter, η . η is not known a priori. It may be found by fitting the data and η to a perfect Maxwellian and minimizing the least squares residue of $\ln \frac{\phi(E)}{E}$ by varying η . It may be measured, in principle, by a two-silicon crystal rocking experiment. For this report we have used the first method. This means the spectrum must be defined as a Maxwellian and the measurements establish the Maxwellian temperature. It is only the shift in T we need to find, but if the data also produces a physically realistic T, our confidence in the shift is reinforced.

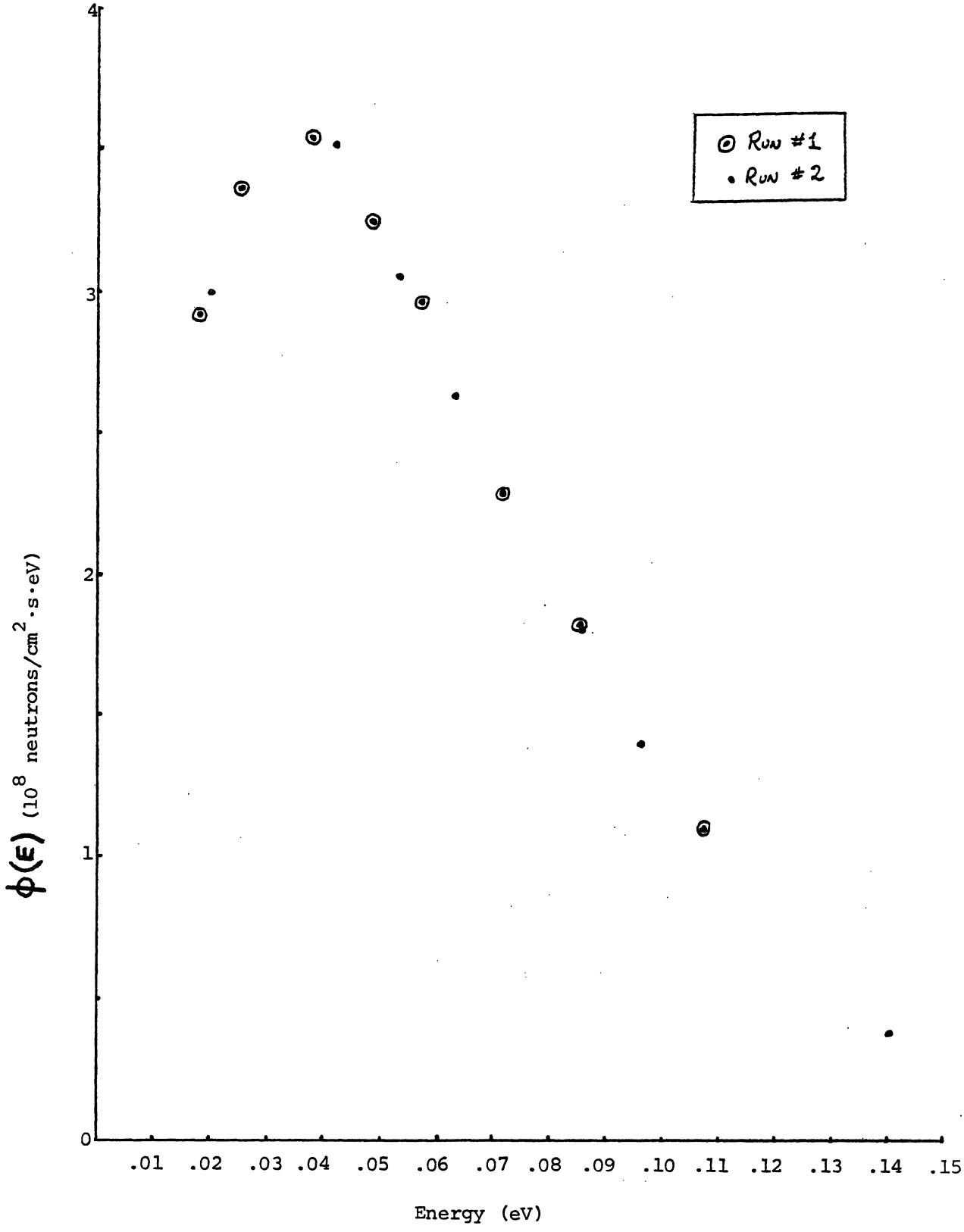

Figure 55. Thermal Flux Spectrum

2. Preliminary Results and Evaluation

Figure 56 gives the data of Figure 55 plotted as $\ln \frac{\Phi(E)}{E}$ versus E, for two η values. For a Maxwellian, the inverse of the slope of a straight line fitted to the data points gives kT. Figures 57 and 58 show the quality of fit for two values of η. It is apparent that η is closer to a Maxwellian fit in Figure 57. It is also apparent that data points below 0.04 eV are systematically too low. This we attribute to inadequate beam geometry constancy in these data runs. Only data points above 0.04 eV have therefore been used. (The systematic departure is opposite to that which would occur from third order beam contamination, which is assessed to be negligible, in any event, above about 0.018 eV).

Figure 59 is the result of a least square best fit to a Maxwellian temperature T as a function of the variation of η to minimize the fitting residue. The results were obtained from a program SPECTRA2 written to perform the minimzation. The residue is somewhat insensitive to η, unfortunately, but indicates a minimum value near 1.65×10^{-4} radians. This choice gives the following results

$$T = 352 \pm 5 \ ^\circ K$$

where the uncertainty corresponds to one standard deviation in η.

This result is believed to be of order 10 to 15°K too high. The value of T is very sensitive to small fluctuations in the data. The uncertainty in T is satisfactory for core comparison purposes.

Both T and its uncertainty must be confirmed by additional measurements. Closer attention to wide angle beam geometry is necessary. If possible a measurement of η will be attempted.

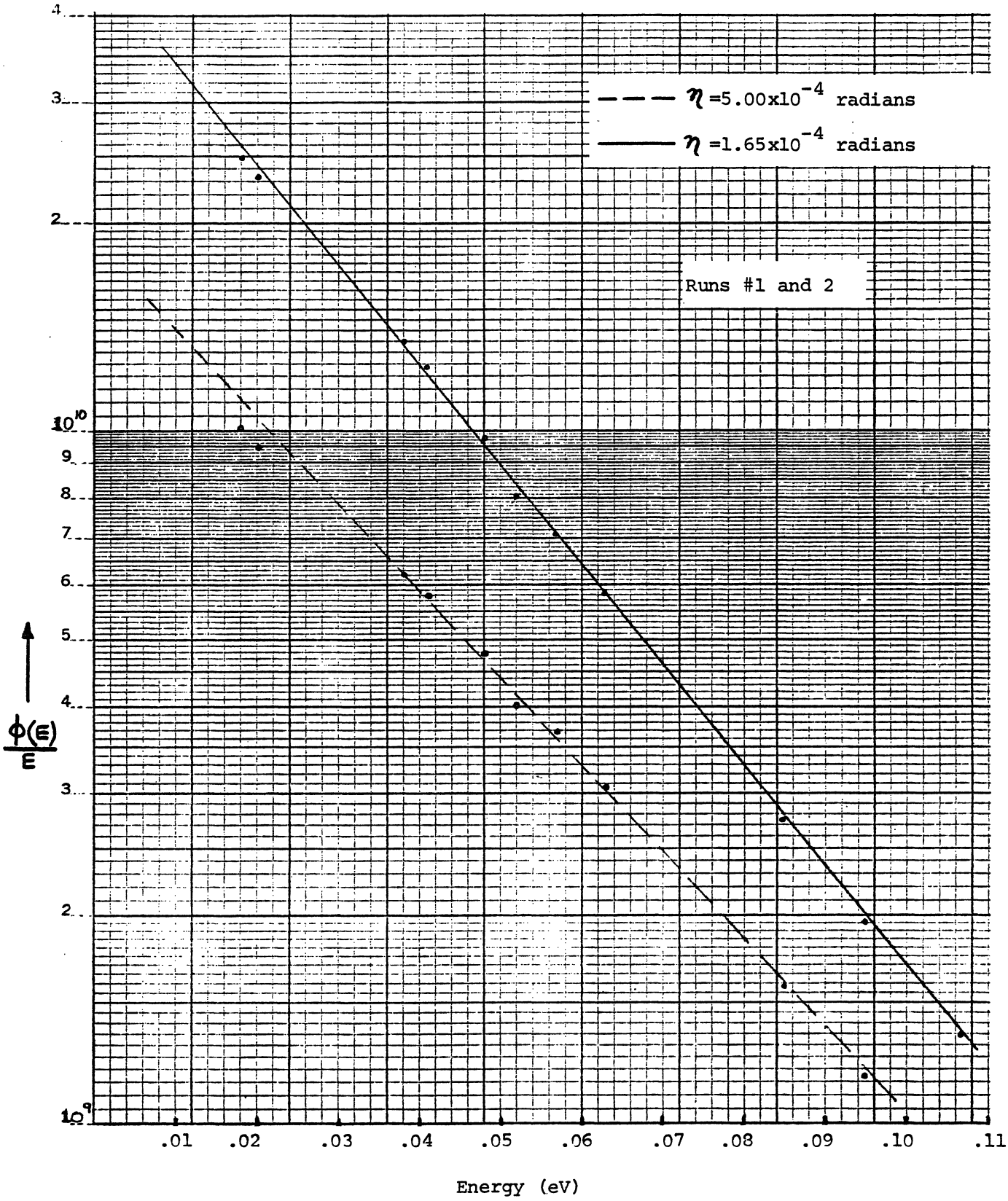

Figure 56. $\frac{\phi(E)}{E}$ versus E

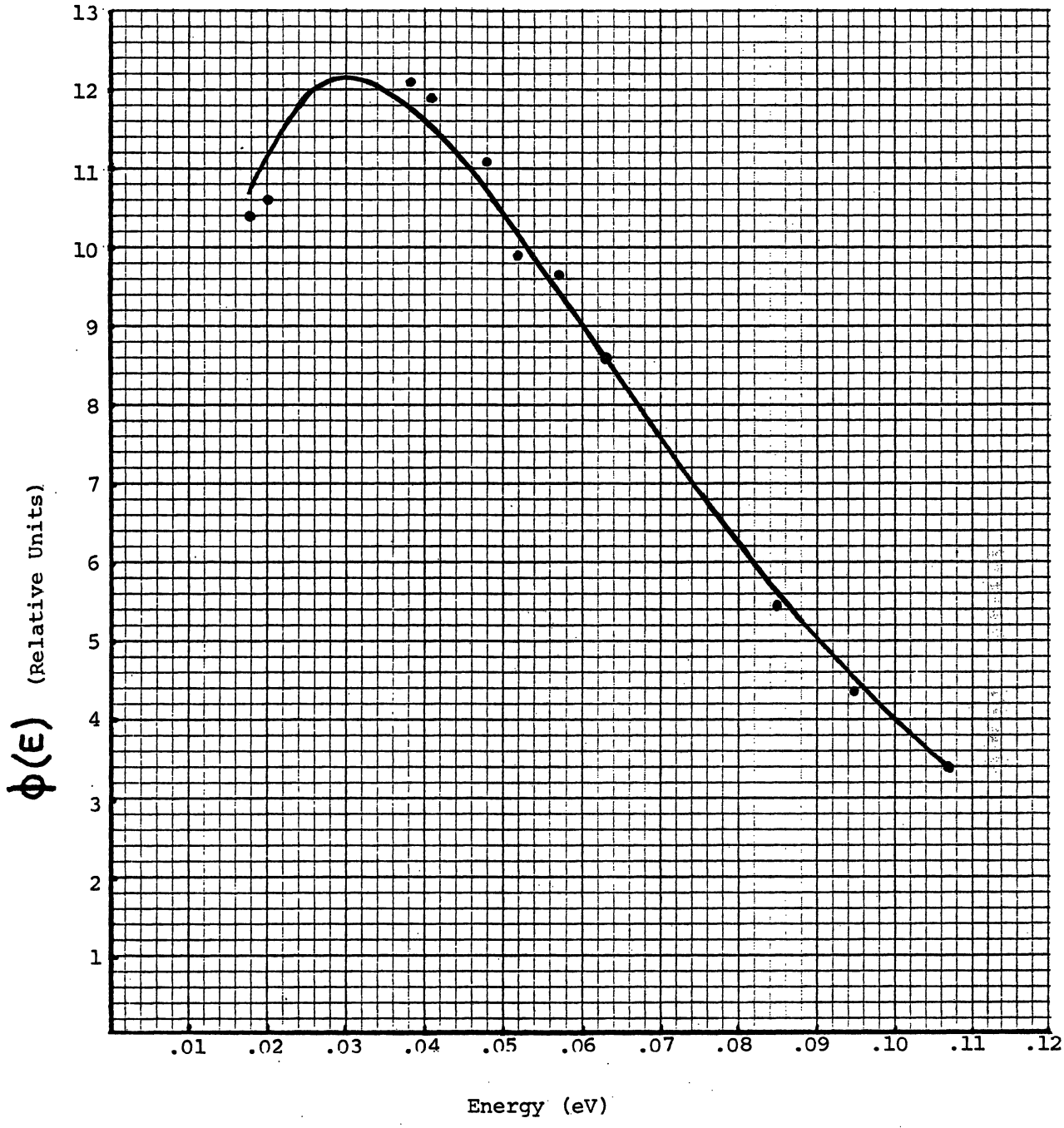

Figure 57. $\phi(E)$ vs E for $\eta = 1.65 \times 10^{-4}$ Radians

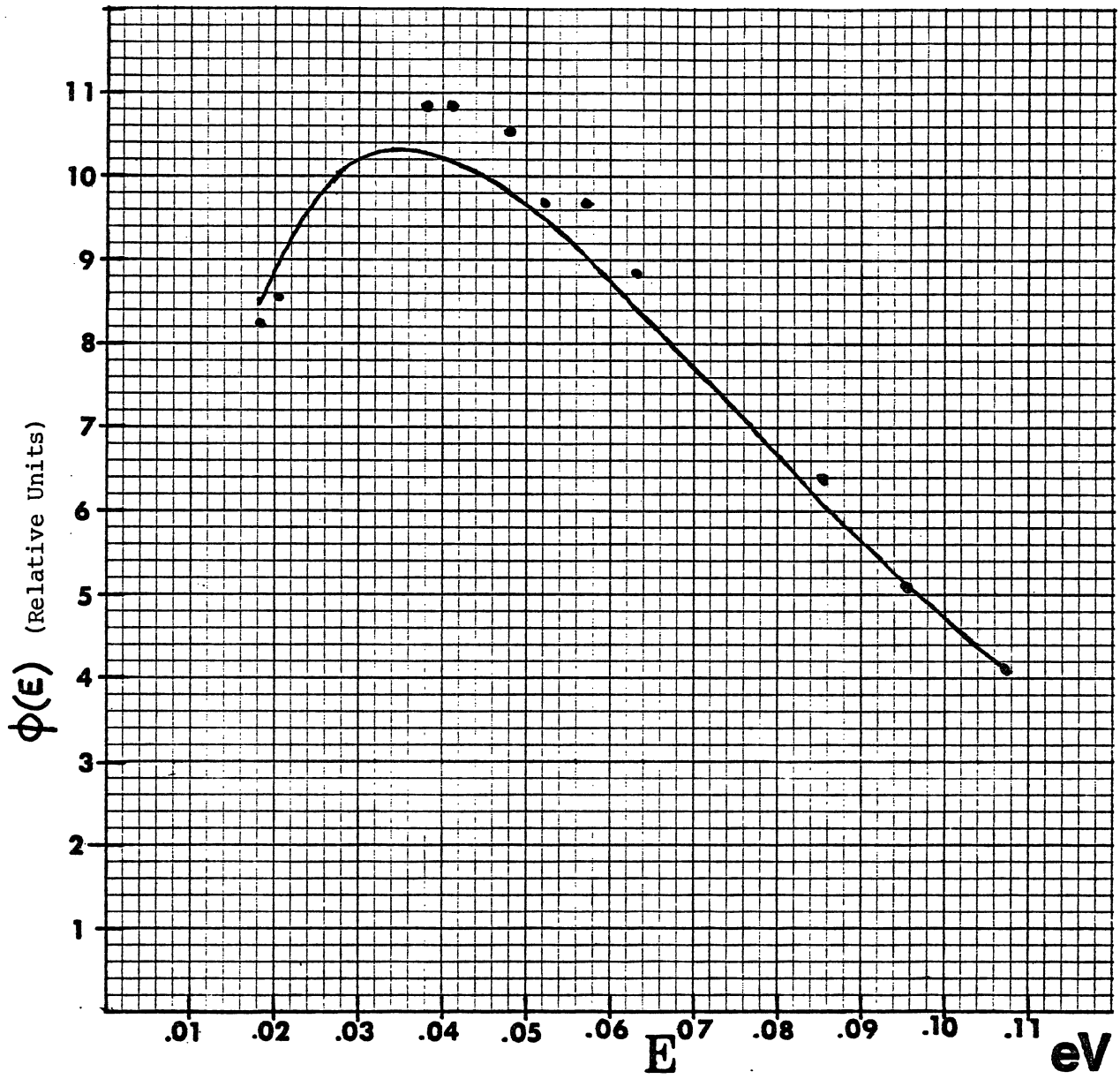

Figure 58. Φ (E) vs E for $\eta = 5 \times 10^{-4}$ Radians

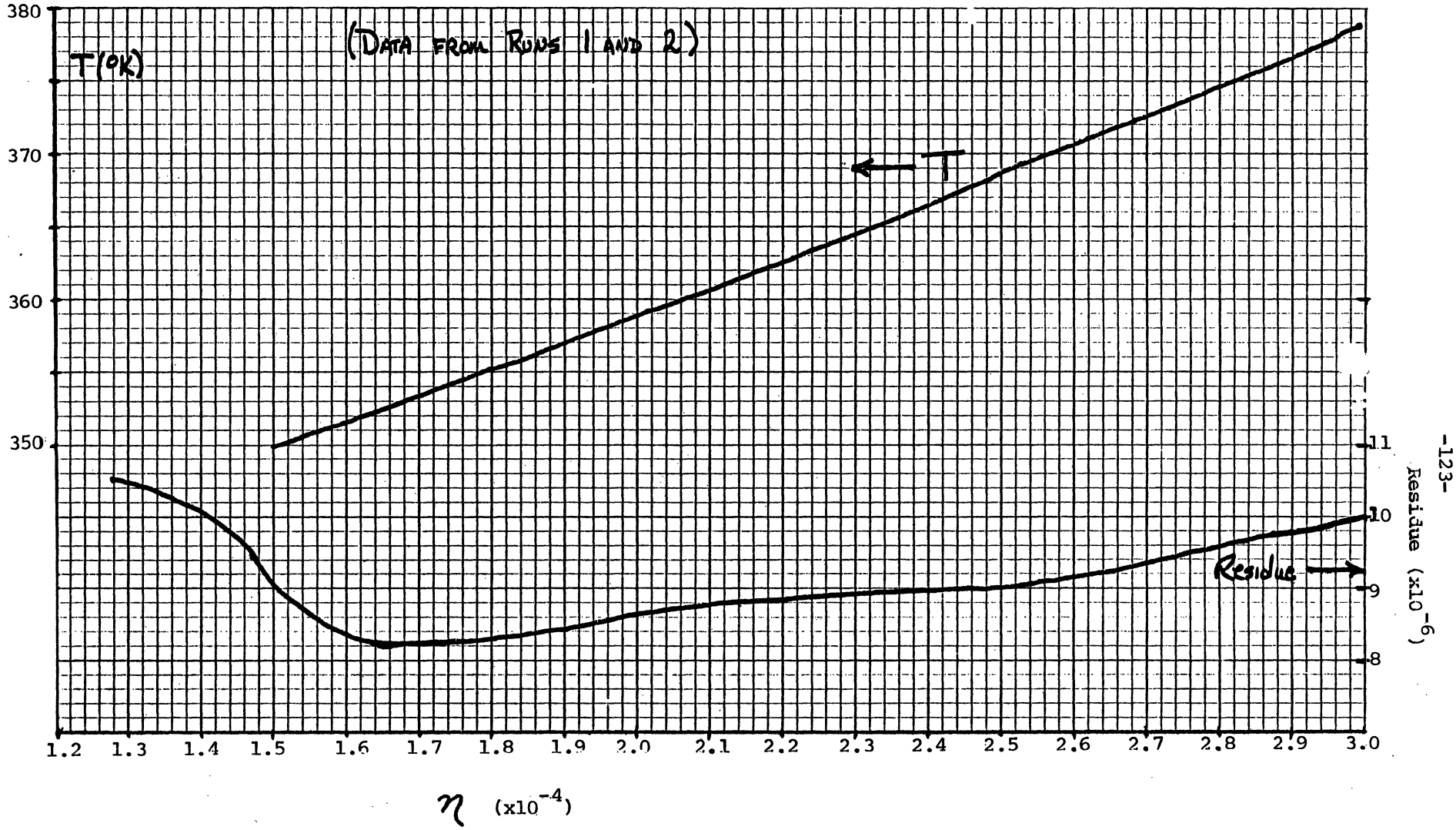

Figure 59. Neutron Temperature and Residue vs

VII. Summary and Conclusions

The following summary and conclusions concerning the current status and future direction of the subject program correspond to, and are based on, the previous sections of this report

A. Generic Neutronic Model Development and Verification

1. The LEOPARD code has been modified and verified for application to MTR-type fuel and is considered to be acceptable for routine analyses. However, the LEOPARD library is quite old and should be replaced with a ENDF/B-IV version.

2. The EPRI-HAMMER code has been verified for MTR-type fuel plate configurations and is a valuable tool for benchmark and control rod analyses. However, it does not have a depletion capability which would be valuable for control rod calculations in a depleted core. Incorporating a depletion capability into the EPRI-HAMMER code should be examined.

3. The 2DB code has been verified for MTR-type reactor calculations and has proven to be a capable and valuable tool for global FNR calculations. Coupled with the macroscopic depletion and fuel shuffling modifications, extremely complicated fuel cycle patterns may be simulated. Future effort with the 2DB code should include examination of albedo type boundary conditions and allowing an irregular outer boundary. This could result in significant savings in computer time and possibly increased accuracy depending on the methods used for computing the albedoes.

4. The ANISN code has had only minor modifications and is assumed to work correctly for configurations that can be modeled with one-dimensional geometry. There is some uncertainty in the use of a transverse buckling for ANISN, especially in the D_2O tank, and this question should be resolved.

5. The determination of an axial buckling for use in two-dimensional diffusion theory calculations is still incomplete. Further effort to resolve this question is being undertaken.

6. The calculation of neutron flux distributions at the beam ports in the D_2O tank and in H_2O reflectors is at a preliminary stage. As mentioned above, uncertainties in the transverse buckling treatment affect this calculation as well as uncertainties in the calculation of reflector cross sections including the representation of material heterogeneities. This item is currently under examination.

7. More use of three-dimensional diffusion codes is envisioned as the calculational model is refined. Limited use has been made of the VENTURE code to compute transverse bucklings for two-dimensional calculations and to provide axial flux/power distributions for comparison with experimental results. Because of the success we have had with the 2DB code, effort is being expended to adapt the 3DB code on MTS, including incorporation of the various 2DB modifications such as the macroscopic depletion scheme and the fuel shuffling capability.

8. The method used to compute control rod worth is considered to be acceptable and effort is now being expended to examine the rod worth that is inferred from the asymptotic reactor period measurements. There is some uncertainty in this rod worth measurement due to the assumed value for the kinetics parameter β_{eff} which accounts for the effect of leakage on the delayed neutron fraction. Effort is being expended to examine this question.

B. Confirmation of Fuel Specifications

1. The specifications for the UAlx fuel plate have been confirmed.

2. Further effort is needed to confirm the specifications for the oxide fuel.

C. Safety Analysis Report (SAR)

1. A draft version of the revised SAR has been completed and forwarded to the Nuclear Regulatory Commission (NRC) for comment. Upon receipt of comments from the NRC, a final version of the SAR will be prepared and submitted for review and approval.

2. Due to the complexity of the calculation to determine the power coefficient of reactivity, this coefficient was inferred indirectly from the calculated isothermal temperature coefficients. As noted in Appendix A, there is no significant change in the overall core shutdown margin; however, further effort is needed to compute the power coefficient of reactivity more precisely.

D. Thermal-Hydraulics Test Program

1. The experimental apparatus has been constructed and preliminary tests have been performed. The results indicate that all heat transfer mechanisms have not been accounted for and that an improved test model is necessary.

2. Effort is continuing to simulate the test model analytically.

E. Demonstration Experiment Program

1. The determination of experimental procedures for iron wire activation and the methodology for interpreting the results is complete although additional refinement and repetition of the experimental methods is envisioned. In addition to providing experimental flux profiles in the core and D_2O tank, this effort provided for an absolute determination of the rhodium detector sensitivity as a function and hence an accurate determination of the thermal flux.

2. Experimental procedures for performing rhodium detector flux maps are complete. Special adapters to allow fluc mapping in the D_2O tank and H_2O reflector regions have been built and several full core flux maps have been measured. The methodology for determining the absolute sensitivity of the rhodium detector has been developed and applied. This effort involves the use of an "epithermal correction factor" to account for that portion of the detector output that is attributable to epithermal neutrons. When applied to the flux maps, the effect of the correction factor is found to be significant.

3. Estimates of the errors in the experimental flux values have been made and suggest ways for reducing the errors.

4. Effort is being expended to develop an analytical technique for interpreting rhodium detector output signals without waiting for the detector signal to equilibrate in time. If successful this will allow considerable savings in manpower to perform a full core flux map.

5. A current version of the SAND-II code package has been received and is being implemented on MTS. This will be utilized for unfolding the in-core neutron spectrum with foil activation measurements. In addition to using the standard unfolding techniques embodied in the codes, effort is being expended to examine the potential for unfolding thermal spectra and the spectra in the range 1 KeV to 1 MeV.

6. The selection of activation foils (including fissile and fissionable foils) has been completed and the foils are being delivered. Experimental procedures for activating and analyzing the foils are being developed.

7. The crystal diffractometer at beam port I is being used to determine the thermal flux spectrum at the beam port exit. The experimental and analytical procedures are being refined although preliminary results have been obtained and appear to be satisfactory.

APPENDIX A

PRELIMINARY SAFETY ANALYSIS

Utilization of Low Enrichment Uranium (LEU) Fuel in The Ford Nuclear Reactor

SAFETY ANALYSIS

UTILIZATION OF LOW ENRICHMENT URANIUM (LEU) FUEL IN THE FORD NUCLEAR REACTOR

FORD NUCLEAR REACTOR
MICHIGAN MEMORIAL-PHOENIX PROJECT
THE UNIVERSITY OF MICHIGAN
Ann Arbor

October , 1979

ABSTRACT

This analysis reviews the safety aspects of utilizing low enrichment uranium (LEU-less than 20% enrichment) fuel in the Ford Nuclear Reactor (FNR). A brief description of the proposed fuel is followed by an examination of fuel swelling, high temperature blistering, and failure data for similar operational and test fuels under operating conditions similar to those in the FNR. Fuel specifications have been developed with technical requirements identical to those for reactors which use equivalent fuel. Heat transfer characteristics are not examined in detail because fuel and coolant flow channel dimensions are identical to those in present FNR fuel. Core physics analyses show some variation in fast and thermal neutron flux distributions within the core and in the reflector regions. The available data and the analyses performed indicate that no reduction in safety margins are expected from utilizing LEU fuel in the FNR core.

TABLE OF CONTENTS

LIST OF FIGURES

LIST OF TABLES

1. INTRODUCTION

As part of the national plan for development of high uranium density research and test reactor fuel to accomodate the use of low enrichment uranium (LEU) fuel, the Ford Nuclear Reactor (FNR) proposes to test the use of 19.5 wt% enriched uranium fuel in the form of uranium aluminide (UAl_x) or uranium oxide (U_3O_8) in place of the present 93 wt% uranium aluminide fuel.

The use of less than 20% enrichment fuel gives the potential benefit of reducing the probability of uranium-235 diversion. An additional benefit is a possible reduction in the cost of security requirements for both fuel fabrication and fuel handling and storage.

This report includes information on fuel which is physically similar to the proposed LEU fuel and which has been satisfactorily tested under operating conditions similar to those of the Ford Nuclear Reactor.

Core physics calculations indicate that utilization of LEU fuel in the FNR core will result in a decrease in thermal flux of 12-20% in the core region and a decrease of 6-10% in the reflector region.

2. FUEL DESCRIPTION

The proposed LEU fuel meat is to be intermetallic uranium aluminide (UAL_3, UAL_4, UAL_2) or uranium oxide (U_3O_8) cermet, both of which are licensed for use by the FNR, clad in 6061 aluminum.

Fuel element overall dimensions and internal dimensions will remain identical to the dimensions of fuel presently being used in the FNR at two megawatts. Plate thickness will be 0.060 inches. The meat will be 0.030 inches and cladding 0.015 inches. Two plate thicknesses are presently in use at the FNR. Uranium-aluminum alloy fuel plates are 0.060 inches thick with 0.020 clad-0.020 meat-0.020 clad. Aluminide fuel plates are 0.050 inches thick with 0.015 clad-0.020 meat-0.015 clad. The FNR has operating experience with fuel plates which are 0.060 inches thick and which have 0.015 inch clad, and no problems have arisen.

The proposed meat thickness of 0.030 inches is dictated by an attempt to provide fuel with the same reactivity as present FNR fuel while reducing the enrichment from 93% to just under 20%. In order to provide the proper uranium-235 loading, the weight percent of the fissile compound in the fuel meat must be increased from the present 19.1 weight percent UAL_x or 16.8 weight percent U_3O_8 to approximately 56.5 weight percent UAL_x or 49.6 weight percent U_3O_8. Present uranium loading is 14.2 weight percent; the proposed loading is 42.0 weight percent.

3. OPERATING CONDITIONS

Fuel swelling data and fuel blister data, which were obtained for fuel plates made of materials similar to those in the FNR and which were determined at fuel temperature, pressure, and pH conditions similar to FNR conditions, were extracted from the data contained in reports referenced in the Safety Analysis bibliography and are tabulated in TABLE 1 and TABLE 2. All available data points are included.

The aluminum powder used in the proposed FNR fuel and in the test cores is a blend of nearly pure aluminum. 1100 aluminum is pure aluminum. The various powder blends (PB-01, PB-04, PB-32, PB-36) are essentially pure aluminum of specific grain sizes. 5214 is spherical aluminum powder with .05% iron and a total of .08% iron plus silicon permitted. X8001 is a nickel alloy of aluminum which is only slightly harder than 1100.

4. FUEL SWELLING

Table 1A provides UAL_x fuel swelling data. [1, 2, 3, 4, 5] Table 1B contains U_3O_8 fuel swelling data. 4 Test temperatures are as close as possible to the FNR peak operating temperature of 172°F. All test data were obtained at significantly higher pressures. Figure 1 is a plot of the UAL_x and U_3O_8 data points. Also shown on Figure 1 is the FNR fission density limit of 15×10^{20} fissions/cc and the calculated swelling rate for 100% dense fuels.

With the exception of one data point, the measured swelling rate is below the calculated swelling rate. It is expected that the measured swelling rate would be less than calculated because some voids are expected in core compacts and voids generally tend to reduce swelling.

No fuel failures were observed for the fission density-fuel swelling combinations plotted on Figure 1. Therefore, all of the available fuel swelling data at operating conditions similar to those in the FNR indicate that UAL_x and U_3O_8 fuel can be safely used in the FNR without failure due to swelling and that no reduction in the safety margin is expected.

5. FUEL BLISTERING

Table 2A provides UAL_x fuel blister data. [1, 2, 3, 5, 7] Table 2B contains U_3O_8 fuel blister data. [1, 8] Figure 2, a plot of fuel blister temperature verus fission density for the Table 2A and 2B data, shows that all blister failures occurred in fuel being operated at temperatures well above the FNR peak operating temperature of 172°F.

TABLE 1A

UAL_x FUEL CORE SWELLING DATA

Reactor	Fuel Characteristics									
Sample ID	Clad	Core	Weight Percent UAL_x	Weight Percent U	Core Temp, °F (°C)	Operating Pressure PSIG	pH	Fission Density f/cc X 10^{20}	Volume Change % Δ V/V	Ref
FNR	6061	5214	19.1	14.2	172 (78)	9.2	5-7	15.0		
MTR										
113-1	6061	6061	46.7	34.7	239 (115)	50	5-7	7.5	7.5	1
113-2	6061	6061	46.7	34.7	239 (115)	50	5-7	10.1	6.8	1
113-3	6061	6061	46.7	34.7	239 (115)	50	5-7	9.4	6.2	1
113-4	6061	6061	46.7	34.7	239 (115)	50	5-7	9.8	3.7	1
113-5	6061	6061	46.7	34.7	239 (115)	50	5-7	13.5	7.3	1
113-6	6061	6061	46.7	34.7	239 (115)	50	5-7	14.1	7.3	1
113-7	6061	6061	46.7	34.7	239 (115)	50	5-7	14.5	5.5	1
ETR										
I-1-1095	6061	X8001	51.0	37.9	230 (110)	200	5-7	6.9	0.8	2
I-1-1097	6061	X8001	51.0	37.9	230 (110)	200	5-7	5.6	0.8	2
I-12-727	APM786	X8001	51.0	37.9	230 (110)	200	5-7	10.9	3.9	2
I-1-584	6061	X8001	51.0	37.9	302 (150)	200	5-7	7.2	0.6	2
I-69-1579	6061	MD101	60.0	44.6	302 (150)	200	5-7	16.5	3.6	2
I-71-1594	6061	MD101	77.0	57.2	302 (150)	200	5-7	24.7	1.1	2
I-69-1580	6061	MD101	60.0	44.6	338 (170)	200	5-7	9.4	1.8	2
I-70-1583	6061	MD101	65.0	48.3	338 (170)	200	5-7	11.0	1.2	2
I-70-1584	6061	MD101	65.0	48.3	338 (170)	200	5-7	16.2	4.9	2

TABLE 1A

UAL_x FUEL CORE SWELLING DATA

Reactor	Fuel Characteristics									
Sample ID	Clad	Core	Weight Percent UAL_x	Weight Percent U	Core Temp, °F (°C)	Operating Pressure PSIG	pH	Fission Density $f/cc \times 10^{20}$	Volume Change % ΔV/V	Ref
FNR	6061	5214	19.1	14.2	172 (78)	9.2	5-7	15.0		
ETR										
169-4	6061	X8001	61.9	46.0	228 (109)	200	5-7	26.3	2.0	3
169-5	6061	X8001	61.9	46.0	228 (109)	200	5-7	28.8	4.7	3
169-11	6061	X8001	52.0	38.7	228 (109)	200	5-7	23.1	4.7	3
169-12	6061	X8001	52.0	38.7	228 (109)	200	5-7	24.3	5.9	3
169-19	6061	X8001	43.0	32.0	228 (109)	200	5-7	19.7	4.7	3
169-36	6061	X8001	52.8	39.2	228 (109)	200	5-7	25.1	6.4	3
169-37	6061	X8001	52.7	39.2	228 (109)	200	5-7	25.5	6.0	3
169-38	6061	X8001	52.7	39.2	228 (109)	200	5-7	25.0	7.4	3
169-39	6061	X8001	52.7	39.2	228 (109)	200	5-7	23.9	5.7	3
HFIR										
32-4	6061	PB-32*	51.0	37.9	176 (80)	1000	5-7	17.9	8.8	4
34-2	6061	PB-36	53.0	39.4	190 (88)	1000	5-7	19.5	6.8	4
14-3	6061	PB-32	53.0	39.4	198 (92)	1000	5-7	20.2	7.4	4
15-4	6061	PB-32	63.0	46.8	208 (98)	1000	5-7	22.2	6.1	4
35-4	6061	PB-36	63.0	46.8	201 (94)	1000	5-7	21.4	4.8	4
25-4	6061	PB-32	64.0	47.6	205 (96)	1000	5-7	21.7	4.1	4

* Aluminum Powder Blends

TABLE 1A

UAL_x FUEL CORE SWELLING DATA

Reactor	Fuel Characteristics									
Sample ID	Clad	Core	Weight Percent UAL_x	Weight Percent U	Core Temp, °F (°C)	Operating Pressure PSIG	pH	Fission Density f/cc X 10^{20}	Volume Change % Δ V/V	Ref
FNR	6061	5214	19.1	14.2	172 (78)	9.2	5-7	15.0		
FR2 (Kalsruhe, Germany)										
1-4	1100	1100	50	37.1	158 (70)	50	5-7	5.8	2.0	5
2-4	1100	1100	50	37.1	158 (70)	50	5-7	16.9	4.5	5
3-4	1100	1100	50	37.1	158 (70)	50	5-7	12.2	4.0	5
4-1	1100	1100	50	37.1	158 (70)	50	5-7	9.4	3.5	5
5-3	1100	1100	45.5	33.8	158 (70)	50	5-7	9.4	3.5	5
6-4	1100	1100	45.5	33.8	158 (70)	50	5-7	7.6	4.0	5
7-2	1100	1100	50	37.1	158 (70)	50	5-7	15.8	5.0	5
8-2	1100	1100	45.5	33.8	158 (70)	50	5-7	15.8	4.0	5

TABLE 1B

U_3O_8 FUEL CORE SWELLING DATA

Reactor	Fuel Characteristics									
Sample ID	Clad	Core	Weight Percent U_3O_8	Weight Percent U	Core Temp, °F (°C)	Operating Pressure PSIG	pH	Fission Density $f/cc \times 10^{20}$	Volume Change % ΔV/V	Ref
FNR	6061	5214	16.8	14.2	172 (78)	9.2	5-7	15.0		
HFIR										
12-3	6061	PB-01*	47	39.7	192 (89)	1000	5-7	19.8	3.0	4
13-4	6061	PB-01	40	33.8	183 (84)	1000	5-7	18.1	3.8	4
22-4	6061	PB-04	50	42.3	187 (86)	1000	5-7	19.7	2.9	4
23-1	6061	PB-04	42	35.5	181 (83)	1000	5-7	18.1	3.1	4
ETR										
67-974	6061	PB-01*	40	33.8	401 (205)	200	5-7	17.9	4.7	4
67-982	6061	PB-01	40	33.8	383 (195)	200	5-7	18.0	5.1	4
67-986	6061	PB-01	40	33.8	392 (200)	200	5-7	18.1	6.2	4
56-899	6061	PB-01	50	42.3	302 (150)	200	5-7	11.7	1.4	4
56-957	6061	PB-01	50	42.3	302 (150)	200	5-7	22.4	7.6	4
3-893	6061	PB-04	45	38.0	347 (175)	200	5-7	15.5	2.0	4
68-997	6061	PB-04	49	41.4	347 (175)	200	5-7	19.7	3.6	4
68-1638	6061	PB-04	49	41.4	428 (220)	200	5-7	12.7	0.4	4
68-1633	6061	PB-04	49	41.4	419 (215)	200	5-7	12.7	0.4	4
68-1642	6061	PB-04	49	41.4	410 (210)	200	5-7	12.7	1.7	4
68-1605	6061	PB-04	49	41.4	329 (165)	200	5-7	19.9	3.0	4
68-1607	6061	PB-04	49	41.4	338 (170)	200	5-7	19.5	3.1	4

* Aluminum Powder Blends

FIGURE 1

FUEL CORE SWELLING

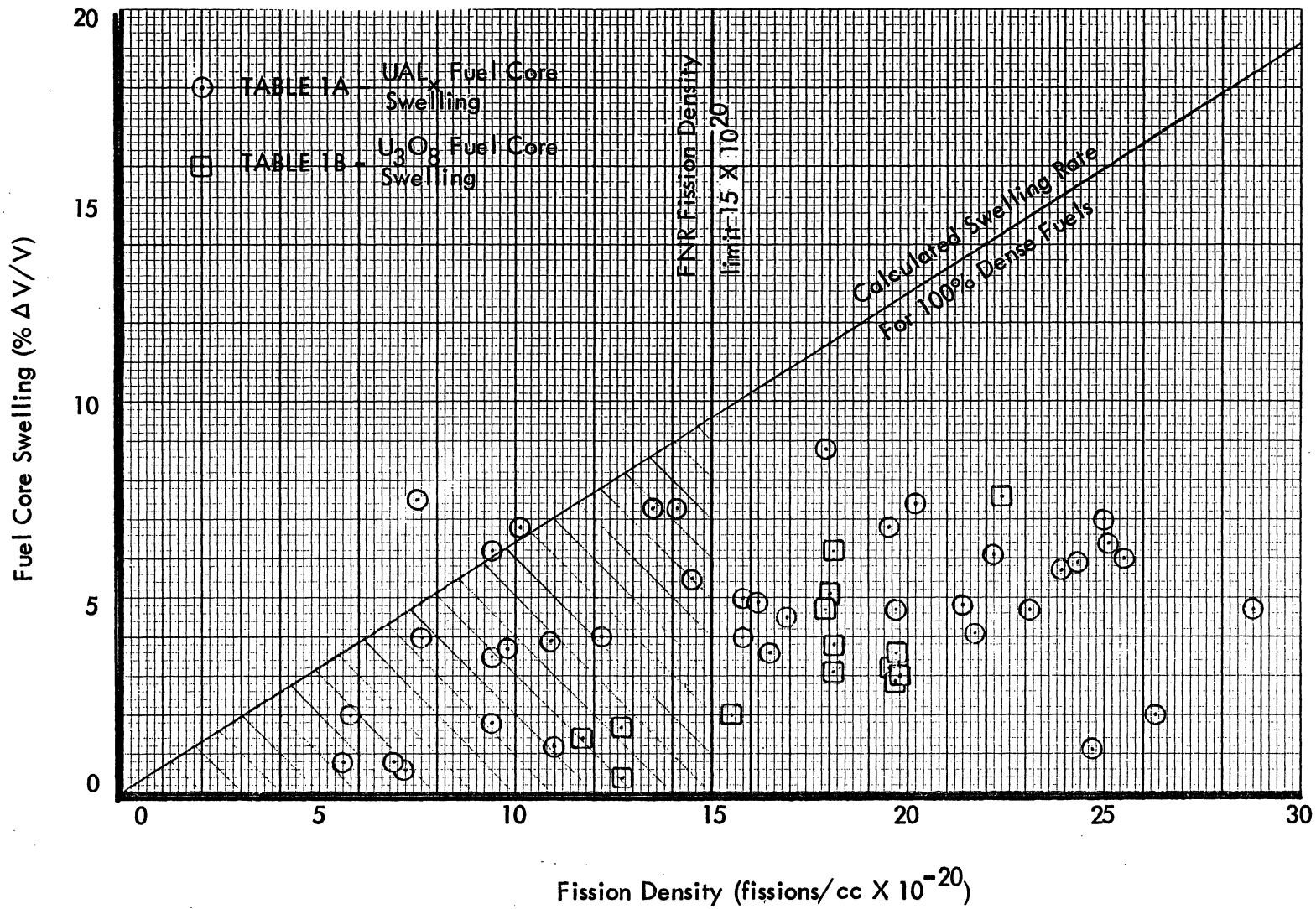

TABLE 2A

UAL_x FUEL CORE BLISTER DATA

Reactor	Fuel Characteristics									
			Weight Percent		Core	Operating		Fission	Blister	
Sample ID	Clad	Core	UAL_x	U	Temp, °F (°C)	Pressure PSIG	pH	Density f/cc X 10^{20}	Temp, °F (°C)	Ref
FNR	6061	5214	19.1	14.2	172 (78)	9.2	5-7	15.0		
ETR										
E-107	6061	X8001	54.0	40.1	403 (206)	200	5-7	10.4	1094 (590)	7
E-508	6061	X8001	54.0	40.1	403 (206)	200	5-7	10.7	1094 (590)	7
E-510	6061	X8001	54.0	40.1	403 (206)	200	5-7	11.0	1094 (590)	7
E-507	6061	X8001	54.0	40.1	403 (206)	200	5-7	11.2	1094 (590)	7
I-1-1095	6061	X8001	51.0	37.9	230 (110)	200	5-7	6.9	1004 (540)	2
I-1-1097	6061	X8001	51.0	37.9	230 (110)	200	5-7	5.6	1004 (540)	2
I-12-727	APM786	X8001	51.0	37.9	230 (110)	200	5-7	10.9	1004 (540)	2
I-69-1579	6061	MD101	60.0	44.6	302 (150)	200	5-7	7.2	1112 (600)	2
I-71-1594	6061	MD101	77.0	57.2	302 (150)	200	5-7	24.7	806 (430)	2
I-69-1580	6061	MD101	60.0	44.6	338 (170)	200	5-7	9.4	1112 (600)	2
I-70-1583	6061	MD101	65.0	48.3	338 (170)	200	5-7	11.0	1112 (600)	2
I-70-1584	6061	MD101	65.0	48.3	338 (170)	200	5-7	16.2	1112 (600)	2
I-71-1593	6061	MD101	77.0	57.2	338 (170)	200	5-7	12.6	1112 (600)	2
169-4	6061	X8001	61.9	46.0	228 (109)	200	5-7	26.3	1050 (565)	3
169-5	6061	X8001	61.9	46.0	228 (109)	200	5-7	28.8	> 1050 (> 565)	3
169-11	6061	X8001	52.0	38.7	228 (109)	200	5-7	23.1	1000 (538)	3
169-12	6061	X8001	52.0	38.7	228 (109)	200	5-7	24.3	1050 (565)	3
169-19	6061	X8001	43.0	32.0	228 (109)	200	5-7	19.7	1050 (565)	3
169-36	6061	X8001	52.8	39.2	228 (109)	200	5-7	25.1	>1050 (> 565)	3
169-37	6061	X8001	52.7	39.2	228 (109)	200	5-7	25.5	1000 (538)	3
169-38	6061	X8001	52.7	39.2	228 (109)	200	5-7	25.0	1000 (538)	3
169-39	6061	X8001	52.7	39.2	228 (109)	200	5-7	23.9	1050 (565)	3

TABLE 2A

UAL_x FUEL CORE BLISTER DATA

Reactor	Fuel Characteristics									
			Weight Percent							
Sample ID	Clad	Core	UAL_x	U	Core Temp, °F (°C)	Operating Pressure PSIG	pH	Fission Density $f/cc \times 10^{20}$	Blister Temp, °F (°C)	Ref
FNR	6061	5214	19.1	14.2	172 (78)	9.2	5-7	15.0		
MTR										
113-8	6061	6061	46.7	34.7	239 (115)	50	5-7	4.5	> 1100 (> 594)	1
113-9	6061	6061	46.7	34.7	239 (115)	50	5-7	5.7	> 1100 (> 594)	1
113-10	6061	6061	46.7	34.7	239 (115)	50	5-7	6.2	> 1100 (> 594)	1
113-11	6061	6061	46.7	34.7	239 (115)	50	5-7	7.2	> 1100 (> 594)	1
113-12	6061	6061	46.7	34.7	239 (115)	50	5-7	10.5	> 1100 (> 594)	1
113-13	6061	6061	46.7	34.7	239 (115)	50	5-7	9.2	1022 (550)	1
113-14	6061	6061	46.7	34.7	239 (115)	50	5-7	9.5	932 (500)	1
113-15	6061	6061	46.7	34.7	239 (115)	50	5-7	11.3	932 (500)	1
113-16	6061	6061	46.7	34.7	239 (115)	50	5-7	12.5	1067 (575)	1
113-17	6061	6061	46.7	34.7	239 (115)	50	5-7	20.3	932 (500)	1
FR2 (Kalsruhe, Germany)										
1-4	1100	1100	50	37.2	158 (70)	50	5-7	5.8	> 932 (> 500)	5
2-4	1100	1100	50	37.2	158 (70)	50	5-7	16.9	> 932 (> 500)	5
3-4	1100	1100	50	37.2	158 (70)	50	5-7	12.2	> 932 (> 500)	5
4-1	1100	1100	50	37.2	158 (70)	50	5-7	9.4	> 932 (> 500)	5
5-3	1100	1100	45.5	33.8	158 (70)	50	5-7	9.4	> 932 (> 500)	5
6-4	1100	1100	45.5	33.8	158 (70)	50	5-7	7.6	> 932 (> 500)	5
7-2	1100	1100	50	37.2	158 (70)	50	5-7	15.8	> 932 (> 500)	5
8-2	1100	1100	45.5	33.8	158 (70)	50	5-7	15.8	> 932 (> 500)	5
9-3	1100	1100	50	37.2	158 (70)	50	5-7	5.8	> 932 (> 500)	5
10-1	1100	1100	45.5	33.8	158 (70)	50	5-7	5.8	> 932 (> 500)	5
11-4	1100	1100	50	37.2	248 (120)	50	5-7	10.0	> 932 (> 500)	5
12-4	1100	1100	50	37.2	275 (135)	50	5-7	10.0	> 932 (> 500)	5

TABLE 2A

UAL_x FUEL CORE BLISTER DATA

Reactor	Fuel Characteristics									
Sample ID	Clad	Core	Weight Percent UAL_x	Weight Percent U	Core Temp, °F (°C)	Operating Pressure PSIG	pH	Fission Density f/cc X 10^{20}	Blister Temp, °F (°C)	Ref
FNR	6061	5214	19.1	14.2	172 (78)	9.2	5-7	15.0		
FR2 (Kalsruhe, Germany)										
13-2	1100	1100	50	37.2	302 (150)	50	5-7	10.0	> 932 (> 500)	5
14-2	1100	1100	50	37.2	302 (150)	50	5-7	19.0	> 932 (> 500)	5
15-2	1100	1100	45.5	33.8	302 (150)	50	5-7	19.0	> 932 (> 500)	5
16-2	1100	1100	50	37.2	302 (150)	50	5-7	25.9	> 932 (> 500)	5
17-2	1100	1100	45.5	33.8	302 (150)	50	5-7	25.9	> 932 (> 500)	5
18-1	1100	1100	50	37.2	302 (150)	50	5-7	21.6	> 932 (> 500)	5
19-1	1100	1100	45.5	33.8	302 (150)	50	5-7	21.6	> 932 (> 500)	5
20-2	1100	1100	45.5	33.8	302 (150)	50	5-7	21.6	> 932 (> 500)	5

TABLE 2B

U_3O_8 FUEL CORE BLISTER DATA

Reactor	Fuel Characteristics									
			Weight Percent		Core	Operating		Fission	Blister	
Sample ID	Clad	Core	U_3O_8	U	Temp, °F (°C)	Pressure PSIG	pH	Density f/cc X 10^{20}	Temp, °F (°C)	Ref
FNR	6061	5214	16.8	14.2	172 (78)	9.2	5-7	15.0		
MTR										
1	6061	X8001	----	----	239 (115)	50	5-7	2.5	716 (380)	1
2	6061	X8001	----	----	239 (115)	50	5-7	5.0	716 (380)	1
3	6061	X8001	----	----	239 (115)	50	5-7	5.0	824 (440)	1
4	6061	X8001	----	----	239 (115)	50	5-7	8.0	716 (380)	1
5	6061	X8001	----	----	239 (115)	50	5-7	8.2	824 (440)	1
6	6061	X8001	----	----	239 (115)	50	5-7	8.3	716 (380)	1
7	6061	X8001	----	----	239 (115)	50	5-7	10.5	716 (380)	1
ETR										
68-1633	6061	PB-04*	49	41.4	419 (215)	200	5-7	12.7	1022 (550)	8
68-1638	6061	PB-04	49	41.4	428 (220)	200	5-7	12.7	1022 (550)	8
68-1643	6061	PB-04	49	41.4	410 (210)	200	5-7	12.7	1022 (550)	8
68-997	6061	PB-04	49	41.4	347 (175)	200	5-7	19.7	932 (500)	8
68-1605	6061	PB-04	49	41.4	329 (165)	200	5-7	19.9	932 (500)	8
68-1607	6061	PB-04	49	41.4	338 (170)	200	5-7	19.5	932 (500)	8

* Aluminum Powder Blends

FIGURE 2

FUEL CORE BLISTER TEMPERATURES

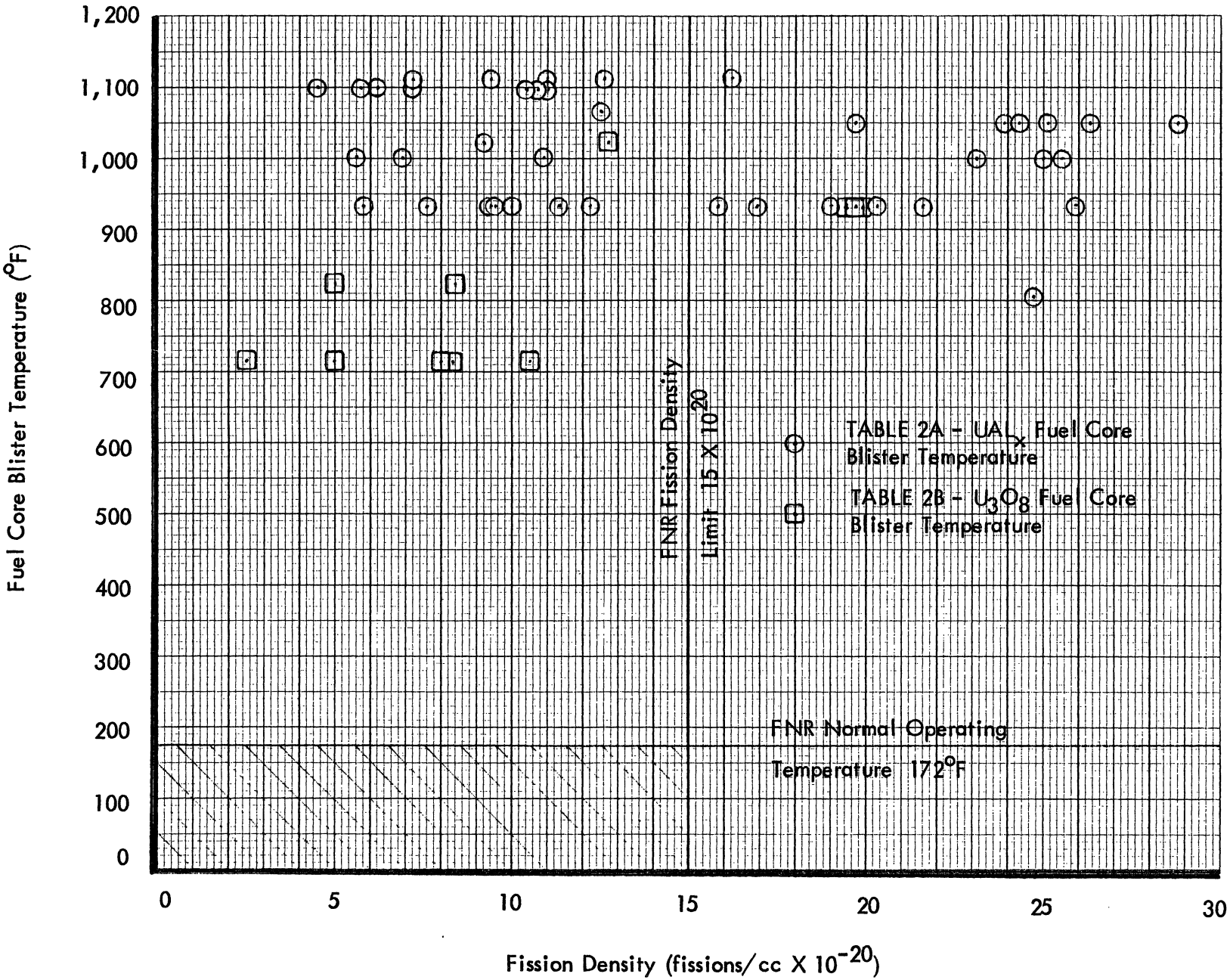

All of the available fuel blister data for UAL_x and U_3O_8 fuel which has been operated under conditions similar to those in the FNR indicate that UAL_x and U_3O_8 fuel can be safely used in the FNR without failure due to blistering and without reducing the safety margin.

6. FAILURE HISTORY

Table 3 provides a listing of reactor operating parameters for those reactors for which test data were provided in Table 1 and Table 2. Table 3 shows that the Advanced Test Reactor (ATR) routinely uses fuel with higher UAL_x loading than that proposed for FNR low enrichment uranium fuel. Similarly, the High Flux Isotope Reactor (HFIR) routinely uses fuel with U_3O_8 loadings equivalent to that proposed for the FNR.

6.1 Uranium Aluminide (UAL_x)

To date, the Advanced Test Reactor has operated over 89,000 UAL fuel plates up to the depletion limit of 2.3×10^{21} fissions/cc. In all of these fuel plates, only one (and this one was found to have thinly rolled clad) allowed fission product leakage into the ATR coolant. The plate was operated to depletion.

The thin clad was attributed to "dogboning" in the fuel core which has since been eliminated by sloping the edges of the core ingot before rolling.

6.2 Uranium Oxide (U_3O_8)

To date, the High Flux Isotope Reactor has operated over 76,000 U_3O_8 fuel plates to the depletion limit 1.9×10^{21} fissions/cc with no failures. On two occasions, fuel plates developed suspected fission product leaks. In one case, the apparent leak was so insignificant that the element was operated to depletion. In the second case, the element was removed after 1500 MWD.[9] Destructive tests showed no evidence of blisters, cladding separation, matrix cracking, or any defects indicative of incipient failure.

7. FUEL SPECIFICATIONS

7.1 Uranium Aluminide (UAL_x)

FNR fuel specifications have been developed in co-operation with the ATR staff at the Idaho National Engineering Laboratory and Atomics International (AI), the ATR fuel manufacturer. The UAL_x specification is identical to that specified by ATR. The present ATR fission density limit is 23×10^{20} fissions/cc.

TABLE 3

TRAINING, RESEARCH, AND TEST REACTOR OPERATING PARAMETERS

Parameter	Materials Testing Reactor (MTR)[1]	Engineering Test Reactor (ETR)[1]	Advanced Test Reactor (ATR)[1]	High Flux Isotope Reactor (HFIR)[9]	High Flux Beam Reactor (HFBR)[10]	Ford Nuclear Reactor (FNR)	
							Proposed
Year placed in service	1952	1956	1967	1965	1965	1958	
Thermal power (MW)	40	175	40	100	40	2	
Thermal power density (MW/l)	0.75	1.2	2.8	1.5	0.5	.025	
Fuel element meat volume (cc)	365	550	798	3475	870	354	
U-235 per element (gm)	200	400	975	2600	315	140	
U-235 burnup (%)	--	25	25	30.6	34	35	
Peak fission density (fiss/cc)	--	1.8×10^{21}	2.3×10^{21}	1.9×10^{21}	1.24×10^{21}	1.5×10^{21}	
Fuel element surface area (ft^2)	15	23	34	147	36	15	
Heat flux (BTU/ft^2-hr)	3.5×10^5	5×10^5	4×10^5	2.5×10^6	3.8×10^5	3.68×10^4	
Coolant flow rate (gpm)	24,000	44,000	16,000	17,000	16,600	980	
Fuel element materials:							
Cladding	1100 Al	1100 Al	6061 Al	6061 Al	6061 Al	5214 Al	
Core Fissile Compound (Weight %)	UAL_x 46.0	UAL_x 40.6	UAL_x 45.1-60.8	U_3O_8 25.6	U_3O_8 40.6	UAL_x 56.5	U_3O_8 49.6
Core Uranium (Weight %)	34.2	30.2	33.5-45.2	21.6	34.3	42.0	42.0

The fuel swelling and blister data in the references and tables often refer to aluminide as UAL_3. The early intermetallic fuel development work in Idaho was for the fabrication and testing of UAL_3 material and so the early designation was UAL_3. During this early fuel testing work, it was recognized that aluminide was not pure UAL_3. In 1966, UAL_3 was identified as the major crystalline component with UAL_2 and UAL_4 present.[11] Current ATR fuel powder specifications require the UAL_3 content to be at least 50%.

The FNR fuel powder specification calls for uranium aluminide powder containing at least 50% UAL_3.

7.2 Uranium Oxide (U_3O_8)

U_3O_8 fuel specifications will be developed in co-operation with Oak Ridge National Laboratory (ORNL) and Brookhaven National Laboratory (BNL) should U_3O_8 fuel be used in the FNR.

8. HEAT TRANSFER CHARACTERISTICS

The proposed LEU fuel heat transfer characteristics will be essentially identical to those of alloy fuel which has been used in the FNR core since 1957 and still comprises the majority of the fuel elements in the core. Overall element dimensions, fuel plate dimensions, and coolant flow channel width and thickness are unchanged.

Peak fuel temperature in the hottest FNR fuel plate is calculated to be 172°F. The margin of operational safety will not be changed by the use of LEU fuel.

9. CORE PHYSICS

The core physics analysis of the proposed LEU fuel reflects two basic differences from the HEU fuel currently used in the FNR core: (1) the fuel loading will be increased from 140 grams to 167.3 grams of ^{235}U per 18-plate element to compensate for increased neutron absorption in ^{238}U and spectrum hardening, and (2) the fuel meat thickness will be increased from .020 inches to .030 inches, with clad thickness decreased from .020 to .015 inches, to maintain the same total fuel plate thickness while allowing for the larger amount of ^{238}U. The proposed LEU fuel specifications are selected so that the excess reactivity of a batch fresh core configuration is the same for both the current HEU fuel and the proposed LEU fuel.

The core physics analysis includes examination of the effect of LEU fuel on core power distribution, in-core and ex-core flux distribution, cycle length and operating characteristics, core excess reactivity and shutdown margin.

9.1 Description of Calculational Methods

9.1.1 Computer Codes Used for Core Physics Analysis

All analysis was performed with the standard, well-verified production codes LEOPARD[12], EPRI-HAMMER[13], 2DB[14], ANISN[15], TWOTRAN[16], and VENTURE[17]. Brief descriptions of code capabilities are:

1) LEOPARD - a zero-dimensional unit-cell code using the MUFT/SOFOCATE scheme (54 fast and 172 thermal groups); has depletion capability; cross-section library consists of an early industrial data set.

2) EPRI-HAMMER - a one-dimensional integral transport theory code using 54 fast and 30 thermal groups; cross-section library constructed from ENDF/B-IV data.

3) 2DB - a two-dimensional multi-group diffusion theory code with depletion capability.

4) ANISN - a one-dimensional discrete ordinates transport theory code.

5) TWOTRAN-II - a two-dimensional discrete ordinates transport theory code.

6) VENTURE - a three-dimensional multi-group diffusion theory code

9.1.2 Code Modifications

The LEOPARD code originally performed a spectrum calculation for lattices consisting of cylindrical fuel rods. The code was modified

to allow slab geometry and separate few-group edits for both lattice and non-lattice regions. The principal modification was in the calculation of thermal disadvantage factors by the ABH method for slab geometry[18].

The modified LEOPARD code compares satisfactorily with the EPRI-HAMMER code, an accurate, well-verified code used in the analysis of benchmark critical experiments.[19] A typical comparison of k_∞ and two-group parameters in Table 4 shows that despite the many engineering approximations in the LEOPARD code, it compares quite well with the more accurate HAMMER code. Differences in few-group constants are due primarily to differences in the cross-section libraries - HAMMER uses ENDF/B-IV data while LEOPARD uses an early industrial data set.

The 2DB code has been modified to allow a macroscopic depletion capability via interpolation of macroscopic cross sections as a function of depletion. In addition, the isotopic balance equations for xenon and iodine have been included to allow the correct xenon levels within the core as a function of position and time (and macroscopic absorption cross sections are appropriately modified). Other modifications to 2DB have been aimed at automating data handling (e.g., the link with LEOPARD to produce macroscopic cross sections as a function of depletion) and improving fuel shuffling and edit capabilities.

9.1.3 Basic Calculation Method

The LEOPARD and 2DB codes were used for routine calculations of core reactivity, depletion effects, and power and flux distributions. Special methods for control rods and core leakage flux are described in subsequent sections. For both HEU and the proposed LEU fuel, the following scheme was followed:

1) The LEOPARD code was used to generate few-group cross sections. For most applications, two energy groups (fast and thermal) were used, although four energy groups were chosen for several detailed calculations.

   The geometry chosen was a unit cell in slab geometry consisting of a lattice region and a non-lattice or extra region. The lattice region was composed of fuel meat, clad and water channel. For regular assemblies, the extra region consisted of the side plates, non-active portions of fuel plates, and inter-assembly water gaps, which were homogenized on a volume basis. For special* fuel assemblies, the central water hole was also included in the extra region.

   Few-group macroscopic cross-section sets were generated as functions of depletion for the lattice and non-lattice regions and the total assembly.

   For the water reflector and heavy water tank, the extra region was chosen as H_2O or D_2O with a .25% H_2O content with a volume fraction

*Special is used in this section to designate control assemblies.

Table 4. Comparison of LEOPARD and HAMMER Results for MTR-type Fuel

	93% Alloy		19.5% UAl_x	
	LEOPARD	HAMMER	LEOPARD	HAMMER
k_∞	1.5477	1.5500	1.5150	1.5116
ϕ_1/ϕ_2	2.41	2.40	2.76	2.75
Age	51.5	49.9	49.1	47.5
D_1	1.434	1.372	1.424	1.360
Σ_{a1}	0.00204	0.00182	0.00358	0.00344
Σ_{r1}	0.0258	0.0257	0.0254	0.0253
$\nu\Sigma_{f1}$	0.00206	0.00223	0.00256	0.00274
D_2	0.284	0.272	0.280	0.269
Σ_{a2}	0.0597	0.0594	0.0676	0.0668
$\nu\Sigma_{f2}$	0.0948	0.0935	0.110	0.108

arbitrarily set equal to that of the lattice region. The extra region few-group cross sections obtained in this manner were used for the reflector and heavy water tank in the subsequent global calculation.

2) Global diffusion theory calculations were performed with the 2DB code. Three spatial mesh descriptions were used in x-y geometry: a homogeneous description, with a 2x2 mesh per assembly, was used for survey calculations, equilibrium core studies, and cycle length studies. A discrete representation, using a 6x6 mesh per assembly with the lattice and non-lattice portions of an assembly explicitly represented, was used for detailed analysis of power and flux distributions, temperature coefficient, and control rod reactivity worth. A discrete representation with a 12x12 mesh per assembly was used for verifying the adequacy of the 2x2 and 6x6 representations, and for comparison with the measured flux distributions.

   Depletion was accounted for on the assembly level by interpolating macroscopic cross sections as a function of depletion (MWD/MT) for the particular assembly in question. The fuel shuffling capability in the 2DB code allowed actual FNR operation to be simulated. The axial buckling term for the 2DB code used to approximate transverse leakage was based on the active core height with a reflector savings correction.

9.1.4 Control Rod Worth Calculations

FNR control (shim) rods are boron stainless steel containing 1.5 w/o natural boron. They are essentially black to thermal neutrons and cause a drastic thermal flux depression when inserted. The presence of such strong localized absorbers necessitates the use of transport theory codes to adequately describe the large flux gradients. However, in a small high leakage core like the FNR, control rod effects are not strictly local; therefore whole core calculations are needed, but are prohibitively expensive for transport theory codes. To accurately treat both local and global effects, transport theory codes were used for assembly level calculations to develop effective diffusion theory constants for global calculations. The method developed is a variation of the "NGD blackness method"[20] and has proved quite accurate.

Few-group constants for the control rod and surrounding water were obtained from the EPRI-HAMMER code for a cylindricized special assembly. Due to the strong spectral/spatial coupling in the rod it was necessary to obtain few-group cross sections for three control rod regions - a surface layer .1 cm thick, a second layer .3 cm thick, and the central region. Since few thermal neutrons reach the central region, the control rod perimeter, rather than volume, was preserved in the

geometric representation. Few-group constants for the special element lattice and side regions were obtained from the EPRI-HAMMER calculations for one half of a special element in slab geometry.

To accurately model the local effects of an inserted rod, the two-dimensional transport code TWOTRAN was used in fine-mesh calculations for a special assembly surrounded on all sides by one half of a regular assembly. Three regions of the rod and the surrounding water were explicitly represented, while the surrounding lattice regions were homogenized.

To develop effective few-group diffusion theory constants for use in global 2DB calculations, the 2DB code was used for the same geometry as in TWOTRAN calculations, except that the control rod and surrounding water were homogenized. Both fast and thermal absorption cross sections were varied until the 2DB calculation yielded the same relative absorption in the control region as the TWOTRAN result in each group. The resulting few-group constants for the control region were then used in global 2DB calculations. Although the flux distribution within the control region differs from the transport theory results, we believe the relative absorption in the control region and the flux in the surrounding fuel is accurately predicted in this scheme.

Control rod worth was then determined by comparing global 2DB calculations for the 6x6 mesh/assembly description with and without control rod inserted.

9.1.5 Calculational Methods for Temperature Coefficient of Reactivity and Xenon Reactivity Worth

Calculation of the temperature coefficient of reactivity and of reactivity worth of xenon poisoning was performed with global 2DB calculations with a 6x6 mesh/assembly description. The two-group cross sections for these 2DB cases were obtained from unit-cell calculations with the LEOPARD or the EPRI-HAMMER code, essentially following the basic scheme outlined in Section 9.1.3.

9.1.6 Equilibrium Core Model

Although the FNR core configuration and fuel shuffling pattern are, in practice, determined by operational requirements, an equilibrium core model was developed to allow for meaningful comparison of operating characteristics for the HEU and the proposed LEU cores. Our equilibrium core model essentially simulates a typical FNR shuffling pattern. Fresh fuel assemblies are placed near the control assemblies at the core center and are moved outward as they deplete. This pattern maximizes the control rod reactivity worth. The shuffling pattern was varied until the fuel depletion per cycle at each

assembly location obtained with global 2DB calculations closely matched that of the average FNR depletion at each location. The 2DB calculations performed over many cycles led to an equilibrium core model which, although not unique, is a realistic representation of the typical FNR operating cycle.

9.1.7 Ex-core Calculations

The ANISN and 2DB codes were used to calculate flux distributions in the H_2O and D_2O reflectors. Cross sections for the ANISN calculation were taken from the 100 group DLC-2 library and collapsed (with ANISN) to few groups. For 2DB calculations cross sections were generated by the LEOPARD code as explained in Section 9.1.3.

9.2 Comparison of Calculated and Experimental Results

The adequacy of the methods used for calculating core physics parameters for FNR core configurations has been established through comparing the calculated results with the data from several research and test reactors. In these verification efforts the calculated thermal flux and power distributions were compared with the experimental data obtained at the Bulk Shielding Reactor (BSR)[21], the High Flux Beam Reactor (HFBR)[22], and the FNR. The data for the BSR and HFBR cores were obtained at core configurations with MTR-type fuel elements similar to the FNR configurations.

9.2.1 Flux and Power Distributions

The measured thermal flux distributions and the core multiplication constants for the BSR loading 33 provide well documented experimental data[21] for a fresh critical core. The neutron flux distribution for this core was determined with x-y 2DB calculations utilizing a 6x6 and a 12x12 mesh per fuel assembly. Table 5 compares calculated and experimental results for the BSR and representative FNR configurations. Here the high neutron leakage causes the effective multiplication factor of the reactor to be sensitive to the input buckling value used to represent the leakage in the missing transverse direction. These calculations used an axial buckling of 2×10^{-3} cm^{-2}, which includes a calculated reflector savings.

Calculated results have been compared with the experimental data for a number of FNR core configurations. The assembly average power distribution in the Cycle 67 core was measured on March 17, 1971, with the core loading pattern presented in Figure 3. The power distribution was measured by thermocouples, with the coolant inlet temperature for each element measured inside the fuel element boxes and above the fuel plates, and the outlet temperature measured below the fuel plates in the element cone. From the assembly inlet

Case	Mesh/Group Structure	Core Reactivity		RMS Deviation[1] (thermal flux or assembly power)
		Measured	Calculated	
A (BSR #33)	6x6/2 group	1.006	1.009	11.3%[3]
	6x6/4 group	1.006	1.004	10.1%[3]
	12x12/2 group	1.006	1.012	7.8%[3]
B (FNR #67)	6x6/2 group	1.001	1.007[2]	9.3%[4]
C (FNR 1977 critical)	2x2/2 group	1.000	1.000[2]	---
	6x6/2 group	1.000	1.000[2]	---

Notes

1. RMS deviation = $\sqrt{\frac{1}{N-1}\sum_i \left(\frac{calc-exp}{exp}\right)_i^2}$

2. Corrected for measured xenon worth

3. Thermal flux deviation at 17 locations

4. Assembly power fraction deviation at 42 locations

Table 5. Experimental and Calculated Results for Several Reactor Configurations.

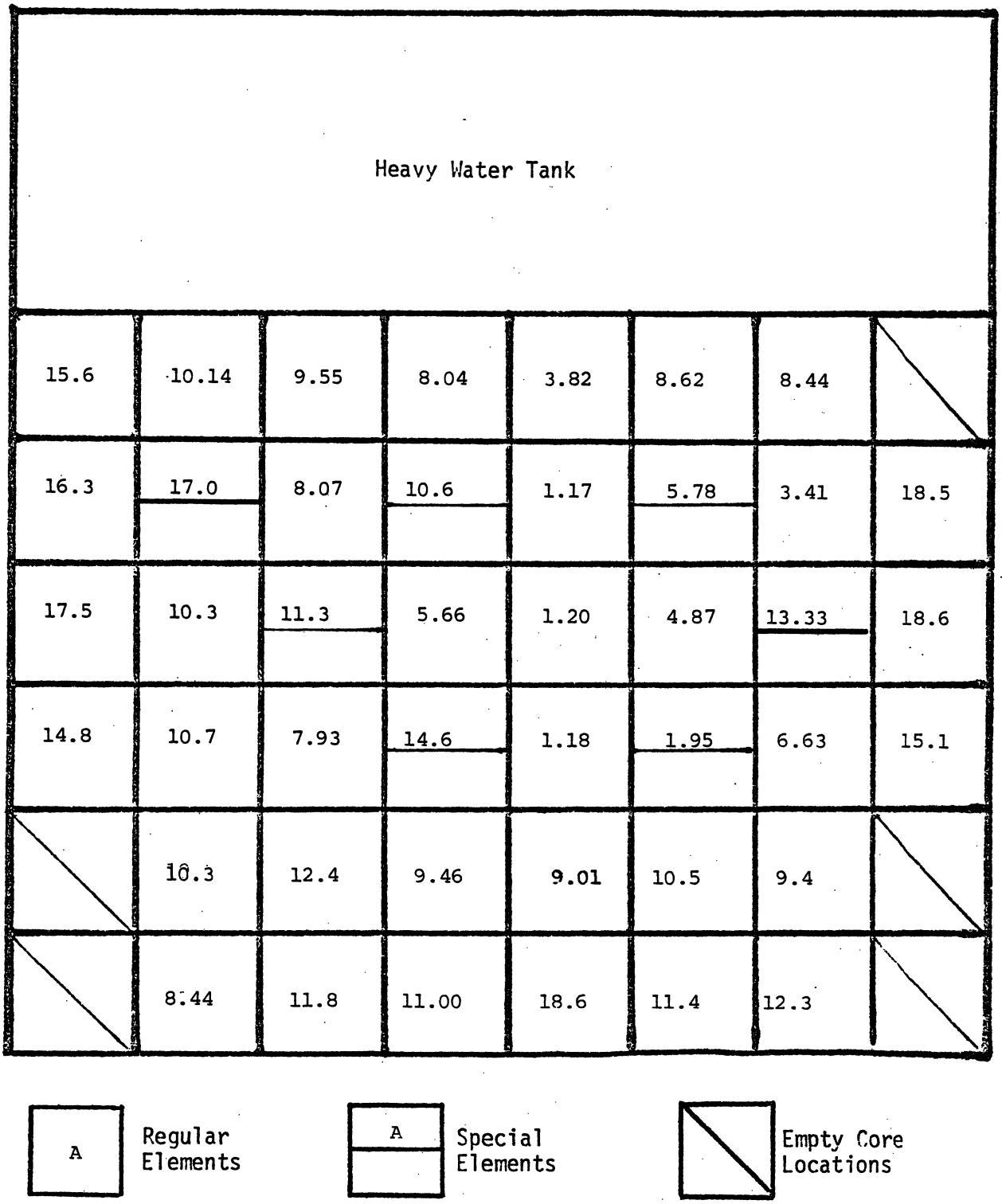

A: Assembly Burnup (MWD/assembly)

Figure 3. Fuel Burnup Distribution for FNR Cycle 67

and outlet temperatures, the power for each regular fuel element was calculated assuming equal coolant flow rate through each element. The assembly-average power distribution calculated by the 2DB code and the measured power distribution for the Cycle 67 core are presented in Figure 4. In this calculation the 2DB code predicted the core power distribution to within an rms deviation of 9.3%, as shown in Table 5

The thermal flux distribution in the FNR Cycle 163B core was determined through flux maps obtained with a self-powered rhodium detector. The measurements were taken at the horizontal midplane of the core at the center of each regular fuel element. The core configuration for this cycle is shown in Figure 5, and a comparison of the calculated and measured thermal flux distributions is given in Figure 6. The calculated flux distribution shows good agreement with the measured distribution, with an rms deviation of 5.1%. Comparisons made for other fuel cycles show similar agreement between the measured and calculated results, with rms deviations in the range of 5 ~ 8%.

9.2.2 Ex-core Flux Distributions

Initial calculations to predict leakage neutron flux in the FNR D_2O tank concentrated on determining the accuracy of diffusion theory vs. transport theory calculations and on identifying critical parameters. Transport theory calculations performed in one-dimensional slab geometry with the ANISN code[15], and diffusion theory calculations performed with one- and two-dimensional codes were compared with experimental measurements for the FNR, BSR, and HFBR. The results indicate that because of the large thermal diffusion length in D_2O, diffusion theory can accurately predict the thermal flux distribution for considerable distances into heavy water. The calculations for D_2O reflectors were sensitive to the transverse buckling due to the small D_2O macroscopic absorption cross-section. In a 2DB model of the HFBR with R-Z geometry, diffusion theory accurately simulated the thermal flux profile[22] at distances of .6-.8 meters into the D_2O reflector.

9.2.3 Control Rod Reactivity Worth

Control rod reactivity worth calculations were performed for the A, B, and C shim rods for FNR Cycle 67. The method for obtaining the rod worths was identical to that discussed in Sec. 9.1.4 except that the depletion of the fuel in the special fuel elements had to be accounted for. Accordingly, isotopic number densities for each of the special fuel element lattice regions were taken from a LEOPARD depletion calculation for a special element at the corresponding burnup points. These number densities were then used in place of BOL number densities, and the sequence of HAMMER calculations described in Sec. 9.1.4 was repeated. Full-core 6x6 2DB calculations were then

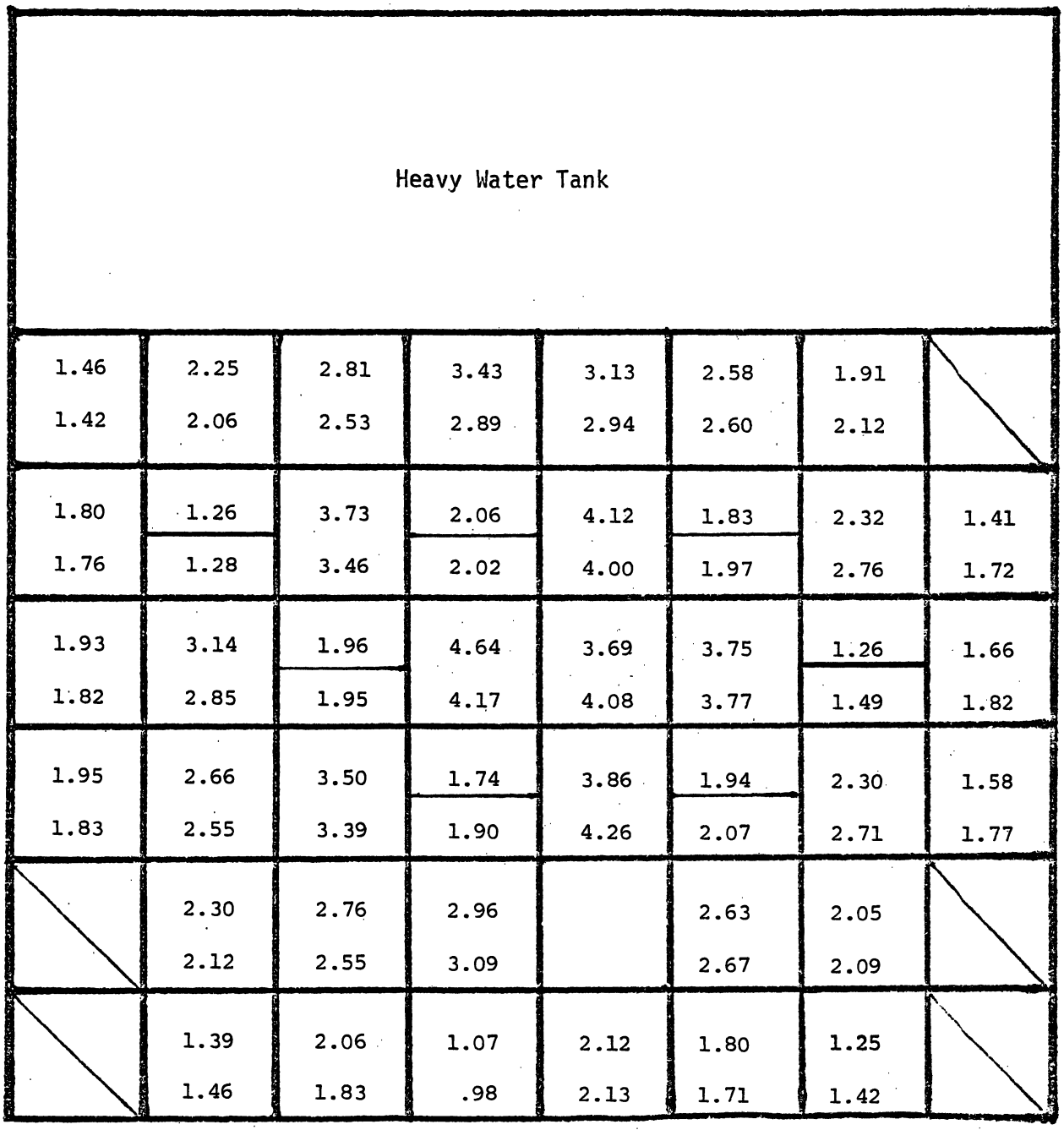

Figure 4. Experimental and Calculated Power Distributions for FNR Cycle 67

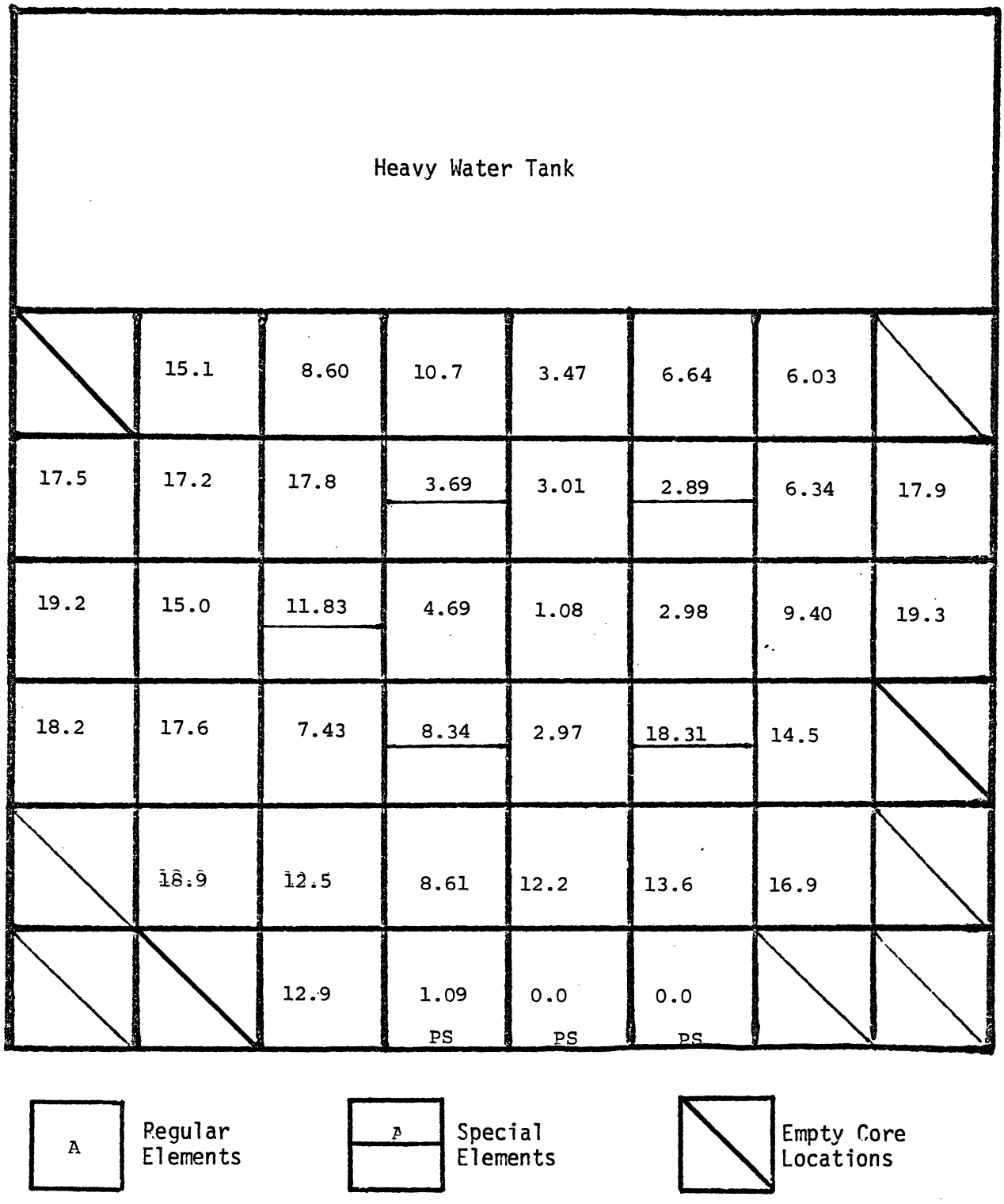

A: Assembly Burnup (MWD/assembly)
PS: Designates Penn State Fuel Elements

Figure 5. Fuel Burnup Distribution for FNR Cycle 163B

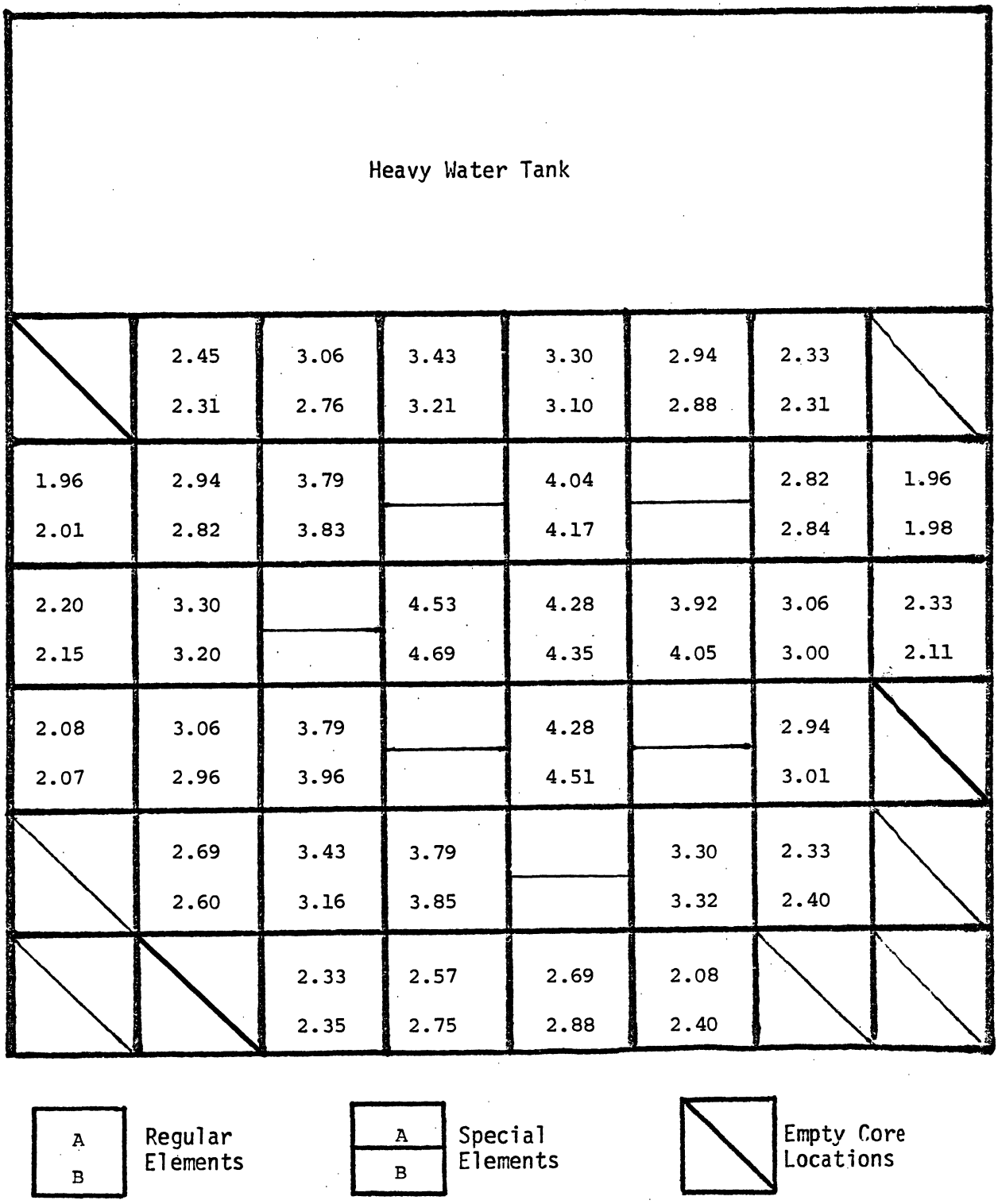

Figure 6. Experimental and Calculated Thermal Flux Distributions for FNR Cycle 163B

performed with all rods out and then separate runs were made with each of the three rods inserted. The calculated and measured rod worths compared as follows:

	Rod worth (% Δk/k)	
Shim rod	Measured	Calculated
A	2.22	2.20
B	2.11	2.11
C	1.72	1.73
Total rod worth	6.05	6.04

The agreement is excellent and provides verification of the methods for computing control rod worth in small, high-leakage cores. While there still exist some uncertainties in the actual measured rod worth, the close agreement indicates that the basic approach is valid.

9.3 Comparison of HEU and Proposed LEU Fueled Cores

To provide a meaningful and comprehensive comparison of HEU and proposed LEU fuels, it is necessary to account for both the intrinsic fuel properties and the FNR operating conditions. For the purpose of comparing core phyiscs parameters, two core configurations were analyzed for both fuels. The first configuration corresponds to a batch core consisting of fresh fuel assemblies, while the second configuration is based on an equilibrium core. The batch core configuration allows a comparison of undepleted HEU and LEU fuels, while the equilibrium core allows comparison of depletion characteristics and shutdown margin for conditions approximating typical FNR operation.

The following sections include a description of the model core configurations and a comparison of core physics parameters.

9.3.1 Description of Batch and Equilibrium Core Models

The batch core model consists of 31 fresh fuel assemblies, with four special assemblies at control rod locations. The configuration is symmetric about the north/south midplane and was analyzed using half-core calculations with a 6x6 mesh/assembly. Figure 7 illustrates this configuration.

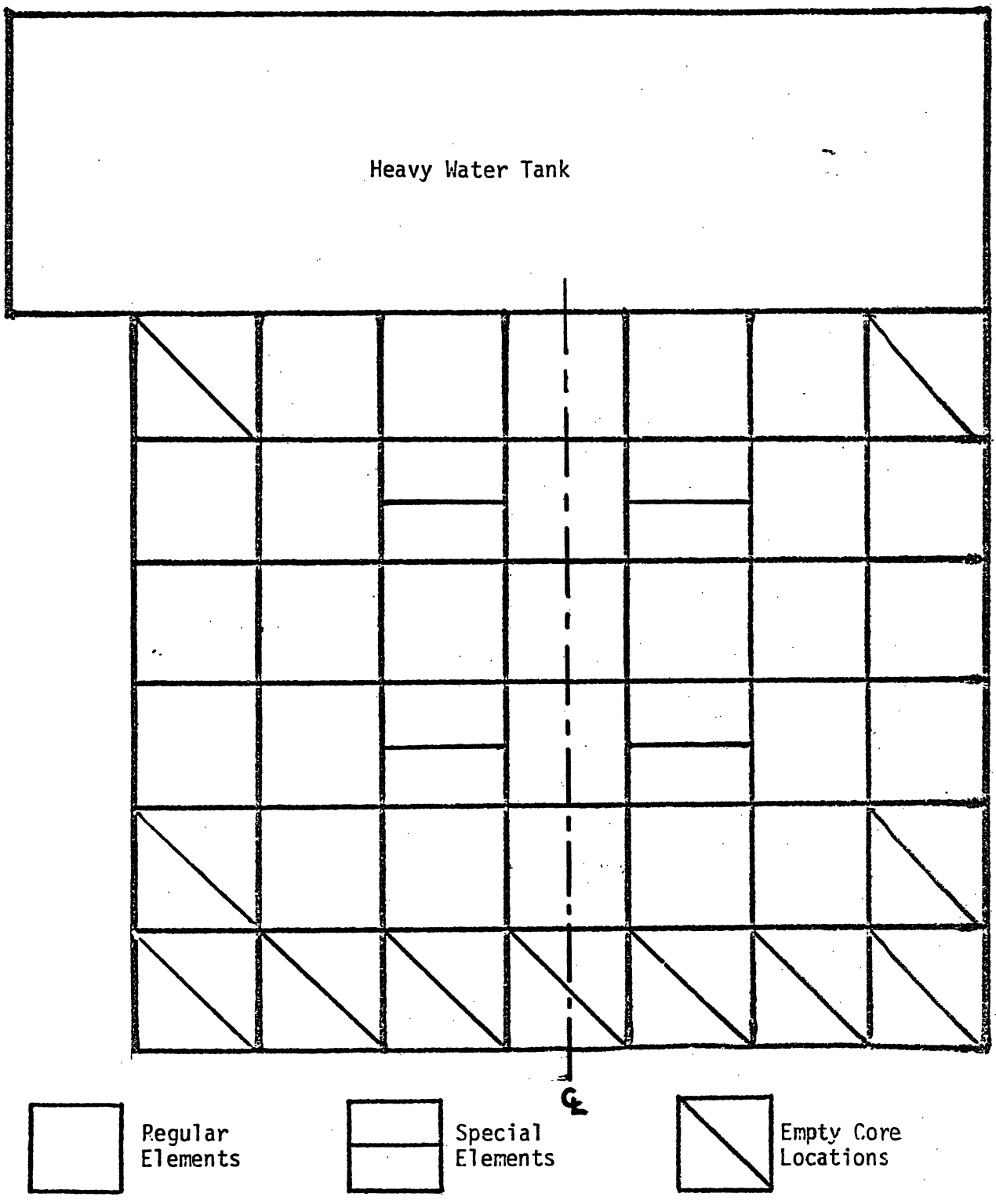

Figure 7. Batch Core Configuration

The equilibrium core configuration shown in Figure 8 essentially simulates a typical FNR shuffling pattern, and is chosen so that the core loading and shuffling patterns repeat every sixth cycle. The core configuration consists of 39 fuel elements including six special fuel elements. The important criteria for choosing the core loading pattern are:

1. Fresh fuel elements are loaded into the central region of the core. This maximizes control rod worth and helps maintain the required shutdown margin. The fuel elements are moved outward in an in/out shuffling scheme as they deplete.

2. The fuel elements are loaded so as to equalize the worths of the three shim rods. Because the B and C Rods tend to be less reactive, the reactivity worth of these shim rods is increased by loading relatively fresh fuel into the vicinity of B and C Rods. In contrast, more depleted fuel is loaded near the A Rod.

With these core loading criteria, an equilibrium core burnup distribution is obtained with 2DB calculations, which repeats cyclically over a given time period. The fuel element shuffling pattern for the equilibrium core divides the 33 regular fuel element locations into eight loading zones as shown in Figure 8. Each regular element loading zone corresponds to core locations having nearly equal fuel burnup, although not necessarily equal burnup rates. New fuel is loaded into Zone 1 and depleted fuel is discharged from Zone 8. At the start of each cycle, one new element is loaded into Zone 1, and the element in Zone 1 is moved to Zone 2. Another element is moved from Zone 2 to 3, and continuing to Zone 8, with a depleted element being discharged from Zone 8. Because the core loading zones have a maximum of six elements, the core burnup distribution repeats every sixth cycle. The eight-zone shuffling pattern for the regular elements is shown in Table 6.

The shuffling pattern for the special fuel elements is somewhat different since there are six special element locations. A new special element is added and a depleted element is discharged only every sixth cycle. With this shuffling pattern a new special element is placed in Special-Zone 1 at the start of cycle 1. The element removed from Special-Zone 1 is placed in ex-core storage for one cycle and then placed in Special-Zone 2 at the start of cycle 2. The element from Special-Zone 2 is moved to storage before being placed into Special-Zone 3 at the start of cycle 3. The sequence continues until the start of cycle 6 when the element from storage is placed into Special-Zone 6 and a depleted special element is discharged from the core. This shuffling pattern for special elements is shown in Table 7 .

While the reactivity decrease and core power distribution are nearly constant over each equilibrium cycle, the burnup distribution will repeat only every sixth cycle or over one macro-cycle. Any core para-

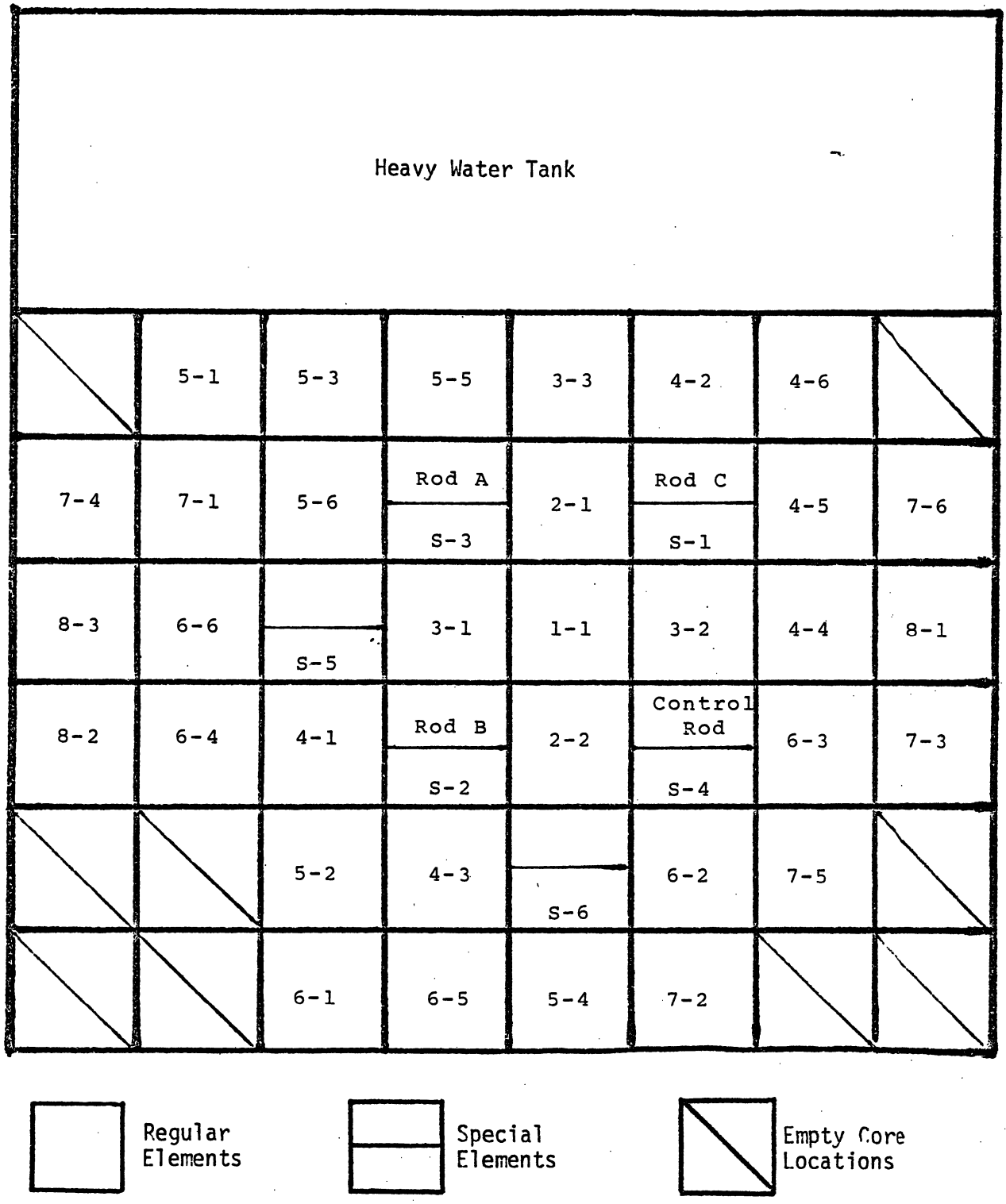

Figure 8. Equilibrium Core Loading Pattern

Table 6
Regular Fuel Element Shuffling Scheme

Equilibrium Core Configuration
with 6 Cycles/Macro-cycle

Cycle		Core Loading Zone 1	2	3	4	5	6	7	8	
	New Fuel									
1	→	1-1	→ 2-1	→ 3-1	→ 4-1	→ 5-1	→ 6-1	→ 7-1	→ 8-1	→
2	→	1-1	→ 2-2	→ 3-2	→ 4-2	→ 5-2	→ 6-2	→ 7-2	→ 8-2	→
3	→	1-1	→ 2-1	→ 3-3	→ 4-3	→ 5-3	→ 6-3	→ 7-3	→ 8-3	→
4	→	1-1	→ 2-2	→ 3-1	→ 4-4	→ 5-4	→ 6-4	→ 7-4	→ 8-1	→
5	→	1-1	→ 2-1	→ 3-2	→ 4-5	→ 5-5	→ 6-5	→ 7-5	→ 8-2	→
6	→	1-1	→ 2-2	→ 3-3	→ 4-6	→ 5-6	→ 6-6	→ 7-6	→ 8-3	→
										↓
										Discharge

Table 7

Special Fuel Element Shuffling Scheme

Equilibrium Core Configuration
with 6 Cycles/Macro-cycle

Cycle	Storage		Core Loading Zone		Storage
1	New fuel	→	S-1	→	X_1
2	X_1	→	S-2	→	X_2
3	X_2	→	S-3	→	X_3
4	X_3	→	S-4	→	X_4
5	X_4	→	S-5	→	X_5
6	X_5	→	S-6	→	Discharge

meter will be exactly the same at a given time into any macro-cycle.

To verify the practicability of the equilibrium cycle, Table 8 presents a comparison of the calculated equilibrium core parameters and actual core parameters based on the FNR operating experience during the past year. These comparisons indicate that the proposed equilibrium cycle represents a reasonably practical configuration, which may be used to compare the characteristics of the LEU and HEU designs for typical FNR operating conditions.

9.3.2 Comparison of Core Physics Parameters for HEU and Proposed LEU Fueled Cores

The major physics parameters which have been analyzed include the power defect of reactivity, xenon reactivity worth, control (shim) rod reactivity worth, cycle length, and shutdown margin. Differences in these parameters, as computed for the two model core configurations should provide a reasonable estimate of any effects of LEU fuel on FNR safety margins. These differences are compared for several equilibrium cores with differing cycle length and the batch core.

9.3.2.1 Temperature Coefficient of Reactivity and Power Defect Comparison

The isothermal temperature coefficient of reactivity was computed for the batch core model to be -8.4 pcm/°F for the HEU fuel and -12.6 pcm/°F for the LEU fuel. The large increase is due almost exclusively to fuel Doppler effects. For the HEU fuel, fuel Doppler effects are negligible due to the small amount of ^{238}U present. For the LEU fuel, the large amount of ^{238}U increases resonance absorptions in ^{238}U, resulting in much larger sensitivity to fuel temperature. The principal contribution to temperature coefficient of reactivity for both the HEU and LEU configurations is the effect of the reduction in moderator density on leakage and moderation.

The power defect of reactivity represents the total of all reactivity effects induced by taking the reactor from a cold zero-power condition to normal operating conditions. Due to the spatially nonuniform temperature and density changes involved, the power defect cannot be predicted solely on the basis of an isothermal temperature coefficient. Since the increased fuel Doppler effect is, however, the principal difference in the temperature effects between the HEU and the LEU designs, the change in power defect of reactivity is estimated in the present analysis on the basis of calculated temperature coefficients. Based on an average core temperature rise of 7°F, the power defect for the LEU fuel is estimated to be about .03% $\Delta k/k$ larger in magnitude than for HEU fuel. For a typical FNR configuration, the excess reactivity required to overcome the power defect would thus change from a measured value of .21% $\Delta k/k$ for HEU to .24% $\Delta k/k$ for LEU.

Table 8

Comparison of the Equilibrium Core Parameters with the Actual FNR Parameters

	Equilibrium Core 93% Enrichment	FNR Experience (Oct. 78 - Sept. 79)
Average cycle length (days)	11	8.17*
Average reactivity swing between shuffles (% $\Delta k/k$)	-0.31	-0.40
Average number of shuffles/day	0.82	0.81
Average discharge burnup (%)		
Regular elements	17	17
Special elements	29	34
Calculated k_{eff}		
Range	1.022 ~ 1.026	1.020 ~ 1.032
Average	1.024	1.025
Control Rod Worth (% $\Delta k/k$)	(at beginning of cycle)	(at beginning of Cycle 67)
Shim Rod A	2.21	2.22
Shim Rod B	2.20	2.11
Shim Rod C	2.00	1.72
Total	6.41	6.05

*Includes periods of operation at 1MW power.

9.3.2.2 Xenon Reactivity Worth Comparison

The xenon reactivity worths for the LEU and HEU equilibrium core configurations are compared in Table 9 and in Table 10 for the batch cores. For the cases considered the xenon worth is slightly lower for the LEU than the HEU fuel. There are two competing effects responsible for this decrease: First, the larger ^{235}U loading for the LEU core results in lower in-core thermal flux levels, with a greater (10-12%) xenon concentration. Second, the increased ^{235}U loading gives the LEU core a larger neutron absorption cross-section. As total core absorption is increased, the fractional absorption in xenon, and thus the xenon reactivity worth, is decreased. Although these two effects tend to cancel one another, the latter effect dominates and xenon reactivity worth is lowered by about .1% $\Delta k/k$.

9.3.2.3 Control Rod Reactivity Worth Comparison

A comparison of the reactivity worths for shim rods A, B, and C is given in Table 9 for equilibrium cores and in Table 10 for batch cores. As expected, the rod worth is lower for the LEU cores. The greatest loss in total rod worth, .33% $\Delta k/k$, is seen for a batch core comparison. For the equilibrium cores, comparing the HEU regular cycle with the LEU cycle corresponding to an equal reactivity change shows a decrease of total rod worth of only .08% $\Delta k/k$, indicating that larger core-average burnup in the LEU core can mitigate the decrease in rod worth for the LEU core.

The decrease in rod worth is an expected result of the increased ^{235}U loading required for LEU fuel. When the loading of the principal core absorber (^{235}U) is increased, the control rods become less effective in competing with fuel for neutron absorption and the rod worth is decreased. Accordingly, fuel depletion should increase control rod effectiveness. This prediction is borne out by the equilibrium core calculations displayed in Table 9 and suggests that a longer LEU cycle could provide a means for increasing both control rod reactivity worth and shutdown margin.

9.3.2.4 Comparison of Depletion Characteristics

Depletion effects on reactivity for several equilibrium-core cycle lengths are presented in Table 9. Comparing the 11-day cycle for HEU and LEU cores shows that for equal cycle lengths, the rate of reactivity loss due to fuel burnup is 25% ~30% lower for the LEU core. This is primarily a direct consequence of the increased ^{235}U loading - for a given absolute loss of fuel mass, the fractional depletion and thus reactivity loss are decreased for higher fuel loading. In addition there is a secondary contribution due to the build-up of ^{239}Pu. While the reduction in the rate of reactivity decrease seen for equal length cycles would reduce the excess reactivity requirement, the reduction in control rod worth could result in a net decrease in shutdown margin. Another consequence of the equal-length fuel cycle is that fuel element discharge burnup is reduced, thus likely increasing fuel costs.

Table 9

Core Physics Parameters for Equilibrium Core

	HEU		LEU		
	Regular	Extended	Equal Length	Equal Burnup	Equal Reactivity change
Cycle length (days)	11.0	13.0	11.0	13.0	15.0
Average discharge burnup (MWD/assembly)	19.2	22.8	18.6	21.8	25.3
Core average burnup at beginning of cycle (MWD/assembly)	10.7	12.6	10.6	12.6	14.6
Average reactivity change/cycle (% Δk/k)	- 0.31	- 0.38	- 0.23	- 0.26	- 0.32
Shim rod worth (% Δk/k)					
A Rod	2.21				2.20
B Rod	2.20				2.18
C Rod	2.00	2.06	1.82	1.86	1.95
Total	6.41				6.33
Excess reactivity required (% Δk/k)					
Xenon poisoning	2.24				2.08
Burnup effect	0.31				0.32
Power defect	0.21				0.24
Total	2.76				2.64
Shutdown margin (% Δk/k)	3.65				3.69

Table 10

Core Physics Parameters for Batch Core

	HEU	LEU
Cycle length (days)	10.0	10.0
Reactivity change per cycle (% Δk/k)	- 0.31	- 0.22
Shim rod worth (% Δk/k)		
A Rod	2.37	2.26
B Rod	2.23	2.12
C Rod	2.37	2.26
Total	6.97	6.64
Excess reactivity required (% Δk/k)		
Xenon poisoning	2.50	2.40
Burnup effect	0.31	0.22
Power defect	0.21	0.24
Total	3.02	2.86
Shutdown margin (% Δk/k)	3.95	3.78

Since control rod worth calculations predict an increase in rod worth as fuel burnup is increased, two extended length cycles were investigated for LEU fuel: The first, with a length of 13 days, is intended to match fuel burnup with the 11-day HEU cycle. The second, with a length of 15 days, is intended to yield the same reactivity change per cycle as the 11-day HEU cycle. Results obtained for the two extended LEU cycles, as well as an extended HEU cycle for comparison, are included in Table 9.

Comparison of the 15-day LEU cycle with the 11-day HEU cycle shows that the fuel element discharge burnup is increased by 30%, and the cycle length is increased by 36%, while maintaining approximately equal reactivity change/cycle. These considerations suggest that fuel utilization is expected to be better for LEU fuel and that, over a long period of time, fuel costs could be lowered. This improvement in fuel utilization can be attributed to the small fissile plutonium buildup, increased fast fission due to ^{238}U, and spectrum hardening which reduces the reactivity effects of fuel depletion.

The most important consequence, however, of the extended 15-day LEU cycle is the effect on control rod reactivity worth. The extended cycle length increases the rod worth to a value approximately equal to the regular 11-day HEU cycle.

Since the 15-day LEU cycle offers distinct advantages over the 11- or 13-day LEU cycles, it has been analyzed in detail. Succeeding comparisons of LEU and HEU equilibrium core models will therefore compare the 11-day HEU cycle with the 15-day LEU cycle.

9.3.2.5 Comparison of Shutdown Margin

The most significant safety parameter related to core physics analysis is the shutdown margin. This parameter is obtained by subtracting the positive core excess reactivity required to overcome xenon poisoning, fuel depletion, and the power defect from the total control rod reactivity worth. The present Technical Specifications require that the shutdown margin be at least 3.0% $\Delta k/k$. Any difference between the estimated shutdown margin and the limiting value represents excess reactivity available for experiments.

For the LEU batch core, it is seen from Table 10 that the lower excess reactivity requirement is overshadowed by the decrease in control rod reactivity worth. The shutdown margin of 3.78% $\Delta k/k$ is lower than for the HEU core, but is still well above the 3% $\Delta k/k$ requirement. Additionally, with the most reactive rod fully withdrawn, the shutdown margin is 1.52% $\Delta k/k$, well in excess of the .75% $\Delta k/k$ required.

Comparing the HEU and LEU equilibrium core results shown in Table 9, it is seen that for cycles having equal reactivity change, the shutdown margin for the LEU core exceeds that

for the HEU core. This rather surprising result is a consequence of the longer cycle length and a higher average fuel burnup in the LEU equilibrium core. With the HEU and LEU control rod worths nearly equalized, the relatively minor effect of lower xenon poisoning increases the shutdown margin slightly. The computed value of 3.69% $\Delta k/k$ is well in excess of the 3.0% $\Delta k/k$ requirement. Also, the shutdown margin with the most reactive control rod fully withdrawn in 1.49% $\Delta k/k$, well above the .75% $\Delta k/k$ required.

9.3.3 Comparison of Flux and Power Distributions

Calculated power distributions for both HEU and LEU cores are compared in Figures 9 and 10 for batch cores and equilibrium cores, respectively. Examination of these figures reveals only minor changes between LEU and HEU cores. The largest change in assembly power, a 3% relative increase, occurs for special element locations. Additionally, there is a small shift in the power distribution away from the heavy water tank and toward a slightly improved overall symmetry about the center. There is no evidence of changes which would require detailed thermal-hydraulic analysis; in fact, the ratio of peak to average assembly power is slightly reduced.

The calculated thermal flux distributions are compared in Figure 11 for batch cores and Figure 12 for equilibrium cores. A major difference between HEU and LEU fuel is apparent from these figures: since for a well moderated core the power is approximately proportional to the product of the macroscopic fission cross-section and thermal flux, an increased fuel loading results in a corresponding reduction in thermal flux for a given power. This effect is readily apparent in Figures 11 and 12, where the thermal flux in regular fuel elements is seen to decrease by about 14%. For special fuel elements, the reduction in thermal flux is only about 9%. This mitigation in the thermal flux decrease results from the effect of the thermal flux peaking in the large waterhole. This peak is primarily dependent on the fast flux, which is not significantly different between the LEU and HEU fuels. Since the thermal flux level within the special element will be affected by the waterhole peaking, the overall effect is to mitigate the decrease in thermal flux. As noted for the power distribution, there is a slight shift in thermal flux away from the heavy water tank toward a slightly improved overall symmetry about the center. Figures 13 and 14 display thermal flux for traverses along the north-south core center lines. It should be noted that the centerline of the equilibrium core is bordered by two special assemblies, whereas the batch core centerline is through the centers of regular assemblies. The general reduction in thermal flux is apparent in both figures, and the mitigating effects of the special assemblies are evident in the equilibrium core traverse.

Calculations of the ex-core thermal flux in the heavy water tank have indicated that the thermal leakage flux will be reduced by 6~10%. While this is an important consideration for experimental usage, it has no impact on the core safety analysis.

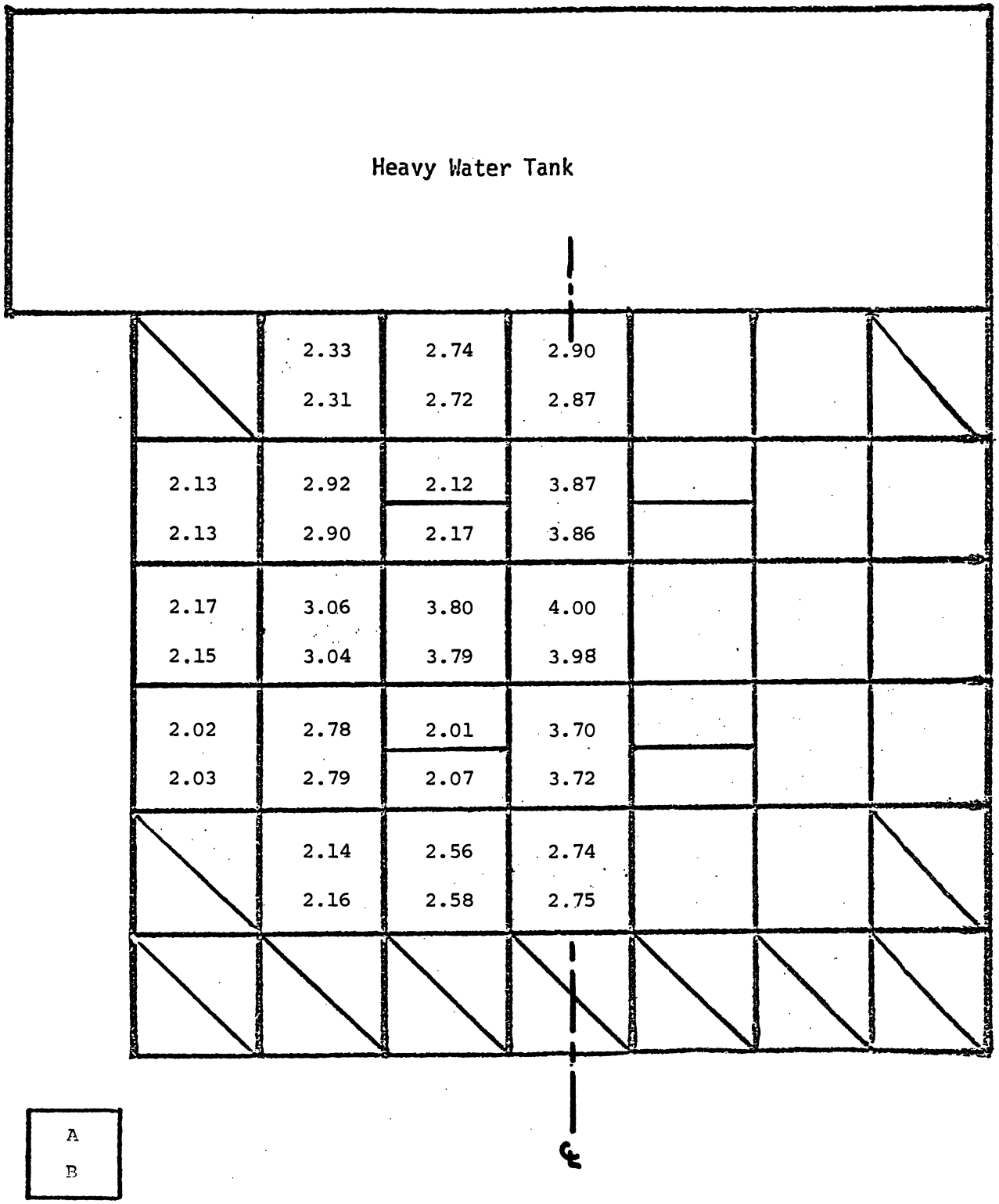

A: Assembly Power (%), HEU Core

B: Assembly Power (%), LEU Core

Figure 9. Assembly Power Distribution for Batch Core

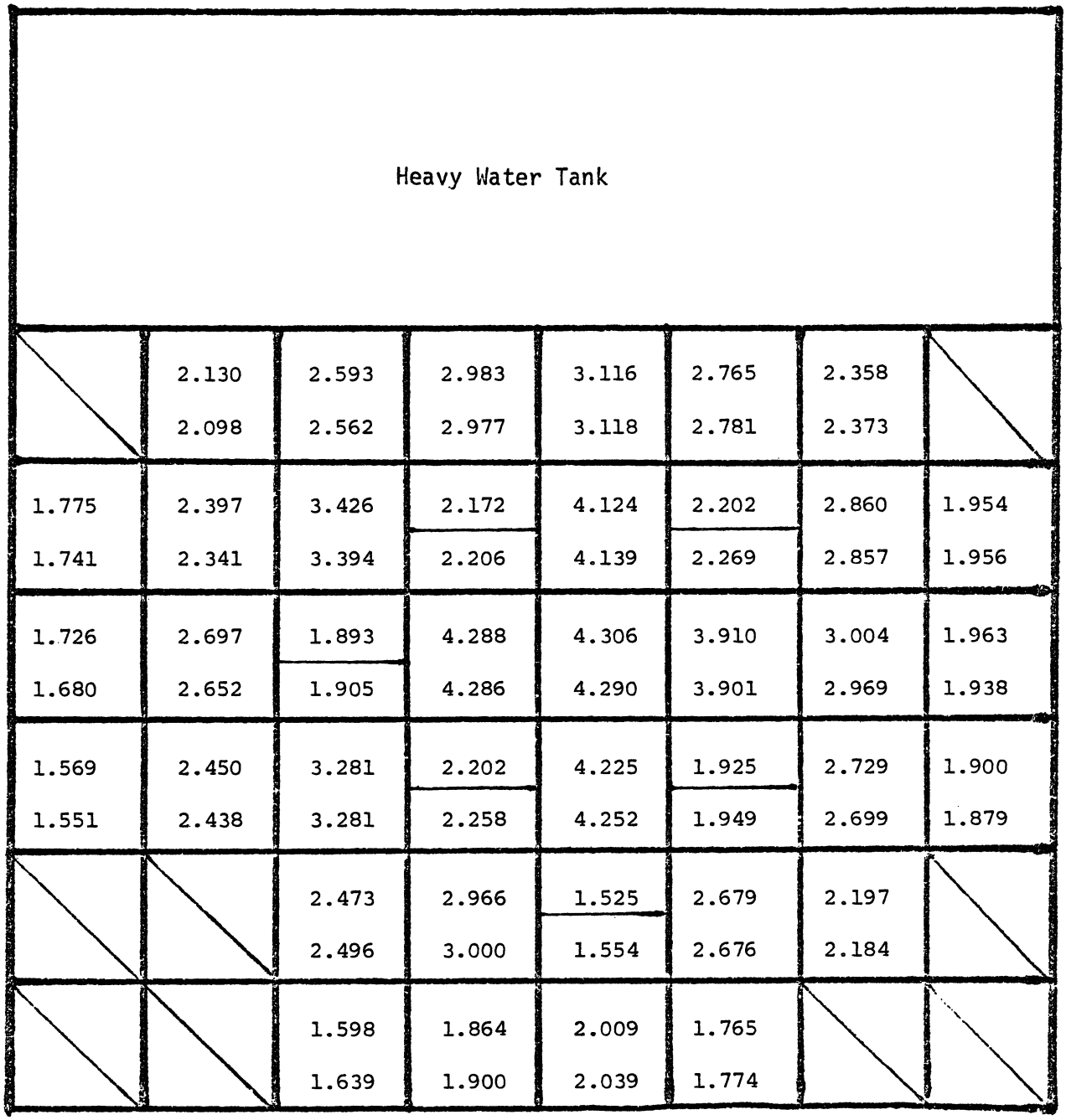

Figure 10. Assembly Power Distribution for Equlibrium Core

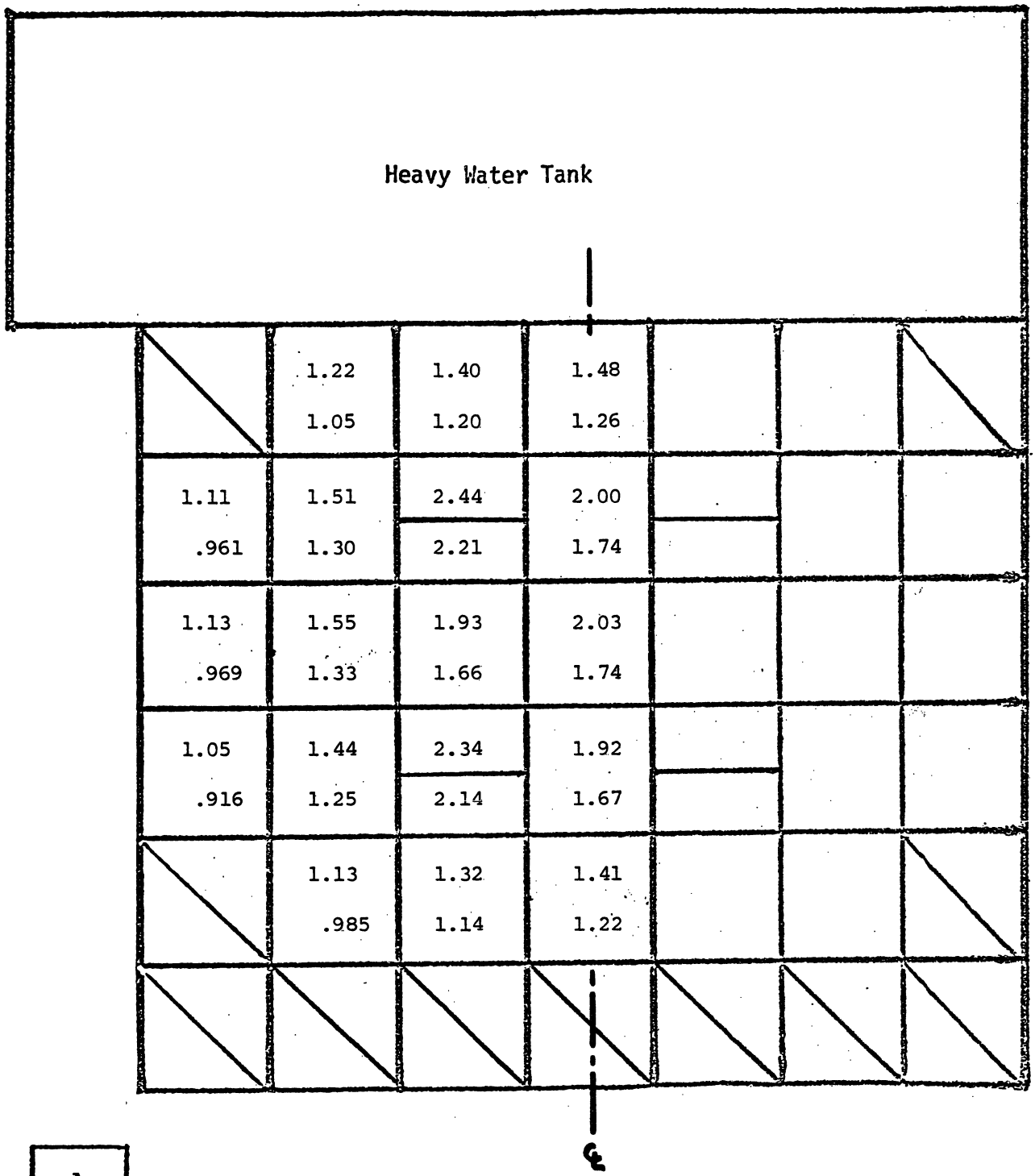

A: Assembly-Average Thermal Flux (10^{13} n/cm^2·s), HEU Core

B: Assembly-Average Thermal Flux (10^{13} n/cm^2·s), LEU Core

Figure 11. Assembly-Average Thermal Flux Distribution for Batch Core

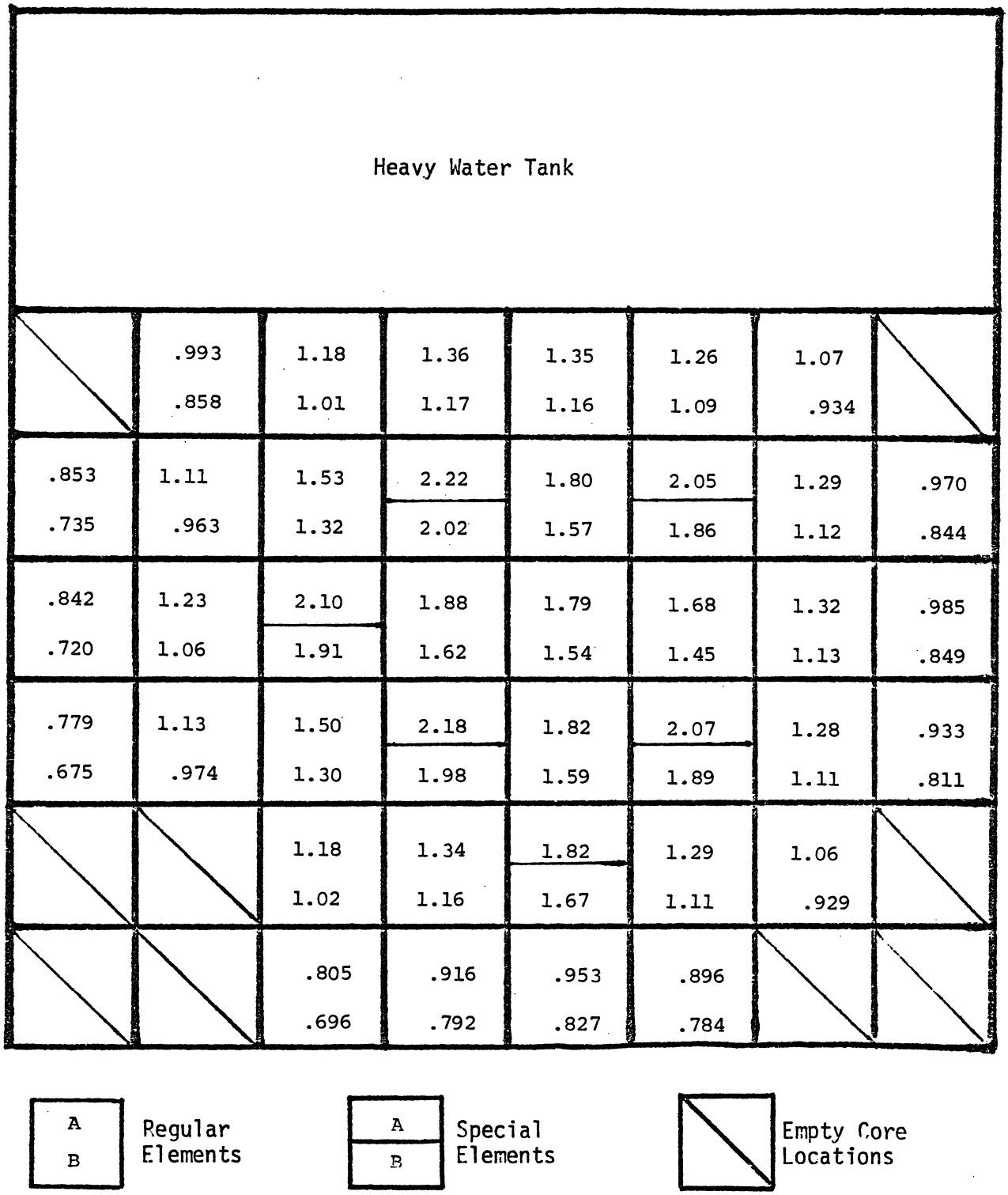

A: Assembly Average Thermal Flux (10^{13} n/cm^2·s), HEU 11-day Cycle

B: Assembly Average Thermal Flux (10^{13} n/cm^2·s), LEU 15-day Cycle

Figure 12. Assembly-Average Thermal Flux Distribution for Equilibrium Core

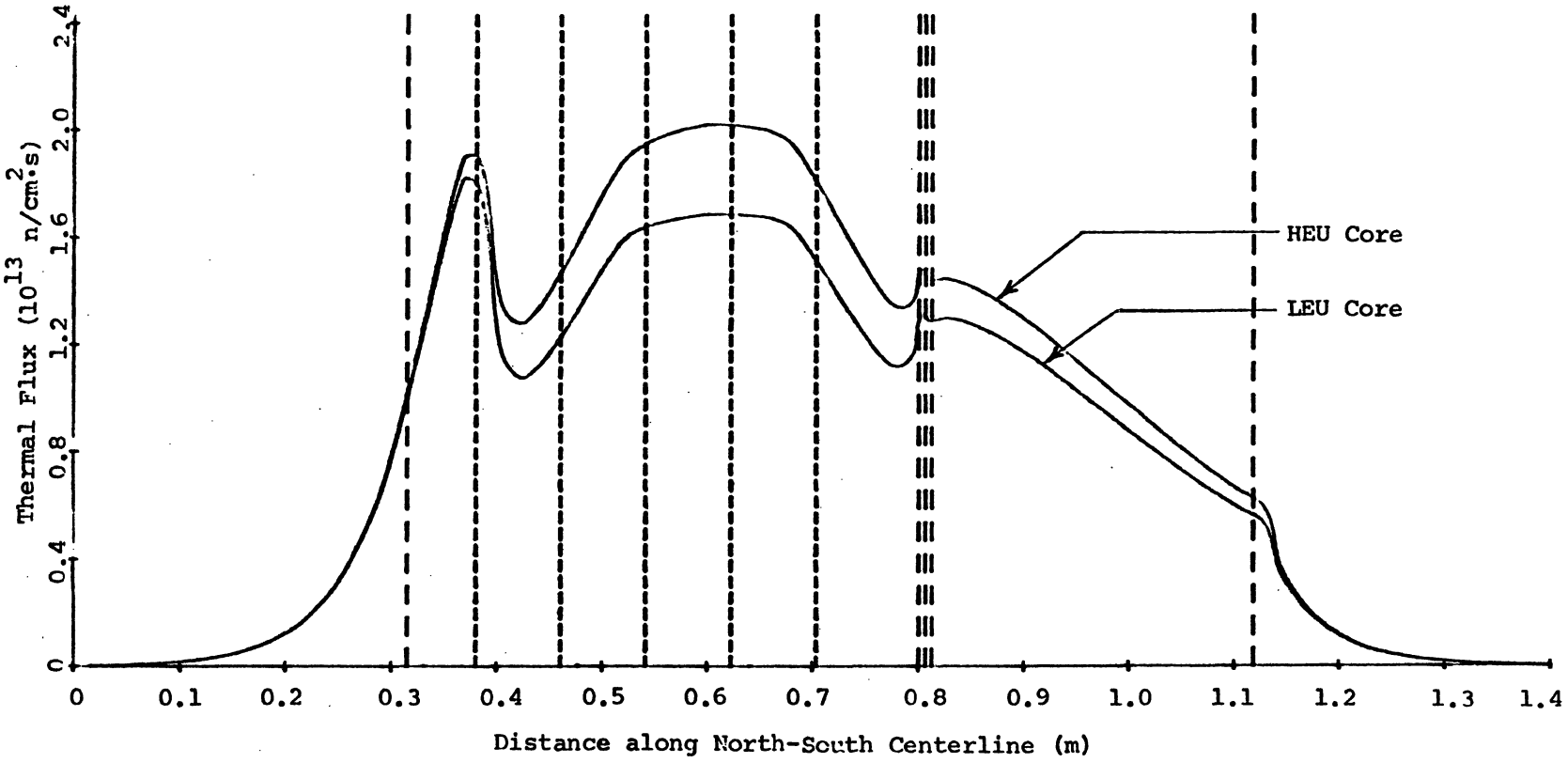

Figure 13. Thermal Flux Distribution for Batch Core

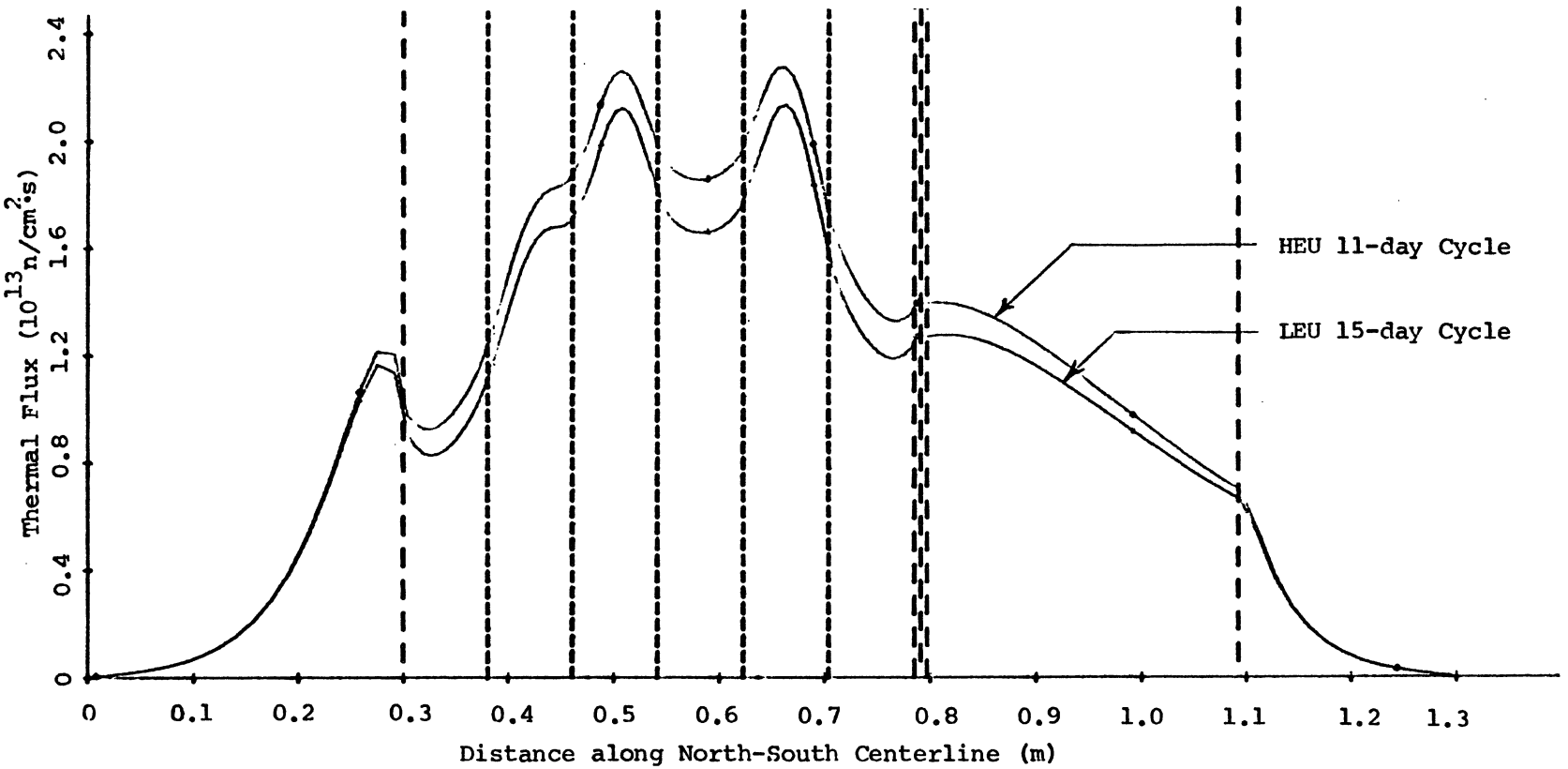

Figure 14. Thermal Flux Distribution for Equilibrium Core

9.4 Summary of the Core Physics Analysis

Extensive effort has been devoted to the development of accurate calculational methods for the analysis of HEU and LEU fueled research reactors. These methods make use of existing well-verified computer codes wherever possible and have been verified through comparison with data from several different research reactor configurations. The accuracy of the computational methods is expected to be equally valid for the prediction of changes in core physics parameters due to the use of LEU fuel. To encompass all expected effects of the proposed LEU fuel, both a batch core model and an equilibrium core model were analyzed in detail and compared with the HEU fuel. The results of these comparisons serve to quantify predictions which can be made on physical grounds: decreasing the fuel enrichment from 93 w/o to 19.5 w/o and increasing the ^{235}U loading from 140 grams to 167.3 grams per 18-plate assembly result in a large decrease in the in-core thermal flux; a small decrease in xenon poisoning; a small increase in power defect due to increased Doppler effects; longer cycle length for a given reactivity change and higher discharge fuel burnup; a reduction in control rod worth, which may be offset by longer cycle; very little change in power distribution; and, most importantly, no significant change in the core shutdown margin.

While there are significant changes in core physics parameters for the proposed LEU fuel, there appear to be no reductions in any safety margins.

REFERENCES

1. G.W. Gibson, "The Development of Powdered Uranium Aluminide Compounds for Use as Nuclear Reactor Fuels," IN-1133, TID-4500, Idaho Nuclear Corporation, December, 1967.

2. R.M. Brugger, "Metallurgy and Materials Science Branch Annual Report Fiscal Year 1970", IN-1437, Idaho Nuclear Corporation, November, 1970.

3. R.R. Hobbins, "INC-16-2 Irradiation Experiment", Idaho Operations Office, U.S. Atomic Energy Commission, July 19, 1974.

4. M.M. Martin, A.E. Richt, and W.R. Martin, "Irradiation Behavior of Aluminum Base Fuel Dispersions," ORNL-4856, Oak Ridge National Laboratory, May, 1973.

5. W. Dienst, S. Nazare, and F. Thummber, "Irradiation Behavior of UAl_x Dispersion Fuels for Thermal High Flux Reactors," Journal of Nuclear Materials, 64, 1977.

6. W.C. Francis, ANNUAL PROGRESS REPORT OF REACTOR FUELS AND MATERIALS DEVELOPMENT FOR FY 1965, USAEC Report IDO-17154, Idaho Operations Office, U.S. Atomic Energy Commission, February, 1966.

7. G.W. Gibson, M.J. Graber, V.A. Walker, and W.C. Francis, "Results of ATR Sample Fuel Plate Irradiation Experiment", IDO-16958, Idaho Operations Office, U.S. Atomic Energy Commission, March 23, 1964.

8. D.J. Rucker, "Fuels and Materials Development Program Quarterly Progress Report for Period Ending March 31, 1970", ORNL-4560, Oak Ridge National Laboratory, March, 1970.

9. "Reactor Safety Evaluation of ORNL Proposal to Modify Fuel in ORR", Oak Ridge National Laboratory, February, 1977.

10. P. Tichler, "Review of Proposed Increase in Fuel Element Loading and Fuel Burnup", Memorandum,Brookhaven National Laboratory, February, 1977.

11. V.A. Walker, M.J. Graber, and G.W. Gibson, "ATR Fuel Materials Development Irradiation Results - Part II," IDO-17157, Idaho Operations Office, U.S. Atomic Energy Commission, June, 1966.

12. R. F. Barry, "LEOPARD - A Spectrum Dependent Non-spatial Depletion Code", WCAP-3269-26, Westinghouse Electric Corporation (September 1963).

13. J. Barhen, W. Rothenstein. E. Taviv, "The HAMMER Code System", NP-565, Electric Power Research Institute (October 1978).

14. W. W. Little, Jr. and R. W. Hardie, "2DB User's Manual-Revision I", BNWL-831 REV1, Battelle Pacific Northwest Laboratory (February 1969).

15. W. W. Engle, Jr., "A User's Manual for ANISN, a One-Dimensionsl Discrete Ordinates Transport Code with Anisotropic Scattering", K-1693, Oak Ridge Gaseous Diffusion Plant (March 1967).

16. K. D. Lathrop and F. W. Brinkley, "TWOTRAN-II - An Interfaced Exportable Version of the TWOTRAN Code for Two-Dimensional Transport", Los Alamos Scientific Laboratory, LA-4848-MS (1973).

17. D. R. Vondy, T. B. Fowler, and G. W. Cunningham, "VENTURE: A Code Block for Solving Multigroup Neutronics Problems Applying the Finite-Difference Diffusion Theory Approximation to Neutron Transport", ORNL-5062 (1975).

18. M. H. Theys, "Integral Transport Theory of Thermal Utilization Factor in Infinite Slab Geometry", Nucl. Sci. Eng., 7, 58 (1960).

19. S. Jabbawy, J. Karni, W. Rothenstein, and S. Velner, "Water Moderated Reactor Analysis with ENDF/B Data", Nuclear Data in Science and Technology, Vol. II, p. 147, IAEA, Vienna (1973).

20. N. G. Demas, "Representation of Two-Dimensional Self-Shielded Poison Lumps in P-1 Calculations", WAPD-BT-21, Westinghouse Electric Corporation, pp. 29-32 (Nov. 1960).

21. E. B. Johnson, "Power Calibration for BSR Loading 33", CF-57-11-30, Oak Ridge National Laboratory (1957).

22. J. M. Hendrie, "Final Safety Analysis Report on the Brookhaven High Flux Beam Research Reactor", BNL-7661, Brookhaven National Laboratory (April 1964).

BIBLIOGRAPHY

1. G.M. Adamson, "Fabrication of Research Reactor Fuel Elements", ORNL-TM-2197, Oak Ridge National Laboratory, June 1968.

2. ALCOA ALUMINUM HANDBOOK, Aluminum Company of America, Pittsburgh, 1962.

3. HANDBOOK OF ALUMINUM, Alcan Aluminum Corporation, Cleveland, 1970.

4. D.M. Alger and C. Julian, "UAl_x Fuel in Research Reactors", Transactions of the American Nuclear Society, Chicago, June 10-14, 1973.

5. C. Allain, H. Aubert, and J. Laniesse, "Irradiation Dans Le Reacteur El 3 De Tubes En Uranium Faiblement Allie", Journal of Nuclear Materials, 31, Number 2, June 1969.

6. ALUMINUM WITH FOOD AND CHEMICALS, The Aluminum Association, New York, February 1969.

7. ALUMINUM STANDARDS AND DATA, The Aluminum Association, New York, December, 1969.

8. W.E. Berry, CORROSION IN NUCLEAR APPLICATIONS, John Wiley and Sons, New York, 1971.

9. J.H. Buddery, M.E. Clark, R.J. Pearce and J.J. Stobbs, "The Development and properties of an Oxidation-Resistant Coating for Uranium", Journal of Nuclear Materials, 13, No. 2, 1964.

10. B.L. Bramfitt and H.P. Leighly, "A Metallographic Study of Solidification and Segregation in Cast Aluminum-Uranium Alloys", Metallography, Vol. 1, No. 2, November 1968.

11. R.M. Brugger, "Metallurgy and Materials Science Branch Annual Report Fiscal Year 1970", IN-1437, Idaho Nuclear Corporation, November 1970.

12. J. Chamberlain, M.P. Johnson, J.R. Kench and A.G. Young, "The Influence of Microstructure on the Behaviour of Uranium Alloys During Temperature Cycling Creep Experiments", Journal of Nuclear Materials, 19, No. 2, 1966.

13. A.K. Chakraborty, R.S. Crouse and W.R. Martin, "Factors Affecting the Swelling During Degassing of Compacts Containing Uranium-Aluminum Inter-Metallics Dispersed in Aluminum", ORNL-TM-2800, Oak Ridge National Laboratory, March 1970.

14. P. Chiotti and J.A. Kateley, "Thermodynamic Properties of Uranium-

Aluminum Alloys", Journal of Nuclear Materials, 32, No. 1, August 1969.

15. J.K.Dawson and R.G. Sowden, CHEMICAL ASPECTS OF NUCLEAR REACTORS, Butterworth and Co., London, 1963.

16. D.R. deBoisblanc, "Reactor Engineering Branch Annual Report Fiscal Year 1968", IN-1228, Idaho Nuclear Corporation, February 1969.

17. D.R. deBoisblanc, "Reactor Engineering Branch Annual Report Fiscal Year 1969", IN-1335, Idaho Nuclear Corporation, November 1969.

18. D.R. Dickinson, R.J. Labsinger and R.B. Richman, "Corrosion of Aluminum-Clad Fuel Elements", TID-7642, Research Reactor Fuel Element Conference, Gatlinburg, Tennessee, September 1962.

19. W. Dienst, S. Nazare, F. Thummler, "Irradiation Behavior of UAl_x-Al Dispersion Fuels for Thermal High Flux Reactors", Journal of Nuclear Materials, 64, 1977.

20. J.O. Dittmer, "A Study of the Compressive Properties of Aluminum Clad Composite Nuclear Reactor Fuel Plates", Master's Thesis, Idaho State University, 1969.

21. E.A. Eldridge and H.W. Deem, "Report on Physical Properties of Metals and Alloys from Cryogenic to Elevated Temperatures", ASTM Special Technical Publication No. 296, American Society for Testing Materials, Philadelphia, April 1961.

22. H.E. Exner and G. Petzow, "Untersuchungen zur Stabilisierung von UAl_3 in Aluminiumreichen Kernbrennstoffen", Metal, No. 3, March 1969.

23. J.D. Fleming and J.W. Johnson, "Aluminum-U_3O_8 Exothermic Reactions", TID-7642, Research Reactor Fuel Element Conference, Gatlinburg, Tennessee, September 1962.

24. W.C. Francis, G.W. Gibson and W.P. Scarrah, "Some Results of Uranium Irradiations at the MTR/ETR", TID-7642, Research Reactor Fuel Element Conference, Gatlinburg, Tennessee, September 1962.

25. W.C. Francis, "Fuel Elements for Thermal Test Reactors - Performance at NRTS", AEC - Industry Meeting on Water Reactor Fuel Element Technology, Germantown, Maryland, January 1968.

26. FUEL ELEMENT FABRICATION, Volume 2, Proceedings of a Symposium in Vienna, Academic Press, New York 1961.

27. G.W. Gibson and D.R. deBoisblanc, "Uranium-Aluminum Alloy Powders for

use as Nuclear Reactor Fuels", CONF-339-5, U.S. Atomic Energy Commission, October 1963.

28. G.W. Gibson, M.J. Graber, V.A. Walker and W.C. Francis, "Results of ATR Sample Fuel Plate Irradiation Experiment", IDO-16958, Idaho Operations Office, U.S. Atomic Energy Commission, March 23, 1964.

29. G.W. Gibson, "The Development of Powdered Uranium-Aluminide Compounds for use as Nuclear Reactor Fuels", IN-1133, Idaho Nuclear Corporation, December 1967.

30. J.C. Griess, H.C. Savage, J.G. Rainwater, J.L. English and T.H. Mauney, "The Corrosion of Aluminum Alloys Under Simulated ATR and HFIR Conditions", TID-7642, Research Reactor Fuel Element Conference, Gatlinburg, Tennessee, September 1962.

31. M.J. Graber, G.W. Gibson and W.C. Francis, "Annual Progress Report on Reactor Fuels and Materials Development for FY 1963", IDO-16934, Idaho Operations Office, U.S. Atomic Energy Commission, November 25, 1963.

32. M.J. Graber, W.F. Zelezny and G.W. Bison, "Annual Progress Report on Reactor Fuels and Materials Development for FY 1964", IDO-17037, Idaho Operations Office, U.S. Atomic Energy Commission, November 1964.

33. M.J. Graber and R.A. Moen, "The Effects of Compatibility on the Performance of Aluminum Fuel Plates Containing Various Fuel Dispersions", Transactions of the American Nuclear Society, Gatlinburg, Tennessee, June 21-24, 1965.

34. D.H. Gurinsky and G.J. Dienes, NUCLEAR FUELS, D. Van Nostrand Co., New York, 1956.

35. L.J. Harrison, "Mechanical Failures of MTR Fuel Assemblies", Nucleonics, Volume 21, No. 10, October 1963.

36. L.J. Harrison, "Heat Transfer from an Aluminum/Uranium Fuel Plate in a Subcooled Pool During a TREAT Transient", Transactions of the American Nuclear Society, Seattle, June 15-19, 1969.

37. H.H. Hausner and J.F. Schumar, NUCLEAR FUEL ELEMENTS, Reinhold Publishing Corp., New York, 1959.

38. R.R. Hobbins and M.J. Graber, "ATR Extended Burnup, XA003F Results and INC-16-1 Review", Idaho Operations Office, U.S. Atomic Energy Commission, 1974.

39. R.R. Hobbins, "INC-16-2 Irradiation Experiment", Idaho Operations Office, U.S. Atomic Energy Commission, July 19, 1974.

40. R.O. Ivins, "A Study of the Reaction of Aluminum Uranium Alloy Fuel Plates

with Water Initiated by a Destructive Reactor Transient", CONF-39-70, U.S. Atomic Energy Commission, February 1963.

41. M. Jovanovic, "The Isothermal Growth of Secondary-Phase Particles in a Dilute Uranium Alloy", Journal of Nuclear Materials, 35, No. 2, May 1970.

42. C. Julian, "Evaluation of a 6.2 Kilogram U^{235} Core Loading for the Missouri University Research Reactor", University of Missouri, July 28, 1970.

43. A.R. Kaufmann, NUCLEAR REACTOR FUEL ELEMENTS, METALLURGY AND FABRICATION, John Wiley and Sons, New York, 1962.

44. R.T. King, E.L. Long, J.O. Stiegler and K. Farrell, "High Neutron Fluence Damage in an Aluminum Alloy", Journal of Nuclear Materials, 35, No. 2, May 1970.

45. J.H. Kittel, A.P. Gavin, C.C Crothers and R. Carlander, "Performance of Aluminum-Uranium Alloy Fuel Plates Under High Temperature and High Burnup Conditions", TID-7642, Research Reactor Fuel Element Conference, Gatlinburg, Tennessee, September 17-19, 1962.

46. D. Lazarevic, "Influence of Neutron Radiation on the Phase Composition of Low-Alloyed Uranium", RADIATION DAMAGE IN REACTOR MATERIALS, Volume 2, International Atomic Energy Agency, Vienna, June 1969.

47. J. Lehmann, P. Paoli and N. Azam, "Gonflement D'Alliages D'Uranium sous Irradiation", Journal of Nuclear Materials, Vol. 26, No. 2, May 1968.

48. J. Lehmann, P. Paoli and N. Azam, "Etude du Gonflement D'Alliages D'Uranium Sous Irradiation", Journal of Nuclear Materials, Vol. 27, No. 3, September 1968.

49. W.R. Martin and J.R. Weir, "Mechanical Properties of X8001 and 6061 Aluminum Alloys and Aluminum-Base Fuel Dispersion at Elevated Temperatures", ORNL-3557, Oak Ridge National Laboratory, February 1964.

50. M.M. Martin, J.H. Erwin and W.R. Martin, "Effect of Type and Concentration of Fuel on the Void Volume in Aluminum Dispersion-Type Fuel Plates", Transactions of the American Nuclear Society, Toronto, June 10-13, 1968.

51. M.M. Martin and A.E. Richt, "Effect of Void Volume on the Irradiation Performance of Aluminum-Base Dispersion-Type Fuel Plates", Transactions of the American Nuclear Society, Seattle, June 15-19, 1969.

52. M.M. Martin and W.R. Martin, "Fabrication Voids in Aluminum-Base Fuel Dispersions", ORNL-4611, Oak Ridge National Laboratory, October 1970.

53. M.M. Martin, A.E. Richt and W.R. Martin, "Irradiation Performance of Aluminum-Base Dispersion-Type Fuel Plates", Transactions of the American Nuclear Soceity, Miami, October 17-21, 1971.

54. M.M. Martin, A.E. Richt and W.R. Martin, "Irradiation Behavior of Aluminum-Base Fuel Dispersions", ORNL-4856, Oak Ridge National Laboratory, May 1973.

55. D.L. McElroy, R.S. Graves and J.P. Moor, "Physical Properties of Two-Phase Materials Used in Fuel Plate Cores", Canadian Journal of Physics, 45, 1967.

56. D.L. McElroy, "Physical Properties of Al Cermets", Oak Ridge National Laboratory, January 5, 1971.

57. Oak Ridge Reactor, "Reactor Safety Evaluation of ORNL Proposal to Modify Fuel in ORR", Oak Ridge National Laboratory, February 1977.

58. B.E. Paige, G.W. Gibson and K.L. Rohde, "The Effect of Silicon on Fabrication and Reprocessing of Aluminum Alloy Reactor Fuels", IN-1194, Idaho Nuclear Corporation, November 1968.

59. C.F. Reinke, "Irradiation and Postirradiation Annealing of Some Aluminum-Base Fuels", ANL-6665, Argonne National Laboratory, September 1963.

60. C.F. Reinke, "Postirradiation Annealing of Some Aluminum-Base Fuels", Transactions of the American Nuclear Society, Vol. 7, No. 1, Philadelphia, June 14-17, 1964.

61. A.E. Richt, C.F. Leitten, and R.J. Beaver, "Radiation Performance and Induced Transformations in Aluminum-Base Fuels", TID-7642, Research Reactor Fuel Element Conference, Gatlinburg, Tennessee, September 1962.

62. J.A.L. Robertson, IRRADIATION EFFECTS IN NUCLEAR FUELS, Gordon and Breach, New York, 1969.

63. D.J. Rucker, "Fuels and Materials Development Program Quarterly Progress Report for Period Ending June 30, 1968", ORNL-4330, Oak Ridge National Laboratory, June 1968.

64. D.J. Rucker, "Fuels and Materials Development Program Quarterly Progress Report for Period Ending September 30, 1968", ORNL-4350, Oak Ridge National Laboratory, September 1968.

65. D.J. Rucker, "Fuels and Materials Development Program Quarterly Progress Report for Period Ending December 31, 1969", ORNL-4520, Oak Ridge National Laboratory, December 1969.

66. D.J. Rucker, "Fuels and Materials Development Program Quarterly Progress Report for Period Ending March 31, 1970", ORNL-4560, Oak Ridge National Laboratory, March 1970.

67. D.J. Rucker, "Fuels and Materials Development Program Quarterly Progress Report for Period Ending September 30, 1970", ORNL-4630, Oak Ridge National Laboratory, September 1970.

68. O.J.C. Runnalls and R.R. Boucher, "Transformations in UAl_4 and $PuAl_4$ ", Transactions of the Metallurgical Society of AIME, Vol. 233, No. 7, New York, September 1965.

69. P. Tichler, "Examination of Reactor Safety Implications of Increased Fuel Loading and Extended Operating Cycle at the HFBR", Brookhaven National Laboratory, February 1977.

70. F. Thummler, H.E. Lilienthal and S. Nazare, "UAl_2-Al Instead of UAl_3-Al in Fuel Element Plates for Advanced Test-Reactors", Powder Metallurgy, Vol. 12, No. 23, London, 1969.

71. K.R. Van Horn, ALUMINUM, American Society for Metals, Metals Park, Ohio, 1967.

72. H.R. Voorhees and J.W. Freeman, "Report on the Elevated-Temperature Properties of Aluminum and Magnesium Alloys", ASTM Special Technical Publication No. 291, American Society for Testing Materials, Philadelphia, October 1960.

73. J.R. Weir, J.E. Cunningham and C.J. McHargue, "Metals and Ceramics Division Annual Progress Report for Period Ending June 30, 1974", ORNL-4970, Oak Ridge National Laboratory, October 1974.

74. R.E. Wison, "Kinetics of the Molten-Aluminum/Steam Reaction by the Levitation Method", Transactions of the American Nuclear Society, Vol. 6, No. 1, Salt Lake City, June 1963.

75. V.S. Yemel'Yanov and A.I. Yevstyukhin, THE METALLURGY OF NUCLEAR FUEL, Pergamon Press, New York, 1969.

76. W.F. Zelezny, G.W. Gibson and M.J. Graber, "A Microprobe Study of the Retention of the Fussion Gas Xenon in Irradiated Uranium Fuels Dispersed in Aluminum Clad Nuclear Reactor Fuel Plates", CONF-690910, United States Atomic Energy Commission, September 1969.

Appendix B

D_2O Tank Geometry

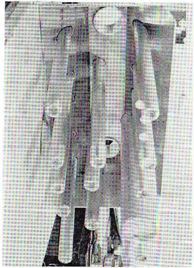

D_2O Tank Top View From Below

B-4

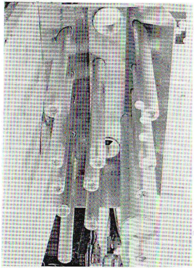

D_2O Tank Top View From Below

B-4

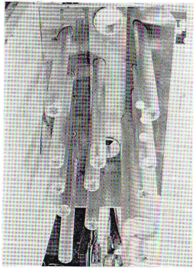

D_2O Tank Top View From Below

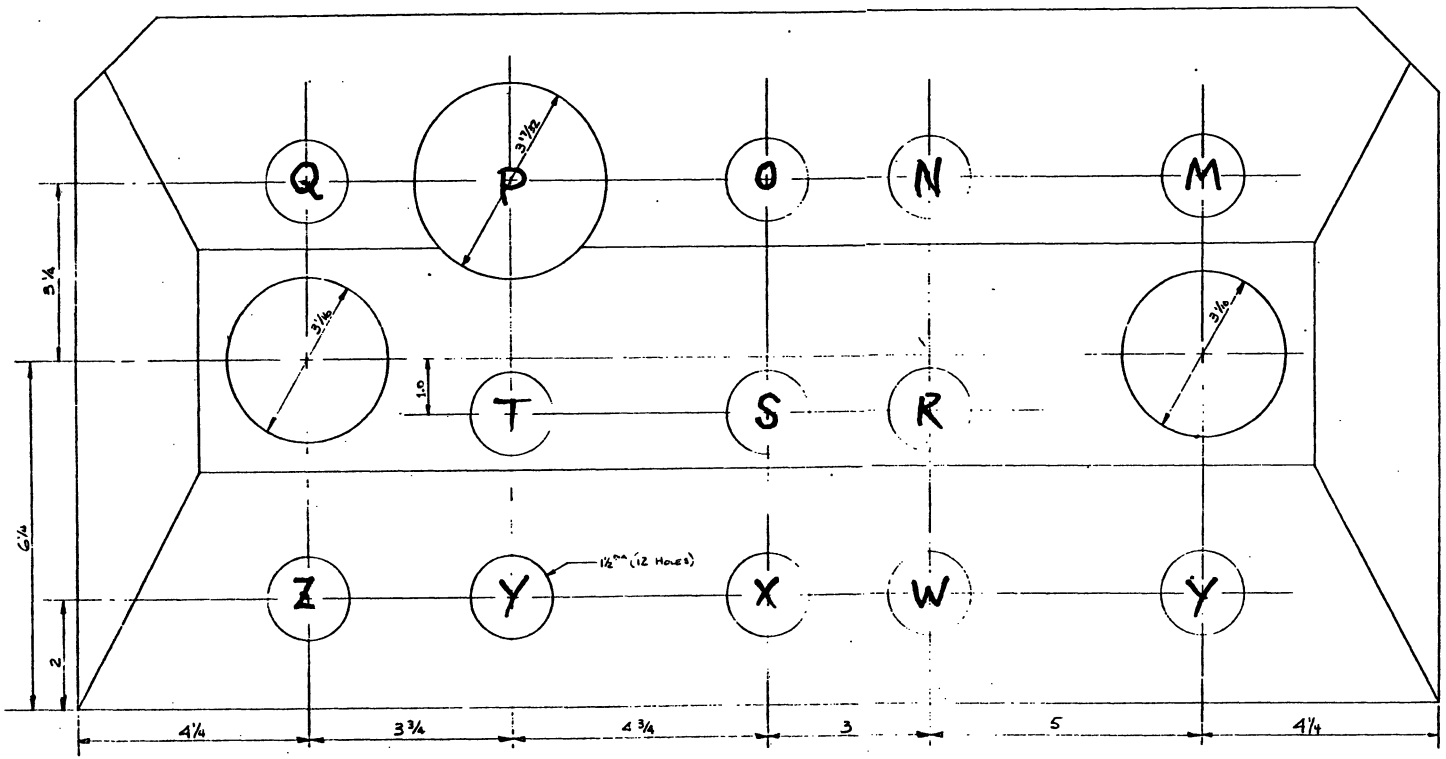

HOLE LAYOUT - TOP OF TANK (FULL SCALE)

IRRADIATION TUBE SCHEDULE

ITEM SYMBOL	NO REQ'D	ACTUAL SIZE	LENGTH
S	1	3" IPS SCH 40 AL PIPE	19"
T	12	1" IPS SCH 40 AL PIPE	19"

TUBE PLUGS

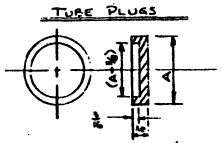

NO REQ'D	'A'
1	3.068
12	1.049

TUBE ADAPTERS

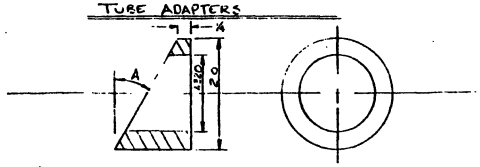

NO REQ'D	'A' DIM
3	0.0
9	56°

UNIVERSITY OF MICHIGAN
PHOENIX MEMORIAL LABORATORY
ANN ARBOR MICHIGAN

D2O TANK
IRRADIATION FACILITIES

DWG NO DT-1

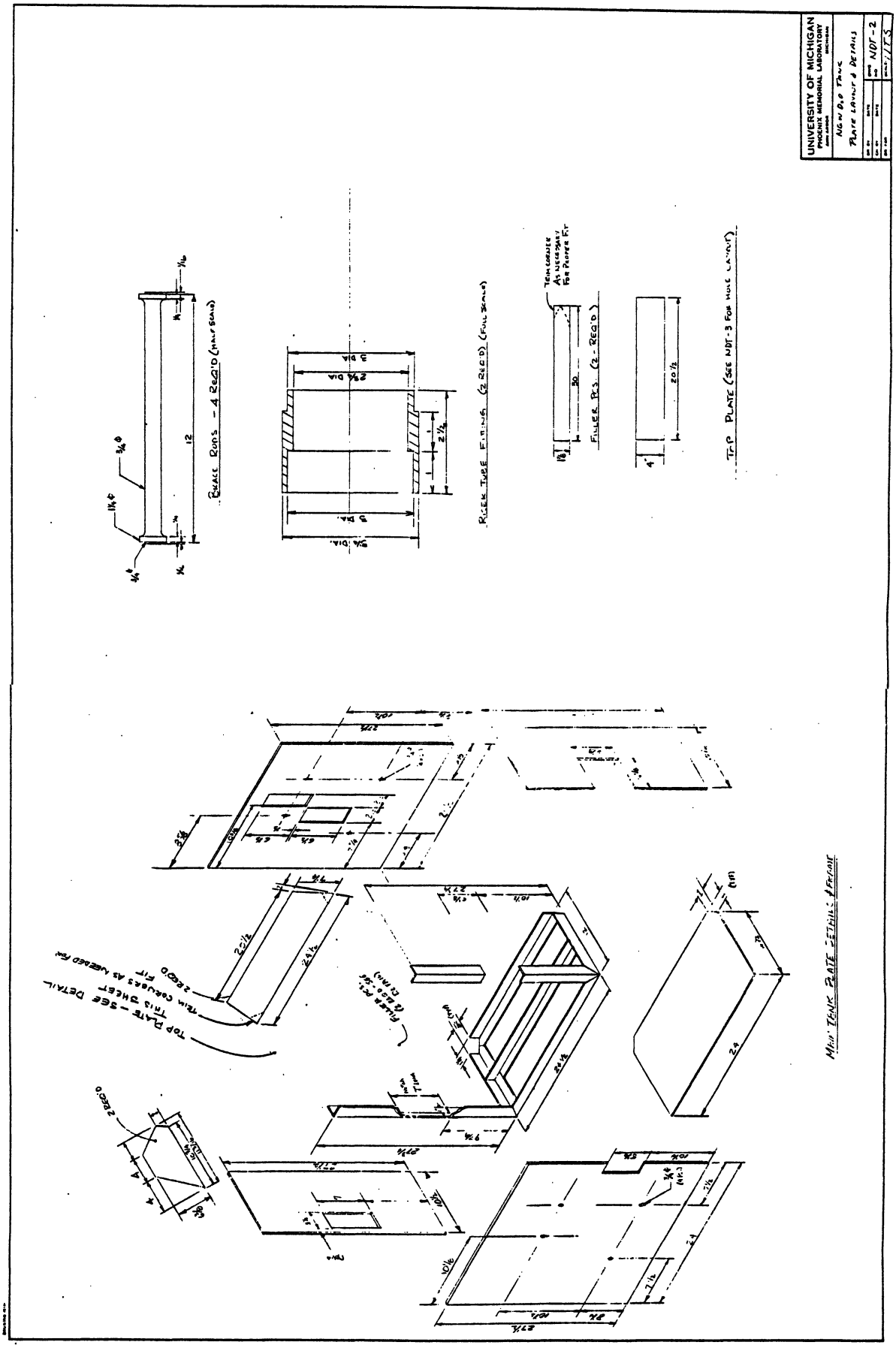
UNIVERSITY OF MICHIGAN
PHOENIX MEMORIAL LABORATORY
NDT-2
Gauge Rods - 4 Reqd (Half Scale)
Fuller Tube Fittings (2 Reqd) (Full Scale)
Fuller Rs. (2 - Reqd.)
Top Plate (See NDT-3 for Hole Layout)
Top Plate - See Detail This Sheet
Trim Coupons As Needed For Reqd Fit
Main Tank Plate Details

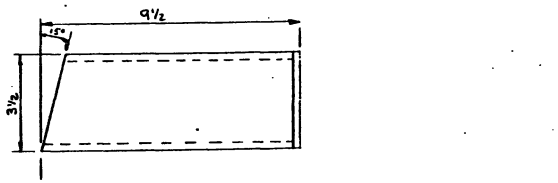

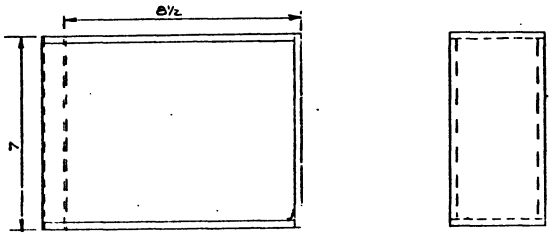

A-PORT VOID (1-REQ'D)

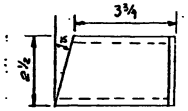

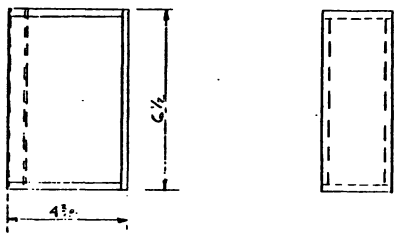

EVG PORT VOID (2-REQ'D)

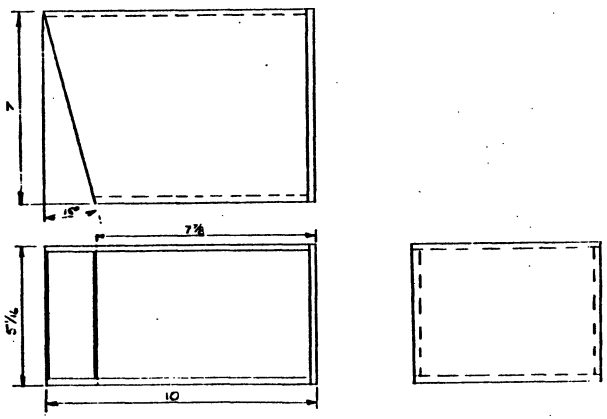

J-PORT VOID (1 REQ'D)

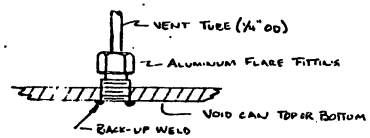

TUBE CONNECTION DETAIL

NOTES

1. ALL CANS MADE FROM ⅛" PLATE
2. ATTACH TUBE FITTINGS (SEE DETAIL) TO EACH TOP AND BOTTOM CAN PLATE BEFORE ASSEMBLY OF CAN.
3. WELD VOID CANS TO TANK PLATES BEFORE ASSEMBLY OF TANK

UNIVERSITY OF MICHIGAN
PHOENIX MEMORIAL LABORATORY
ANN ARBOR MICHIGAN

2 CU FT
VOID TANK DETAILS

DR BY	DATE	DWG NO	VDT-3
CH BY	DATE		
APP FOR		SCALE	NONE

References

1. F. B. Brown, D. C. Losey, D. K. Wehe, J. C. Lee, and W. R. Martin, Trans. Am. Nucl. Soc., 33, 746 (1979).

2. D. C. Losey, F. B. Brown, W. R. Martin, J. C. Lee, and H. Komoriya, Trans. Am. Nuc. Soc., 33, 748 (1970).

3. R. F. Barry, "LEOPARD - A Spectrum Dependent Non-spatial Depletion Code", WCAP-3269-26, Westinghouse Electric Corporation (September 1963).

4. L. E. Strawbridge and R. F. Barry, Nuc. Sci. Eng., 23, 58 (1965).

5. J. Barhen, W. Rothenstein, E. Taviv, "The HAMMER Code System", NP-565, Electric Power Research Institute (October 1978).

6. W. W. Little, Jr. and R. W. Hardie, "2DB User's Manual-Revision I", BNWL-831 REV1, Battelle Pacific Northwest Laboratory (February 1969).

7. W. W. Engle, Jr., "A User's Manual for ANISN, a One-Dimentional Discrete ordinates Transport Code wtih Anisotropic Scattering", K-1693, Oak Ridge Gaseous Diffusion Plant (March 1967).

8. K. D. Lathrop and F. W. Brinkley, "TWOTRAN-II - An Interfaced Exportable Version of the TWOTRAN Code for Two-Dimensional Transport", LA-4848-MS Los Alamos Scinetific Laboratory (1973).

9. D. R. Vondy, T. B. Fowler, and G. W. Cunningham, "VENTURE: A Code Block for Solving Multigroup Neutronics Problems Applying the Finite-Difference Diffusion Theory Approximation to Neutron Transport", ORNL-5062, Oak Ridge National Laboratory (1975).

10. W. R. Cadwell, "PDQ-7 Reference Manual", WAPD-TM-678, Westinghouse Electric Corporation (Jan. 1967).

11. R. W. Hardie and W. W. Little, Jr., "1DX: A One-Dimensional Diffusion Code for Generating Effective Nuclear Cross Sections", BNWL-954, Battelle Pacific Northwest Laboratory (1968).

12. M. H. Theys, Nuc. Sci. Eng., 7, 58 (1960).

13. J. J. Duderstadt and W. R. Martin, Transport Theory, Wiley-Interscience, New York (1979).

14. J. Hardy, D. Klein, and J. J. Volpe, "A Study of Physics Parameters in Several Water-Moderated Lattices of Slightly Enriched and Natural Uranium", WAPD-TM-931, Westinghouse Electric Corporation (March, 1970).

15. W. R. Martin to J. E. Matos, University of Michigan, Department of Nuclear Engineering letter (December 19, 1978).

16. S. Jabbawy, J. Karni, W. Rothenstein, and S. Velner, Nuclear Data in Scinece and Technology, Vol. II, p. 147, International Atomic Energy Agency, Vienna (1973).

17. W. Rothenstein, "ENDF/B-IV Thermal Reactor Lattice Benchmark Analysis with Monte Carlo Resonance Treatment", BNL-NCS-50451, Seminar on U238 Resonance Capture, p. 222, Brookhaven National Laboratory (1975).

18. J. E. Suich and H. C. Honeck, "The HAMMER System", DP-1064, Savannah River Laboratory (Jan. 1967).

19. W. L. Woodruff, "Comparison of EPRI-CELL and VIM (Monte Carlo) Generated Microscopic Cross-Section Data for a Slab Cell Representative of MTR-Type Research and Test Reactors Using Highly-enriched and Reduced-enrichment Uranium Fuels", Argonne National Laboratory Internal Memorandum (Jan. 3, 1979).

20. R. E. Prael and L. J. Milton, "A User's Manual for the Monte Carlo Code VIM", FRA-TM-84, Argonne National Laboratory (1976).

21. W. R. Cobb, W. J. Eich, and D. E. Tivel, "EPRI-CELL Code Description", Advanced Cycle Methodology Program System Documentation, Nuclear Associates International Corporation (October, 1975).

22. E. B. Johnson, "Power Calibration for BSR Loading 33", CF-57-11-30, Oak Ridge National Laboratory (1957).

23. W. K. Anderson, R. L. Eichinger, R. A. Harlow, and G. J. Gosgrove, "Boron-Stainless Steels", Neutron Absorber Materials for Reactor Control, W. K. Anderson and J. S. Theilacker, Eds., p. 235-269, U. S. Gov. Printing Office (1962).

24. H. C. Honeck, Nuc. Sci. & Eng., 8, 193 (1960).

25. H. C. Honeck, "A Thermalization Transport Code for Reactor Lattice Calculations", BNL-5826, Brookhaven National Laboratory (1962).

26. W. C. Bickley and J. Nayler, Jr., Phil. Mag. 20, 343 (1935).

27. I. Carlvik, Proc. Third International Conf. on Peaceful Uses of Atomic Energy, Vol. II, p. 225, International Atomic Energy Agency, Geneva (1965).

28. J. M. Hendrie, "Final Safety Analysis Report on the Brookhaven High Flux Beam Research Reactor", BNL-7661, Brookhaven National Laboratory (1964).

29. A. M. Weinberg and E. P. Wigner, The Physical Theory of Neutron Chain Reactors, Univ. of Chicago Press, Chicago (1956).

30. H. Komoriya to J. L. Snelgrove, "Reduced Enrichment Fuel Element Loading Calculations for the Ford Nuclear Reactor", Argonne National Laboratory Internal Memorandum (February 14, 1979).

31. H. Komoriya, J. C. Lee, and W. R. Martin, Trans. Am. Nucl. Soc., 32, Suppl. 1, 31 (1979).

32. J. E. Matos and K. E. Freese, Trans. Am. Nucl. Soc., 33, 739 (1979).

33. H. Komoriya, Trans. Am. Nucl. Soc., 33, 745 (1979).

34. J. A. Cox and C. C. Webster, "Water Loss at the Low Intensity Testing Reactor", ORNL-TM-632, Oak Ridge National Laboratory (Aug. 1964).

35. S. E. Beall, "An Experimental Determination of Fission Product Heating After Shutdown of the Low Intensity Training Reactor", ORNL-1075, Oak Ridge National Laboratory (Sept. 1951).

36. K. H. Beckurts and K. Wirtz, Neutron Physics, Springer-Verlag (1964).

37. H. D. Warren, Nuc. Sci. Eng., 48, 331 (1972).

38. T. Laaksonen and J. Sasstamoinen, Proceedings of IAEA Specialists' Meeting on In-core Instrumentation and Failed Fuel Detection and Location, pp.111-131, AECL-5124, Atomic Energy of Canada Limited (May 1974).

39. M. N. Baldwin and J. E. Rogers, Physics Verification Program, BAW-3647-23, Babcock and Wilcox Co. (December 1971).

40. C. W. Joslin, Proceedings of IAEA Specialists' Meeting on In-Core Instrumentation and Failed Fuel Detection and Location, pp 151-154 AECL-5124, Atomic Energy of Canada Limited (May 1974).

41. J. M. Carpenter, R. F. Fleming, and H. Bozorgmanesh, Trans. Am. Nucl. Soc., 22, 606 (Nov. 1975).

42. J. Duderstadt and L. Hamilton, Nuclear Reactor Analysis, John Wiley and Sons (1976).

43. C. A. Oster, "Review of Unfolding Methods Used in the U.S. and Their Standardization for Dosimetry", BNWL-SA-6503, Battele Pacific Northwest Laboratory (October 1977).

44. W. L. Zipj, Proceedings of the Second ASTM-EURATOM Symposium on Reactor Dosimetry, pp. 1333-1365, NUREG/CP-0004, National Technical Information Service (Oct. 1977).

45. W. N. McElroy, S. Berg, T. Crockett, and R. Hawkins, "A Computer-Automated Iterative Method for Neutron Flux Spectra Determination by Foil Activation", AFWL-TR-67-41, Atomics International (Sept. 1967).

46. L. Greenwood, Private Communication (1979).

47. F. Schmittroth, Nuc. Sci. Eng., 72, 19 (1979).

48. H. F. Henry, Nuc. Sci. Eng., 72, 65 (1979).

49. R. H. Fulmer and T. F. Ruane, Nucl. Appl., 3, 191 (March 1967).

50. W. H. Zachariasen, Theory of X-ray Diffraction in Crystals, Dover, New York (1945).

51. G. E. Bacon and R. D. Lowde, Acta. Crysta., 1, 303 (1948).

52. G. E. Bacon, Neutron Diffraction, Clarendon Press, London (1962).